広島大学学位請求論文

Distribution mechanism of various ions during coprecipitation with barite and its application to geochemistry and environmental chemistry

(バライト共沈に伴う元素分配機構の解明とその地球化学・環境学的な応用)

2016 年

広島大学大学院理学研究科

地球惑星システム学専攻

徳永 紘平

Distribution mechanism of various ions during coprecipitation with barite and its application to geochemistry and environmental chemistry

by

Kohei Tokunaga

Department of Earth and Planetary Systems Science, Graduate School of Science,

Hiroshima University, Higashi-Hiroshima, Hiroshima 739-8526, Japan

CONTENTS

Abstract

Barite has specific characteristics for applications, which exhibits (i) extremely low solubility, (ii) incorporation of many elements because of the large ionic radii as host ions, (iii) high density compared with other minerals, and (iv) high crystal stability under wide ranges of pH, E_h, temperature, and pressure conditions. In this study, we focused on the characteristics of barite to be utilized as (i) a geochemical tracer for paleo-environmental reconstruction and (ii) a sequester phase for removal of toxic and/or radioactive elements from contaminated solution. The systematics of major and trace element behaviors to barite were also investigated to provide the geochemical rules of incorporation ions to barite.

The systematic of incorporation ions between barite and water in terms of the partition coefficients and unit-cell dimensions of these ions in barite as a function of ionic radius was investigated through batch experiments in Chapter 2. Analysis of the partition coefficients of incorporated ions for barite shows that ions having a smaller or slightly larger radii as a substituted ion can be incorporated more efficiently in a crystal lattice than those with much larger radii. Analysis of unit-cell dimensions of incorporation ions for barite also showed that larger ions formed a larger distortion of crystal lattice in barite structure, which provides larger incorporation of trace elements by

barite. Thus, the systematics of element behaviors provides a good estimates of partition coefficients to mineral for larger incorporation of trace elements.

The partitions of selenate/selenite (Se(VI)/Se(IV)) and arsenate/arsenite (As(V)/As(III)) between barite and solutions were investigated through batch experiments in Chapters 3 and 4 to develop a new geochemical tracers to estimate the redox condition in the past. The results showed that the inorganic Se(VI)/Se(IV) or As(V)/As(III) ratio in water could be estimated as the Se(VI)/Se(IV) or As(V)/As(III) ratio in barite, respectively. Especially under equilibrium, in terms of the redox condition, both species ratios in barite could indicate the redox condition of the depositional environment, and determine whether the redox condition is below or above the redox boundary of Se(VI)/Se(IV) or As(V)/As(III). Given that the redox boundary of Se(VI)/Se(IV) is at a higher redox potential rather than the As(V)/As(III) boundary, the coupling of the As(V)/As(III) ratio with the Se(VI)/Se(IV) ratio in barite could more precisely constrain the redox environment at the time of deposition of barite in natural systems, which can suggest whether barite is precipitated under oxic, suboxic, or anoxic redox environments.

The uptake of Se(IV) and Se(VI) during adsorption and coprecipitation with barite was investigated through batch experiments in Chapter 5 to understand the factors

controlling the distribution of trace elements to barite for effective removal of Se(IV) and Se(VI) from contaminated solutions by barite. The results showed that the uptake of Se in solution by barite were mainly controlled by the chemical affinity related to adsorption on surface and the structural affinity related to geometry of incorporated metals in substituted site. The uptake of Se(IV) by barite is dependent on the speciation by pH, crystal lattice distortion by competitive ion of Ca^{2+}, and sulfate and selenite ratios due to its high chemical and low structural affinity to barite. The uptake of Se(VI) by barite, on the other hand, is dependent on the crystal lattice distortion by competitive ion of Ca^{2+}, crystal lattice distortion by saturation states, and sulfate and selenate ratios due to its low chemical and high structural affinity to barite. Thus, we can effectively remove Se(IV) and Se(VI) from solution by barite to understand mechanisms of coprecipitation with barite.

Thus, barite can be used as (i) a new proxy to estimate redox conditions in the past because of the incorporation and preservation of As(V)/As(III) and Se(VI)/Se(IV) ratio in barite and (ii) a sequestering phase for effective removal of toxic and/or radioactive elements from polluted waters by understanding of factors controlling the distribution of the incorporation ions between barite and water.

Chapter 1. Introduction

1.1. Characteristics of barite for geochemical- and environmental-applications

Barite is a common phase in many geological environments. It has specific characteristics of application for geochemical- and environmental-chemistry. First is the high stability of barite under wide range of conditions, such as E_h, pH, temperature, and pressure. The redox boundaries of mineral phases (barite, calcite, hydrous ferric oxide) in E_h-pH range are shown in Fig. 1, which shows that barite phase little change as a function of pH and E_h compared to calcite (pH dependence) and iron hydroxides (pH and E_h dependence). Second is the larger incorporation of many major and trace elements in its crystal lattice of barium (Ba^{2+}) and sulfate (SO_4^{2-}) site because of the large ionic radii of substituted ion in host phase. The systematics of distribution coefficients of divalent cation as a function of ionic radius between barite and calcite are shown in Fig. 2, which suggested the greater partition of larger size ions into barite than calcite. Third is the extremely low solubility of barite compared to other minerals (ca 10^{-10} at 25 °C, 1 atm; Church and Wolgemuth, 1972), which causes immediate deposition of barite in natural environment by mixing Ba^{2+} and SO_4^{2-} ion.

In this study, we focused on their characteristics of barite to be utilized as (i) a geochemical tracer for paleo-environmental reconstruction and (ii) a sequester phase of

toxic and/or radioactive elements from contaminated solution. Many studies have focused on the search for reliable geochemical tracers to reconstruct past oceanic conditions and productivity changes [Van Beek et al., 2003]. From this point of view, barite appears to be a promising tracer because of its high preservation in sediments and provides a wide range of applications for paleo-environment. In addition, barite works as an effective sequestering phase for toxic and/or radioactive elements from contaminated solutions because of its high stability and low solubility in environments. Thus, in this study, coprecipitation of major and trace elements with barite were investigated and developed as a geochemical tool to know paleo-environments and effective remediation methods to remove toxic and/or radioactive elements from polluted solutions.

1.2. Possible application of barite to geochemical study

1.2.1. The occurrence of barite in natural environments

Seawater is largely under-saturated with respect to barite because of the lack of barium (Ba) ion in seawater [Monnin et al., 1999; Griffith and Paytan, 2012]. Barite is formed under supersaturation conditions, such as the water column (marine barite), hydrothermal vents (hydrothermal barite), and continental margin sediments (cold seep

barite), where the enrichment of Ba^{2+} ion is achieved by many factors. Because of its diverse mode of formation, the occurrence of barite in the ocean can be used as proxies for paleo-environment.

Marine barite is produced in the water column in association with degradation organic matter [McManus et al., 1999; Eagle et al., 2003; Gonneea and Paytan, 2006; Hein et al., 2007; Paytan et al., 2007]. Barium is released to seawater during decay of organic material in microenvironments, which achieves the supersaturation with respect to barite and causes precipitation of barite in the water column. Dymond (1992) noted that Ba export from the upper ocean is closely correlated with the export of organic carbon (C_{org}). Thus, the accumulation rate of marine barite is one of the most promising proxy to reconstruct past biogeochemical processes in the ocean, including export productivity. Barite preservation in sediments has higher burial efficiency than organic carbon. The preservation rate of organic carbon is less than 1%, while that of Ba in barite is as high as 30% in oxic sediments [Dymond et al., 1992; Paytan and Kastner, 1996; Eagle et al., 2003]. Thus, the content of marine barite in sediments work as a proxy to reconstruct past oceanic conditions and productivity changes.

Cold seep barite is formed in submarine vent when Ba-rich fluids are driven out of the sediment by tectonic and hydrological processes [Torres et al., 2003; Hein et al., 2007;

Snyder et al., 2007]. Several source of Ba to fluids is due to the remobilization of marine barite deposited in sulfate reducing sediments in the continental margin. Upon burial, microbial degradation of organic carbon in these environments leads to methanogenesis (CH_4). The escaping CH_4 of pore-water is consumed through anaerobic oxidation of methane (AOM) ($CH_4+SO_4^{2-} \rightarrow HCO_3^- + HS^-+H_2O$), which leads to SO_4^{2-} depletion of pore waters and dislocation of barite under the conditions. The discharge of Ba^{2+} at the seafloor results in barite deposition at cold methane seeps within continental margin sediments. Thus, the marine geochemical cycling of Ba may provide constraints on past CH_4 fluxes from gas hydrate systems, and work as a proxy for AOM.

Hydrothermal barite precipitates from Ba-rich fluids formed in association with volcanic hydrothermal activity ascending from depth and mixing with seawater near the sea floor [Hein et al., 2007; Griffith and Paytan, 2012]. The main Ba source to hydrothermal fluids is from the leaching of oceanic or continental rocks driven by heat from magmatic activity. Hydrothermal fluids contains considerable amounts of trace elements, including redox sensitive elements, such as selenium (Se) and arsenic (As), and these elements are incorporated in the crystal lattice of barite. In the present study, the information of redox sensitive element in hydrothermal barite can also be employed as a geochemical probe of the depositional redox condition in the paleo-environmental study.

1.2.2. Application of selenium and arsenic in barite as redox proxies

Redox potential (E_h, if standardized to hydrogen electrode) is an important physicochemical factor that controls the chemical processes in the hydrosphere on earth because redox reactions strongly affect the behaviors of various chemical species. Previous studies estimated redox condition indirectly and qualitatively based on the solid-water distributions of redox-sensitive elements caused by the variation in their oxidation states, such as the relative enrichment-depletion profiles of particular elements (e.g., iron and manganese) in the environment [Thomson et al., 1993; Calvert et al., 1993; Barnaby and Rimstidt, 1989; Algeo et al., 2004; Lu et al., 2010]. However, the estimation of redox conditions based on these profiles may not be reliable because (i) elemental concentrations are influenced by factors such as secondary adsorption-desorption reactions and subsequent diagenesis, and (ii) only the relative evaluation of the redox condition can be obtained by the depth profiles of particular elements. This study aimed to propose a redox indicator using the oxidation states of redox-sensitive elements in a certain mineral to directly estimate the redox condition at the time of the mineral formation.

We here suggest that five factors must be fulfilled to utilize the valence ratio of trace element in the precipitates as a redox indicator:

(1) The element must be redox sensitive which has several valences variable as a function of the redox condition in the depositional environment.

(2) Each valence species should be readily dissolved into water

(3) The solid-water distribution behavior of each valence species should be similar.

(4) The trace element in the mineral in natural systems must be over several ppm (mg/kg) for XANES analysis.

(5) The mineral is stable under a wide range of pressure, temperature, E_h, and pH conditions to preserve the valence state of the trace element.

In this study, selenium (Se) and arsenic (As) oxyanions were selected as possible elements. This is because (i) Se is dissolved in water either as selenite [$Se^{IV}O_3^{2-}$: Se(IV)] or selenate [$Se^{VI}O_4^{2-}$: Se(VI)] ion under oxic and suboxic conditions, respectively, and (ii) As is dissolved in water either as arsenite [$As^{III}O_3^{3-}$: As(III)] or arsenate [$As^{V}O_4^{3-}$: As(V)] ion under suboxic and anoxic conditions, respectively. Given that the redox boundary of the Se(VI)/Se(IV) ratio is at a higher redox potential compared with the As(V)/As(III) boundary, the combination of the two systems can provide information on the As(III)/As(V) and Se(VI)/Se(IV) ratios in water, and can suggest whether barite is precipitated under oxic, suboxic, or anoxic redox environments.

This work focused on barite ($BaSO_4$) as a host phase of Se and As for our purpose.

Barite, which is stable under a wide range of pressure, temperature, E_h, and pH, can incorporate various trace elements in its crystal. Barite formation occurs in various environments, such as seawater, seafloor hydrothermal fluid, groundwater, and onshore hot spring water. Thus, barite can be employed as a geochemical probe of the depositional redox condition in the paleo-environmental study

Both elemental features validate Factors (1)-(3). Factor (4) is also validated because both Se and As were enriched and incorporated into barite near hot springs and hydrothermal systems by our previous studies. Factor (5) is validated because of its high stability of barite in natural systems, also a variety of condition is assured for barite, whereas the preservation of As(III)/As(V) and Se(VI)/Se(IV) ratios in the mineral during the long-range period has not been studied. Thus, in this study, coprecipitation experiments of Se and As with barite were conducted to investigate the influence of oxidation state on its immobilization into barite through batch experiments, and we can adopt the As(III)/As(V) and Se(VI)/Se(IV) ratios in barite to estimate E_h of the environment, whether it is precipitated under oxic, suboxic, or anoxic redox environments (Fig. 3).

1.3. Possible application of barite to environmental study

1.3.1. Factors controlling the fate of major and trace elements in environments

The mobility and distribution of major and trace elements in solutions are largely controlled by adsorption and coprecipitation with mineral phases. In particular, coprecipitation process is important because incorporation of a contaminant ion in a host mineral can lead to its immobilization in its crystal structure. The incorporation of trace elements into the crystal lattice can retard their migration much more effectively than simple adsorption on crystal surface [Tesoriero and Pankow, 1996; Lakshtanov and Stipp, 2004]. Adsorption ion on surface is easily and quickly redissolve to the water because of only accumulation on surface, while incorporated ion into structure is not released unless the host mineral dissolves. Thus, the incorporation process controls the mobility of major and trace elements in the environment and can be exploited as a remediation procedure to remove toxic and/or radioactive elements from contaminated solutions at Fukushima Daiichi Nuclear Power Station by coprecipitation with iron oxy-hydroxide and calcite before ion exchange treatments (Fig. 4). However, Tesoriero and Pankow (1996) commented the fact that partitions of major and trace elements into mineral phases was not widely considered in environmental assessments, although the incorporation of ion into mineral structure has been known for a long time, and the factor controlling incorporation process has not been well understood.

1.3.2. Application of barite as an effective sequestering phase

Barite is an important phase in many nuclear waste repositories, where the mobility of toxic and/or radioactive elements is strongly decreased by interaction with this mineral. Previous studies showed the effectiveness of barite as a sequestering phase for some divalent cations (Sr^{2+}, Pb^{2+}, Ra^{2+}) and oxyanions (CrO_4^{2-}, SeO_4^{2-}) [Prieto et al., 2002; Bosbach et al., 2010; Rosenberg et al., 2011a; Rosenberg et al., 2011b; Prieto et al., 2013; Nishimura et al., 2007; Widanagamage et al., 2014; Zhang et al., 2014]. The uptake of Ra by barite was widely studied among them, which showed the high partition coefficient values of Ra^{2+} in barite relative to other minerals, such as gypsum, anhydrite, calcite, aragonite, and celestite. These studies have shown that barite works as an ideal host mineral for Ra in brines and fresh water due to the similar ionic radii of Ra^{2+} and Ba^{2+}, their electro-negativities and electronic configuration, and the identical crystallographic structure between barite and pure $RaSO_4$ [Curti, 1999; Zhu, 2004a].

However, except for the Ra^{2+} uptake by barite, the mechanisms influencing the fate of ions during coprecipitation with barite were little understood by previous studies and the partition experiments of major and trace elements between barite and aqueous solutions have not been conducted. There is few studies about the behavior of major and trace elements with barite, and the systematics of the partitions to barite were not well

understood. Thus, in this study, the systematics of partition coefficient between barite and solutions were investigated to understand the mobility and distribution of ionic species to barite in natural systems. In addition, factors controlling the coprecipitation of major and trace elements with barite were also investigated to develop effective removal methods of toxic and/or radioactive elements from polluted waters. Because of the high crystal stability of barite under a wide range of conditions, barite can also work as a barriers for the retention of radioactive elements, such as iodine, selenium, and technetium oxyanions (Fig. 4).

1.4. Objective of this study

In this study, we focused on the characteristics of barite to utilize (i) paleo-environmental tracer and (ii) sequestering phase for toxic and/or radioactive elements from solution. In this paper, I will describe them in four chapters. In Chapter 2, the systematics of partition coefficient between barite and solutions were investigated for understanding the mobility and distribution of ionic species in natural systems [Chapter 2: Distribution of major and trace elements between barite and aqueous solutions]. In the Chapters 3 and 4, the partition of redox sensitive elements, including selenium and arsenic, between barite and solutions were investigated to develop new geochemical

probe of the depositional redox condition in the paleo-environment [Chapter 3: Application of selenium in barite as a redox indicator for oxic/suboxic redox condition; Chapter 4: Application of arsenic in barite as a redox indicator for suboxic/anoxic redox condition]. In Chapter 5, factors controlling the fate of major and trace elements to barite were determined for effective removal of toxic and/or radioactive elements from polluted waters [Chapter 4: Effective removal of selenite and selenate from solutions by barite]. The relationship among these chapters are shown in Fig. 5.

References

Algeo, T. J., Maynard, J. B., 2004. Trace-element behavior and redox facies in core shales of Upper Pennsylvanian Kansas-type cyclothems. Chem. Geol. 206, 289-318.

Bosbach, D., Böttle, M., & Metz, V. (2010). Experimental study on Ra2+ uptake by barite (BaSO4). *Kinetics of solid solution formation via BaSO4*.

Calvert, S.E., Pedersen, T. F., 1993. Geochemistry of recent oxic and anoxic sediments: implications for the geological record. Mar. Geol. 113, 67-88.

Church, T. M., & Wolgemuth, K. (1972). Marine barite saturation. Earth and Planetary Science Letters, 15(1), 35-44.

Curti, E. (1999). Coprecipitation of radionuclides with calcite: estimation of partition coefficients based on a review of laboratory investigations and geochemical data. Applied Geochemistry, 14(4), 433-445.

Dymond, J., Suess, E., & Lyle, M. (1992). Barium in deep - sea sediment: A geochemical proxy for paleoproductivity. Paleoceanography, 7(2), 163-181.

Eagle, M., Paytan, A., Arrigo, K. R., van Dijken, G., & Murray, R. W. (2003). A comparison between excess barium and barite as indicators of carbon export. Paleoceanography, 18(1).

Gonneea, M. E., & Paytan, A. (2006). Phase associations of barium in marine sediments.

Marine Chemistry, 100(1), 124-135.

Griffith, E. M., & Paytan, A. (2012). Barite in the ocean–occurrence, geochemistry and palaeoceanographic applications. Sedimentology, 59(6), 1817-1835.

Hein, J. R., Zierenberg, R. A., Maynard, J. B., & Hannington, M. D. (2007). Barite-forming environments along a rifted continental margin, Southern California Borderland. Deep Sea Research Part II: Topical Studies in Oceanography, 54(11), 1327-1349.

Lakshtanov, L. Z., & Stipp, S. L. S. (2004). Experimental study of europium (III) coprecipitation with calcite. Geochimica et cosmochimica acta, 68(4), 819-827.

McManus, J., Berelson, W. M., Hammond, D. E., & Klinkhammer, G. P. (1999). Barium cycling in the North Pacific: Implications for the utility of Ba as a paleoproductivity and paleoalkalinity proxy.

Monnin, C., Jeandel, C., Cattaldo, T., & Dehairs, F. (1999). The marine barite saturation state of the world's oceans. Marine Chemistry, 65(3), 253-261.

Nishimura, T., Hashimoto, H., & Nakayama, M. (2007). Removal of Selenium (VI) from Aqueous Solution with Polyamine‐type Weakly Basic Ion Exchange Resin. Separation Science and Technology, 42(14), 3155-3167.

Paytan, A., & Kastner, M. (1996). Benthic Ba fluxes in the central Equatorial Pacific,

implications for the oceanic Ba cycle. Earth and Planetary Science Letters, 142(3), 439-450.

Paytan, A., & Griffith, E. M. (2007). Marine barite: Recorder of variations in ocean export productivity. Deep Sea Research Part II: Topical Studies in Oceanography, 54(5), 687-705.

Prieto, M., Fernández-González, Á., & Martín-Díaz, R. (2002). Sorption of chromate ions diffusing through barite-hydrogel composites: Implications for the fate and transport of chromium in the environment. *Geochimica et Cosmochimica Acta*, *66*(5), 783-795.

Prieto, M., Astilleros, J. M., & Fernández-Díaz, L. (2013). Environmental remediation by crystallization of solid solutions. Elements, 9(3), 195-201.

Rosenberg, Y. O., Metz, V., & Ganor, J. (2011). Co-precipitation of radium in high ionic strength systems: 1. Thermodynamic properties of the Na–Ra–Cl–SO 4–H 2 O system–estimating Pitzer parameters for RaCl 2. *Geochimica et Cosmochimica Acta*, *75*(19), 5389-5402.

Rosenberg, Y. O., Metz, V., Oren, Y., Volkman, Y., & Ganor, J. (2011). Co-precipitation of radium in high ionic strength systems: 2. Kinetic and ionic strength effects. *Geochimica et Cosmochimica Acta*, *75*(19), 5403-5422.

Snyder, G. T., Dickens, G. R., & Castellini, D. G. (2007). Labile barite contents and

dissolved barium concentrations on Blake Ridge: new perspectives on barium cycling above gas hydrate systems. Journal of Geochemical Exploration, 95(1), 48-65.

Tesoriero, A. J., & Pankow, J. F. (1996). Solid solution partitioning of Sr 2+, Ba 2+, and Cd 2+ to calcite. Geochimica et Cosmochimica Acta, 60(6), 1053-1063.

Thomson, J., Higgs, N. C., Croudace, I. W., Colley, S., Hydes, D. J., 1993. Redox zonation of elements at an oxic/post-oxic boundary in deep-sea sediments, Geochim. Cosmochim. Acta 57, 579–595.

Torres, M. E., Bohrmann, G., Dubé, T. E., & Poole, F. G. (2003). Formation of modern and Paleozoic stratiform barite at cold methane seeps on continental margins. Geology, 31(10), 897-900.

Van Beek, P., Reyss, J. L., Bonte, P., & Schmidt, S. (2003). Sr/Ba in barite: a proxy of barite preservation in marine sediments?. Marine Geology, 199(3), 205-220.

Widanagamage, I. H., Schauble, E. A., Scher, H. D., & Griffith, E. M. (2014). Stable strontium isotope fractionation in synthetic barite. Geochimica Et Cosmochimica Acta, 147, 58-75.

Zhang, T., Gregory, K., Hammack, R. W., & Vidic, R. D. (2014). Co-precipitation of radium with barium and strontium sulfate and its impact on the fate of radium during treatment of produced water from unconventional gas extraction. *Environmental*

science & technology, *48*(8), 4596-4603.

Figure legends

Figure 1. The existence boundaries of mineral phases such as barite ($BaSO_4$), calcite ($CaCO_3$), and hydrous ferric oxide (FeOOH) in the E_h-pH range.

Figure 2. The apparent K_d values as a function of the ionic radius of cations between barite and calcite.

Figure 3. A new redox indicator based on the As(III)/As(V) and Se(VI)/Se(IV) ratios in barite to estimate E_h range of the depositional environment.

Figure 4. Overview of the multi-nuclide removal equipment (ALPS) at Fukushima Daiichi Nuclear Power Station and the new application of barite as a barriers for the retention of radioactive elements, such as iodine, selenium, and technetium oxyanion.

Figure 5. Overview of the relationship among these chapters.

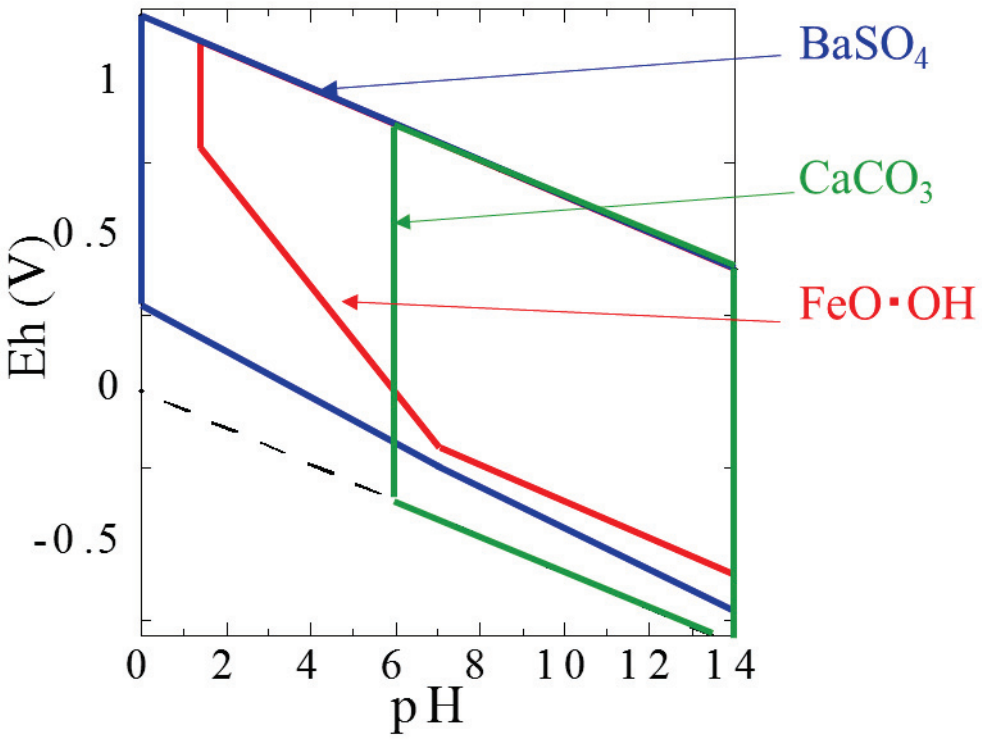

Figure 1. The existence boundaries of mineral phases such as barite ($BaSO_4$), calcite ($CaCO_3$), and hydrous ferric oxide (FeOOH) in the E_h-pH range.

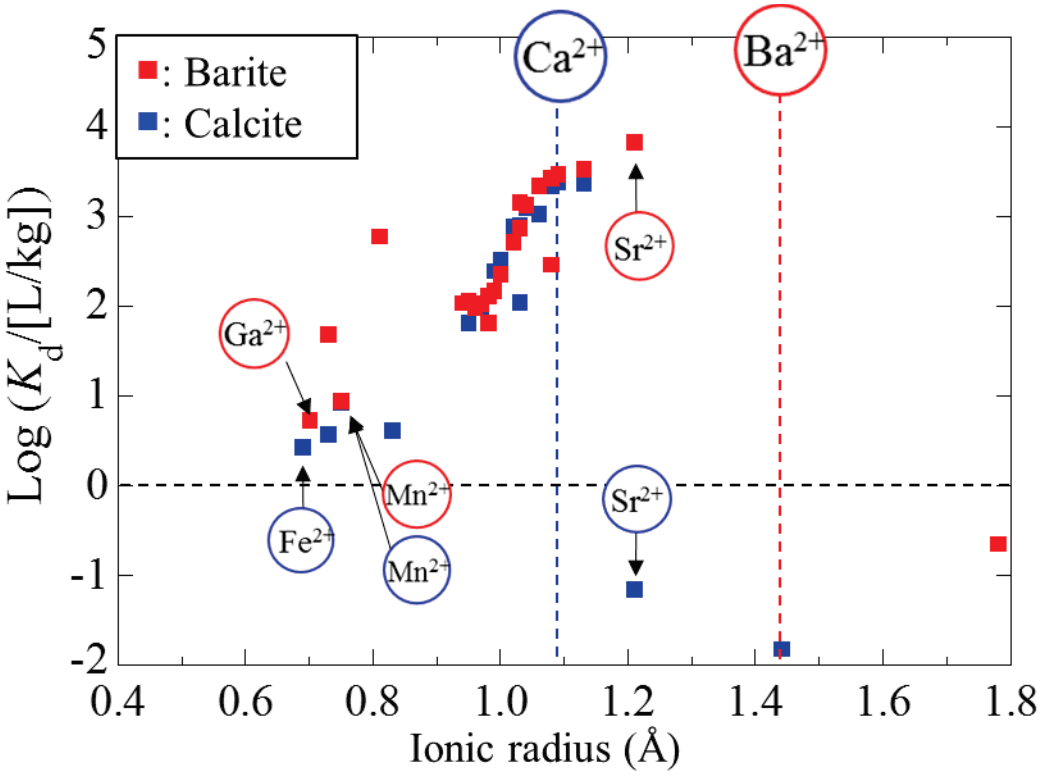

Figure 2. The apparent K_d values as a function of the ionic radius of cations between barite and calcite.

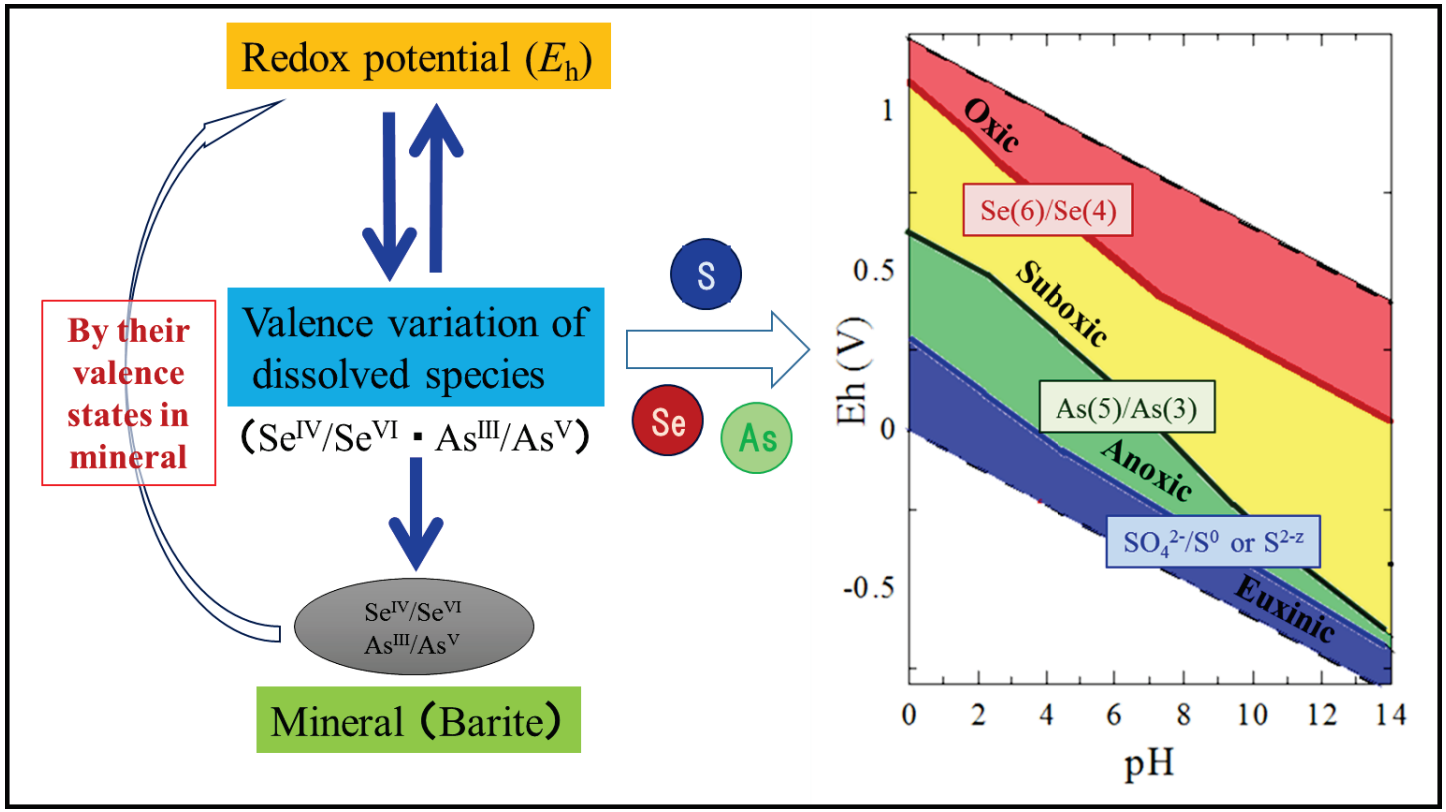

Figure 3. A new redox indicator based on the As(III)/As(V) and Se(VI)/Se(IV) ratios in barite to estimate E_h range of the depositional environment.

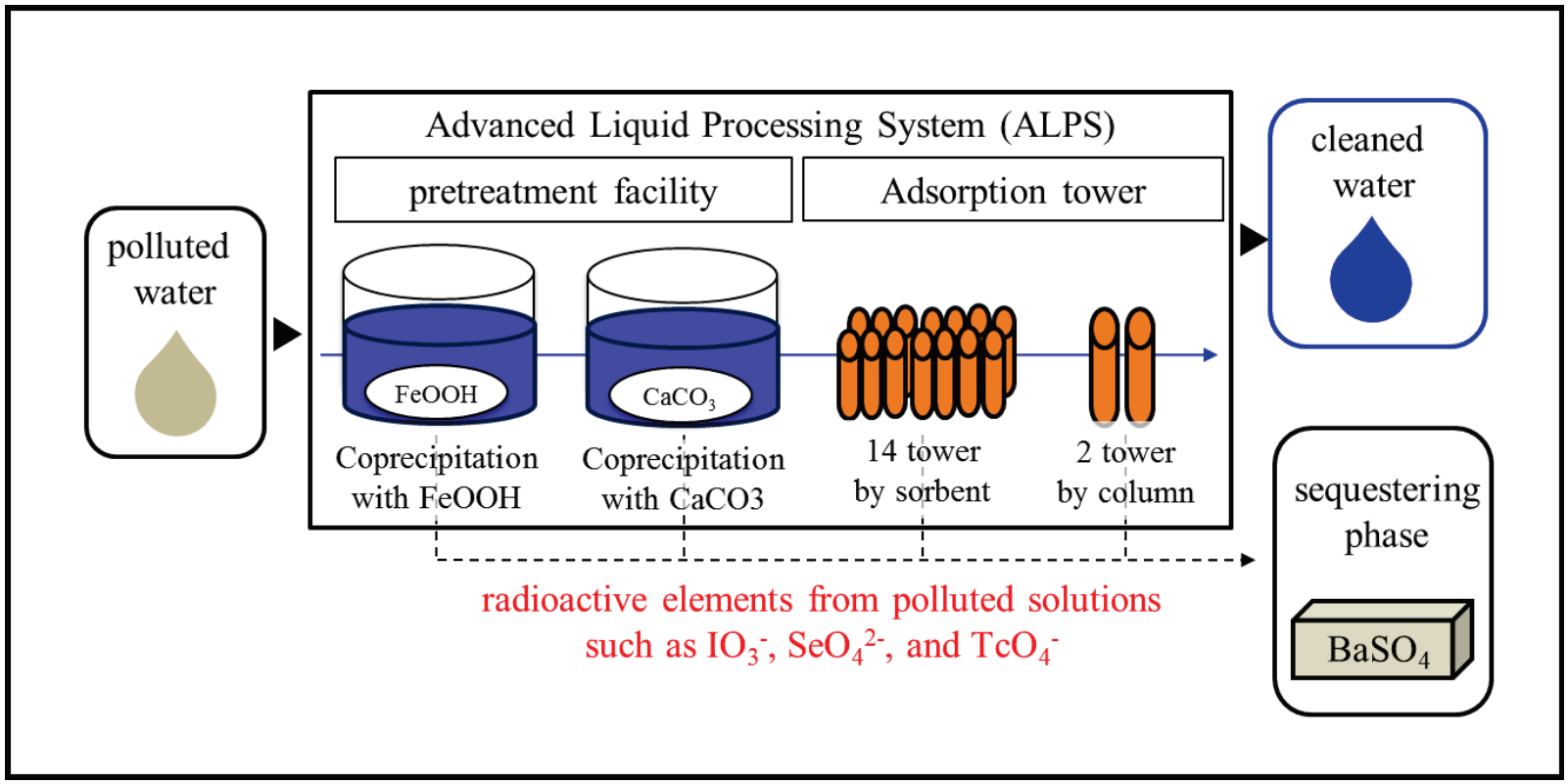

Figure 4. Overview of the multi-nuclide removal equipment (ALPS) at Fukushima Daiichi Nuclear Power Station and the new application of barite as a barriers for the retention of radioactive elements, such as iodine, selenium, and technetium oxyanions.

Figure 5. Overview of the relationship among these chapters.

Chapter 2. Distribution of major and trace elements between barite and aqueous solutions

1. Chapter Introduction

Trace element contents in minerals is widely used as a tool to understand paragenesis of rocks, which reflects distribution of ions between mineral and solution as a geochemical tracer. For example, trace element content in calcite shows information of the depositional and diagenetic environment [Veizer 1983; Rimstidt, 1998]. Barnaby and Rimstidt (1989) showed that the Mn^{2+} and Fe^{2+} contents in calcite are frequently interpreted in terms of the E_h of the depositional or diagenetic environment because the incorporation of both metals in calcite the redox conditions. Lu (2010) also showed the application of iodine/calcium ratios in marine carbonate as a new geochemical proxy to constrain seawater redox change and provide additional insights into the response of ocean chemistry to ancient climatic warming because of the selective incorporation of iodate under oxidizing conditions, which is not the case for iodide under anoxic conditions. These studies showed that, to effectively apply trace element chemistry to the interpretation of ancient environments, the systematics of the trace element distribution between mineral and water must be well understood [Rimstidt, 1998; Curti,

1999].

Barite can also serve as a geochemical tool to reconstruct paleo-environmental conditions, such as marine productivity [Gonneea and Paytan 2006; Paytan et al., 2007], depositional seawater compositions [Beek et al., 2003; Torres et al., 2003; Snyder et al., 2007], and global perturbations to the sulfur cycle [Huston and Graham, 2004]. However, these proxies are dependent on the occurrence and formation of barite in the environments without consideration on the trace element contents in barite. This is because there is few study about the behavior of major and trace elements with barite, and the systematics of the behavior is not well understood. Thus, in this study, the systematic correlations of ionic incorporation between barite and water are determined by the partition coefficients (K_d) and unit-cell dimensions of these ions (k) in barite as a function of ionic radius. Analysis of K_d values for minerals also show the mobility and distribution of ionic species in natural systems, which provides an effective method to sequester or retard migration of toxic and/or radioactive elements from polluted waters. Thus, we can effectively remove toxic and/or radioactive elements to understand the systematics of distribution element to barite, and the goal of this investigation is to develop the methods for incorporation of trace elements by barite to a large degree.

2. Methods

2.1. Coprecipitation experiment procedures

Coprecipitation experiments of major and trace elements with barite were conducted to understand general trends of trace element by distribution coefficients (K_d) and unit-cell dimensions (k) of substitution ion in barite. The periodic table of the elements is shown in Fig. 1, analytical elements are colored in red (cation: Cs^{+}, Ca^{2+}, Cd^{2+}, Co^{2+}, Cu^{2+}, Ga^{2+}, Mg^{2+}, Mn^{2+}, Ni^{2+}, Sr^{2+}, Zn^{2+}, Cr^{3+}, La^{3+}, Ce^{3+}, Pr^{3+}, Nd^{3+}, Sm^{3+}, Eu^{3+}, Gd^{3+}, Tb^{3+}, Dy^{3+}, Ho^{3+}, Er^{3+}, Tm^{3+}, Yb^{3+}, Lu^{3+}, Y^{3+}; $Sb(OH)_6^{-}$, AsO_2^{-}, AsO_3^{-}, I^{-}, IO_3^{-}, ReO_4^{-}, CrO_4^{2-}, MoO_4^{2-}, SeO_3^{2-}, SeO_4^{2-}, TeO_3^{2-}, TeO_4^{2-}, WO_4^{2-}). Barite was precipitated from a mixture of (i) Na_2SO_4 solution and (ii) $BaCl_2 \cdot 2H_2O$ solution [Blount, 1974]. Both cation and anion were added to $BaCl_2 \cdot 2H_2O$ solution and Na_2SO_4 solution, respectively, to avoid the formation of metal precipitation with barium or sulfate. The experimental conditions of pH, saturation states (defined as SI = $\log(IAP/K_{sp})$), barium and sulfate concentration are fixed at pH 8.0, SI 4.2, Ba^{2+} 0.65 mM, SO_4^{2-} 27 mM, respectively.

The precipitates of barite and the aqueous phase were separated by filtration with a 0.20 μm membrane filter (mixed cellulose ester, Advantec, Tokyo, Japan) and then rinsed three times with Milli-Q water. The X-ray diffraction (XRD) patterns of the precipitates were measured using a powder X-ray diffractometer (MultiFlex, Rigaku Co., Tokyo,

Japan), in which the mineral phase was identified by comparing the XRD patterns to the International Center for Diffraction Data file, and calculated the unit-cell parameters of substitution ion in barite. Total metal concentrations in the solution were analyzed by ICP-MS (7700cs, Agilent, Tokyo, Japan) after dilution by 2 wt.% HNO_3 solution. A part of the solid sample was dried in an oven at 60 °C and dissolved into water by adding sodium carbonate [Breit et al., 1985] to determine the metal concentration in the precipitates (discussed in session 2.2). The distribution coefficient values of these metal between barite and water were calculated based on the metal concentration in the water and solid phases. The local structure of metal ions in the precipitates after filtration was determined by extended X-ray absorption fine structure (EXAFS). A portion of the precipitate was immediately packed into an airtight polyethylene bag and stored at 4 °C until XAFS measurement.

2.2. Methods for barite dissolution

Barite is stable over the wide range of pressures, temperatures, E_h, and pH of the Earth's crust in the absence of other reactive components. However, due to the high stability of barite in natural systems, we cannot easily dissolve barite by acids and a chelating ligand to provide reliable measurements of trace components in barite.

Previous studies have been conducted for the complete separation of marine barite from potential sources of sediments or selective dissolution of this barite because Ba^{2+} content from barite can be used to quantify the initial organic carbon content of the sediment [Putnis et al., 1995; Rutten and Lange, 2002; Eagle et al., 2003; Beek et al., 2003]. However, these techniques cannot be used to completely dissolve barite from water and the maximum solubility of barite by aqua regia is approximately 1 mg/mL-acid [Snyder et al., 2007]. Figure 2 showed the recovery rate of Ba with acids by Rutten and Lange (2002) technique, which showed that we can extract a small amount of Ba by barite digestions in mixture of strong acids such as hydrofluoric, nitric, and perchloric acids. Thus, in this study, barite was dissolved into water by adding sodium carbonate reported on Breit (1985), not by the digestion of strong acids. Breit (1985) showed that barite can be dissolved to sodium carbonate solution by formation of $BaCO_3$ (stage 1), which is significantly dissolved by 5% HNO_3 (stage 2) (Fig. 3). At stage 1, we can recover the substituted ions in sulfate site as anions and incompatible ion to Ba^{2+} site in $BaCO_3$ as monovalent cations. At stage 2, we can also recover the substituted ions in Ba^{2+} site as divalent and trivalent cations. X-ray diffraction patterns before- and after-the separation of $BaCO_3$ are plotted in Fig. 4, which showed the transformation of $BaSO_4$ to $BaCO_3$. The enrichments of these ions at each stage are shown in Fig. 5, which showed the

recovering of compatible and incompatible ions with Ba^{2+} at each stage. Thus, barite can be completely dissolved by this technique for reliable measurements of major and trace components in barite.

3. Results and discussion

3.1. Distribution coefficients of elements between barite and water

The experimental distribution coefficients, K_d, can be used to understand general trends in trace element behavior. The apparent K_d values show a systematic pattern of the distribution and give good estimates of the ability for efficient removal of toxic and/or radioactive elements from water. However, there is few studies about the behavior of major and trace elements with barite, and the systematics of the behavior is not well understood. Thus, the aim of this study is to provide a systematic pattern of elemental coprecipitation with barite by analysis of K_d values through batch experiments.

Batch experiments were performed at pH 8.0 and SI 4.2 in initial solution to understand the systematics distributions of cations and anions between barite and water. Analysis of apparent K_d values are shown in Tables 1 and 2. In Fig. 6, the apparent K_d values listed in Tables 1 and 2 are plotted as a function of the ionic radius of the incorporation ions. Each ionic radius is fixed as a six-fold coordination ionic radius [Whittaker, 1970] in this graph to compare a systematic pattern of calcite although Ba^{2+} and SO_4^{2-} ion in barite exist as twelve- and four-fold coordination with oxygen atoms, respectively [Zheng, 1999; Griffith, 2012]. The results showed a good correlation between the log K_d and ionic radius, which indicated that the systematics of elemental

behavior were controlled by the ionic radius of substituted ion. A positive correlation was found for many cations smaller or slightly larger than substituted ion of Ba^{2+} (Fig. 7a). The K_d values for Ca^{2+} and Sr^{2+}, which have ionic radii smaller than Ba^{2+} ion, increased as a function of ionic radius. On the other hand, the K_d values for Cs^{+}, which has ionic radius larger than Ba^{2+}, was negative and the partition to barite was very small. This is because Cs^{+} is too large to substitute Ba^{2+} site in the barite lattice [Rimstidt et al., 1998]. Similar trends have been also observed at incorporation of various ions in calcite shown in Fig. 7b [Curti, 1999]. It is shown that ions having a smaller or slightly larger radii as a substituted ion (Ca^{2+}) can be incorporated more efficiently in a crystal lattice than those with much larger ions, such as Ba^{2+} and Sr^{2+}. A larger ion can be efficiently incorporated into barite than calcite because of the larger substituted site of Ba^{2+} (1.68 Å) in barite lattice than that of Ca^{2+} (1.08 Å) in calcite lattice. Similar trends were also found for many anions fixed ionic radius of each oxyanion reported in Goh (2008), which is smaller or larger than substituted ion of SO_4^{2-} (Fig. 8). Thus, the systematics of element behavior controlled by ionic radius of substitution ion can be reasonably understood, and which provides a good estimates of partition coefficients to the mineral.

3.2. Unit cell dimensions of pure- and substitution-barite

Previous studies showed the changes of the unit-cell parameter depending on the

degree of substitution ion and the changes of the unit-cell dimension with increasing substitution can be related to the ionic radii of incorporated ions in the substituted site [Gerth, 1990; Gasser et al., 1996; Kaur et al., 2009]. Gerth (1990) showed that the goethite structure became distorted along the crystallographic a-axis by the incorporation of different foreign elements which have smaller ionic radii than Fe^{2+} and causes a reduction of the unit-cell parameters depending on the degree of the substitution. A good correlation between the unit-cell dimensions and ionic radius of incorporation metal in goethite was also observed and a higher dimension of a-axis was believed to be the result of structural defects. The aim of this study is to determine what extent for the changes in the unit-cell dimensions can be related to the behavior of the incorporation metal with barite. The unit-cell parameters of pure- and single substituted-barite were calculated by XRD analysis. The initial unit-cell parameters and atomic coordinates were determined based on the Pnma space group of barite (Lee et al., 2005).

The unit-cell parameters of the substituted barite are listed in Tables 3 and 4. The pure- and the substituted-barite showed little change in the b-parameter but considerable differences in the a- and c-parameters. The a-parameter of single substituted barite (cation: calcium ion (Ca^{2+}); anion: selenite (SeO_3^{2-}) and selenate (SeO_4^{2-})) changed linearly with an increase in incorporation (Fig. 9a, 9b). Each ion caused different a-

parameter changes with an increase in substitution, which is also expressed by the different slopes of ions, which showed a larger distortion of Ca^{2+} than that of SeO_3^{2-} and SeO_4^{2-}. This is because Ca^{2+} has a larger distribution coefficients than SeO_3^{2-} and SeO_4^{2-}, and thus barite become more distorted along the crystallographic a-axis in barite by the substitution of larger ion. The unit-cell dimensions, which is calculated by a-parameter difference between pure- and single substituted-barite and defined as k_a value, is shown in Fig. 10 as a function of ionic radius. The results show a good correlation between the k_a value and ionic radius. The k_a values can be linearly related to the respective ionic radii of incorporation in barite, which shows that the larger ions formed a larger distortion of crystal lattice in barite structure. The k_a values depend on the degree of substitution ion in barite (Fig. 11). At higher levels of foreign element incorporation to barite, the expansion of the unit cell in the structure can become so strong and caused a larger distortion in the presence of larger ions. These results showed the systematics of elemental incorporation controlled by crystal lattice distortion on the partition coefficients to barite, which provides larger incorporation of trace elements by barite (Fig. 8).

4. Conclusion

The systematic analysis of coprecipitation with barite reveals that the major and trace elements are incorporated into this mineral following well-defined and predictable geochemical rules. Analysis of K_d values for barite shows that ions having a smaller or slightly larger radii as a substituted ion can be incorporated more efficiently in a crystal lattice than those with much larger radii. Thus, because of the larger substituted ion of Ba^{2+} (1.68 Å) in barite than that of Ca^{2+} (1.08 Å) in calcite, larger ions can be efficiently removed from solution by barite. Analysis of k_a values for barite also showed a good correlation between the ionic radius of incorporation and unit-cell dimensions of a-axis in barite structure, which suggested the dependence of crystal lattice distortion on the partition coefficients of metal in barite. Thus, in the presence of slightly larger ions which have large K_d values for barite, smaller ions, which have low K_d values for barite, can be efficiently removed from solution by barite. Thus, the systematics of element behaviors provides a good estimates of partition coefficients to mineral and caused larger incorporation of trace elements by mineral.

References

Barnaby, R. J., & Rimstidt, J. D. (1989). Redox conditions of calcite cementation interpreted from Mn and Fe contents of authigenic calcites. Geological Society of America Bulletin, 101(6), 795-804.

Breit, George N., Simmons, E. C., Goldhaber, M. B., 1985. Dissolution of barite for the analysis of strontium isotopes and other chemical and isotopic variations using aqueous sodium carbonate. Chemical Geology: Isotope Geoscience section 52.3, 333-336.

Curti, E. (1999). Coprecipitation of radionuclides with calcite: estimation of partition coefficients based on a review of laboratory investigations and geochemical data. Applied Geochemistry, 14(4), 433-445.

Eagle, M., Paytan, A., Arrigo, K. R., van Dijken, G., & Murray, R. W. (2003). A comparison between excess barium and barite as indicators of carbon export.*Paleoceanography*, *18*(1).

Gasser, U. G., Jeanroy, E., Mustin, C., Barres, O., Nüesch, R., Berthelin, J., & Herbillon, A. J. (1996). Properties of synthetic goethites with Co for Fe substitution. Clay Minerals, 31(4), 465-476.

Gerth, J. (1990). Unit-cell dimensions of pure and trace metal-associated goethites.

Geochimica et Cosmochimica Acta, 54(2), 363-371.

Goh, K. H., Lim, T. T., & Dong, Z. (2008). Application of layered double hydroxides for removal of oxyanions: a review. Water research, 42(6), 1343-1368.

Gonneea, M. E., Paytan, A., 2006. Phase associations of barium in marine sediments. Mar. Chem. 100.1, 124-135.

Griffith, M.E., and A. Paytan (2012), Barite in the Ocean – Occurrence, Geochemistry and Paleoceanographic Applicators, Sedimentology, *Sedimentology*, *59*, 1817–1835.

Huston, D. L., Logan, G. A., 2004. Barite, BIFs and bugs: evidence for the evolution of the Earth's early hydrosphere, Earth Planet. Sci. Lett. 220.1, 41-55.

Kaur, N., Singh, B., & Kennedy, B. J. (2009). Copper substitution alone and in the presence of chromium, zinc, cadmium and lead in goethite (α-FeOOH). Clay Minerals, 44(3), 293-310.

Lee, J. S., Wang, H. R., Iizuka, Y., and Yu, S. C., 2005. Crystal structure and Raman spectral studies of $BaSO_4$-$PbSO_4$ solid solution. Zeitschrift für Kristallographie-Crystalline Materials, 220.1, 1-9.

Lu, Z., Jenkyns, H. C., & Rickaby, R. E. (2010). Iodine to calcium ratios in marine carbonate as a paleo-redox proxy during oceanic anoxic events.Geology, 38(12), 1107-1110.

Paytan, A., Griffith, E. M., 2007. Marine barite: Recorder of variations in ocean export productivity. Deep Sea Research Part II: Topical Studies in Oceanography 54.5, 687-705.

Putnis, A., Junta-Rosso, J. L., & Hochella, M. F. (1995). Dissolution of barite by a chelating ligand: An atomic force microscopy study. Geochimica et Cosmochimica Acta, 59(22), 4623-4632.

Rimstidt, J. D., Balog, A., & Webb, J. (1998). Distribution of trace elements between carbonate minerals and aqueous solutions. Geochimica et Cosmochimica Acta, 62(11), 1851-1863.

Rutten, A., & de Lange, G. J. (2002). A novel selective extraction of barite, and its application to eastern Mediterranean sediments. Earth and Planetary Science Letters, 198(1), 11-24.

Torres, M. E., G. Bohrmann, T. E. Dube´, F. G. Poole, (2003), Formation of modern and Paleozoic stratiform barite at cold methane seeps on continental margins, *Geology*, *31*, 897–900.

Snyder, G. T., Dickens, G. R., Castellini, D. G., 2007. Labile barite contents and dissolved barium concentrations on Blake Ridge: new perspectives on barium cycling above gas hydrate systems. Journal of Geochemical Exploration, 95.1, 48-65.

Van Beek, P, Reyss, J. L., Bonte, P., Schmidt, S., 2003. Sr/Ba in barite: a proxy of barite preservation in marine sediments? Mar. Geol. 199, 205-220.

Veizer, J. (1983). Chemical diagenesis of carbonates: theory and application of trace element technique.

Whittaker, E. J. W., & Muntus, R. (1970). Ionic radii for use in geochemistry. Geochimica et Cosmochimica Acta, 34(9), 945-956.

Zheng, Y. F. (1999). Oxygen isotope fractionation in carbonate and sulfate minerals. Geochemical Journal, 33(2), 109-126.

Figure legends

Figure 1. The periodic table of the analytical elements in this study (red).

Figure 2. The recovery rate of Ba from barite dissolution by the addition of acids.

Figure 3. Experimental procedure of barite dissolution by sodium carbonate technique.

Figure 4. X-ray diffraction patterns before- and after-the separation of $BaCO_3$.

Figure 5. The periodic table of the elements recovered form barite dissolution at each stage (blue elements are recovered at stage 1, while red elements are at stage 2).

Figure 6. The apparent K_d values as a function of the ionic radius of the incorporation ions

Figure 7. The apparent K_d values as a function of the ionic radius of cations at (a) barite and (b) calcite.

Figure 8. The apparent K_d values as a function of the ionic radius of oxyanions between barite and water.

Figure 9. The unit-cell dimensions of substituted barite as a function of (a) Ca^{2+} and (b) SeO_3^{2-} and SeO_4^{2-} ions.

Figure 10. The unit-cell dimensions of a-axis in substituted barite as a function of ionic radius.

Figure 11. The unit-cell dimensions of substituted barite as a function of the degree of

substitution ion in barite.

Table 1. Analysis of apparent K_d values of cations in barite.

Table 2. Analysis of apparent K_d values of oxyanions in barite.

Table 3. Analysis of the unit-cell parameter of substituted cations in barite.

Table 4. Analysis of the unit-cell parameter of substituted oxyanions in barite.

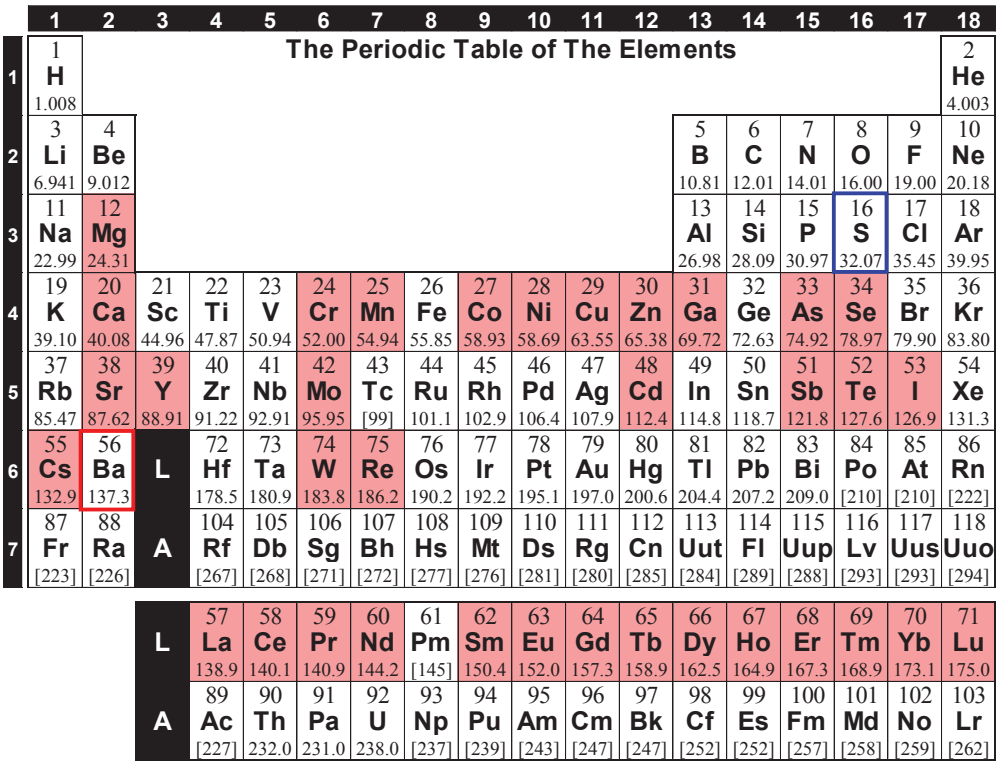

Figure 1. The periodic table of the analytical elements in this study (red).

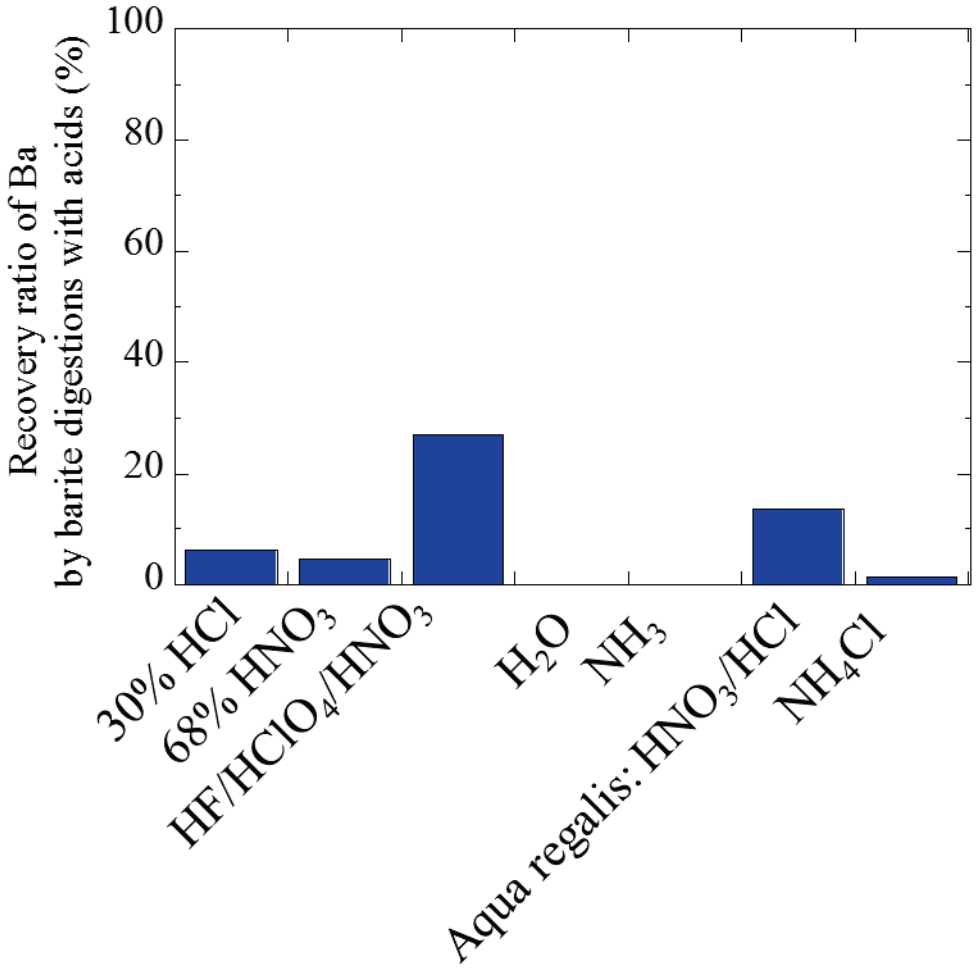

Figure 2. The recovery rate of Ba from barite dissolution by the addition of acids.

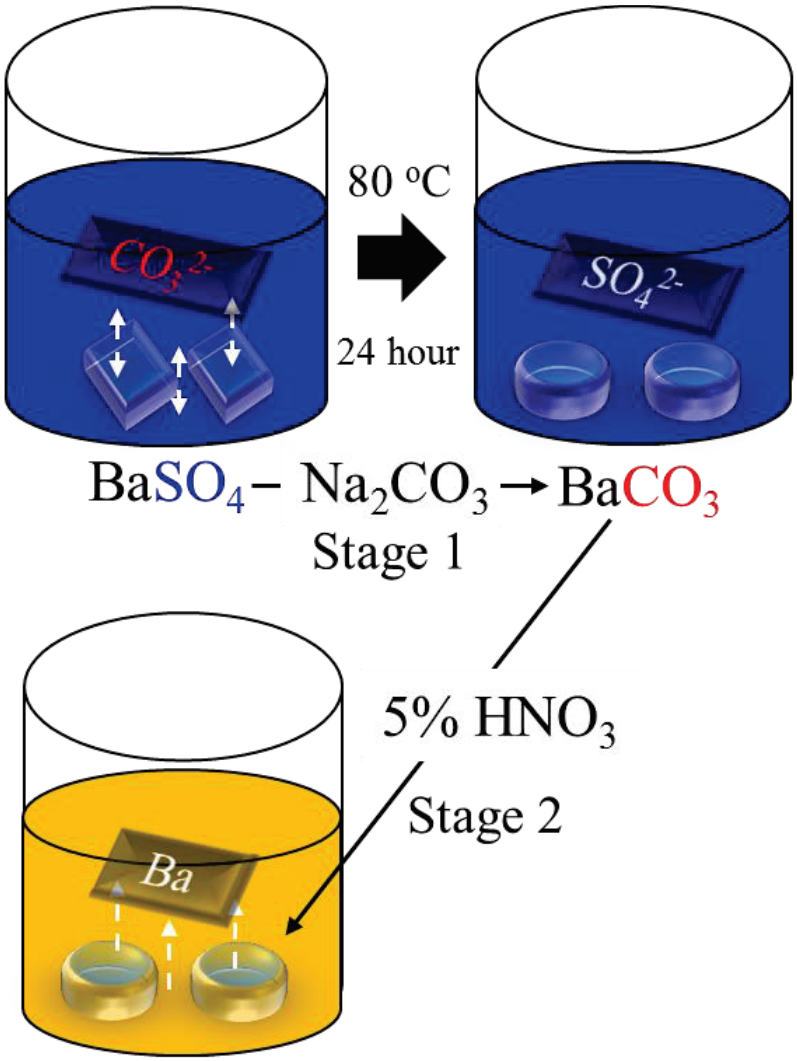

Figure 3. Experimental procedure of barite dissolution by sodium carbonate technique.

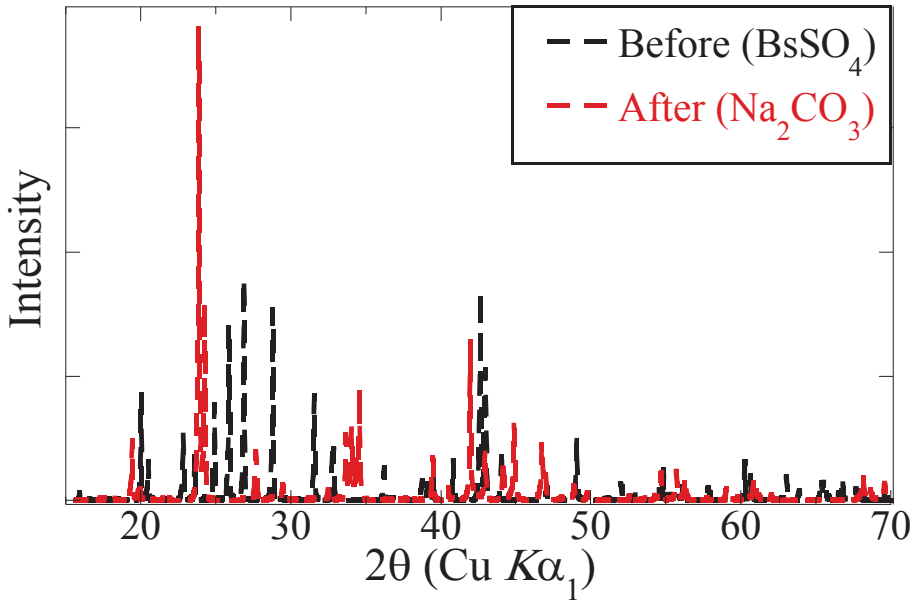

Figure 4. X-ray diffraction patterns before- and after-the separation of $BaCO_3$.

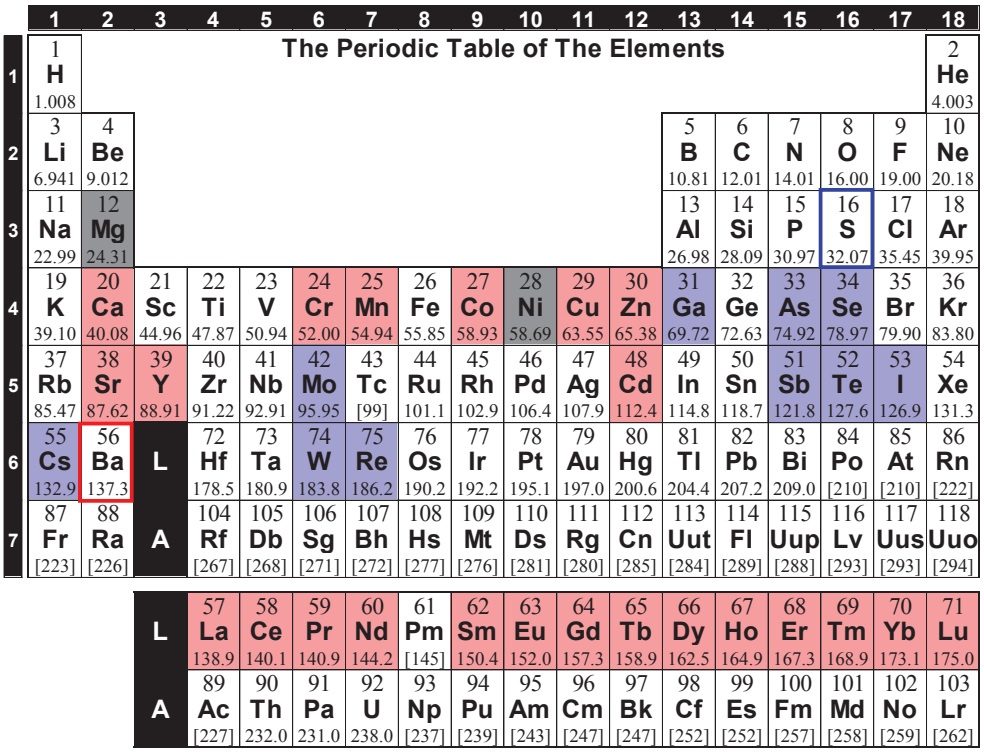

Figure 5. The periodic table of the elements recovered form barite dissolution at each stage (blue elements are recovered at stage 1, while red elements are at stage 2).

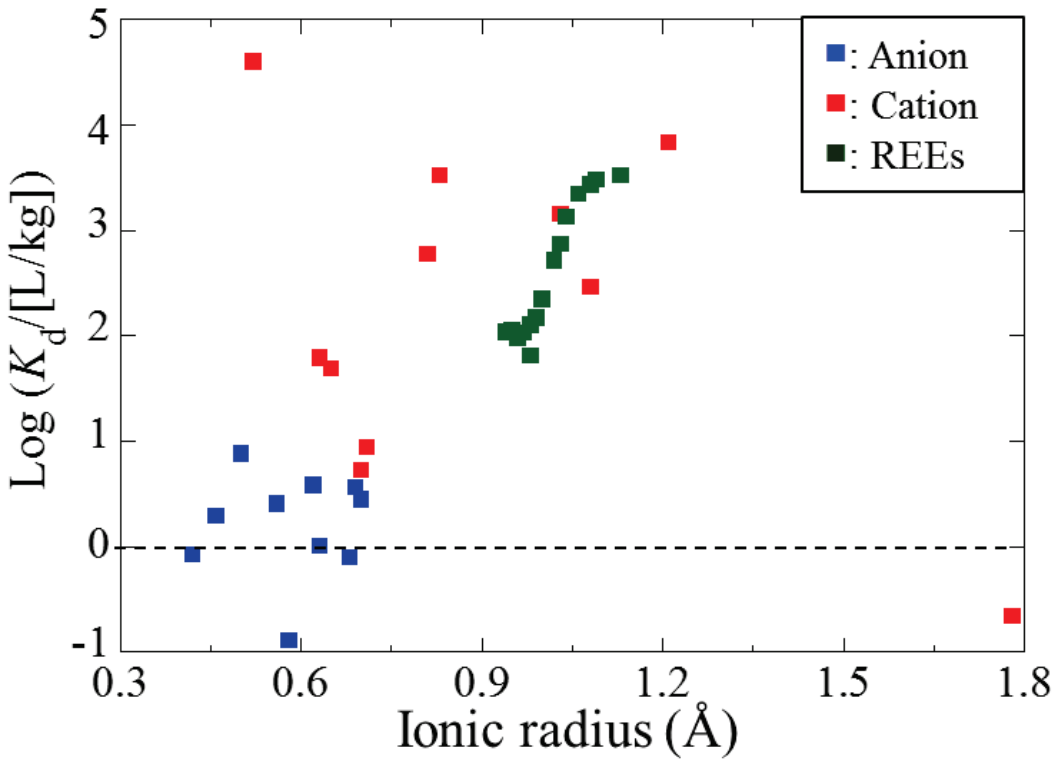

Figure 6. The apparent K_d values as a function of the ionic radius of the incorporation ions

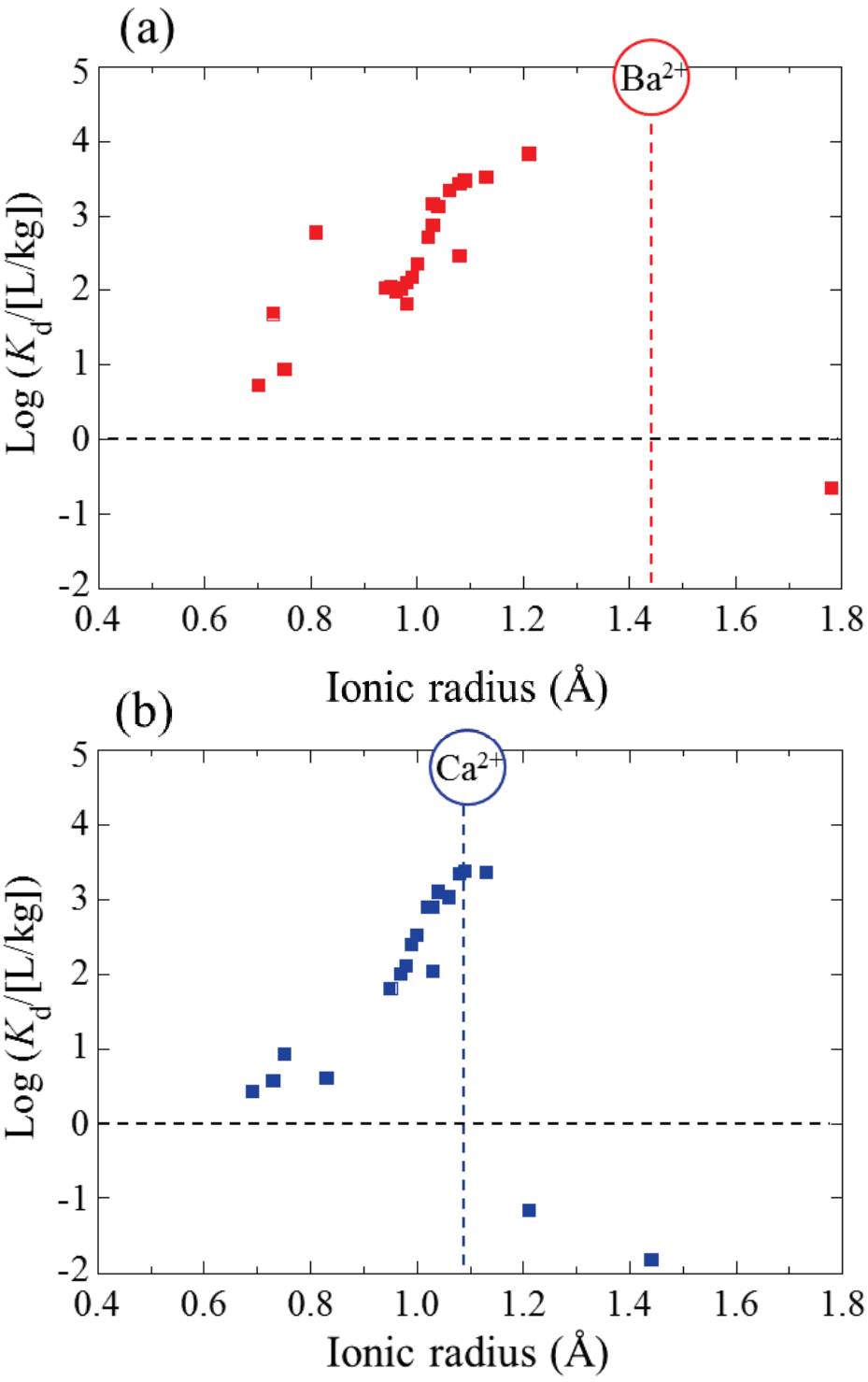

Figure 7. The apparent K_d values as a function of the ionic radius of cations at (a) barite and (b) calcite.

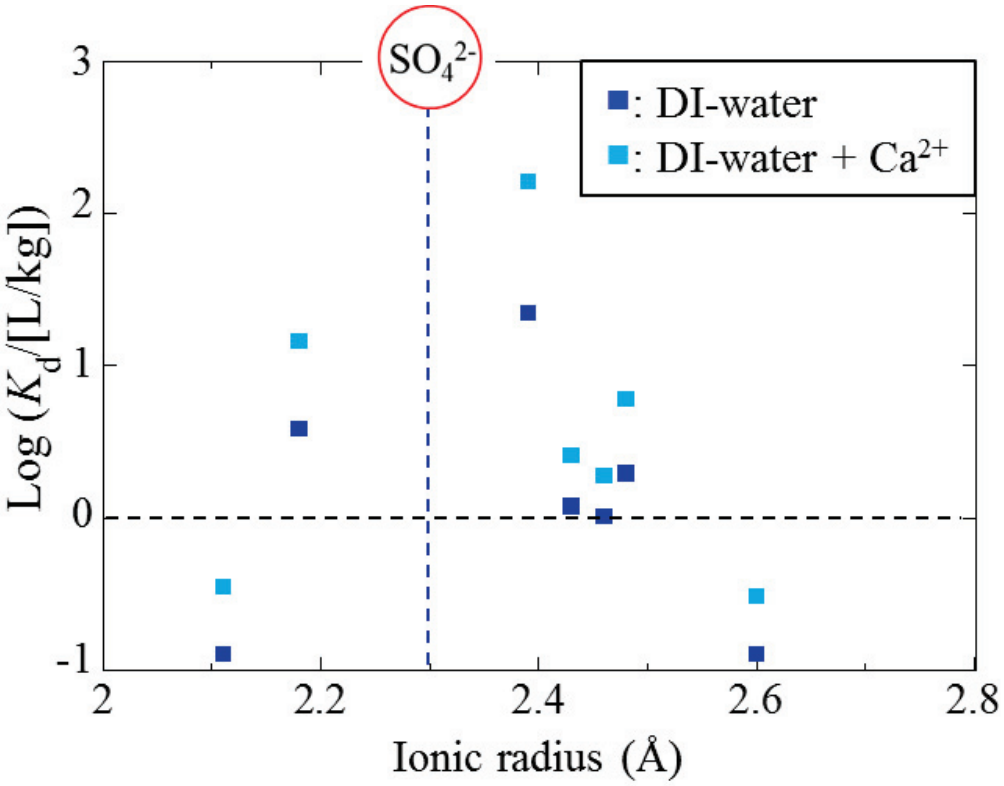

Figure 8. The apparent K_d values as a function of the ionic radius of oxyanions between barite and water.

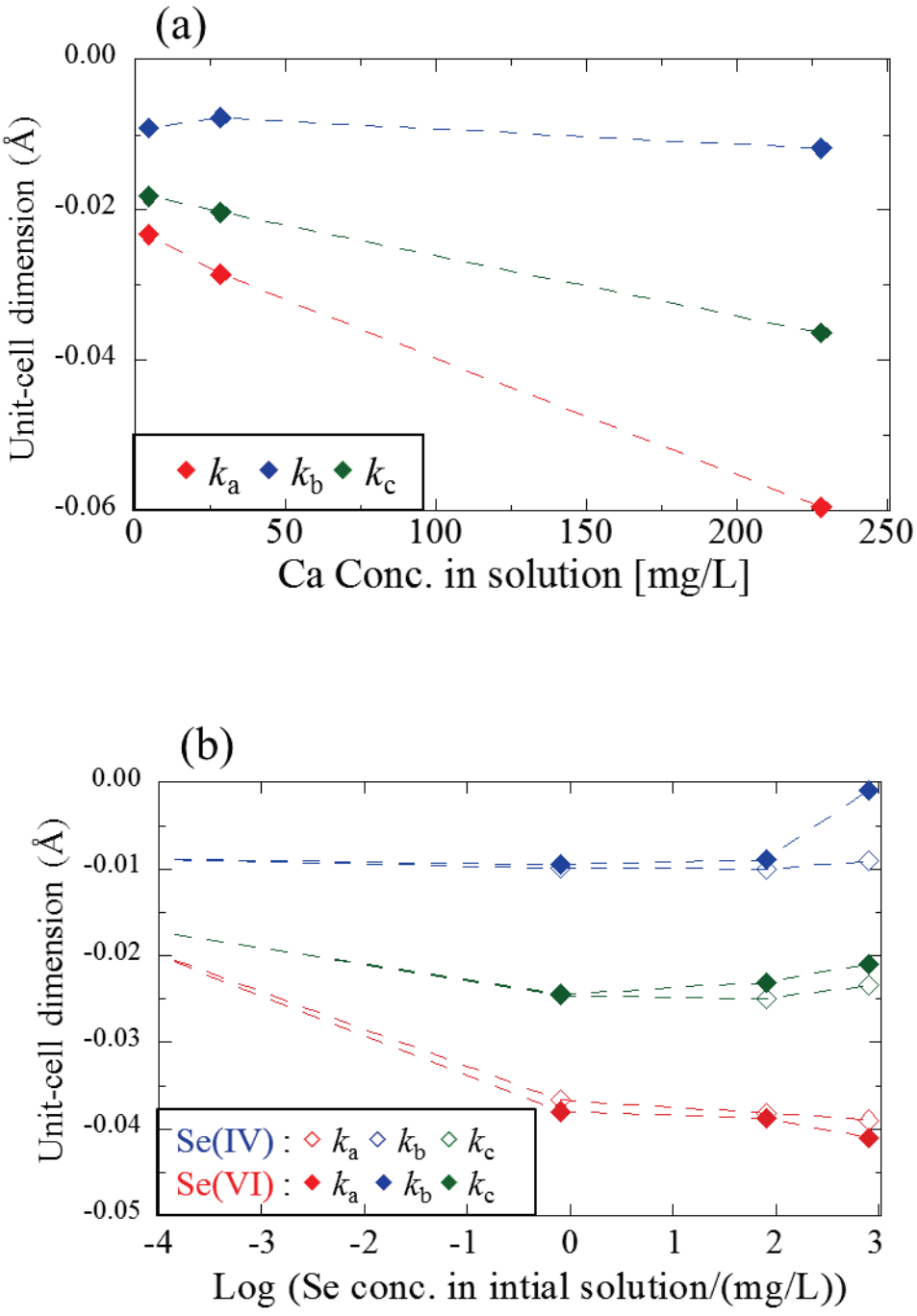

Figure 9. The unit-cell dimensions of substituted barite as a function of (a) Ca^{2+} and (b) SeO_3^{2-} and SeO_4^{2-} ions.

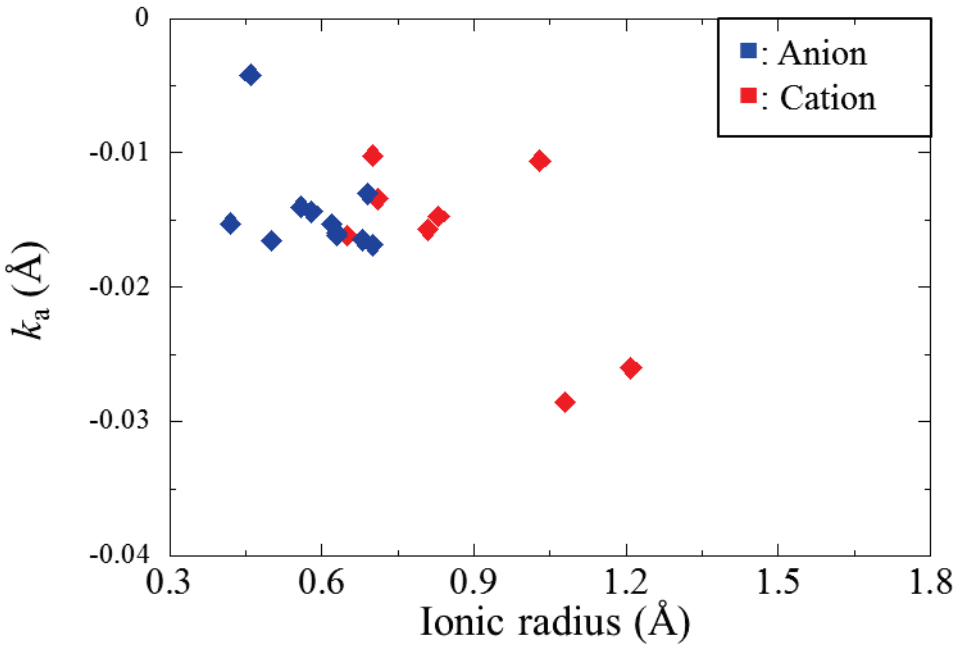

Figure 10. The unit-cell dimensions of a-axis in substituted barite as a function of ionic radius.

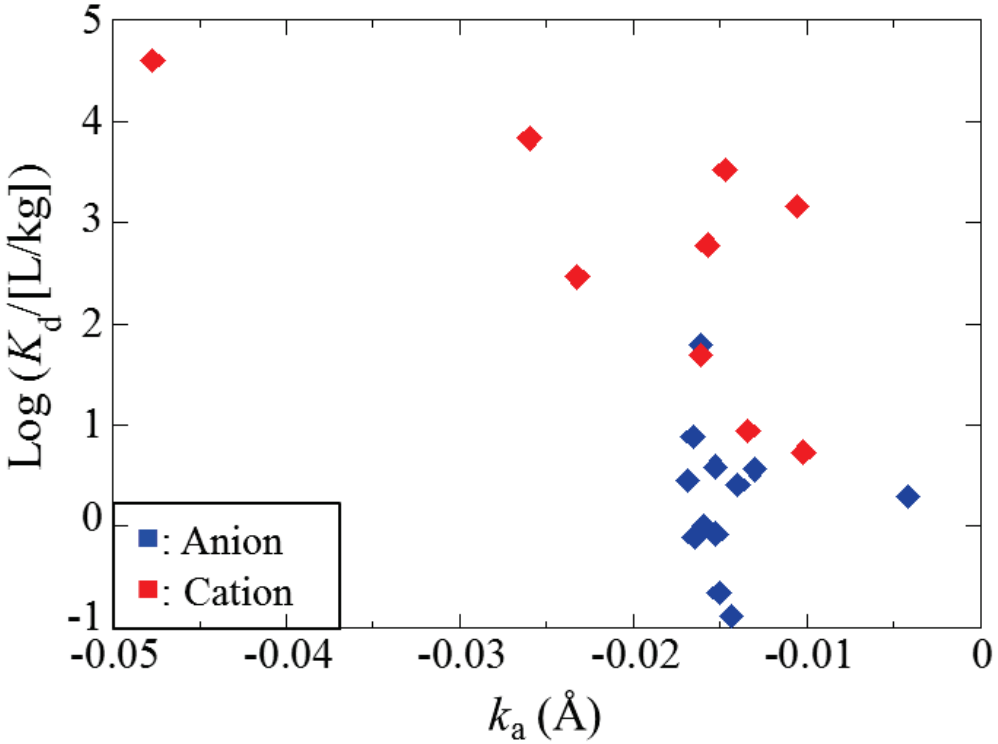

Figure 11. The unit-cell dimensions of substituted barite as a function of the degree of substitution ion in barite.

Table 1. Analysis of apparent K_d values of cations in barite.

Valent	Trace Cations	R (Å)	Input solutions		Log K_d [L/kg]		
			$Tr_{initial}$ [mM]	SI of barite	pH 8.0	pH 2.0	ASW
Monovalent	Cs(I)	1.78	1.0×10^{0}	4.21	-0.65	0.40	-0.42
Divalent	Co(II)	0.65	1.0×10^{-1}	4.21	0.83	-1.10	0.687
	Ga(II)	0.70	1.0×10^{-1}	4.21	0.73		
	Mn(II)	0.71	1.0×10^{-1}	4.21	0.95	0.04	
	Cu(II)	0.81	1.0×10^{-1}	4.21	1.55	0.19	
	Zn(II)	0.83	1.0×10^{-1}	4.21	3.52	2.05	
	Cd(II)	1.03	1.0×10^{0}	4.21	3.16	1.14	1.235
	Ca(II)	1.08	1.0×10^{-1}	4.21	2.47	2.87	
	Sr(II)	1.21	1.0×10^{-2}	4.21	3.83	3.83	
Trivalent	Cr(III)	0.63	1.0×10^{-2}	4.21	1.79	1.78	
	La (III)	1.13	1.0×10^{-3}	4.21		3.53	
	Ce (III)	1.09	1.0×10^{-3}	4.21		3.48	
	Pr (III)	1.08	1.0×10^{-3}	4.21		3.43	
	Nd (III)	1.06	1.0×10^{-3}	4.21		3.35	
	Sm (III)	1.04	1.0×10^{-3}	4.21		3.13	
	Eu (III)	1.03	1.0×10^{-3}	4.21		2.88	
	Gd (III)	1.02	1.0×10^{-3}	4.21		2.72	
	Tb (III)	1.00	1.0×10^{-3}	4.21		2.35	
	Dy (III)	0.99	1.0×10^{-3}	4.21		2.17	
	Ho (III)	0.98	1.0×10^{-3}	4.21		2.11	
	Er (III)	0.97	1.0×10^{-3}	4.21		2.03	
	Tm (III)	0.96	1.0×10^{-3}	4.21		1.99	
	Yb (III)	0.95	1.0×10^{-3}	4.21		2.06	
	Lu (III)	0.94	1.0×10^{-3}	4.21		2.04	
	Y (III)	0.98	1.0×10^{-3}	4.21		1.82	

Table 2. Analysis of apparent K_d values of oxyanions in barite.

Trace Anions	Ionic radius VI (Å)	Ionic radius oxyanion (Å)	Input solution		Log K_d [L/kg]		
			$Tr_{initial}$ [mM]	SI of barite	pH 8.0	pH 2.0	ASW
ReO_4^-	0.26	2.60	1.0×10^{0}	4.21	-0.89	-0.51	
SeO_4^{2-}	0.42	2.43	1.0×10^{0}	4.21	0.08	0.23	0.42
AsO_3^-	0.46	2.48	1.0×10^{0}	4.21	0.30		0.79
SeO_3^{2-}	0.50	2.39	1.0×10^{0}	4.21	1.35	0.59	2.21
CrO_4^{2-}	0.52	2.30	1.0×10^{-4}	4.21	4.60	1.69	3.84
TeO_3^{2-}	0.56		1.0×10^{-1}	4.21	0.41	3.28	
AsO_2^-	0.58	2.11	1.0×10^{0}	4.21	-0.89		-0.44
IO_3^-	0.62	2.18	1.0×10^{0}	4.21	0.59		1.17
MoO_4^{2-}	0.63	2.46	1.0×10^{-1}	4.21	0.01		0.28
WO_4^{2-}	0.68		1.0×10^{-1}	4.21	-0.10		0.27
$Sb(OH)_6^-$	0.69		1.0×10^{-2}	4.21	0.57		0.74
TeO_4^{2-}	0.70		1.0×10^{-1}	4.21	0.45	3.35	

Table 3. Analysis of the unit-cell parameter of substituted cations in barite.

Valent	Trace Cations	R (Å)	Input solution			Log K_d [L/kg]	DI-water							
			pH	$Tr_{initial}$ [mM]	SI of barite		a(Å)	b(Å)	c(Å)	Rwp(%)	S	Δa(Å)	Δb(Å)	Δc(Å)
Monovalent	Cs(I)	1.78	8.0	1.0×10^{0}	4.21	-0.65	8.88094	5.45570	7.15750	7.64	3.41	-0.01506	-0.00630	-0.01350
Divalent	Co(II)	0.65	8.0	1.0×10^{-1}	4.21	0.83								
	Ga(II)	0.70	8.0	1.0×10^{-1}	4.21	0.73	8.88580	5.45600	7.15980	10.41	8.65	-0.01020	-0.00600	-0.01120
	Mn(II)	0.71	8.0	1.0×10^{-1}	4.21	0.95	8.88260	5.45450	7.15760	9.81	4.45	-0.01340	-0.00750	-0.01340
	Cu(II)	0.81	8.0	1.0×10^{-1}	4.21	1.55	8.88028	5.45389	7.15610	5.17	2.56	-0.01572	-0.00811	-0.01490
	Zn(II)	0.83	8.0	1.0×10^{-1}	4.21	3.52	8.88127	5.45415	7.15660	4.86	2.36	-0.01473	-0.00785	-0.01440
	Cd(II)	1.03	8.0	1.0×10^{0}	4.21	3.16	8.87930	5.45340	7.15560	10.37	5.20	-0.01670	-0.00860	-0.01540
	Ca(II)	1.08	8.0	1.0×10^{-1}	4.21	2.47	8.87276	5.45295	7.15283	4.72	2.36	-0.02324	-0.00905	-0.01817
	Sr(II)	1.21	8.0	1.0×10^{-2}	4.21	3.83	8.87000	5.45490	7.15100	30.65	14.98	-0.02600	-0.00710	-0.02000
Trivalent	Cr(III)	0.63	8.0	1.0×10^{-2}	4.21	1.79	8.87989	5.45507	7.15790	4.16	2.33	-0.01611	-0.00693	-0.01310
	La (III)	1.13	2.0	1.0×10^{-3}	4.21	3.53								
	Ce (III)	1.09	2.0	1.0×10^{-3}	4.21	3.48								
	Pr (III)	1.08	2.0	1.0×10^{-3}	4.21	3.43								
	Nd (III)	1.06	2.0	1.0×10^{-3}	4.21	3.35								
	Sm (III)	1.04	2.0	1.0×10^{-3}	4.21	3.13								
	Eu (III)	1.03	2.0	1.0×10^{-3}	4.21	2.88								
	Gd (III)	1.02	2.0	1.0×10^{-3}	4.21	2.72								
	Tb (III)	1.00	2.0	1.0×10^{-3}	4.21	2.35								
	Dy (III)	0.99	2.0	1.0×10^{-3}	4.21	2.17								
	Ho (III)	0.98	2.0	1.0×10^{-3}	4.21	2.11								
	Er (III)	0.97	2.0	1.0×10^{-3}	4.21	2.03								
	Tm (III)	0.96	2.0	1.0×10^{-3}	4.21	1.99								
	Yb (III)	0.95	2.0	1.0×10^{-3}	4.21	2.06								
	Lu (III)	0.94	2.0	1.0×10^{-3}	4.21	2.04								
	Y (III)	0.98	2.0	1.0×10^{-3}	4.21	1.82								

Table 4. Analysis of the unit-cell parameter of substituted oxyanions in barite.

Trace Anions	Ionic radius VI (Å)	Ionic radius oxyanion (Å)	Se in input solution			Log K_d	Unit-cell parameter of substitution ion					Unit-cell dimensions		
			pH	$Tr_{initial}$ [mM]	SI of barite	[L/kg]	a [Å]	b [Å]	c [Å]	R_{wp} [%]	S	k_a(Å)	k_b(Å)	k_c(Å)
ReO_4^-	0.26	2.60	8.0	1.0×10^{0}	4.21	-0.89	8.88161	5.45565	7.15730	6.10	2.90	-0.01439	-0.00635	-0.01370
SeO_4^{2-}	0.42	2.43	8.0	1.0×10^{0}	4.21	0.08	8.88075	5.45450	7.15490	7.08	1.44	-0.01525	-0.00750	-0.01610
AsO_3^-	0.46	2.48	8.0	1.0×10^{0}	4.21	0.30	8.89181	5.46020	7.16460	9.86	1.98	-0.00419	-0.00180	-0.00640
SeO_3^{2-}	0.50	2.39	8.0	1.0×10^{0}	4.21	1.35	8.87945	5.45420	7.15590	6.89	1.46	-0.01655	-0.00780	-0.01510
CrO_4^{2-}	0.52	2.30	8.0	1.0×10^{-4}	4.21	4.60	8.84830	5.45420	7.13970	13.26	10.02	-0.04770	-0.00780	-0.03130
TeO_3^{2-}	0.56		8.0	1.0×10^{-1}	4.21	0.41	8.88200	5.45510	7.15680	19.62	9.15	-0.01400	-0.00690	-0.01420
AsO_2^-	0.58	2.11	8.0	1.0×10^{0}	4.21	-0.89	8.88163	5.45396	7.15590	7.67	1.63	-0.01437	-0.00804	-0.01510
IO_3^-	0.62	2.18	8.0	1.0×10^{0}	4.21	0.59	8.88071	5.45435	7.15650	5.72	3.96	-0.01529	-0.00765	-0.01450
MoO_4^{2-}	0.63	2.46	8.0	1.0×10^{-1}	4.21	0.01	8.88002	5.45544	7.15740	5.42	2.46	-0.01598	-0.00656	-0.01360
WO_4^{2-}	0.68		8.0	1.0×10^{-1}	4.21	-0.10	8.87953	5.45340	7.15540	6.36	2.87	-0.01647	-0.00860	-0.01560
$Sb(OH)_6^-$	0.69		8.0	1.0×10^{-2}	4.21	0.57	8.88301	5.45520	7.15850	8.88	4.16	-0.01299	-0.00680	-0.01250
TeO_4^{2-}	0.70		8.0	1.0×10^{-1}	4.21	0.45	8.87914	5.45270	7.15480	6.63	3.30	-0.01686	-0.00930	-0.01620

Chapter 3. Application of selenium in barite as a redox indicator for oxic/suboxic redox condition

1. Chapter Introduction

Generally speaking, oxyanions in water show conservative behavior compared with polyvalent cations that can be strongly affected by their adsorption on particulate matter in water. Among various elements that form oxyanions, such as sulfur, chromium, arsenic (As), selenium (Se), molybdenum, and rhenium, Se is unique in terms of having two oxidation states that form oxyanions in natural water. At equilibrium, the concentration ratios of various redox species such as Se(VI) and Se(IV) can be affected by the redox potential (E_h, if standardized to hydrogen electrode) in the environment. It is often the case, however, that the oxidation states of inorganic ions in seawater, selenate or selenite, are kinetically controlled, where thermodynamically unstable species can be present [Cutter and Bruland, 1984; Cutter, 1992; Rue et al., 1997]. The presence of such unstable species can be caused by biological effects, transport of the species by lateral advection and sinking particles, and so on. Thus, the Se(VI)/Se(IV) ratio in water can be influenced by various factors including redox condition, biological activities, and mixing of these species of different origins.

If we confine the system at equilibrium, the Se(VI)/Se(IV) ratio can be primarily

controlled by the redox condition of the environment. On the other hand, previous studies have shown that redox condition tends to be controlled by the redox reactions of major elements (O, C, N, S and Fe), whereas trace elements (As, Se, Co, Ni, V, Mo, Cr, U, and Re) respond to the redox conditions rather than control it [Thomson. et al., 1998; Algeo et al., 2004; Takahashi et al., 2004; Pufahl and Hiatt, 2012]. Consequently, the soluble Mn(II), soluble Fe(II), and S(-II) redox species in water were directly measured to make the quantitative redox potential amendable to quantitative interpretation [Masscheleyn et al., 1991].

Selenium is dissolved in water as selenate (SeO_4^{2-}) or selenite/hydroselenite (SeO_3^{2-} /$HSeO_3^-$) ion under oxic and suboxic conditions, respectively, but can be immobilized under reducing condition by its reduction to native selenium (Se(0)) because of its low solubility [Sharmasarkar et al., 1998; Bujdos et al., 2005; Harada and Takahashi, 2009]. Selenate and selenite are highly soluble ions, but they can be incorporated into the solid phase by adsorption or coprecipitation with minerals. The distribution behavior of Se between the solid phase and water is variable depending on its oxidation state and chemical form [Fernandez and Charlet, 2009]. Thus, the Se(VI)/Se(IV) ratio recorded in the solid phase by coprecipitation can be used to estimate the Se(VI)/Se(IV) ratio in water.

Barite ($BaSO_4$), which is stable under a wide range of pressure, temperature, E_h, and pH, can incorporate various trace elements that may record geochemical information in water and eventually reflect depositional condition [Torres et al., 2003; Van Beek et al., 2003; Paytan et al., 2007; Snyder et al., 2007; Torres Griffith and Paytan, 2012] (Fig. 1a). Several elements (for example, cations: Sr^{2+}, Ca^{2+}, Ra^{2+}, Pb^{2+}, and Nd^{3+}; anions: SeO_4^{2-}, CrO_4^{2-}, and MnO_4^{2-}) are incorporated into barite by substituting Ba^{2+} or SO_4^{2-}, respectively [Guichard et al., 1979; Prieto et al., 2002; Hein et al., 2000; Zhu, 2004]. It has been reported that Se is strongly bound mainly in the sulfate site of the crystal lattice of barite [Andara et al., 2005]. If both selenite and selenate can be incorporated into barite, Se may preserve information about the Se(VI)/Se(IV) ratio of the depositional environment. Especially under equilibrium condition, the Se(VI)/Se(IV) ratio in barite may indicate the Se(VI)/Se(IV) ratio in water, which shows whether the redox condition of the environment is below or above the redox boundary of Se(VI)/Se(IV), or oxic/suboxic boundary (Fig. 1(b)).

The purpose of this study is to know whether it is possible to estimate the Se(VI)/Se(IV) ratio in water based on the Se(VI)/Se(IV) ratio in barite, which may reveal the redox condition in the water under equilibrium condition. No study has been conducted on the utilization of the oxidation states of trace elements in precipitates to

estimate the redox state of the element in the coexisting water. We already have conducted related studies based on a similar idea for As and Se incorporation into calcite [Yokoyama et al., 2011 and 2012]. However, we found that arsenate and selenite were selectively incorporated into calcite even when only arsenite or selenate was initially added into the solution, respectively. The results suggested that As and Se in calcite are not appropriate to estimate the As(V)/As(III) and Se(VI)/Se(IV) ratios in water. Therefore, the distribution behaviors of Se between water and barite needs to be examined with speciation analyses of Se both in water and solid phases to establish it as a method for estimating the Se(VI)/Se(IV) ratio in water.

In this study, batch experiments were conducted at artificial seawater (ASW) conditions to estimate the partitions of Se to barite in seawater. X-ray absorption near-edge structure (XANES) was used to determine the oxidation state of Se in the solid phase directly, whereas high-performance liquid chromatography (HPLC) connected to inductively-coupled plasma mass spectrometry (ICP-MS) was used to determine the oxidation state of Se in water. The apparent distribution coefficient (K_d) of Se between barite and water was also measured by ICP-MS to clarify the difference in the immobilization mechanisms between Se(IV) and Se(VI) at pH 4.0 and 8.0. In addition, the local structure of Se in barite was examined from Se K-edge EXAFS to clarify the

structure of Se in barite, not adsorbed on barite.

In this study, natural barite samples collected in high Se concentration areas were also analyzed by micro-X-ray fluorescence (μ-XRF) and micro-X-ray-adsorption fine structure (μ-XAFS) to investigate whether this method can be applied to natural systems where barite precipitates. Natural barite samples obtained near the hydrothermal vent system at the seafloor in Okinawa Trough (Izena Hole) in Japan without information of the depositional E_h-pH condition were analyzed. In natural system, the partitions of major and trace elements to minerals were influenced by several factors, such as pH, ionic strength, precipitation rate, competitions, and others [Lorens, 1981; Alexandratos et al, 2007]. Thus, in this study, natural barite samples in marine sediment were analyzed whether the Se(VI)/Se(IV) ratio in barite may indicate the Se(VI)/Se(IV) ratio in water, or oxic/suboxic boundary, as observed in laboratory experiments. Thus, if the Se(VI)/Se(IV) ratio in barite can also be applied as a redox indicator in natural system, barite can provide information on whether it is precipitated under oxic or suboxic redox environments.

2. Methods

2.1. Experimental procedures

Coprecipitation of Se with barite was conducted through the spontaneous precipitation of barite. Laboratory experiments were conducted at various Se(VI)/[total Se] ratios in water (= R_w^{VI}), as determined by high-performance liquid chromatography-inductively coupled plasma-mass spectrometry (HPLC-ICP-MS), to investigate the influence of oxidation state on the immobilization Se(IV) or Se(VI) into barite. Se(IV) and Se(VI) stock solutions were prepared from $NaHSeO_3$ and Na_2SeO_4 (Wako, Japan), respectively. Barite was precipitated from a mixture of (i) ASW containing 27 mM sulfate and (ii) 2.0 mM $BaCl_2 \cdot 2H_2O$ solution [Blount, 1974]. The ASW consisted of 440 mM NaCl, 50 mM $MgCl_2 \cdot 2H_2O$, 27 mM Na_2SO_4, 9.6 mM $CaCl_2 \cdot 2H_2O$, and 2.2 mM $NaHCO_3$. Right before the addition of $BaCl_2 \cdot 2H_2O$ solution, Se(IV) and/or Se(VI) were added to ASW. This solution was continuously adjusted to a specific pH (pH 4.0 or 8.0) by adding a small amount of HCl or NaOH solution during the experiments. The two pH conditions were used to assume (i) general hydrothermal pH condition (pH = 3.0 to 4.0) and (ii) seawater condition (pH = 8.0) [Von Damm, 1990]. The mixed solution was stirred under ambient condition with a magnetic stirrer at 25 °C for 168 h (= 7 days). The saturation indices of barite (SI_{barite}) in the initial solutions

were fixed at 4.2 by adjusting the Ba^{2+} concentration to keep the same initial precipitation rate of barite for all experiments in this study (Table 1). Under this condition, barite rapidly precipitated because of its high supersaturated condition. SI is defined as SI = log(IAP/K_{sp}), where IAP is the ion activity product and K_{sp} is the solubility product of a mineral. The initial solution of Se (concentration: 0.10–1.0 mM) was unsaturated with respect to the solid phases of barium selenite and barium selenate to avoid the formation of these Se precipitates in the system (Table 1).

2.2. Analysis of natural samples

The hydrothermal barite sample was analyzed to estimate the depositional E_h condition in water where barite precipitated. The barite samples used in this study were found in a marine sediment (depth from sea floor: 0–4 cm) within a core sample collected in the Jade site during NT10-17 cruise (Yokoyama et al., 2015), a hydrothermal vent system located along the northeastern slope of the Izena Hole at water depths of 1300–1550 m in the Izena Cauldron, Okinawa Trough (Kawagucci et al., 2010; Ishibashi et al., 2014). E_h and pH of the pore water in the sediment were 150 mV and 7.1, respectively. However, the depositional E_h-pH condition of the barite sample when barite precipitated is unknown.

2.3. Analysis methods

2.3.1. HPLC-ICP-MS

The Se(VI)/Se(IV) ratio in the water sample was determined by HPLC-ICP-MS. The Pu-2089 Plus pump and a Co-2065 Plus (JASCO) oven were used in the experiment. An anion exchange column (Hamilton, PRP-X100; column length: 25 cm) was used at 40 °C. The mobile phase was the aqueous solution containing 10 mM EDTA (Wako, Japan), 2.0 mM potassium hydrogen phthalate (Wako, Japan), and 3.0 wt% methyl alcohol (Wako, Japan). To remove any Se remaining in the inlet and syringe, about 100 μL of Milli-Q water was injected into the syringe and also into the HPLC system after measurement to avoid contamination in subsequent analyses.

2.3.2. XAFS measurement and data analysis

XANES technique is a suitable method to determine the Se(VI)/Se(IV) ratio in barite, because it is a nondestructive analytical method. The K-edge XANES spectra of Se were obtained in the beamline BL01B1 of SPring-8 (Hyogo, Japan) and in the beamline BL-12C of Photon Factory, KEK (Tsukuba, Japan) with an Si(111) double-crystal monochromator and two mirrors. The monochromator was calibrated using a reference sample, $NaHSeO_3$, which was prepared as a pellet after dilution with boron nitride powder

and the energy value of 12.6545 keV was assigned to the peak maximum in the XANES region for the compound. The XANES spectra of the reference compounds were collected in transmission mode, whereas those of the experimental samples were obtained in fluorescence mode using a 19-element germanium semiconductor detector at 90° to the incident beam. In the fluorescence mode, the samples were positioned at 45° with respect to the incident beam. Multiple scans were obtained to check the radiation damage that can change the valence ratio of Se in the samples, where no appreciable change was found in every spectrum obtained here. The measurements were carried out at room temperature under ambient condition. The XANES data were analyzed using a REX2000 (Rigaku Co.) for fitting the sample spectra by linear combination of the reference materials. The Se(VI)/Se(IV) ratio in the solid sample was determined by least-squares fitting using the reference spectra of $BaSeO_3$ (Wako Pure Chem., Ltd., Japan) and $BaSeO_4$ (Alfa Aesar, UK), which were received as analytical grade reagents.

The EXAFS spectra for both reference compounds and experimental samples were obtained to confirm the local structure of Se in barite by normal procedures using a REX2000 software (Rigaku Co. Ltd.) with parameters generated by the FEFF 7.0 code. After background subtraction and normalization, EXAFS oscillations. The $\chi(k)$ functions were extracted from the raw the samples studied. After extracting EXAFS

oscillation and its Fourier transformation, the inversely Fourier filtered data were analyzed with a usual curve fitting method (Zabinsky et al., 1995). The theoretical phase shifts and amplitude functions for Se-O, Se-Ba pairs employed in this fitting procedure were extracted from FEFF 7.0 (Zabinsky et al., 1995).

The initial structural data for the FEFF calculation was provided by the ATOMS code (Ravel, 2001) based on the 3-dimensional structural data of $BaSeO_3$ for Se (Giester, G., and C. L. Lengauer, 1998). The error estimates of interatomic distance and coordination number obtained by the fitting were ±0.02 Å and ±20 %, respectively (O'Day et al., 1994). The quality of the fit was given by the goodness-of-fit parameter *R*, defined by

$$R(\%) = \frac{\Sigma\{k^3\chi_{dat}(k) - k^3\chi_{cal}(k)\}^2}{\Sigma\{k^3\chi_{dat}(k)\}^2}$$

where $\chi(k)_{dat}$ and $\chi(k)_{cal}$ are experimental and theoretical data points, respectively.

For the simulation of EXAFS for Se in samples, the spectra at *k* space were simulated by the linear combination of the spectra of possible Se in samples, such as Se adsorbed on/in barite.

2.3.3. μ-XRF and μ-XANES

Each natural barite sample was embedded in a high-purity epoxy resin (Eposet,

Maruto Co., Ltd.) and polished to create a thin section for EPMA and μ-XRF analyses. The distribution of arsenic within the barite sample at the micrometer scale was obtained at beamline 37XU (SPring-8) via μ-XRF (Terada et al., 2004). The beamline consisted of a Si(111) double crystal monochromator with a Kirkpatrick–Baez mirror to obtain a 0.5×0.5 μm^2 X-ray beam at the sample position. The X-ray energy was fixed at 12.8 keV to obtain the μ-XRF image of As (Kα line), Ba (Lα line), and other elements. Two-dimensional (2D) mapping was conducted using an X-Y axis stage. The sample was fixed on a sample holder oriented at 10° to the orthogonal direction of the incident X-ray beam. The XRF intensity of each line was measured by a silicon drift detector. The step size of the stage was set to 2.0 μm, and the exposure time at each point was 0.1 s. Measurements were carried out under ambient condition

2.3.4. EPMA

Quantitative electron probe micro analyzer (EPMA; back-scattered electron image) analyses were conducted to specify the barite components in this sample. It performed by wavelength dispersive spectrometry (WDS) operated at 15 kV with a beam current of 15 nA. The beam size was set to 2×2 μm^2. The counting time was 20 s for each element except for Se (30 s) and S (10 s), and raw datum corrections were made for ZAF

method (i.e., correction for atomic number, absorption, and fluorescence effects in X-ray microanalysis). The following X-ray lines and standards were used: Ba Kα (BaO), Sr Kα (synthetic SrO), Ca Kα (synthetic CaO), Se Kα (synthetic SeO_2), S Kα (SO_3).

2.3.5. LA-ICP-MS

The concentration of Se in depositional barite were measured by LA-ICP-MS (7500cs, Agilent, Tokyo, Japan) based on analytical method by Tanaka et al. (2006) to determine whether the oxidation states of Se in barite can be detected by the μ-XRF-XANES analysis. The concentration of Se in barite was calculated compared with the Se/Ba ratio in the sample and in reference materials of barite with known amount of Se synthesized in this study.

3. Results and discussion

3.1. Laboratory experiments

3.1.1. The oxidation state of Se in barite

3.1.1.1. At pH 8.0 system

Coprecipitation experiments at various R_W^{VI} were conducted at pH 8.0 to investigate the effect of the oxidation state on its immobilization into barite at seawater systems. X-ray diffraction results for the samples showed that the precipitates consisted of only barite. The formations of barium selenite and barium selenate are not likely, because they were under saturation in terms of their solubility products. Barium sulfate mineral can be exclusively present as barite in nature without any other polymorphs based on the survey of Inorganic Crystal Structure Database (ICSD). Thus, the transformation of barite to other minerals associated with aging or pH condition is not likely. This result suggested that if Se was strongly bound mainly in the sulfate site in the crystal of barite, the Se(VI)/Se(IV) ratio in barite can be preserved during aging. The intensities and widths of the peaks in the XRD were similar to those of the reference sample of barite, suggesting that the incorporation of Se did not altered the main mineralogy of barite because of the low Se concentration added to the system.

The oxidation state of Se in the precipitates was determined by XANES based on

the fitting of the spectra of samples by the linear combination of the spectra of $BaSeO_3$ and $BaSeO_4$, where most of the samples could be fitted by these two reference materials (Fig. 2; Table 1). The Se(VI)/Se(IV) ratios obtained from this method showed that (i) most Se in the precipitates were coprecipitated as Se(IV) for the samples when R_W^{VI} (= [Se(VI)]/[total Se] ratio in water determined by HPLC-ICP-MS) was lower than 0.8, but (ii) R_B^{VI} (= [Se(VI)]/[total Se] ratio in barite determined by XANES) increased when R_W^{VI} was over 0.8 (Fig. 3). These findings indicated that R_B^{VI} was primarily correlated with R_W^{VI} in water. When $R_W^{IV} = 1$ (R_W^{IV}: [Se(IV)]/[total Se] ratio in water determined by HPLC-ICP-MS), Se was incorporated only as Se(IV) in the precipitates. When $R_W^{VI} = 1$, on the other hand, a part of Se was incorporated as Se(IV), but more than 80% of Se was mainly incorporated as Se(VI). All these results were reproducible at least under our experimental conditions based on our repeated coprecipitation experiments ($N = 3$) with XANES and HPLC-ICP-MS analyses. These analyses suggested that the reduction of Se(VI) occurred at $R_W^{VI} = 1$ possibly because the stability of Ba-selenite is larger than that of Ba-selenate, which promotes Se(VI) reduction. To confirm this result, the R_W^{VI} was also measured during the formation of barite by HPLC-ICP-MS. The results showed that R_W^{VI} did not change before and after coprecipitation, suggesting that the initial R_W^{VI} was preserved during the experimental period. The redox change induced

by the complexation reaction was also confirmed by Yokoyama et al. (2012), showing that As was immobilized in calcite as As(V) after the oxidation of As(III) to As(V) because of the larger stability of Ca-arsenate than that of Ca-arsenite.

When R_W^{VI} was above 0.8, R_B^{VI} shows a positive correlation with R_W^{VI} at pH 8.0. At R_W^{VI} below 0.8, Se(VI) was not found in barite within the detection limit of XANES analysis (= about 5% as shown for the arsenate-arsenite system in Takahashi et al., 2003). Thus, although the reduction of Se(VI) to Se(IV) inhibits precise determination of R_W^{VI} by R_B^{VI}, we can estimate whether more than 80% of dissolved Se is Se(VI) or not based on the presence or absence of Se(VI) in barite determined by XANES analysis.

3.1.1.2. At pH 4.0 system

Coprecipitation experiments at various R_W^{VI} were also conducted at pH 4.0 to simulate Se distribution to barite in hydrothermal systems. XRD results showed that the precipitates consisted only of barite without other minerals above the detection limit (> 5%). The initial R_W^{VI} was preserved again at pH 4.0 during aging as revealed by HPLC-ICP-MS analysis, indicating that the direct reduction of Se(VI) to Se(IV) and/or Se(IV) to Se(0) cannot be observed in water.

As for Se species in the solid phase, however, Se(IV), Se(VI), and a smaller amount

of Se(0) were detected at pH 4.0 by Se K-edge XANES (Fig. 2b). Unfortunately, it was impossible to unequivocally verify the Se(0) precipitates by XRD, because the Se(0) concentration was lower than the detection limit of XRD (> 5%). The oxidation state of Se in barite showed that Se(VI) was incorporated into barite to a larger degree than that at pH 8.0 as shown by XANES analysis (Fig. 3). Results showed that (i) R_B^{VI} was strongly correlated with R_W^{VI}, (ii) Se(0) was also detected under high R_W^{IV} condition in water at pH 4.0. In particular, Se was incorporated as multiple Se species of 72% Se(IV), 23% Se(0), and 5% Se(VI) in the precipitates at R_W^{IV} = 1.0. On the other hand, at R_W^{IV} = 1.0, 13% Se(IV) and 87% Se(VI) were detected in the precipitates without any contribution of Se(0). The R_B^{VI} represented a positive correlation against R_W^{VI} (Fig 3), as we also found in the pH 8.0 system. Selenium(0) was detected as well in barite at a high R_W^{IV} in this experiment. This result suggested that Se(0) was formed more readily in the presence of barite, because R_W^{VI} was stably conserved without the formation of Se(0) in a barite-free system for the experimental period of this study. To exclude the effect of Se(0) formation, the ratio of [Se(VI)]/{[Se(IV)]+[Se(VI)]} was also plotted against R_W^{VI} (note that Se(0) is not present as dissolved species), where a good correlation was still observed between them. Thus, it is suggested that the Se(VI)/Se(IV) ratio in barite can reflect the ratio in water at pH 4.0 even in the presence of Se(0) in the solid

phase.

As shown above, reduction of Se(VI) to Se(IV) or Se(IV) to Se(0) was observed during the incorporation of Se into barite, but the reductant in the reactions is not clear at present. The effect of X-ray beams on the redox change of Se was carefully examined by repeated scans of XANES spectra, which shows that no radiation effect was observed in our measurement. Given the low Se concentration, we believe that the reduction of Se(IV) to Se(0) can occur by any reductants in the system. One possibility can be water itself by the reaction of $H_2O \rightarrow 2\ H^+ + 1/2\ O_2 + 2\ e^-$. Selenium(0) was not found at pH 8.0, but only found at pH 4.0, where the stability field of Se(0) in the E_h-pH diagram is larger (Fig. 1b). In addition, Se(0) was found only in the presence of barite, possibly because the precipitation of Se(0) can be promoted in the presence of the solid surface.

Similarly, we think that the reduction of Se(VI) at $R_W^{VI} = 1$ occurred due to the increase in stability of Se(IV) in the system through the formation of barium selenite, which is a much more stable complex than barium selenate. The redox change during the incorporation into such precipitates was also reported by (i) Yokoyama et al. (2012), who have shown As(III) oxidation during its incorporation into calcite, and (ii) Tsuno et al. (2003), who have shown the reduction of Yb(III) to Yb(II) during its incorporation into calcite. Thus, it is suggested that the immobilization of Se(IV) was promoted by

the reduction of Se(VI) to Se(IV) via formation of barium selenite complexes. The electron donor in the solution was unclear, but we think that water can be a reductant because of the oxidation of water into O_2 ($H_2O \rightarrow 2\ H^+ + 1/2\ O_2 + 2\ e^-$) as suggested above.

3.1.1.3. Comparison of the distribution behavior of Se in both pH systems

In addition to the examination of two different pH conditions, similar coprecipitation experiments were conducted at various systems as summarized in Table 2. All experiments were conducted at $R_W^{VI} = 1$ or $R_W^{IV} = 1$ at pH 8.0. At first, other chemical compositions of the solution was tested, including the use of ASW (results were already shown above), ASW without bicarbonate (carbonate), ASW added with phosphate, and just Milli-Q water, where the saturation index (SI) of barite and Se concentration added to the system were kept constant. Second, the SI of barite was also varied from 2.9 to 4.2 at constant Se concentration with various barium concentrations to evaluate the effect of the precipitation rate. Previous studies showed that the precipitation rate depends on the saturation state in solution, which has a significant influence on the distribution behavior of several ions between mineral and water [Lorens, 1981; Alexandratos et al, 2007].

The results showed that the apparent K_d value can be variable under different conditions: K_d increased (i) in the absence of carbonate, (ii) at a larger initial Se concentration, and (iii) at a lower SI. Especially, SI had strong influence on the partitioning of Se into barite, showing that K_d linearly decreased with increasing SI (Fig. 4). Based on the XANES analyses, however, the R_B^{VI} was constant at 83%±5 %, which showed that the R_B^{VI} was not changed at various SI employed in this study. All these results suggested that the relationship between R_W^{VI} and R_B^{VI} was not affected even when the chemical composition, SI, and Se concentration were changed to a certain degree.

Compared with these parameters, pH markedly affected the incorporation of Se into barite, possibly because of the different chemical forms of dissolved species of Se(IV) at different pH values, as will be discussed later. The effect of temperature, which has not been examined here, must be studied in the future especially to estimate the Se(VI)/Se(IV) ratio in hydrothermal water based on the ratio in barite. Similarly, the vital effect on the Se(VI)/Se(IV) ratio must be studied if barite precipitated in biogenic debris.

3.1.1.4. Local structure of Se in barite

The local structure of Se in barite was examined from Se K-edge EXAFS to clarify the structure of Se in barite. The EXAFS spectra for four barite samples were measured:

Se(IV) adsorbed on barite, Se(IV) coprecipitated into barite, Se(VI) adsorbed on barite, and Se(VI) coprecipitated into barite. $BaSeO_3$ and $BaSeO_4$ samples were employed as a reference compounds.

Figures 5 and Fig. 6 showed the k^3-weighted EXAFS function and Fourier-transformed EXAFS spectra, respectively. The EXAFS fit results for the barite samples showed that Se in/on barite can be explained by the three shells of one Se-O and two Se-Ba (Table 3). The Se-O shell shows that Se(IV) or Se(VI) are incorporated into barite as selenite in a trihedral coordination with oxygen or selenate in a trihedral coordination with oxygen, respectively. The two Se-Ba shells show that the distance and coordination number of Se-Ba in the coprecipitated samples are similar to that of S-Ba in barite (Gupta et al., 2010), indicating that Se is incorporated into the barite structure via the substitution for sulfate anion during the coprecipitation. When the local structures of Se (IV) in the coprecipitated and adsorption samples were compared based on EXAFS, it is shown that the coordination number of Se-Ba in the coprecipitation sample is larger than that in adsorption system. These features in the EXAFS spectra are reasonable because the difference between adsorption and incorporation samples can be expected in the number of Ba atoms surrounding Se(IV), which is less for Se at the surface (= adsorption sample) than in the bulk (= coprecipitation sample). Thus, it is found that Se

is incorporated into barite by substitution of sulfur site in barite, not precipitates solid solution or independently $BaSeO_3$ and $BaSeO_4$ mineral. Based on these results, it is demonstrated that both Se(IV) and Se(VI) were incorporated into barite crystal lattice, not adsorbed on barite surface.

3.1.2. Distribution coefficient of Se between barite and aqueous solutions

Variation of the apparent distribution coefficient (= K_d) of Se between barite and water were plotted against R_W^{VI} for systems aged at pH 8.0 and 4.0 (Fig. 7). The apparent distribution coefficient of Se between barite and water is defined as

$$K_d \text{ (L/kg)} = [Se]_B / [Se]_W$$

where $[Se]_B$ and $[Se]_W$ are the total Se concentration in the barite (mol/kg) and in water (mol/L), respectively. In this study, the amount of barite was calculated from the difference in concentration of barium between the input (initial) and final solutions by ICP-AES measurements (Yokoyama et al., 2012). The calculated amount of barite formed in each solution was $(1.1 \pm 0.03) \times 10^{-1}$ g in the experiment at SI = 4.2.

For the pH 8.0 system, the total Se concentration in barite and water were determined after 168 h, when the precipitation process of barite was completed. Consequently, a much larger amount of Se was incorporated into barite at $R_W^{IV} = 1$ compared with that at

$R_W^{VI} = 1$ (Table 2). The apparent K_d values at pH 8.0 decreased from 4.0×10^2 L/kg to 1.0×10^2 L/kg with increasing R_W^{VI} in water (Fig. 8). Thus, Se(IV) was more preferentially incorporated into barite than Se(VI) under surface seawater condition at pH 8.0. As for the pH 4.0 system, on the other hand, the distribution of Se to barite showed a different trend from that at pH 8.0; the apparent K_d value remained nearly constant at various Se(VI)/Se(IV) ratios in water; K_d values were 9.5×10^1 L/kg and 8.1×10^1 L/kg at $R_W^{IV} = 1$ and $R_W^{VI} = 1$, respectively (Fig. 8).

The apparent K_d of Se(IV) and Se(VI) defined as $K_{Se(IV)}$ and $K_{Se(VI)}$ were determined from the equation:

$$K_{Se(IV)} = K_d \times \frac{R_B^{IV}}{R_W^{IV}}$$

and

$$K_{Se(VI)} = K_d \times \frac{R_B^{VI}}{R_W^{VI}}$$

where R_B^{IV} is [Se(IV)]/[total Se] ratio in barite determined by XANES. In addition, the apparent K_d value can be written as

$$K_d = (1 - R_W^{VI})\, K_{Se(IV)} + R_W^{VI} K_{Se(VI)}.$$

This equation implies that K_d is correlated with R_W^{VI} if $K_{Se(IV)}$ and $K_{Se(VI)}$ are constant at various R_W^{VI}. The results showed a linear correlation between R_W^{VI} and apparent K_d values at pH 8.0 ($r^2 = 0.95$; Fig. 8). Calculations showed that $K_{Se(IV)}$ and $K_{Se(VI)}$ at pH

8.0 were 4.0×10^2 L/kg and 8.5×10^1 L/kg, respectively. The $K_{Se(IV)}/K_{Se(VI)}$ can be estimated as 4.7, indicating that Se(IV) was preferentially coprecipitated into barite compared with Se(VI) in the pH 8.0 system (Table 4). On the other hand, in the pH 4.0 system, $K_{Se(IV)}$ and $K_{Se(VI)}$ are calculated as 9.0×10^1 L/kg and 7.0×10^1 L/kg, respectively, indicating that the distribution of Se to barite was almost identical between Se(IV) and Se(VI) in the pH 4.0 system.

3.1.3. Comparison of the distribution behaviors of Se in both pH systems

The degree of adsorption of Se depends on pH, especially for Se(IV) [Sharmasarkar et al., 1998; Seby et al., 2001; Torres et al., 2010] (Fig.8). Selenium(IV) is a weak acid that can exist as H_2SeO_3, $HSeO_3^-$, or SeO_3^{2-}, depending on the solution pH ($pKa_1 = 2.70$, $pKa_2 = 8.54$). On the other hand, Se(VI) is dissolved only as SeO_4^{2-} in the pH region of natural water due to the low pKa_1 and pKa_2 ($pKa_1 = -2.01$, $pKa_2 = 1.80$) [Torres et al., 2011; Tanaka et al., 2013]. Speciation calculations based on pKa showed that Se(IV) dissolved as $HSeO_3^-$ in the pH range from 2.7 to 8.5 and as SeO_3^{2-} at pH above 8.5 under our experimental conditions. Thus, Se(IV) is dissolved only as the monovalent anion $HeSeO_3^-$ in the pH 4.0 system, whereas 60% SeO_3^{2-} and 40% $HSeO_3^-$ were present in the pH 8.0 system in this study. A number of previous studies have shown that SeO_3^{2-}

forms more stable complexes with cations than SeO_4^{2-}, whereas $HSeO_3^-$ forms less stable complex than SeO_3^{2-} because of the lower charge on $HSeO_3^-$ [Abdullah et al., 1995; Smedley and Kinniburgh, 2002]. As a result, an obvious trend between Se speciation and the incorporation behavior of Se into barite was observed in this study. In the pH 8.0 system, Se(IV) was incorporated into barite to a larger degree than Se(VI). This result was possibly due to the larger stability of surface complex of SeO_3^{2-} to barite surface compared with SeO_4^{2-}, which was suggested from the larger stability of $BaSeO_3$ complex than that of $BaSeO_4$ based on the Linear Free Energy Relationship (LFER; Stumm, 1992), describing the linear relationship between the logarithms of stabilities of the surface complex and corresponding complex in solution. In the pH 4.0 system, on the other hand, Se(IV) was incorporated to a lesser degree compared with the pH 8.0 system because of the relative decrease in the affinity of Se(IV) for barite as the Se(IV) species in water changes from SeO_3^{2-} to $HSeO_3$.

Similar coprecipitation experiments at another pH conditions (pH=2.0, 5.0, 9.0) were conducted to confirm the reliability of this hypothesis. These pH condition were determined to assume the variation of Se species in water: (i) Se(IV) was mainly dissolved as H_2SeO_3, $HSeO_3$, SeO_3^{2-} at pH 2.0, 5.0, 9.0 conditions, respectively, while (ii) Se(VI) was mainly dissolved as SeO_4^{2-} at pH 5.0 and 9.0, and 40 % $HSeO_4^-$ was also presented

at pH 2.0 (Fig. 8). All experiments were conducted at $R_W^{VI} = 1$ or $R_W^{IV} = 1$ and calculate the apparent distribution coefficient rate between them to investigate the influence between Se speciation and the incorporation behavior of Se into barite.

The Se(VI)/Se(IV) ratio in barite as a function of R_w^{VI} under different pH conditions is also plotted at Fig. 9. The results showed that (i) the Se(VI)/Se(IV) ratio in barite strongly reflected the Se(VI)/Se(IV) ratio in water at lower pH, while (ii) the Se(VI)/Se(IV) ratio in barite little depends on the Se(VI)/Se(IV) ratio in water at higher pH. This is dependent on metal speciation of Se(IV) and Se(VI) by pH, which related to the electrostatic repulsion between dissolved ion and the charged surfaces site, and explain in chapter 4.

3.1.4. Implications extracted from the Se(VI)/Se(IV) ratio in water

If the Se(VI)/Se(IV) ratio in water can be estimated by the ratio in barite, what are the geochemical implications obtained by the estimated ratio? In most case, Se(VI)/Se(IV) in natural water is known to be controlled by kinetic factors, where (i) thermodynamically unstable species can be found such as Se(IV) and Se(VI) under oxic and reducing conditions, respectively, and (ii) organo selenium species are also prevalent [Cutter and Bruland, 1984; Cutter, 1992; Rue et al., 1997]. These phenomena observed

as a disequilibrium state in terms of the redox reactions for inorganic selenium species can be due to (i) biological effects and (ii) supply of species by lateral transport or vertical input by sinking particles [Cutter and Bruland, 1984; Cutter, 1992; Rue et al., 1997]. Thus, if we could recover barite in various environment, the Se(VI)/Se(IV) ratio in barite may provide information on these processes such as biological effect and transport of specific species of Se from other sources. Thus, it is expected that the Se(VI)/Se(IV) ratio in water estimated by the ratio in barite can have implications on biogeochemical processes of Se and transport of Se(VI) or Se(IV) in the environment where barite was deposited.

If it is under equilibrium condition in terms of redox reactions, the Se(VI)/Se(IV) ratio in barite can be more straightforwardly used. In this case, the variation of Se(VI)/Se(IV) ratios in water corresponds to the change of E_h of the depositional environment; a larger Se(VI)/Se(IV) ratio corresponds to oxic condition, while a low ratio corresponded to reducing. Thus, the experimental system with various Se(VI)/Se(IV) ratios in water enables us to reproduce the incorporation of Se into barite under various E_h conditions in a natural system that can be calculated from the Se(VI)/Se(IV) ratios in water if we can assume equilibrium and if the pH is known. Consequently, the relationship between R_B^{IV} and E_h in water, which was calculated from the Se(VI)/Se(IV)

ratio in water, is shown in Fig. 10a as an example for the case of pH 4.0; barite precipitated under reducing conditions at E_h < 0.63 V the R_B^{IV} in barite was > 96%. Meanwhile, barite precipitated under an oxic condition at E_h > 0.80 V at pH 4.0 if the R_B^{VI} in barite was > 80%. A similar relationship between R_B^{IV} and E_h can be obtained also for the case of pH 8.0 in Fig. 10b. Based on the laboratory experiments presented, it is suggested that barite-selenium system work as a reliable redox indicator to estimate E_h range where barite precipitated.

3.2. Application to natural samples

3.2.1. Identify the mineral compositions

EPMA analysis carried out to gain information on the mineralogical composition in the marine sediments samples (Table 5). The barite minerals were also identified in backscattered electron (BSE) photographs based on quantitative chemical analysis by EPMA (Fig. 11a, 11b). Results of the BSE images also revealed that the barite minerals were either presented with pyrite (spot 1 in Fig. 11a) or feldspar (spot 4 in Fig. 11b). Quantitative EPMA results showed that the concentration of Se in barite sample (spot 3 in Fig. 11b) was lower than detection limited (> 90 mg/kg).

3.2.2. Elemental Distribution and Concentration of Se in barite

Micro-XRF elemental mapping was performed for several parts in marine sediments to determine the spatial distribution of Ba, Se and Fe, some of which are shown in Fig. 12. An example of elemental maps for Ba, Se, and Fe in the grain in Fig. 12, especially in the left part, showed that the spatial distributions of Se was correlated with that of Ba in the samples, suggesting that Se was incorporated into barite. The correlation coefficient (r) between Ba and Se intensities was relatively high especially in the left side of Fig. 12 (r = 0.75-0.77), as shown in Fig. 13b (r = 0.77) and Fig. 13c (r = 0.75). However, the r value was not high enough possibly due to the different probing depths of XRF using Se Kα and Ba Lα lines. In order to determine whether the oxidation states of Se in barite can be detected by the μ-XRF-XANES analysis, the concentration of Se in depositional barite at spot 3 was measured by LA-ICP-MS (7500cs, Agilent, Tokyo, Japan) based on analytical method by Tanaka et al. (2006). Fig. 14 show a correlation between Ba and Se signal by LA-ICP-MS measurement, showing that concentration of Se in barite is about 150 to 250 mg/kg compared with the Se/Ba signal ratio in sample to reference materials. Thus, it was found that the concentration of Se in natural barite is strong enough to be detected in the μ-XRF XANES for the oxidation states of Se in barite.

3.2.3. The oxidation state of Se in marine barite

Micro X-ray absorption near-edge structure spectra (μ-XANES) analysis were performed at a relatively high concentration of Se spot observed in barite (spot 2 in Fig. 11a and spot 3 in Fig. 11b). The μ-XANES spectra from spot 2 and spot 3 are similar in Fig. 15, suggesting that relatively homogeneous Se species are distributed in barite at the depth in the sediment. The XANES spectra obtained from these spots showed that Se was mainly incorporated as Se(IV) in this marine sediment. Based on laboratory experiments discussed in session 3.1, it is suggested that barite was precipitated under suboxic condition where Se was dissolved as Se(IV). This is consistent with the fact that the pore water of sample collected in sediments was under mildly reducing condition (E_h = 150 mV at pH 7.1) where Se(IV) can be main Se species in the water (Fig. 16). Thus, a good correlation between laboratory experiments and natural analysis, it is suggested that the Se(VI)/Se(IV) ratio in barite can be used to estimate roughly the redox condition of the coexistent water during the formation of barite.

4. Conclusion

Many trace elements show variations in their oxidation state and solubility as a function of redox condition of the depositional environment. Based on the laboratory experiments (discussed in session 3.1) and natural barite sample analysis (discussed in sessions 3.2), it is confirmed that the inorganic Se(VI)/Se(IV) ratio in barite reflects the Se(VI)/Se(IV) ratio in water, or redox environment in the coexistent water where barite precipitated. To the best of our knowledge, this is a first study to report a redox indicator using the valance ratio of a trace element in the precipitates, although the solid-water distribution of redox-sensitive elements has been used as a redox indicator based on the effect of change of the oxidation state on its distribution to the solid phase [Calvert and Pedersen, 1993; Thomson et al., 2001; Tribovillard et al., 2006].

The redox indicator of this study suggested that the oxidation state of Se in barite can directly estimate the particular redox condition at the time of barite formation. Barite can record the original Se(IV)/Se(VI) ratios in water unless it is dissolved or recrystallized, which may exclude the influence by secondary adsorption-desorption processes due to the preservation of their species in crystal lattice in barite structure [Guichard et al., 1979]. However, the valence ratio of redox-sensitive elements in the precipitates could not always be used as a redox indicator because of the selective incorporation of the particular oxidation state of the trace element. For instance,

Yokoyama [2011, 2012] demonstrated that, in the case of arsenic and selenium incorporation into calcite, calcite selectively incorporates arsenate rather than arsenite, and selenite rather than selenate. These phenomena are associated with the higher stability of calcium arsenate and calcium selenite complexes than those of arsenite and selenate, respectively. However, in the barite-selenium system, the affinities of selenite and selenate for barite are more or less similar, which enables us to use the Se(VI)/Se(IV) ratio in barite to estimate the redox condition in water.

If the Se(VI)/Se(IV) ratio can be used as a redox indicator, various applications can be suggested such as (i) to estimate the redox condition in the past when barite was deposited and (ii) to estimate the redox condition in environment where we cannot use *Pt* electrode to measure E_h such as in hydrothermal water. The method has several unique characteristics such as (i) sensitivity to the E_h condition between the high E_h condition indicated by Mn(IV)/Mn(II) boundary and the low E_h condition suggested by Fe(III)/Fe(II) boundary (Fig. 1) and (ii) capability to estimate the absolute E_h value based on the valence ratio of Se using one barite sample, whereas other geochemical data such as depth profile of redox-sensitive element can be used when systematic depth profile is measured to evaluate the redox condition.

References

Abdullah, M. I., Z. Shiyu, K. Mosgren (1995), Arsenic and selenium species in the oxic and anoxic waters of the Oslofjord, Norway, *Mar. Pollut. Bull.*, *31*, 116-126.

Alexandratos, G., E. J. Elzinga, R.J. Reeder, Arsenate uptake by calcite: Macroscopic and spectroscopic characterization of adsorption and incorporation mechanisms (2007), *Geochim. Cosmochim. Acta, 71*, 4172-4187.

Algeo, T. J., J. B. Maynard (2004), Trace-element behavior and redox facies in core shales of Upper Pennsylvanian Kansas-type cyclothems, *Chem. Geol*., *206*, 289-318.

Andara, A. J., D. M. Heasman, A. Fernandez-Gonzalez, M. Prieto (2005), Characterization and crystallization of $Ba(SO_4,SeO_4)$ solid solution, *Cryst. Growth Des., 5*, 1371-1378.

Blount, C. W. (1974), Synthesis of barite, celestite, anglesite, witherite. and strontianite from aqueous solutions, *Amer. Mineral*., *59*. 1209-1219.

Bujdos, M., A. Mul'ova, J. Kubova, J. Medved (2005), Selenium fractionation and speciation in rocks, soils, waters and plants in polluted surface mine environment, *Environ. Geol*., *47*, 353–360.

Calvert, S.E., and T. F. Pedersen (1993), Geochemistry of recent oxic and anoxic sediments: implications for the geological record, *Mar. Geol*., *113*, 67-88.

Cutter, G. A., and K. W. Bruland (1984), The marine biogeochemistry of selenium: A re-evaluation, *Limnol. Oceanogr., 29*, 1179-1192.

Cutter, G. A. (1992), Kinetic controls on metalloid speciation in seawater, *Mar. Chem., 40*, 65-80.

Fernandez-Martýnez, A., and L. Charlet (2009), Selenium environmental cycling and bioavailability: a structural chemist point of view, *Rev. Environ. Sci. Biotechnol*., *8*, 81-110.

Giester, G., and C. L. Lengauer (1998), A Contribution to the Stereochemistry of Earth Alkaline Selenites: Synthesis and Crystal Structure of Ca_2 $(SeO_3)(Se_2O_5)$, Ba (SeO_3), and Ba (Se_2O_5), *Monatsh. Chem*., *129*, 445-454.

Gupta, A., P. Singh, and C. Shivakumara (2010), Synthesis of nanoparticles by precipitation method using sodium hexa metaphosphate as a stabilizer, *Solid State Communications*, *150*, 386-388.

Gustafsson, J. P. (2009), Visual MINTEQ ver. 2.61, <http:// www.lwr.kth.se/English/OurSoftware/vminteq/>.

Griffith, M.E., and A. Paytan (2012), Barite in the Ocean – Occurrence, Geochemistry and Paleoceanographic Applicators, Sedimentology, *Sedimentology*, *59*, 1817–1835.

Guichard, F., T. M. Church, M. Treuil, H. Jaffreic (1979) Rare earths in barites:

distribution and effects on aqueous partitioning, *Geochim. Cosmochim. Acta, 43*, 983-997.

Harada, T., and Y. Takahashi (2009), Origin of the difference in the distribution behavior of tellurium and selenium in a soil.water system, *Geochim. Cosmochim. Acta*, *72* ,1281-1294.

Hein, J. R., M. G. Stamataki, J. Dowling (2000), Trace metal-rich Quaternary hydrothermal manganese-oxide and barite deposit, Milos Island, Greece, *Trans. Inst. Min. Metall., Sect. B 109*, B67–B76.

Kawagucci, S., K. Shirai, T. F. Lan, N. Takahata, U. Tsunogai, Y. Sano, T. Gamo (2010), Gas geochemical characteristics of hydrothermal plumes at the HAKUREI and JADE vent sites, the Izena Cauldron, Okinawa Trough, *Geochem. J*., *44,* 507-518.

Lorens, R. B. (1981), Sr, Cd, Mn and Co distribution coefficients in calcite as a function of calcite precipitation rate, *Geochim. Cosmochim. Acta, 45*, 553-561.

Masscheleyn, P. H, R. D. DeLaune, W. H. Patrick (1991), Effect of Redox Potential and pH on Arsenic Speciation and Solubility in a Contaminated Soil, *Environ. Sci. Technol*., *25*, 1414-1419.

National Institute of Standards and Technology (2003), NIST Standard Reference Database 46, Version 7.0.

Noguchi, T., R. Shinjo, M. Ito, J. Takada, T. Oomori (2011), Barite geochemistry from hydrothermal chimneys of the Okinawa Trough: insight into chimney formation and fluid/sediment interaction, *J. Mineral. Petrol. Sci.*, *106*, 26-35.

O'Day P. A., Rehr J. J., Zabinsky S. I. and Brown G. E. (1994) Extended X-ray absorption fine structures (EXAFS) analysis of disorder and multiple scattering in complex crystalline solids. J. Am. Chem. Soc. 116, 2938–2949.

Paytan, A., and E. M. Griffith (2007), Marine barite: Recorder of variations in ocean export productivity, *Deep-Sea Res. II*, *54*, 687–705.

Prieto M., A. Fernandez-Gonzalez, R. Martin-Diaz (2002), Sorption of chromate ions diffusing through barite-hydrogel composites: Implications for the fate and transport of chromium in the environment, *Geochim. Cosmochim. Acta*, *66*, 783–795.

Rouxel, O., Y. Fouquet, J. N. Ludden (2004), Subsurface processes at the Lucky Strike hydrothermal field, Mid-Atlantic Ridge: evidence from sulfur, selenium, and iron isotopes, *Geochim. Cosmochim. Acta*, *68*, 2295-2311.

Pufahl, P. K., E. E. Hiatt (2012), Oxygenation of the Earth's atmosphere-ocean system: A review of physical and chemical sedimentologic responses, *Marine and Petroleum Geology, 32*, 1-20.

Ravel B. (2001) ATOMS: crystallography for the X-ray absorption spectroscopist. J.

Synchrotron Radiation 8, 314–316.

Rue, E.L., G. J. Smith, G.A. Cutter, K. W. Bruland (1997), The response of trace element redox couples to suboxic conditions in the water column, *Deep-Sea Research*, *44*, 113-134.

Seby, F., M. Potin-Gautier, E. Giffaut, G. Borge, O. F. X. Donard (2001), A critical review of thermodynamic data for selenium species at 25C, *Chem Geol*., *171*, 173–194.

Sharmasarkar, S., G. F. Vance, F. C. Sharmasarkar (1998), Analysis and speciation of selenium ions in coal mine environments, *Environ. Geol.*, *34*, 31-38.

Smedley, P. L., and D. G. Kinniburgh (2002), A review of the source, behavior and distribution of arsenic in natural waters, *Applied Geochemistry*, *17*, 517-568.

Stumm ,W. (1992) *Chemistry of the Solid-Water Interface*, John Wiley & Sons, New York.

Snyder, G.T., G. R. Dickens, D. G. Castellini (2007), Labile barite contents and dissolved barium concentrations on Blake Ridge: New perspectives on barium cycling above gas hydrate systems, *Geochem. Explor*., *95*, 48-65.

Takahashi, Y., N. Ohtaku, S. Mitsunobu, K. Yuita, M. Nomura (2003), Determination of the As(III)/As(V) ratio in soil by X-ray absorption near-edge structure (XANES) and its application to the arsenic distribution between soil and water, *Anal. Sci..,* 19, 891-896.

Tanaka, K., Y. Takahashi, H. Shimizu (2007), Determination of rare earth element in carbonate using laser-ablation inductivelycoupled plasma mass spectrometry: an examination of the influence of the matrix on laser-ablation inductively-coupled plasma mass spectrometry analysis, *Anal. Chim. Acta., 583*, 303-309.

Tanaka, M., D. Ariga, Y. Takahashi (2013), Estimation of pKa of selenic acid by the correlation of experimental pKa values with those estimated by DFT calculation for inorganic oxoacids, *Chem Lett.*, in press .

Terada, Y., S. Goto, N. Takimoto, K. Takeshita, H. Yamazaki, Y. Shimizu, S. Takahashi, H. Ohashi, Y. Furukawa, T. Matsushita, T. Ohata, Y. Ishizawa, T. Uruga, H. Kitamura, T. Ishikawa, S. Hayakawa (2004). AIP Conf. Proc. 705, 376–379.

Teo B. K. (1986) EXAFS: basic principles and data analysis. Springer-Verlag, Berlin

Torres, M. E., G. Bohrmann, T. E. Dube´, F. G. Poole, (2003), Formation of modern and Paleozoic stratiform barite at cold methane seeps on continental margins, *Geology*, *31*, 897–900.

Thomson, J., N. C. Higgs, I. W. Croudace, S. Colley, D. J. Hydes (1993), Redox zonation of elements at an oxic/post-oxic boundary in deep-sea sediments, *Geochim. Cosmochim. Acta*, *57*, 579–595.

Thomson, J., I. Jarvis, D. R. H Green, D. A. Green, T. Clayton, (1998), Mobility and

immobility of redox-sensitive elements in deep-sea turbidites during shallow burial, *Geochim. Cosmochim. Acta, 62*, 643-656.

Thomson, J., S. Nixon, I. W. Croudace, T. F. Pedersen, L. Brown, G. T. Cook, A. B. MacKenzie, (2001), Redox-sensitive element uptake in north-east Atlantic Ocean sediments (Benthic Boundary Layer Experiment sites), *Earth Planet. Sci. Lett.*, *184*, 535-547.

Torres, J., V. Pintos, S. Dominguez, C. Kremer, E. Kremer (2010), Selenite and Selenate Speciation in Natural Waters: Interaction with Divalent Metal Ions, *J Solution Chem* , *39*, 1-10.

Torres, J., V. Pintos, L. Gonzatto, S. Domínguez , C. Kremer , E. Kremer (2011), Selenium chemical speciation in natural waters: Protonation and complexation behavior of selenite and selenate in the presence of environmentally relevant cations. *Chemical Geology*, *288*, 32–38.

Tribovillard, N., T. Algeo, T. Lyons, A. Riboulleau (2006), Trace metals as paleoredox and paleoproductivity proxies: an update. *Chem. Geol.*, *232*, 12-32.

Tsuno, H., H. Kagi, Y. Takahashi, T. Akagi, M. Nomura (2003), Spontaneously induced reduction of trivalent ytterbium in synthesized crystal of calcite. *Chem. Lett.*, *32*, 500-501.

Von Damm, K. L. (1990), Seafloor hydrothermal activity: Black smoker chemistry and chimneys, *Ann. Rev. Earth Planet. Sci.*, *18*, 173-204.

Van Beek, P., J. L. Reyss, P. Bonte, S. Schmidt (2003), Sr/Ba in barite: a proxy of barite preservation in marine sediments? , *Marine Geology*, *199 (3-4),* 205- 220.

Yokoyama, Y. and Y. Takahashi (2011), Effect of oxidation state on arsenic and selenium incorporation into calcite, *Goldschmidt Conference Abstract*, 2223.

Yokoyama, Y., Tanaka. K., Takahashi, Y. (2012), Differences in the immobilization of arsenite and arsenate by calcite, *Geochim. Cosmochim. Acta*, *91*, 202–219.

Zabinsky S. I., Rehr J. J., Ankudinov A., Albers R. C. and Eller M. J. (1995) Multiple-scattering calculations of X-ray-absorption spectra. Phys. Rev. B 52, 2995–3009.

Zhu, C. (2004), Coprecipitation in the barite isostructural family: 1. Binary mixing properties, *Geochim. Cosmochim. Acta*, *68*, 3327-3337.

Figure legends

Figure 1. E_h- pH diagrams for Ba-S-H_2O (a), Se-H_2O (b), Fe-H_2O (c), Mn–H_2O (d) at 25ºC and 1.0 bar calculated based on the Visual MINTEQ. The total dissolved concentrations of Ba, Se, and S used for the calculations were 270 μg L^{-1}, 140 μg L^{-1}, 2600 μg L^{-1}, respectively, which correspond approximately to their concentrations in our experimental systems. The system Fe-O-H and Mn-O-H are also drawn at assumed activity of dissolved species of Fe or Mn as10^{-6} M.

Figure 2. Normalized Se K-edge XANES spectra of the reference materials ($BaSeO_3$, $BaSeO_4$, and native Se) and Se in barite at pH 8.0 (a) and pH 4.0 (b) as a function of R_W^{VI} (= Se(VI)/total Se).

Figure 3. Relationship between R_W^{VI} and R_B^{VI}. The Se(VI)/Se(IV) ratios in barite and in solution were measured by XANES and HPLC-ICP-MS, respectively.

Figure 4. Relationship between the saturation index (SI) and apparent distribution coefficient (K_d) at pH 8.0. SI = log(IAP/K_{sp}), where IAP and K_{sp} are the ion activity product and solubility product of barite, respectively.

Figure 5. Normalized k^3-weighted EXAFS spectra at the Se K-edge for Se in/on barite.

Figure 6. Fourier-transformed EXAFS spectra at the Se K-edge for Se in/on barite.

Figure 7. Apparent distribution coefficient of Se(VI) and Se(IV) at various R_W^{VI} obtained

by the experiments at pH 8.0 and pH 4.0.

Figure 8. Aqueous (a) Se(VI) and (b) Se(V) species in water as function of pH calculated by *Visual Minteq*

Figure 9. Relationship between R_W^{VI} and R_B^{VI} at various pH conditions

Figure 10. Relationship between R_B^{VI} and E_h calculated by R_w^{VI} at pH 8.0 and pH 4.0

Figure 11. BSE images of samples from marine surface sediment (depth: 0-4 cm). The mark as spots show the measured points by EPMA (back-scattered electron image) to identify mineral compositions. X-ray beam size, 2.0×2.0 mm^2;; Counting time, 20 s for each elements expect for Se (30 s) and S(10 s).

Figure 12. BSE and μ-XRF images of samples. (A): BSE images of barite. (B), (C), (D) μ-XRF images of Ba, Se, and Fe, respectively. The mark on (B), (C) show the measured points by m-XANES as spot 1. X-ray beam size, 0.3×0.3 mm^2; Step size, 5 mm; Measurement time, 0.1 s/point.

Figure 13. (a) Correlation of Ba and Se in μ-XRF analysis for the bulk in Fig. 1; (b)Correlation of Ba and Se in μ-XRF analysis for the lower left part in Fig. 1b; (c) Correlation of Ba and Se in μ-XRF analysis for the upper left part in Fig. 1b

Figure 14. The correlation between Ba and Se intensities in the barite samples by LA-ICP-MS.

Figure 15. Normalized Se K-edge XANES of Se reference materials ($BaSeO_3$ and $BaSeO_4$), Se in barite at pH 8.0 added as Se(IV) or Se(VI), and Se in natural barite at spots 1 and 2 in barite. The vertical dashed lines indicate the absorption peaks of $BaSeO_3$ and $BaSeO_4$.

Figure 16. Depositional condition of Se estimated by E_h (150 mV) and pH (7.1) of the pore water in the sediment

Table 1. Experimental condition of coprecipitation experiments

1) Each saturation index (SI) zwas calculated by Visual MINTEQ and minerals were identified by XRD.

2) $BaSeO_3$ and $BaSeO_4$ are typical barium selenite and barium selenate minerals, respectively.

3) K_d is apparent distribution coefficient.

* $K_d = [Se]_B / [Se]_W$ ($[Se]_B$: Se concentration in barite; $[Se]_W$: Se concentration in water)

Table 2. Additional experiments with various initial solution, where pH was fixed at 8.0.

*$K_{Se(IV)} = K_d \times (R_B^{IV} / R_W^{IV})$, where R_B^{IV} and R_W^{IV} are the Se(IV)/ΣSe ratio in the barite and in the solution, respectively.

Table 3. Structural data on the local atomic environment of Se derived from the simulation

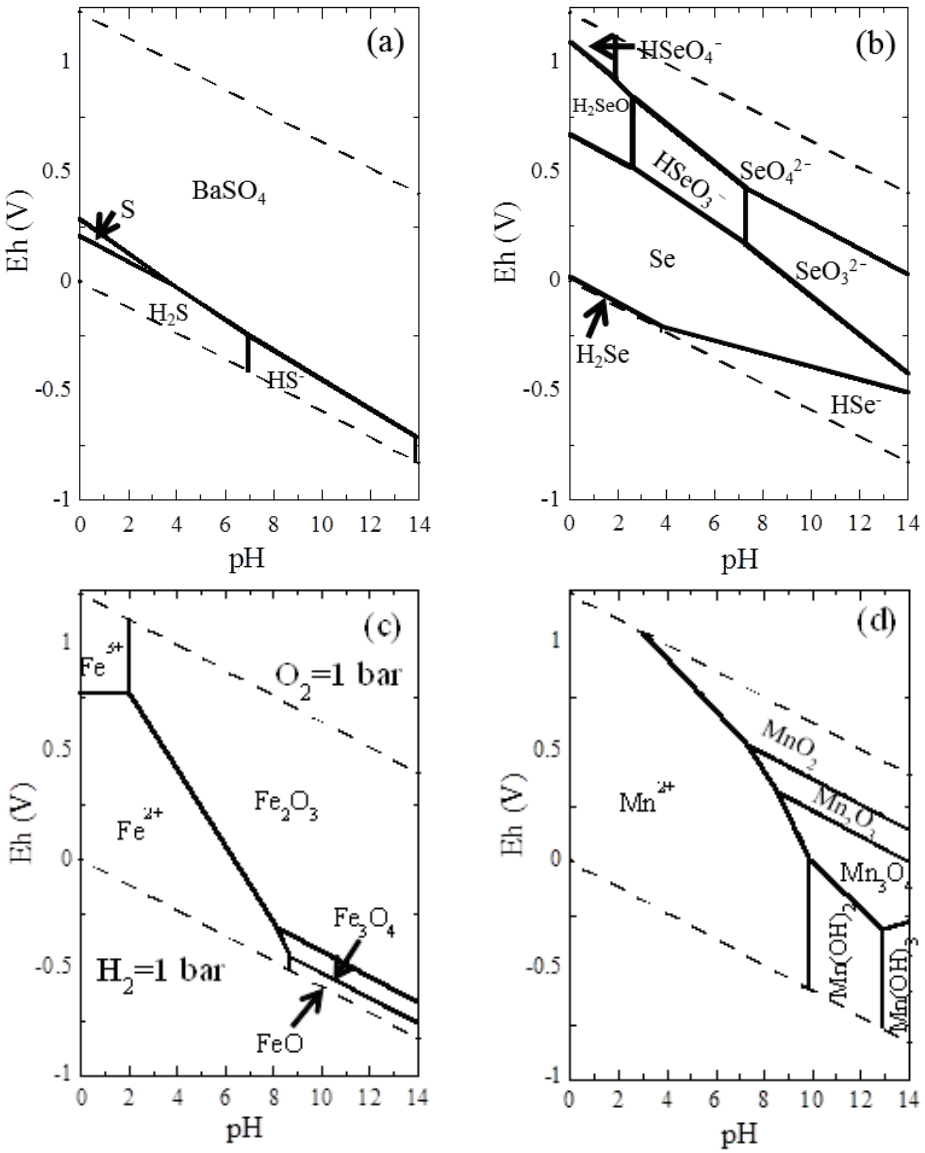

Figure 1. E_h- pH diagrams for Ba-S-H_2O (a), Se-H_2O (b), Fe-H_2O (c), Mn–H_2O (d) at 25ºC and 1.0 bar calculated based on the Visual MINTEQ. The total dissolved concentrations of Ba, Se, and S used for the calculations were 270 μg L^{-1}, 140 μg L^{-1}, 2600 μg L^{-1}, respectively, which correspond approximately to their concentrations in our experimental systems. The system Fe-O-H and Mn-O-H are also drawn at assumed activity of dissolved species of Fe or Mn as10^{-6} M.

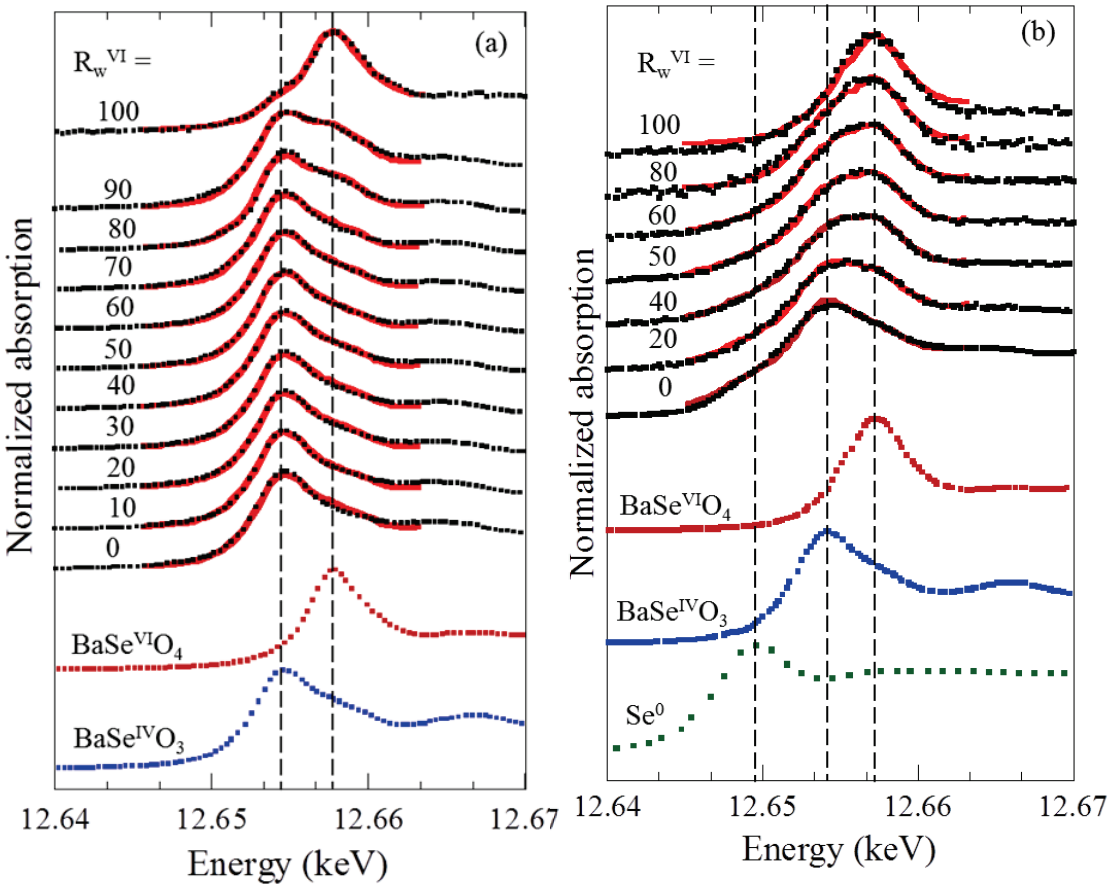

Figure 2. Normalized Se K-edge XANES spectra of the reference materials ($BaSeO_3$, $BaSeO_4$, and native Se) and Se in barite at pH 8.0 (a) and pH 4.0 (b) as a function of R_W^{VI} (= Se(VI)/total Se).

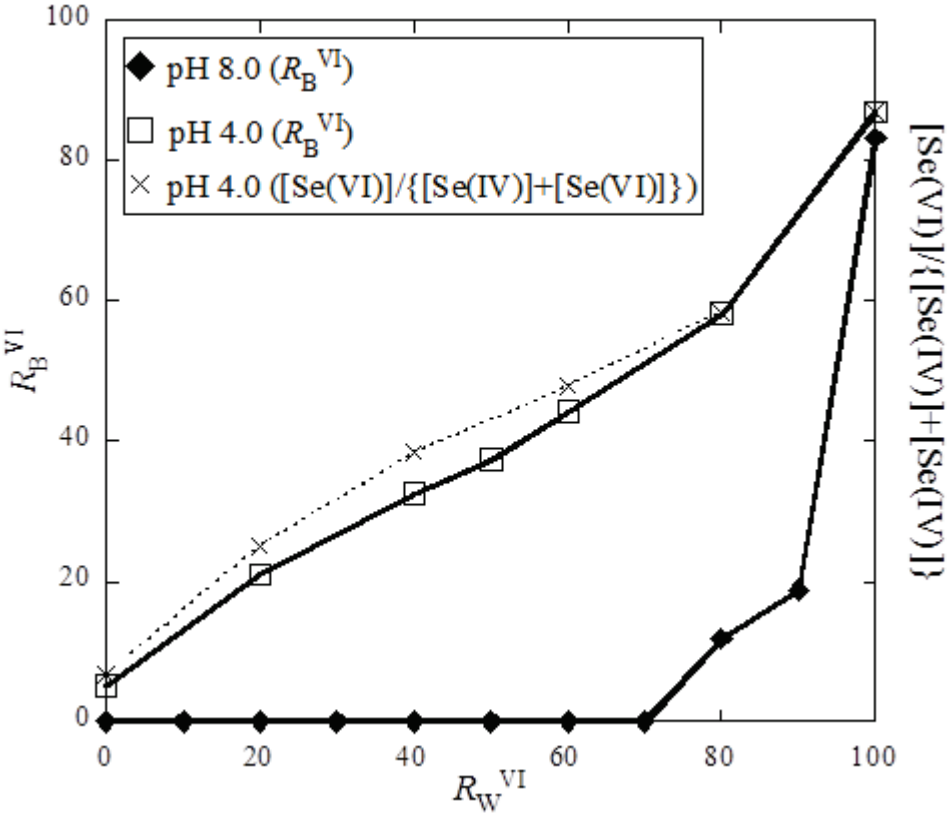

Figure 3. Relationship between R_W^{VI} and R_B^{VI}. The Se(VI)/Se(IV) ratios in barite and in solution were measured by XANES and HPLC-ICP-MS, respectively.

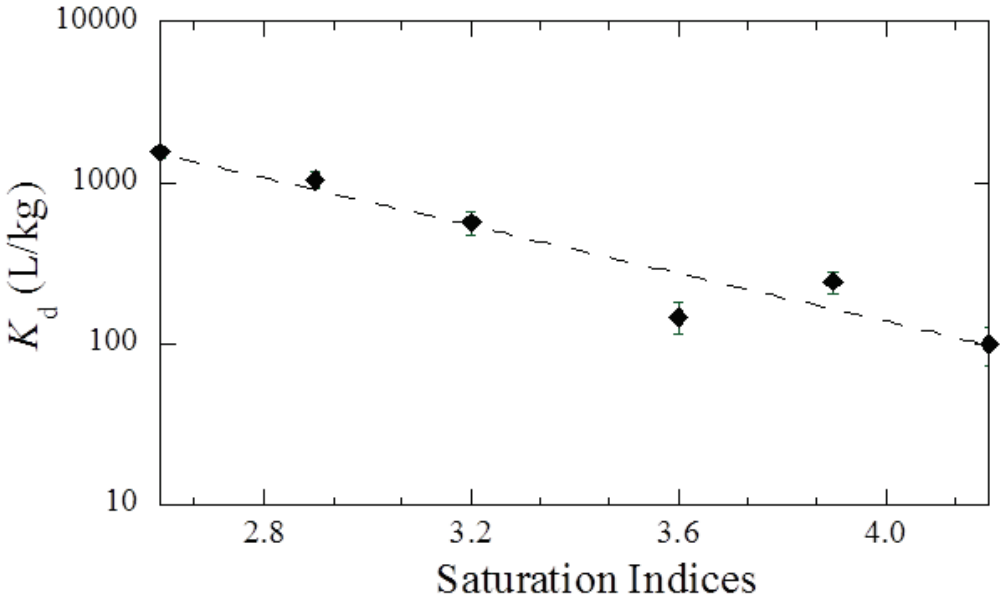

Figure 4. Relationship between the saturation index (SI) and apparent distribution coefficient (K_d) at pH 8.0. SI = log(IAP/K_{sp}), where IAP and K_{sp} are the ion activity product and solubility product of barite, respectively.

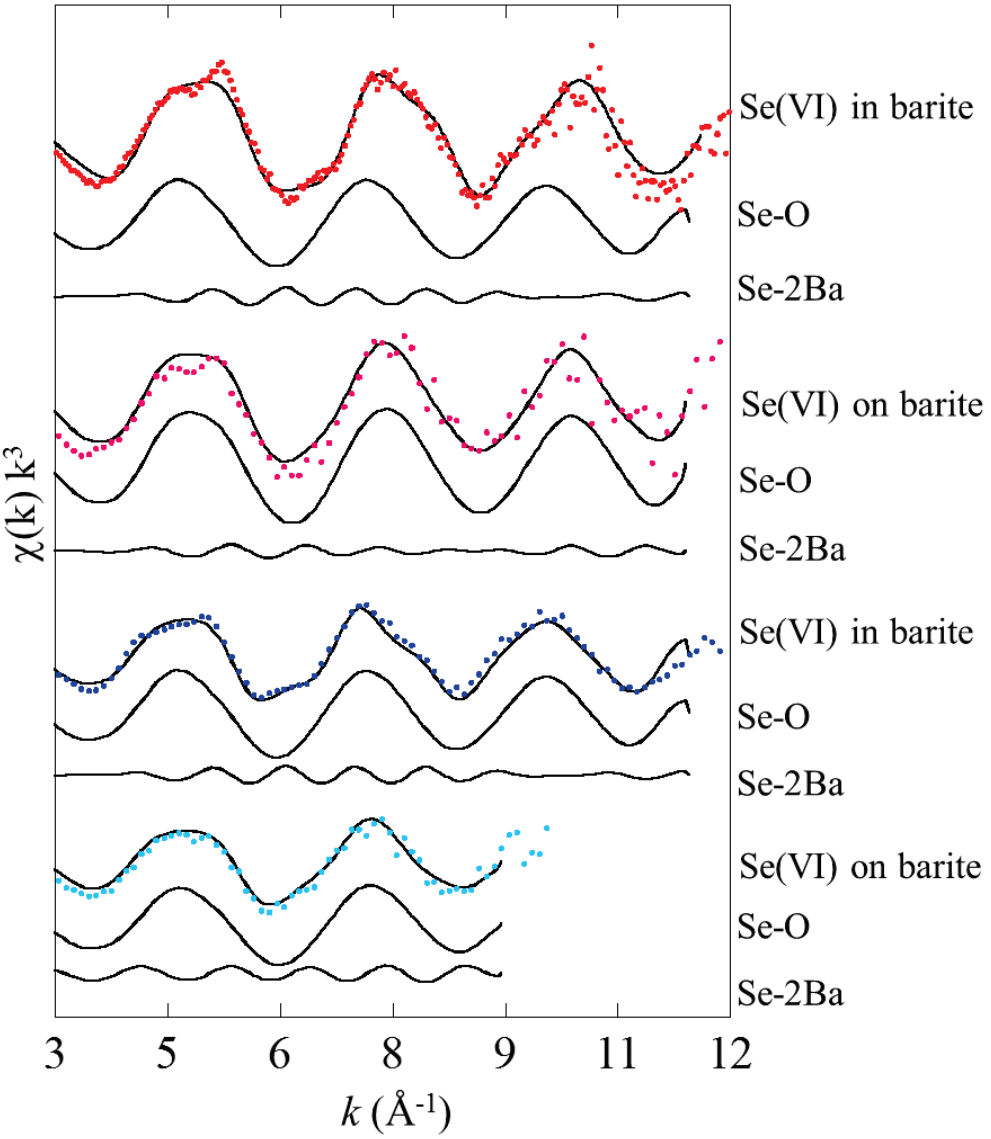

Figure 5. Normalized k^3-weighted EXAFS spectra at the Se K-edge for Se in/on barite.

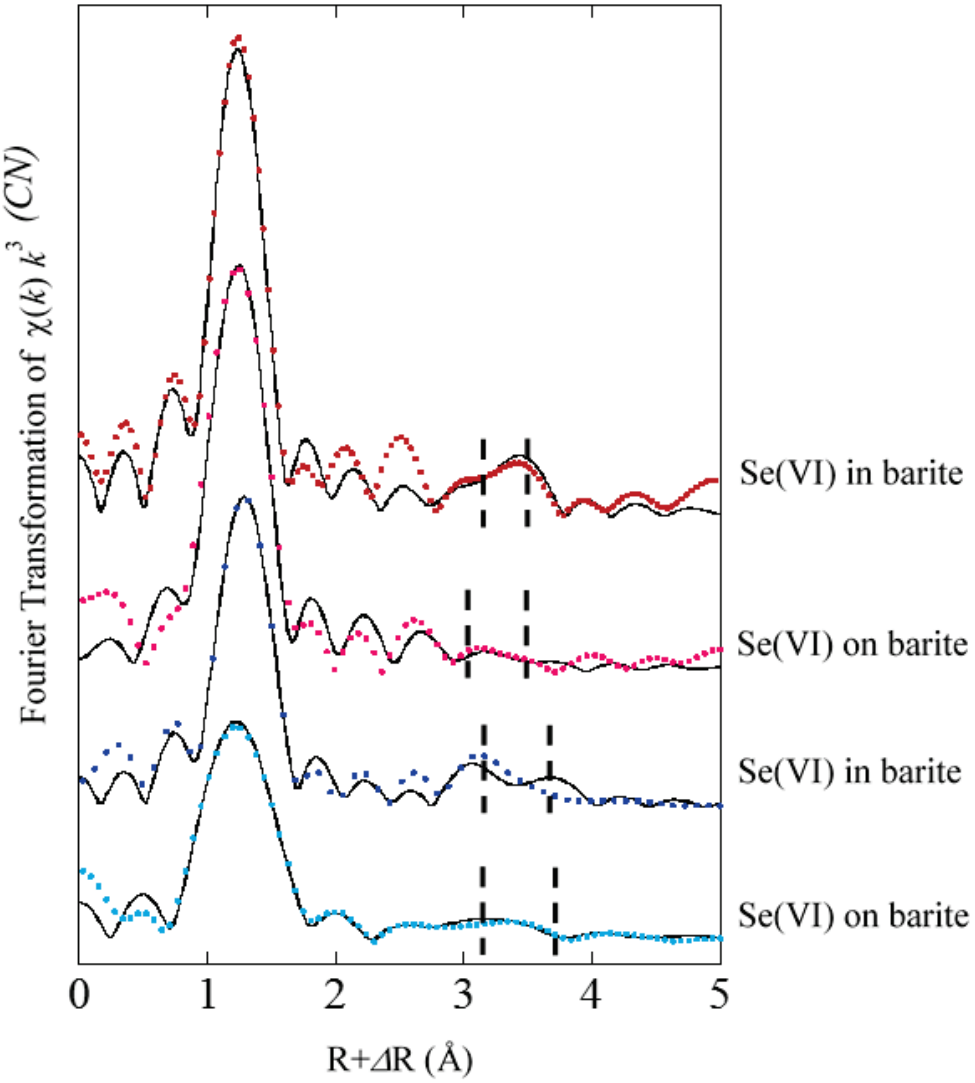

Figure 6. Fourier-transformed EXAFS spectra at the Se K-edge for Se in/on barite.

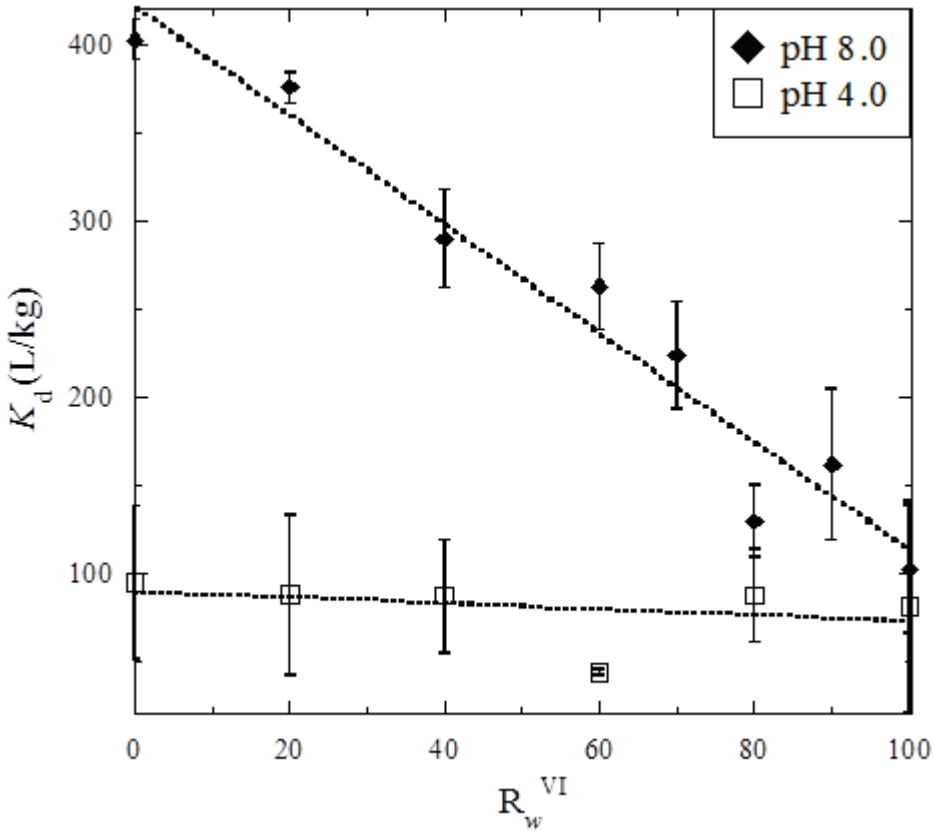

Figure 7. Apparent distribution coefficient of Se(VI) and Se(IV) at various R_W^{VI} obtained by the experiments at pH 8.0 and pH 4.0.

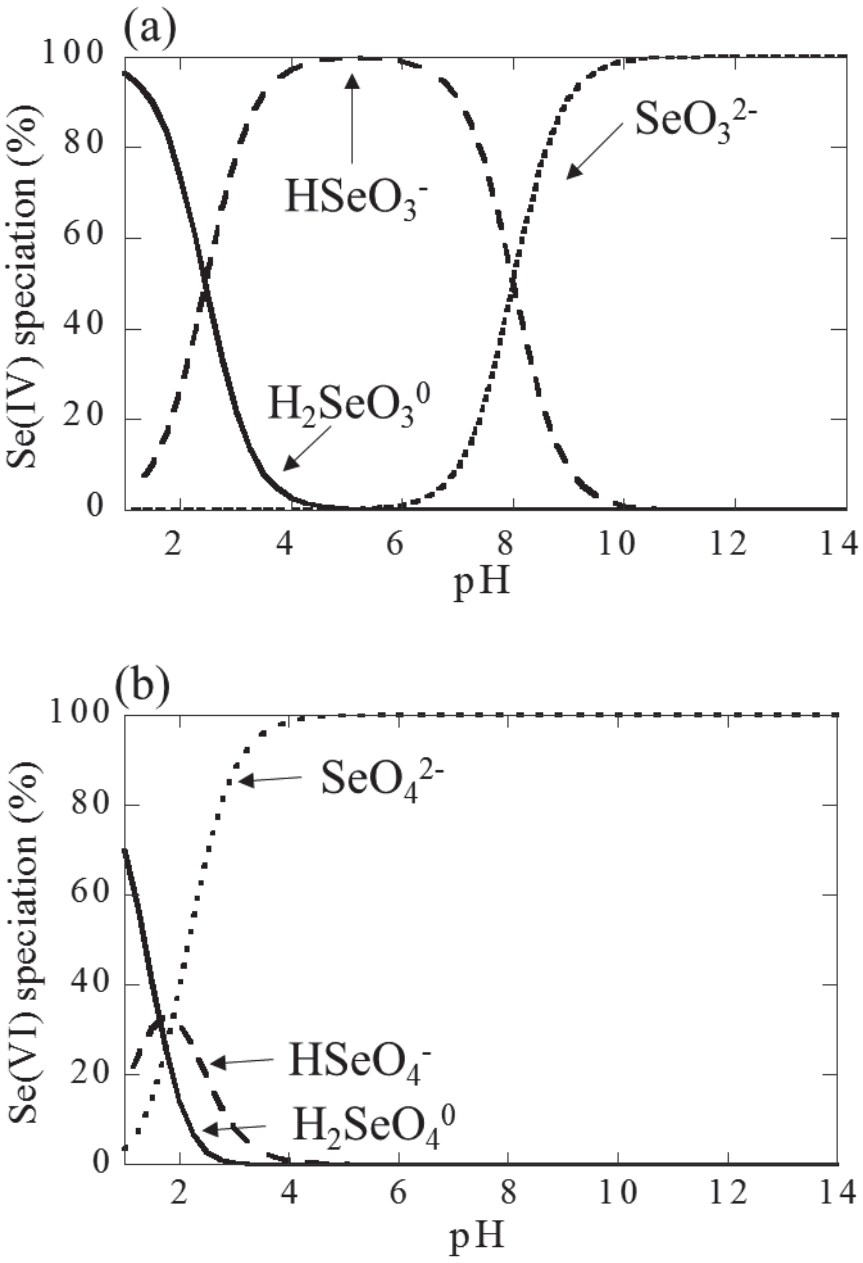

Figure 8. Aqueous (a) Se(VI) and (b) Se(V) species in water as function of pH calculated by *Visual Minteq*

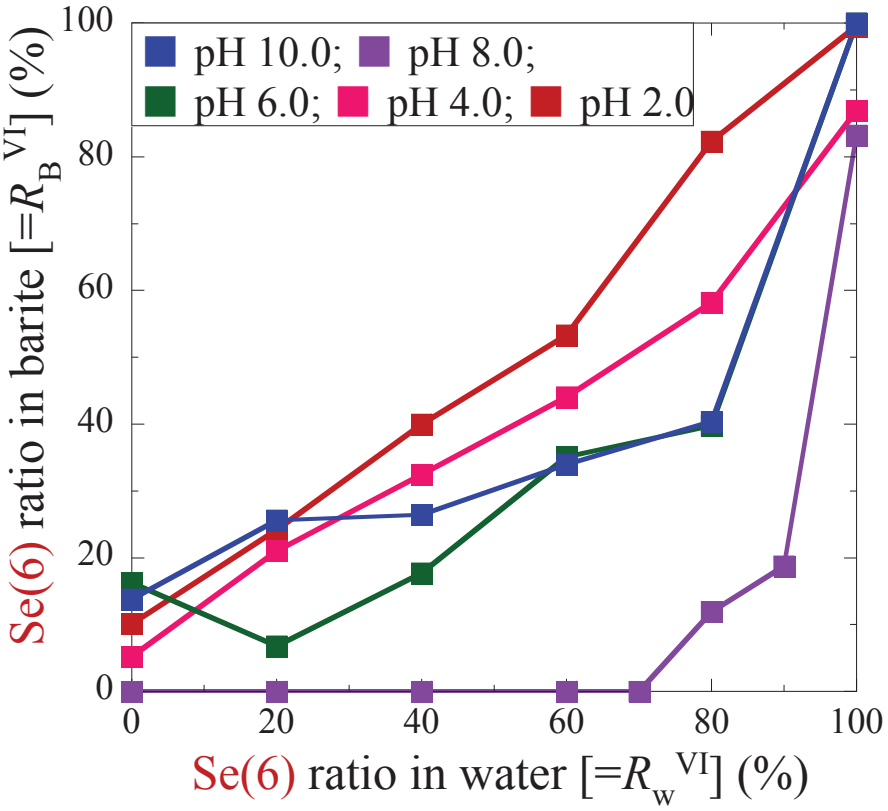

Figure 9. Relationship between R_W^{VI} and R_B^{VI} at various pH conditions

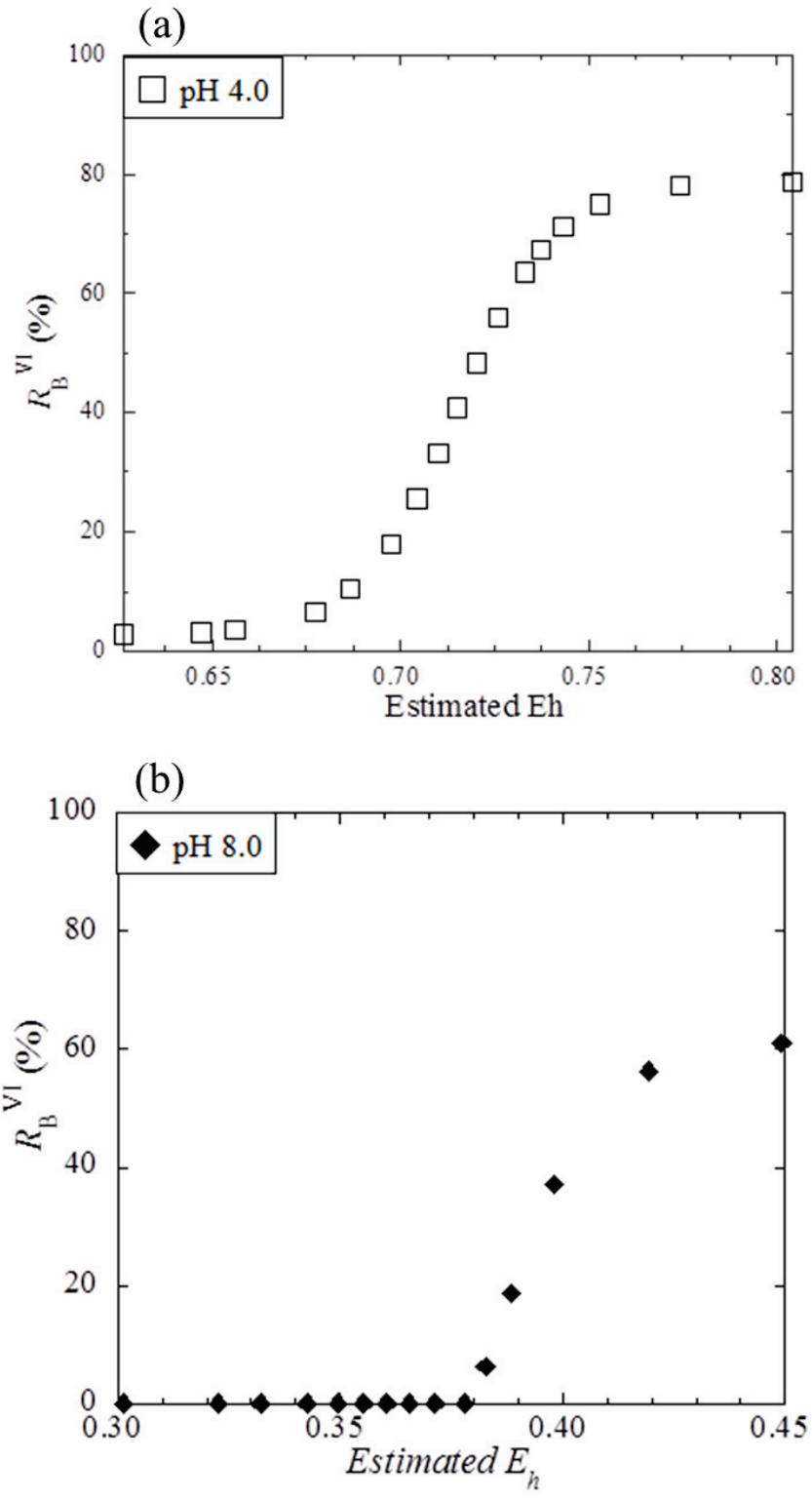

Figure 10. Relationship between R_B^{VI} and E_h calculated by R_w^{VI} at pH 8.0 and pH 4.0

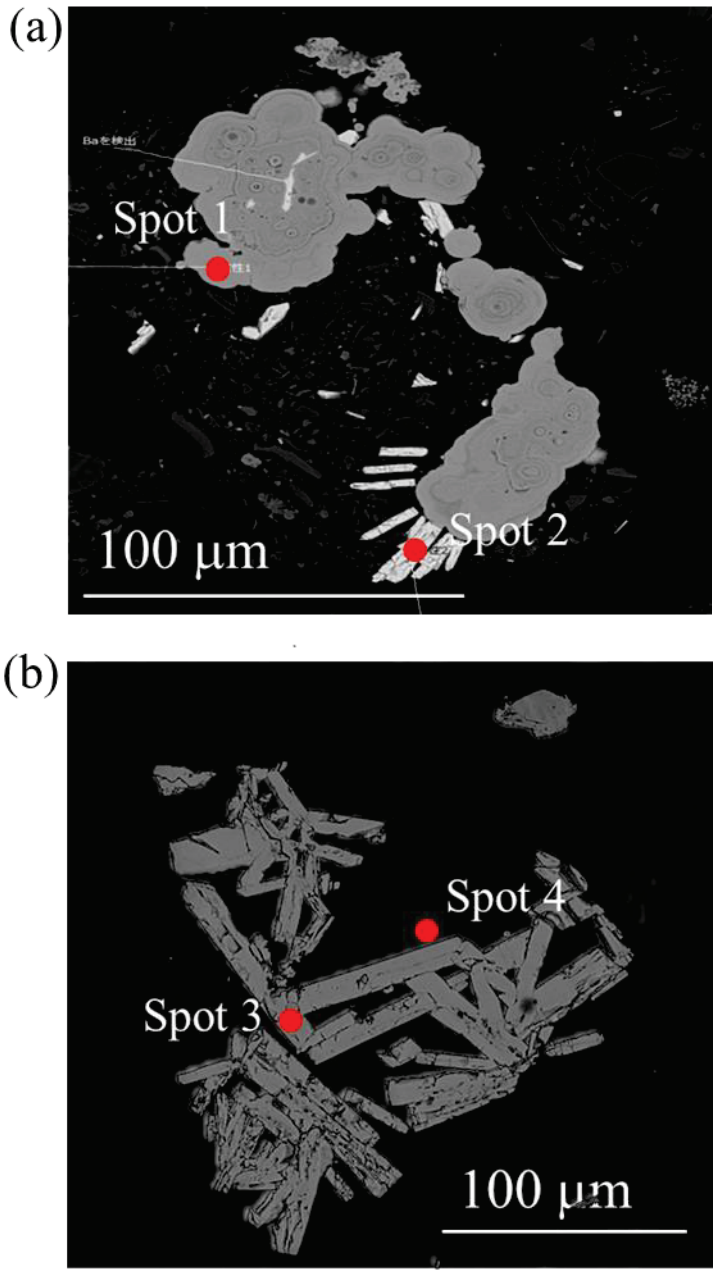

Figure 11. BSE images of samples from marine surface sediment (depth: 0-4 cm). The mark as spots show the measured points by EPMA (back-scattered electron image) to identify mineral compositions. X-ray beam size, 2.0×2.0 mm^2;; Counting time, 20 s for each elements expect for Se (30 s) and S(10 s).

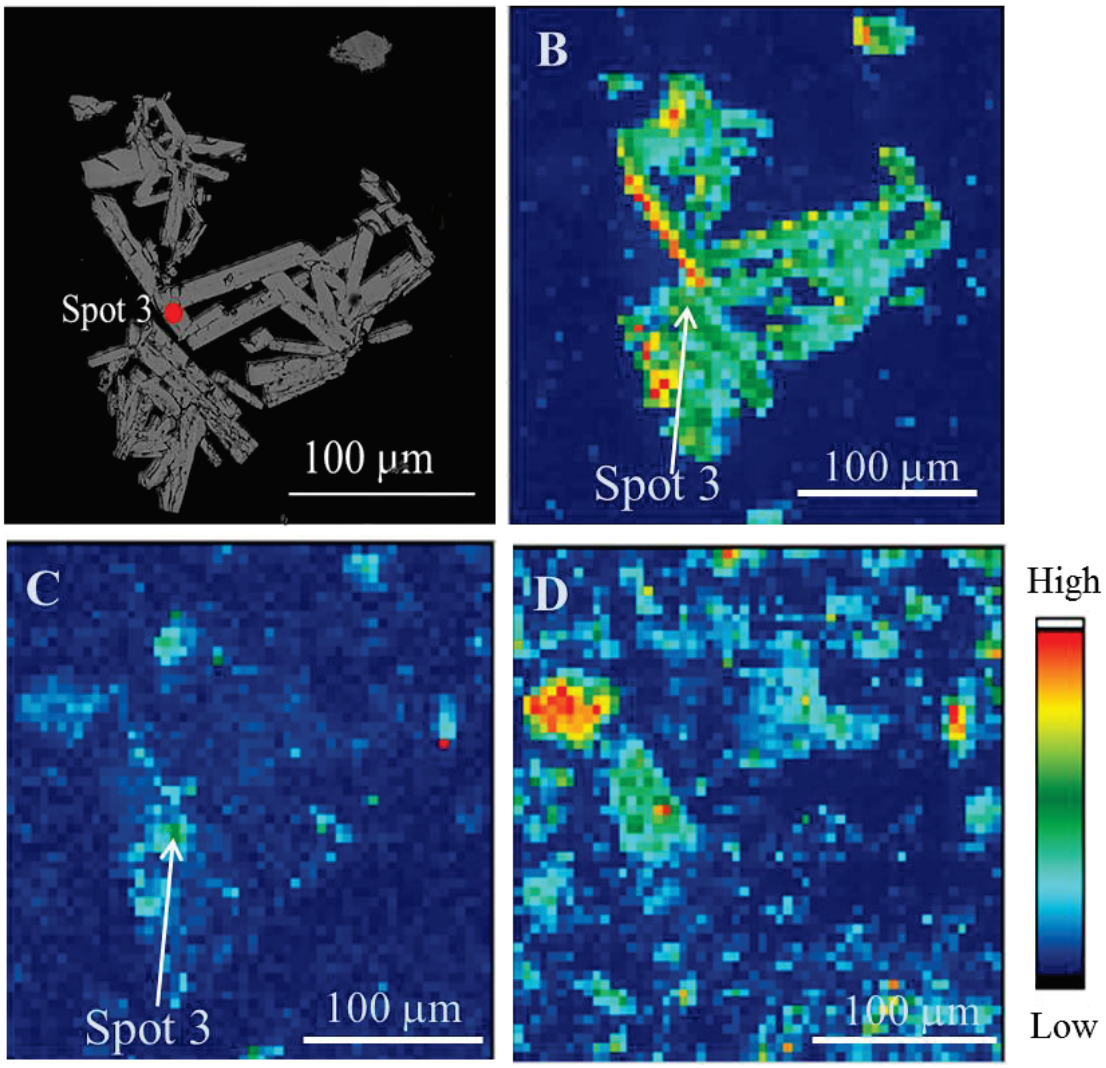

Figure 12. BSE and μ-XRF images of samples. (A): BSE images of barite. (B), (C), (D) μ-XRF images of Ba, Se, and Fe, respectively. The mark on (B), (C) show the measured points by m-XANES as spot 1. X-ray beam size, 0.3×0.3 mm^2; Step size, 5 mm; Measurement time, 0.1 s/point.

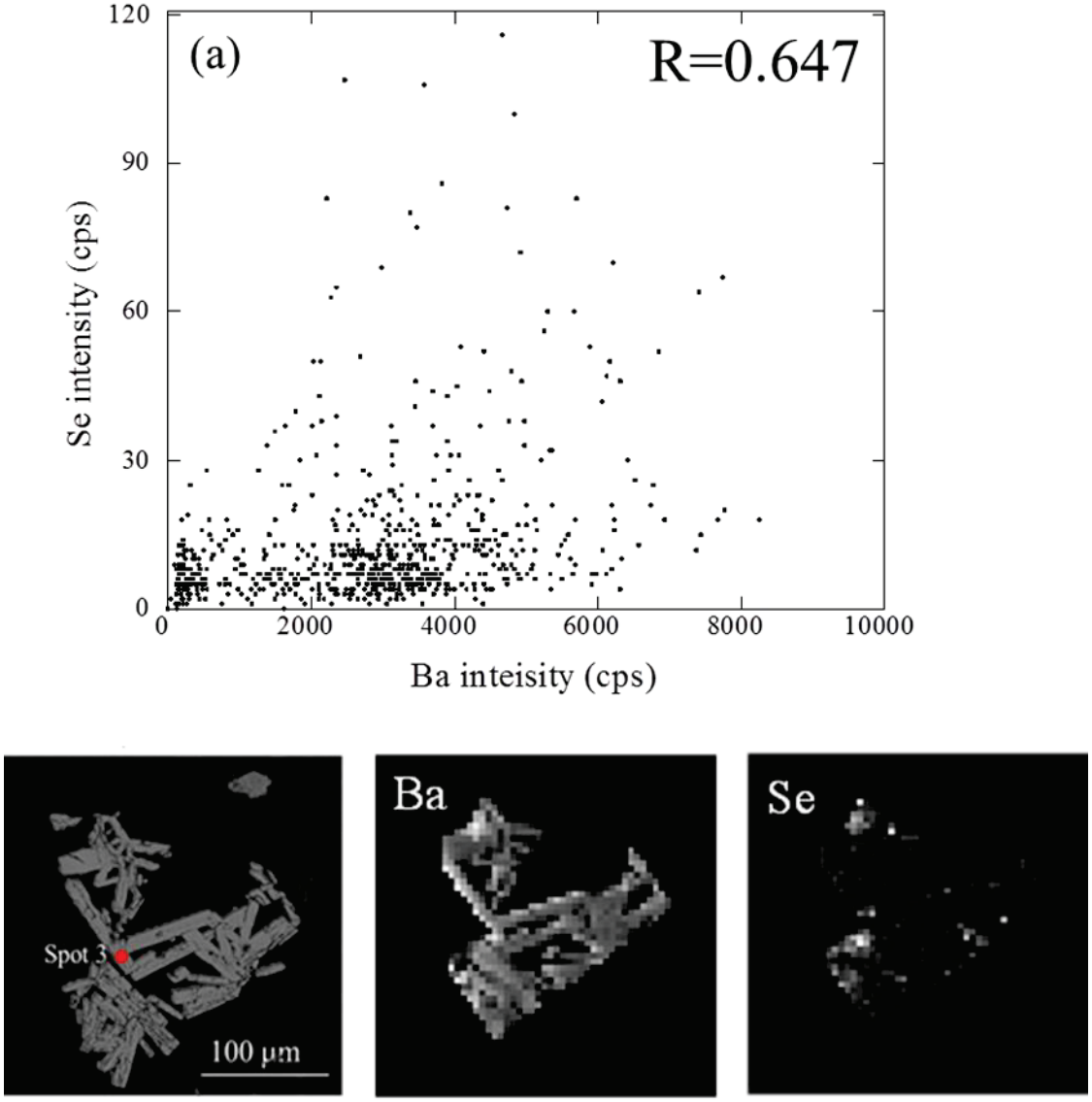

Figure 13. (a) Correlation of Ba and Se in μ-XRF analysis for the bulk in Fig. 1; (b)Correlation of Ba and Se in μ-XRF analysis for the lower left part in Fig. 1b; (c) Correlation of Ba and Se in μ-XRF analysis for the upper left part in Fig. 1b

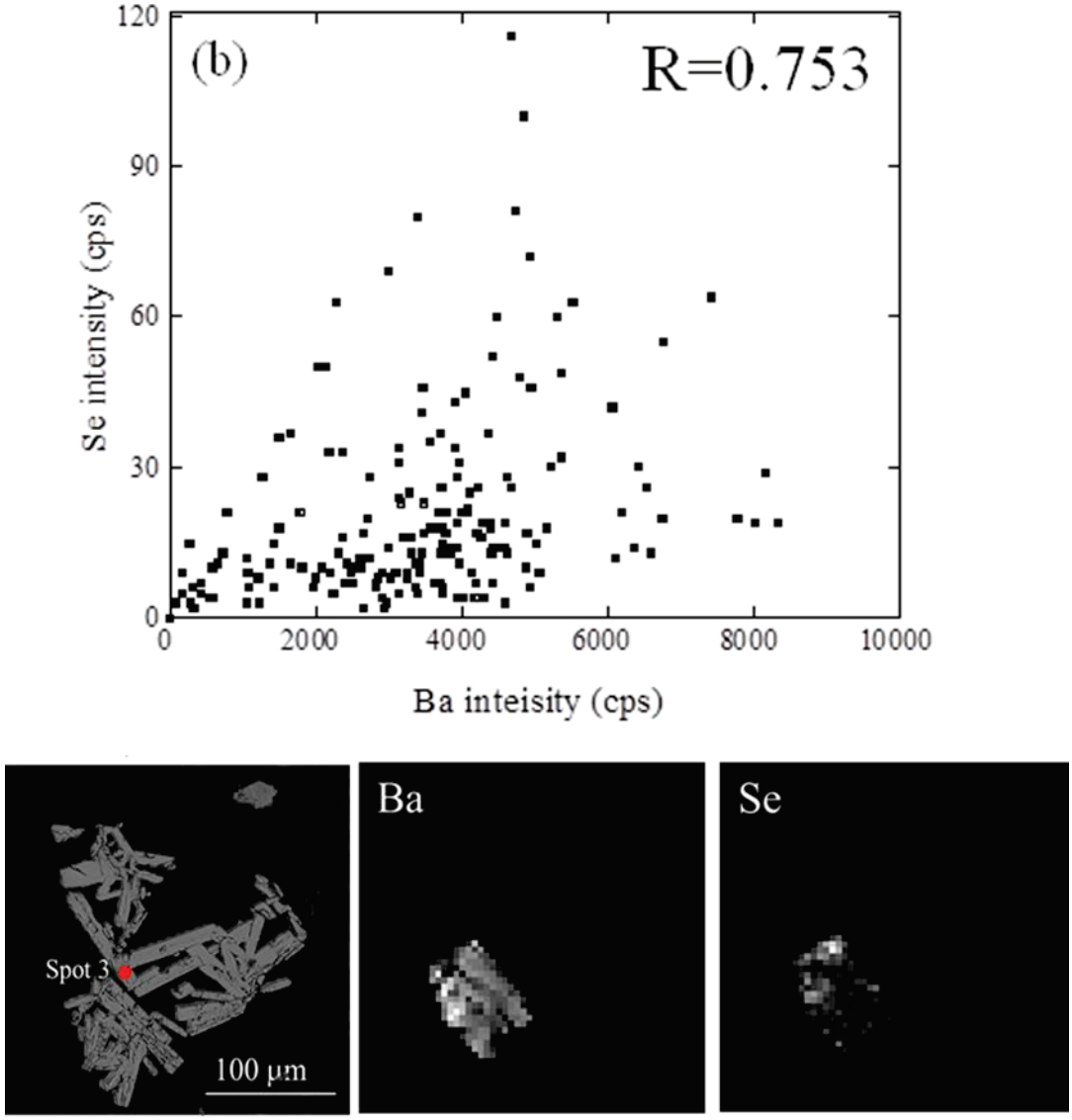

Figure 13. (a) Correlation of Ba and Se in μ-XRF analysis for the bulk in Fig. 1; (b)Correlation of Ba and Se in μ-XRF analysis for the lower left part in Fig. 1b; (c) Correlation of Ba and Se in μ-XRF analysis for the upper left part in Fig. 1b

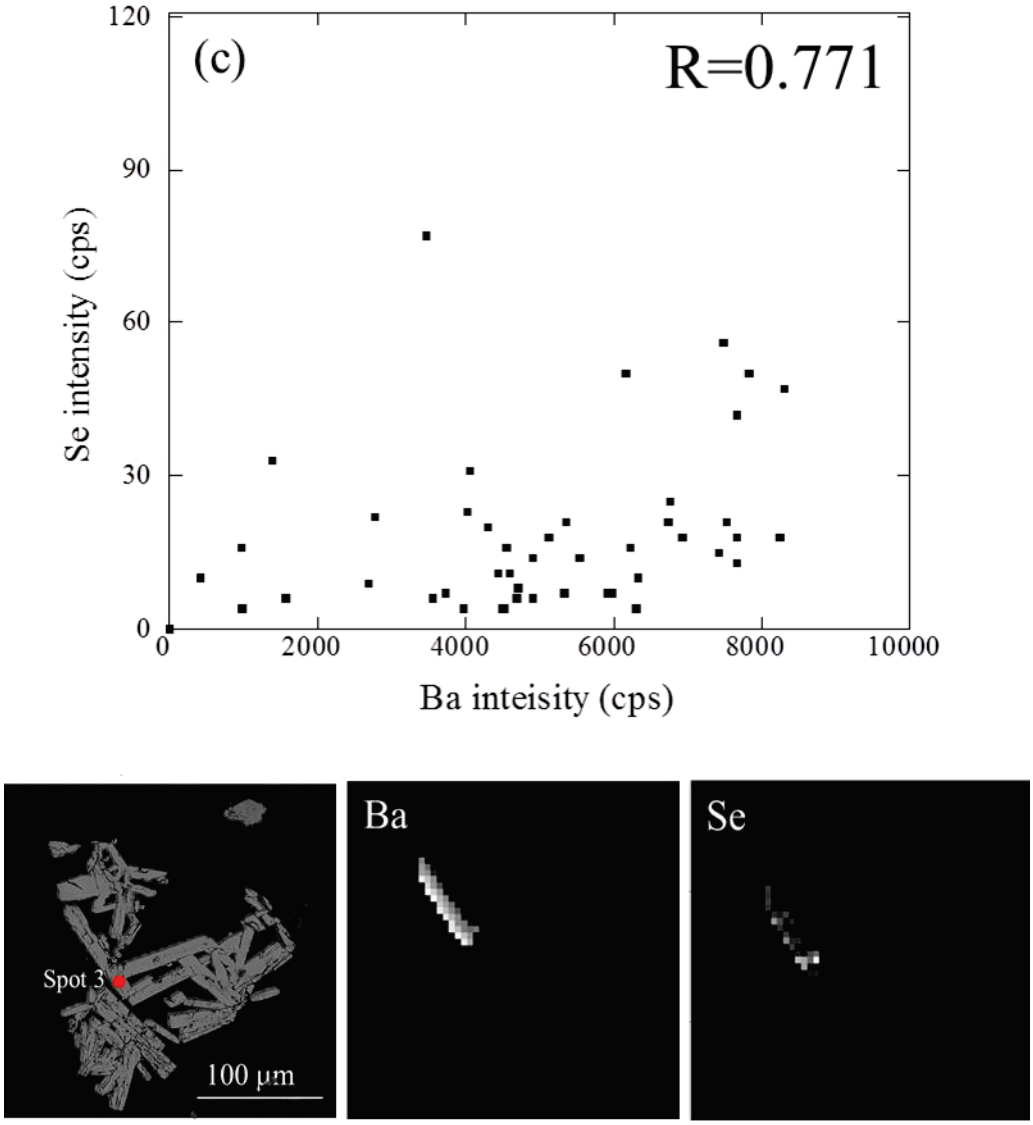

Figure 13. (a) Correlation of Ba and Se in μ-XRF analysis for the bulk in Fig. 1; (b)Correlation of Ba and Se in μ-XRF analysis for the lower left part in Fig. 1b; (c) Correlation of Ba and Se in μ-XRF analysis for the upper left part in Fig. 1b

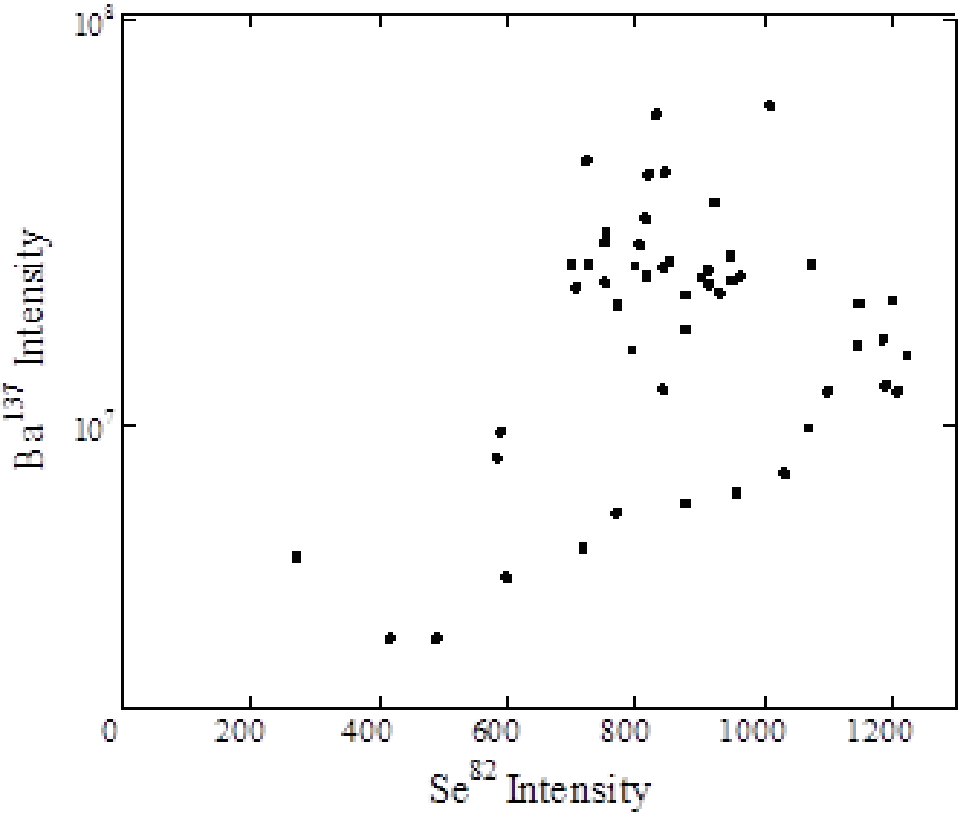

Figure 14. The correlation between Ba and Se intensities in the barite samples by LA-ICP-MS.

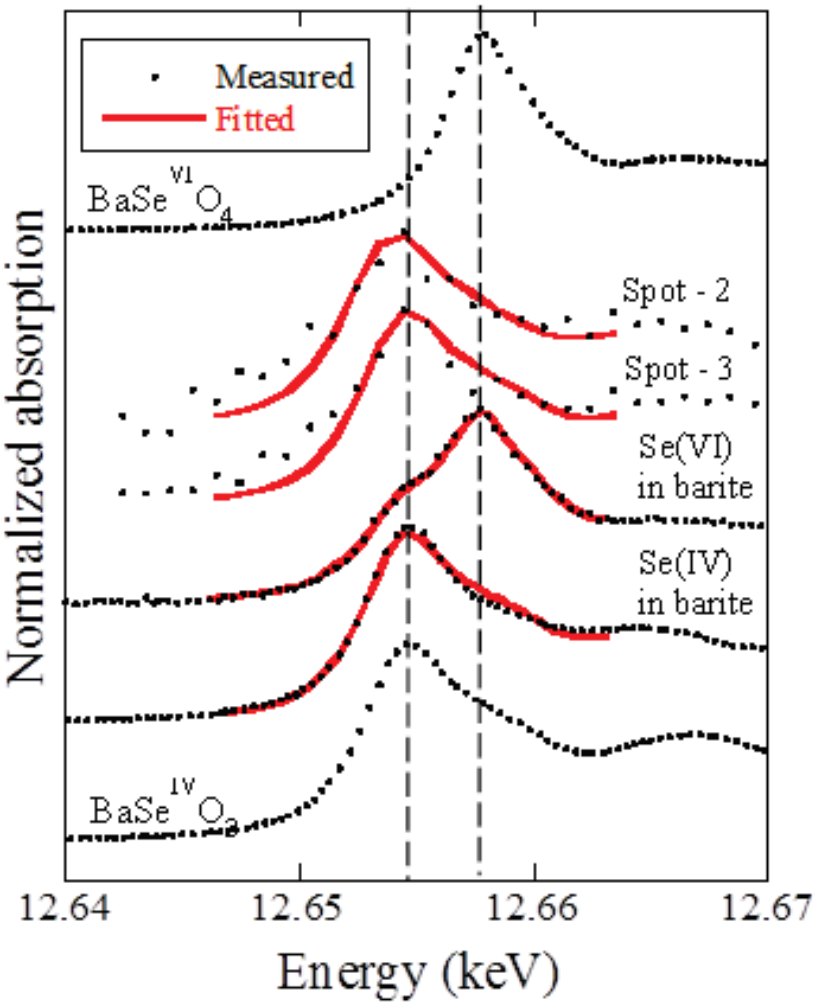

Figure 15. Normalized Se K-edge XANES of Se reference materials ($BaSeO_3$ and $BaSeO_4$), Se in barite at pH 8.0 added as Se(IV) or Se(VI), and Se in natural barite at spots 1 and 2 in barite. The vertical dashed lines indicate the absorption peaks of $BaSeO_3$ and $BaSeO_4$.

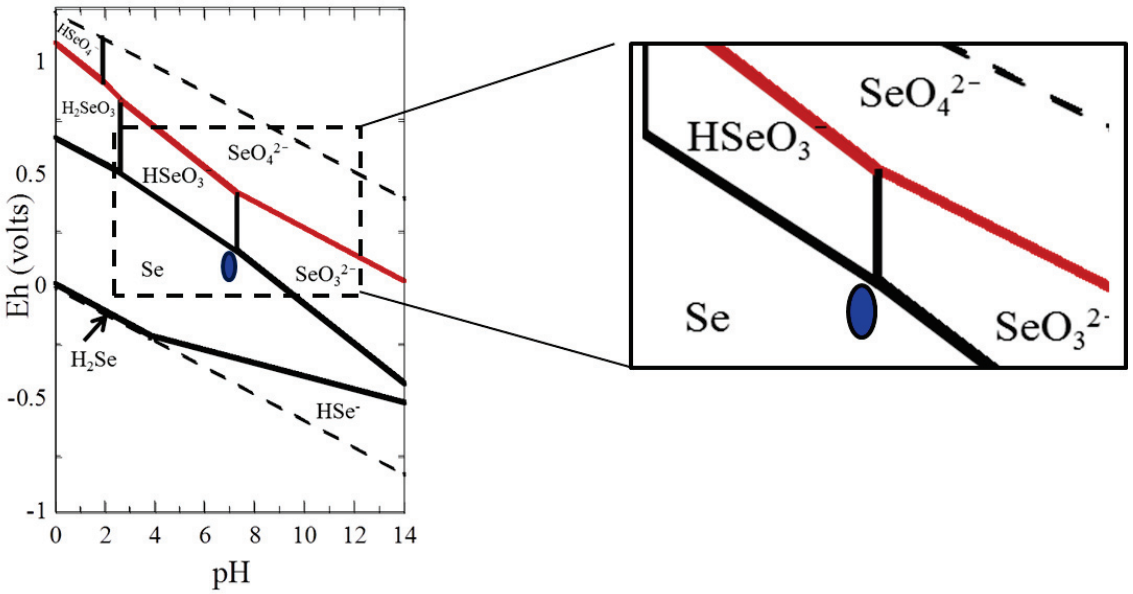

Figure 16. Depositional condition of Se estimated by E_h (150 mV) and pH (7.1) of the pore water in the sediment

Table 1. Experimental condition of coprecipitation experiments

Run no.	Se in input solution					pH		Se after the coprecipitations							Se in barite	K_d [3]
	Concentration [mg/L]	R_W^{VI}	SI_{barite} [1]	SI_{BaSeO3} [2]	SI_{BaSeO4} [2]	Input solution	Reaction	Concentration [mg/L]	R_W^0	R_W^{IV}	R_W^{VI}	R_B^0	R_B^{IV}	R_B^{VI}	Concentration [mg/L]	[L/kg]
ba-1	8.6	0	4.21	-1.89		8.0	7.9	7.8	0	100	0	0	100	0	3.1×10^3	4.0×10^2
ba-2	8.8	20	4.21	-1.93	-1.13	8.0	7.9	7.9	0	80	20	0	100	0	3.0×10^3	3.8×10^2
ba-3	8.8	40	4.21	-2.11	-0.83	8.0	8.0	8.2	0	60	40	0	100	0	2.4×10^3	2.9×10^2
ba-4	8.7	60	4.21	-2.28	-0.65	8.0	7.9	8.2	0	40	60	0	100	0	2.1×10^3	2.6×10^2
ba-5	8.7	70	4.21	-2.41	-0.58	8.0	8.0	8.2	0	30	70	0	100	0	1.8×10^3	2.2×10^2
ba-6	8.6	80	4.21	-2.59	-0.53	8.0	8.0	8.3	0	20	80	0	88.1	11.9	1.1×10^3	1.3×10^2
ba-7	8.7	90	4.21	-2.89	-0.47	8.0	8.0	8.3	0	10	90	0	81.2	18.8	1.3×10^3	1.6×10^2
ba-8	8.7	100	4.21		-0.43	8.0	8.0	8.4	0	0	100	0	16.8	83.2	8.6×10^2	1.0×10^2
ba-1'	8.7	0	4.21	-5.32		4.0	4.0	8.6	0	100	0	22.5	72.3	5.2	8.1×10^2	9.5×10^1
ba-2'	8.6	20	4.21	-5.41	-1.13	4.0	4.1	8.4	0	80	20	16.6	62.4	21	7.4×10^2	8.8×10^1
ba-3'	8.6	40	4.21	-5.54	-0.83	4.0	3.9	8.4	0	60	40	15.1	52.3	32.5	7.3×10^2	8.7×10^1
ba-4'	8.3	60	4.21	-5.72	-0.65	4.0	4.1	8.2	0	40	60	7.1	48.2	44.1	3.6×10^2	4.4×10^1
ba-5'	8.5	80	4.21	-6.02	-0.53	4.0	3.9	8.3	0	20	80	0	41.7	58.2	7.2×10^2	8.7×10^1
ba-6'	8.4	100	4.21		-0.43	4.0	3.9	8.2	0	0	100	0	13.1	86.9	6.6×10^2	8.1×10^1

1) Each saturation index (SI) zwas calculated by Visual MINTEQ and minerals were identified by XRD.

2) $BaSeO_3$ and $BaSeO_4$ are typical barium selenite and barium selenate minerals, respectively.

3) K_d is apparent distribution coefficient.

* $K_d = [Se]_B / [Se]_W$ ($[Se]_B$: Se concentration in barite; $[Se]_W$: Se concentration in water)

Table 2. Additional experiments with various initial solution, where pH was fixed at 8.0.

Run No.	Sample	Se in input solution			Se in barite			
		Tr_{ini} [mg/L]	Initial species	SI of barite	R_B^{IV} [%]	R_B^{VI} [%]	$K_{Se(IV)}$ [mg/L]	$K_{Se(VI)}$ [mg/L]
Exp 1	Milli-Q water	10.5	Se(VI)	4.21	16.3	83.7		7.0×10^{1}
Exp 2	Artificial Sea Water (ASW)	8.6		4.21	12.0	88.0		8.7×10^{1}
Exp 3	ASW without carbonate	9.1		4.21	12.1	87.9		1.3×10^{2}
Exp 4	ASW with phosphate	8.9		4.21	13.8	86.2		8.2×10^{1}
Exp 5	ASW with higher Se conc.	93.6		4.21	10.1	89.9		2.7×10^{2}
Exp 6	ASW with various SI of barite	7.6		3.91	19.2	80.8		2.4×10^{2}
Exp 7	ASW with various SI of barite	7.5		3.61	22.7	77.3		1.5×10^{2}
Exp 8	ASW with various SI of barite	7.6		3.21	18.4	81.6		5.6×10^{2}
Exp 9	ASW with various SI of barite	7.7		2.91	25.9	74.1		1.0×10^{3}
Exp 10	ASW with various SI of barite	7.8		2.61	20.4	79.6		1.5×10^{3}
Exp 11	AWS	8.6	Se(IV)	4.21	100	0	3.6×10^{2}	
Exp 12	ASW with various SI of barite	9.0		3.21	100	0	1.2×10^{3}	

*$K_{Se(IV)} = K_d \times (R_B^{IV} / R_W^{IV})$, where R_B^{IV} and R_W^{IV} are the Se(IV)/ΣSe ratio in the barite and in the solution, respectively.

Table 3. Structural data on the local atomic environment of Se derived from the simulation of EXAFS data for samples

Sample	Shell	CN	R(Å)	ΔE_0 (eV)	δ^2(Å)	Residual (%)
Se(IV) in barite	Se-O	3.2 (0.2)	1.69 (0.01)	7.5	0.410	2.901
	Se-Ba	1.9 (1.1)	3.20 (0.04)		1.030	
	Se-Ba	2.2 (1.4)	3.70 (0.04)		1.030	
Se(IV) on barite	Se-O	2.9 (0.3)	1.69(0.01)	6.8	0.410	5.491
	Se-Ba	1.7 (1.1)	3.14 (0.06)		1.030	
	Se-Ba	0.9 (1.6)	3.74 (0.13)		1.030	
Se(VI) in barite	Se-O	4.3 (0.2)	1.64 (0.00)	7.8	0.410	2.036
	Se-Ba	1.4 (1.0)	3.15 (0.05)		1.030	
	Se-Ba	3.1 (1.2)	3.58 (0.03)		1.030	
Se(VI) on barite	Se-O	4.1 (0.3)	1.65 (0.01)	7.7	0.410	0.323
	Se-Ba	1.0 (1.3)	3.02 (0.08)		1.030	
	Se-Ba	1.1 (1.8)	3.58 (0.11)		1.030	
Barite (Gupta et al., 2010)	Se-O	4	1.48			
	Se-Ba	1	3.38			
	Se-Ba	4	3.62			

Table 4. Apparent K_d at R_w^{IV} =1 and R_w^{VI} =1 between water and barite and their ratios at various pH conditions

	K_d (L/kg)				
	pH 2.0	pH 4.0	pH 5.0	pH 8.0	pH 9.0
K_d [Se(IV]	9.1×10^{1}	9.3×10^{1}	1.3×10^{2}	3.6×10^{2}	7.7×10^{2}
K_d [Se(VI]	6.5×10^{1}	7.8×10^{1}	1.0×10^{2}	9.9×10^{1}	
K_d [Se(IV)]/K_d [Se(VI)]	1.4	1.2	1.3	3.7	

Table 5. Mineralogical composition in the marine sediments samples by EPMA analysis

	Ba	S	O	Fe	Cu	As	Si	Al	Na	Probable Mineral
Spot 1	19.8	21.4	58.8							Barite
Spot 2		58.7	7.6	30.2	2.2	1.3				Pyrite
Spot 3	15.3	16.9	66.9							Barite
Spot 4			61.0				23.8	11.4	3.5	Feldspar

Chapter 4. Application of arsenic in barite as a redox indicator for suboxic/anoxic redox condition

1. Chapter Introduction

In this study, arsenic (As) oxyanion was selected as a possible element because As is dissolved in water either as arsenite [$As^{III}O_3^{3-}$: As(III)] or arsenate [$As^{V}O_4^{3-}$: As(V)] ion under suboxic and anoxic conditions, respectively [Jain and Ali, 2000]. Arsenite and arsenate are highly soluble ions, but these ions can be retained on various minerals through ion exchange, sorption/desorption, and coprecipitation/dissolution processes. Understanding the distribution process between minerals and water is important to predict arsenic mobility on earth surfaces in the presence of water. Previous studies have compared the immobilization mechanism of As(III) and As(V) via coprecipitation with minerals, such as calcium carbonate ($CaCO_3$) [Lowers et al., 2007; Helle et al., 2008; Yokoyama et al., 2012; Renard et al., 2015], pyrite (FeS_2) [Savage et al., 2000], and iron hydroxides (FeOOH) [Carbonel et al., 1999; Dixit and Hering, 2003]. These studies revealed that the distribution of As(V) on minerals was larger than that of As(III) because of the larger complexation stability of arsenate than that of arsenite. For instance, Yokoyama (2011, 2012) demonstrated that in the case

of arsenic incorporation into calcite, calcite selectively incorporates arsenate rather than arsenite. This result suggested that As in calcite was not an appropriate proxy to estimate the As(V)/As(III) ratio in water because of the selective incorporation of As(V). Similar phenomena were also observed in other systems with As and sulfide minerals in environments [Savage et al., 2000; Smedley and Kinniburgh, 2002].

This work focused on barite ($BaSO_4$) as a host phase of As for our purpose. Barite, which is stable under a wide range of pressure, temperature, E_h, and pH, can incorporate various trace elements that may record geochemical information of coexistent water and depositional condition (Fig. 1a). Several elements (e.g., cations: Sr^{2+}, Ca^{2+}, Ra^{2+}, Pb^{2+}, and rare earth elements; anions: SeO_4^{2-}, CrO_4^{2-}, and MnO_4^{2-}) were incorporated into barite by substituting Ba^{2+} or SO_4^{2-} [Guichard et al., 1979; Hein et al., 2000; Prieto et al., 2002; Zhu, 2004; Griffith and Paytan, 2012]. Barite formation occurs in various environments, such as seawater, seafloor hydrothermal fluid, groundwater, and onshore hot spring water. In particular, barite precipitated from hot spring water contains considerable amounts of trace elements in its crystal lattice, such as radium (Ra), other alkaline earth elements, and As [Boyle, 1973; Chao et al., 2009]. Several studies characterized the behavior of arsenate in barite in terms of solubility and stability of barium arsenate [Robins, 1985; Zhu et al., 2005].

However, the distributions of As(III) and As(V) between barite and water remains poorly understood. Thus, in this study, coprecipitation experiments of As with barite were conducted to investigate the influence of oxidation state on its immobilization into barite through batch experiments. If both As(III) and As(V) are incorporated into barite to a similar degree, the As(V)/As(III) ratio recorded in barite reflects the ratio in water. In particular, if As(III) and As(V) are under equilibrium in terms of redox reactions, the As(V)/As(III) ratio in barite can be a useful indicator of redox potential in natural water [Cherry et al. 1979; Yan et al., 2000]. Thus, the As(V)/As(III) ratio in barite may be adopted to estimate E_h of the environment, whether the environment is below or above the redox boundary of As(V)/As(III), or suboxic/anoxic boundary (Fig. 1(b)).

In this study, natural barite samples collected in high As concentration areas were also analyzed by micro-X-ray fluorescence (μ-XRF) and micro-X-ray-adsorption fine structure (μ-XAFS) to investigate whether this method can be applied to natural systems where barite precipitates. Two natural barite samples were analyzed: (i) one sample was collected from the Tamagawa Hot Spring (Obuki Hot Spring, Tamagawa Geothermal System, Akita Prefecture, Japan) where the depositional E_h-pH condition is known (pH: 3.4; E_h: 0.59 V) [Ogawa et al., 2012]; (ii) the other was obtained near

the hydrothermal vent system at the seafloor in Okinawa Trough (Izena Hole) in Japan without information of the depositional E_h-pH condition. These analyses were carried out to (i) evaluate the reliability of the As(V)/As(III) ratio in barite as a redox indicator based on the analysis of the Tamagawa sample and (ii) estimate the depositional E_h condition in water whether barite precipitated below or above the redox boundary of As(V)/As(III), or the suboxic/anoxic boundary for the Okinawa sample.

Session 2 showed that the barite–selenium oxyanion system could be used as a redox indicator for the oxic-suboxic boundary because the selenate/selenite [Se(VI)/Se(IV)] ratio in barite is primarily correlated with that of the ratio in water [Tokunaga et al., 2013a]. In particular, the Se(VI)/Se(IV) system is sensitive to more oxic condition compared with the As(V)/As(III) system (Fig. 1(c)). Thus, if the As(V)/As(III) ratio in barite can also be applied to the natural system as a proxy for the suboxic/anoxic boundary, barite can provide more accurate information on whether it is precipitated under oxic, suboxic, or anoxic redox environments.

2. Methods

2.1. Experimental procedures

2.1.1. Coprecipitation experiment

Coprecipitation of As with barite was conducted through the spontaneous precipitation of barite. Laboratory experiments were conducted at various [As(III)]/[total As] ratios in water (= R_w^{III}), as determined by high-performance liquid chromatography-inductively coupled plasma-mass spectrometry (HPLC-ICP-MS), to investigate the influence of oxidation state on the immobilization As(III) or As(V) into barite. As(III) and As(V) stock solutions were prepared from $KAsO_2$ and $K_2HAsO_4 \cdot 7H_2O$ (Wako, Japan), respectively. Barite was precipitated from a mixture of (i) 27 mM Na_2SO_4 solution and (ii) 0.65 mM $BaCl_2 \cdot 2H_2O$ solution [Blount, 1974]. Right before the addition of the $BaCl_2 \cdot 2H_2O$ solution, As(III) and/or As(V) were added to the sulfate solution. This solution was continuously adjusted to a specific pH (pH 2.0, 5.0, 8.0, or 11.0) by adding a small amount of a HCl or NaOH solution during the experiments. The pH condition during the experiments was examined to account for the pH dependence of As species encountered in natural water: (i) As(III) is mainly dissolved as $H_3AsO_3^0$ from pH 2.0 to 8.0 and $H_2AsO_3^-$ at pH above 11.0, whereas (ii) As(V) is mainly dissolved as $H_3AsO_4^0$, $H_2AsO_4^-$, or $HAsO_4^{2-}$ at pH 2.0, 5.0, 8.0, and

11.0, respectively (Fig. 2). The dissolved species at various pH values was calculated based on the p*Ka* values of arsenous acid (H_3AsO_3) and arsenic acid (H_3AsO_4) (arsenous acid: $pK_1 = 9.22$, $pK_2 = 12.13$, and $pK_3 = 13.4$; arsenic acid: $pK_1 = 2.20$, $pK_2 = 6.97$, and $pK_3 = 11.53$) [Helle et al., 2008]. The saturation indices of barite (SI_{barite}) in the initial solution were fixed at 4.2 by adjusting the Ba^{2+} concentration to keep the same initial precipitation rate of barite for all experiments (Table 1). SI is defined as $SI = \log(IAP/K_{sp})$, where IAP and K_{sp} are the ion activity product and solubility product of the mineral, respectively. As in the initial solution (concentration: 0.10–10.0 mM) was unsaturated with respect to the solid phases of barium arsenite and barium arsenate to avoid the formation of these Ba-As precipitates in the system (Table 1).

The precipitates of barite and the aqueous phase were separated by filtration with a 0.20 μm membrane filter (mixed cellulose ester, Advantec, Tokyo, Japan) and then rinsed three times with Milli-Q water. The X-ray diffraction (XRD) patterns of the precipitates were measured using a powder X-ray diffractometer (MultiFlex, Rigaku Co., Tokyo, Japan), in which the mineral phase was identified by matching the XRD patterns to the International Center for Diffraction Data file. Total As concentrations in the solution before and after filtration were analyzed by ICP-MS (7700cs, Agilent,

Tokyo, Japan) after dilution by 2 wt.% HNO_3 solution. The distribution coefficient of As between barite and water was calculated based on the As concentration in the water and solid phase. After filtration, a part of the solid sample was dried in an oven at 60 °C and dissolved into water by adding sodium carbonate [Breit et al., 1985] to determine the As concentration in the precipitates. The oxidation states of As in the precipitates and the remaining solution after filtration were determined by As K-edge X-ray absorption near-edge structure (XANES) and HPLC-ICP-MS (7500cs, Agilent, Tokyo, Japan), respectively. A portion of the precipitate was immediately packed into an airtight polyethylene bag and stored at 4 °C until XANES measurement. The drying process was not conducted to avoid altering the As(V)/As(III) ratio in barite.

2.2. Analysis of natural samples

Two barite samples were used to (i) validate the method for estimating E_h and (ii) provide an example of its application to natural samples.

2.2.1. Tamagawa hot spring samples

The hot spring barite sample, for which depositional E_h-pH conditions are known, was analyzed to test the reliability of the As(V)/As(III) ratio in barite as a redox indicator. The natural barite samples used in this study were collected from the

Tamagawa Hot Spring (latitude 39°58; longitude 140°43), which is one of the chloride-rich volcanic hot springs in Japan. The Tamagawa Hot Spring is characterized by its strong acidity (pH 1.2), high temperature (98 °C), large fluid discharge (9000 L/min), and high concentrations of trace elements, such as As, rare earth elements, and others [Sanada et al., 2006; Ogawa et al., 2012]. The concentration of SO_4^{2-} in this area is remarkably higher (about 1200–2600 mg/L) compared with other hot springs in Japan, which controls the cation concentrations in the hot spring, such as Ba^{2+}, Pb^{2+}, and Sr^{2+} [Sasaki and Watanuki, 1988; Yoshiike, 2003]. These cations are the main components of Pb-bearing barite (so called hokutolite) precipitating from hot spring water, which is a solid solution of barite ($BaSO_4$) and anglesite ($PbSO_4$). Hokutolite, which is found only in the Tamagawa Hot Spring (Akita, Japan) and Peitou Hot Spring (northern Taiwan), is a famous radioactive mineral deposited on sediments in a stream of hot spring and contains a considerable amount of radium and other alkaline earth elements [Takano, 1969; Chao et al., 2009]. Numerous studies have been carried out to understand the crystal structure, chemical composition, and growth rate of natural hokutolite, along with related environmental factors [Chen and Yu, 1984; Su et al., 2002; Chao et al., 2009]. Ogawa et al. (2012) revealed that the As concentration in the Tamagawa area is about 1000 μg/L, and dissolved As occurs predominantly as arsenite,

as determined by the anion exchange resin method. However, the relationship between the distribution of arsenic and barium in Tamagawa Hot Spring has not been well studied. Thus, in the current study, μ-XRF and μ-XAFS were conducted to directly detect trace amounts of As and As(V)/As(III) ratio in barite collected from the Tamagawa Hot Spring. A barite sample was embedded in epoxy resin and polished for EPMA and μ-XRF analyses.

2.2.2. Barite formed at the Jade Hydrothermal site in the Okinawa Trough

The hydrothermal barite sample was analyzed to estimate the depositional E_h condition in water where barite precipitated. The barite samples used in this study were found in a marine sediment (depth from sea floor: 0–4 cm) within a core sample collected in the Jade site during NT10-17 cruise [Yokoyama et al., 2015], a hydrothermal vent system located along the northeastern slope of the Izena Hole at water depths of 1300–1550 m in the Izena Cauldron, Okinawa Trough [Kawagucci et al., 2010; Ishibashi et al., 2014]. E_h and pH of the pore water in the sediment were 150 mV and 7.1, respectively. However, the depositional E_h-pH condition of the barite sample when barite precipitated is unknown.

As described in the Introduction, our previous study showed that the

Se(VI)/Se(IV) ratio in barite can be used to estimate the redox condition of the coexistent water during the formation of barite. We found that Se was mainly incorporated into barite as Se(IV) in the Okinawa barite sample, suggesting that the barite precipitated below the redox boundary of Se(VI)/Se(IV) [Tokunaga et al., 2013a]. Thus, the As(V)/ As(III) ratio in the same barite sample in this study was also analyzed by μ-XAFS analysis to more accurately estimate redox information, and determine whether barite precipitates under suboxic or anoxic condition.

2.3. Analytical methods

2.3.1. HPLC-ICP-MS

The As(V)/As(III) ratio in the water sample was determined by HPLC-ICP-MS. The Pu-2089 Plus pump and a Co-2065 Plus (JASCO) oven were used in the experiment. An anion exchange column (TSK gel Super IC-AP, Tosoh) was used at 40 °C. The mobile phase was the aqueous solution containing 30 mM NH_4HCO_3 (Wako, Japan) at pH 7.9; thus, As(III) and As(V) were separated as H_3AsO_3 and $HAsO_4^{2-}$, respectively, as described by Yokoyama et al. (2012). The flow rate of the mobile phase was 1.0 mL/min. Approximately 100 μL of Milli-Q water was injected into the chromatographic system between the measurements to remove any remaining

As in the inlet and syringed solution. Subsequently, the ^{75}As chromatogram was verified to confirm that detectable ^{75}As did not remain in the measurement system.

2.3.2. XAFS measurement and data analysis

The XANES technique is a method suitable to determine the As(V)/As(III) ratio in barite because it is a nondestructive analytical method. The K-edge XANES spectra of As were obtained in the beamline BL01B1 of SPring-8 (Hyogo, Japan) and in the beamline BL-12C of Photon Factory, KEK (Tsukuba, Japan), with an Si(111) double-crystal monochromator and two mirrors. The monochromator was calibrated using a reference sample, $KAsO_2$, which was prepared as a pellet after dilution with boron nitride powder. The energy value of 11.880 keV was assigned to the highest peak in the XANES region for the compound. The XANES spectra of the reference compounds were collected in the transmission mode, whereas those of the experimental samples were obtained in the fluorescence mode using a 19-element germanium semiconductor detector placed at 90° to the incident beam. In the fluorescence mode, the samples were positioned at 45° with respect to the incident beam. Multiple scans were obtained to verify the radiation damage that can change the oxidation state of As in the samples; no appreciable change was observed in every

spectrum obtained. The measurements were carried out at room temperature under ambient condition. The XANES data were analyzed using a REX2000 (Rigaku Co.) to fit the sample spectra by linear combination of the reference materials. The As(V)/As(III) ratio in the solid sample was determined by least-squares fitting using the reference spectra of $KAsO_2$ and KH_2AsO_4 (Wako Pure Chem., Ltd., Japan), which were received as analytical grade reagents.

2.3.3. μ-XRF and μ-XANES

Each natural barite sample was embedded in a high-purity epoxy resin (Eposet, Maruto Co., Ltd.) and polished to create a thin section for EPMA and μ-XRF analyses. The distribution of arsenic within the barite sample at the micrometer scale was obtained at beamline 37XU (SPring-8) via μ-XRF [Terada et al., 2004]. The beamline consisted of a Si(111) double crystal monochromator with a Kirkpatrick–Baez mirror to obtain a 0.5×0.5 μm^2 X-ray beam at the sample position. The X-ray energy was fixed at 12.8 keV to obtain the μ-XRF image of As (Kα line), Ba (Lα line), and other elements. Two-dimensional (2D) mapping was conducted using an X-Y axis stage. The sample was fixed on a sample holder oriented at 10° to the orthogonal direction of the incident X-ray beam. The XRF intensity of each line was measured by a silicon

drift detector. The step size of the stage was set to 2.0 μm, and the exposure time at each point was 0.1 s. Measurements were carried out under ambient condition.

3. Results and discussion

3.1. Laboratory experiments

3.1.1. Incorporation of As(III) and As(V) into barite

Coprecipitation experiments at $R_W^{III} = 0$ or 1 were conducted under various pH conditions to investigate the effect of the oxidation state on its immobilization into barite. The XRD results showed that the precipitates consisted only of barite without other minerals, such as $Ba(AsO_2)_2$, $Ba_3(AsO_4)_2$, or $BaHAsO_4 \cdot H_2O$, as reported in previous studies [Robins, 1985; Zhu et al., 2005], because the intensities and widths of the peaks in XRD were similar to those of the barite reference sample. The results showed that (i) As was incorporated into barite and (ii) the transformation of the As-coprecipitated barite to other minerals and pH values could be ignored. Barium sulfate mineral can be exclusively present as barite in nature without any other polymorphs based on the survey of Inorganic Crystal Structure Database [Lee et al., 2005]. For the As species in the aqueous phase, HPLC-ICP-MS analysis showed that the initial As species was preserved during aging, indicating that direct reduction/oxidation of As(V) to As(III) or As(III) to As(V) was not observed in water during the experimental period.

The oxidation state of As in the precipitates was determined by XANES based on the fitting of the spectra of the samples by linear combination of the spectra of $KAsO_2$

and KH_2AsO_4 because most of the samples could be fitted by these two reference materials (Fig. 3; Table 1). The fitting results showed that both As(III) and As(V) were incorporated into barite depending on its initial As species in water. In the As(V) system ($R_W^{III} = 0$), As was incorporated only as As(V) in the precipitate. In the As(III) system ($R_W^{III} = 1$), on the other hand, a part of As was incorporated into barite as As(V), but more than 30% of As was mainly incorporated as As(III). All the results were reproducible at least under our experimental conditions based on our repeated coprecipitation experiments ($N = 3$).

The oxidation of As(III) to As(V) occurring in the As(III) system might be caused by the different stabilities of the immobilized species between As(III) and As(V). The redox change during the incorporation into such minerals was also reported for various systems, such as (i) Se(IV) to Se(VI) during its incorporation into barite [Tokunaga et al., 2013b], (ii) As(III) to As(V) during incorporation into calcite [Yokoyama et al., 2013; Francois et al., 2015], and (iii) Yb(III) to Yb(II) in the calcite coprecipitation system [Tsuno et al., 2003]. Given the larger complexation and stabilization of As(V) anion [Goh, 2004; Sø et al., 2008; Yokoyama et al., 2012], it is suggested that a part of As can be incorporated into barite as As(V) at $R_W^{III} = 1$. Although a part of As(III) was immobilized in barite as As(V), both As(III) and As(V) could be incorporated into

barite as As(III)- and As(V)-coprecipitated barite, respectively, to reflect more or less its initial species in water. These findings indicated that barite could host both As(III) and As(V), which was not the case for calcite that selectively incorporated As(V) [Yokoyama et al., 2013; Francois et al., 2015].

3.1.2. The As(V)/As(III) ratio in barite to estimate E_h

In this section, the relationship between R_w^{III} and R_B^{III} (=[As(III)]/[total As] ratio in barite determined by XANES) was examined to verify whether the As(V) or As(III) ratio in barite reflects the ratio in coexistent water. Coprecipitation experiments at various R_w^{III} were conducted at pH 2.0 and 11.0 to examine the influence of the charges of the As(V)/As(III) ratio on arsenic immobilization into barite (Fig. 2). The results of the experiments showed that (i) considerable amount of As in barite could be incorporated as As(V)-coprecipitated barite, but (ii) R_B^{III} increased with increasing R_w^{III} at both pH values (Figs. 4 and 5). These findings showed that R_B^{III} was primarily correlated with R_W^{III} suggesting that the As(V)/As(III) ratio in barite could be used as a proxy of the As(V)/As(III) ratio in water.

If the As(V)/As(III) ratio in water could be estimated by the ratio in barite, what are the geochemical implications obtained by the estimated ratio? In most cases, the

As(V)/As(III) ratio in natural water is controlled by kinetic factors, such as chemically and/or microbiologically mediated oxidation–reduction reactions [Seyler and Martin, 1989; Masscheleyn et al., 1991; Smedley and Kinniburgh, 2002]. For example, Masscheleyn et al. (1991) suggested that both As(III) and As(V) are often discovered under anoxic conditions because of the microbiological redox transformation of As(III). However, other studies showed the suitability of the As(V)-As(III) redox couple to reflect the redox condition in water over long time periods [Andreae et al., 1979; Cherry et al. 1979]. Several studies showed a good agreement between E_h calculated from the As(V)-As(III) couple and those measured by a *Pt* electrode, indicating that the As(V)/As(III) ratio in water is a useful indicator of redox conditions in groundwater systems [Cherry et al. 1979; Yan et al., 2000]: a larger As(V)/As(III) ratio corresponds to a suboxic condition, whereas a lower ratio corresponds to an anoxic condition (Fig. 1b). Thus, the As(V)/As(III) ratios in water estimated by the present method enables us to estimate the E_h condition, if we can assume the redox equilibrium in the system.

3.1.3. Distribution coefficient of As between barite and water

Variations in the apparent distribution coefficient (= K_d) of As between barite and

water were also measured by ICP-MS to determine the difference in the immobilization mechanisms between As(III) and As(V). The apparent distribution coefficient of As between barite and water is defined as

$$K_d\ (\mathrm{L/kg}) = [\mathrm{As}]_B / [\mathrm{As}]_W$$

where $[\mathrm{As}]_B$ and $[\mathrm{As}]_W$ are the total As concentrations in barite (mg/kg) and water (mg/L), respectively. In this study, $[\mathrm{As}]_B$ was calculated directly from the dissolution of barite by employing the sodium carbonate method [Breitn et al., 1985] because of its low concentration, but not by the difference in the concentration of As between the initial and final solutions.

The apparent K_d values of As(III) and As(V) defined as $K_{As(III)}$ and $K_{As(V)}$ were determined from the following equations:

$$K_{As(III)} = K_d \times \frac{R_B^{III}}{R_W^{III}} \quad \text{and} \quad K_{As(V)} = K_d \times \frac{R_B^{V}}{R_W^{V}} \ .$$

Calculations of $K_{As(III)}$ and $K_{As(V)}$ are summarized in Table 1. An obvious trend between As species and immobilization mechanisms was observed (Fig. 6). At pH 2.0, both $K_{As(III)}$ and $K_{As(V)}$ were almost identical because both species were dissolved as zerovalent oxyacids ($H_3AsO_2^0$ and $H_3AsO_4^0$). Above pH 5.0, on the other hand, $K_{As(V)}$ was larger than $K_{As(III)}$, possibly because of their different negative charges: As(V) was present as monovalent anion ($H_2AsO_4^-$) at pH 5.0 and divalent ($HAsO_4^{2-}$) from pH 8.0

to 11.0, whereas As(III) was mainly dissolved as zerovalent anion ($H_3AsO_3^0$) from pH 2.0 to 8.0 and monovalent ($H_2AsO_3^-$) above pH 11.0. Similar phenomena were also observed in barite–selenium oxyanion systems [Tokunaga et al., 2013b], suggesting that a relationship between stabilities of the surface complex and corresponding complex in solution controls its partition behavior.

3.2. Application to natural samples

3.2.1. Effect of temperature in both sites

We here extend the estimation method of redox condition using speciation of As (present study) and Se [Tokunaga et al. 2013a] in barite to natural barite samples. However, the effect of the difference in the temperatures in the hydrothermal water where the natural barite samples formed and in our laboratory exepriments must be considered. Previous studies showed that the temperature that precipitaed barite at the Tamagawa Hot Spring was about 60 °C [Takano, 1969; Sasaki and Minato, 1983; Sasaki et al., 1992]. As for Okinawa samples, the pore water temperature of the samples collected in this site was not measured, but we can estimate the temperature based on the Mg content [Mg^{2+}] in pore water within the sediments [Raja, 2007]. High-temperature hydrothermal fluid (320 °C) and ambient seawater (4 °C) were mixed

within the sediment in this site (Yokoyama et al., 2015). The [Mg^{2+}] of this sample was about 1000 mg/L, which should be mainly derived from seawater (1200 mg/L), because [Mg^{2+}] is practically absent in hydrothermal fluid relative to seawater. Thus, the pore water temperature can be estimated as about 60 °C based on the hydrothermal fluid temperature (320 °C), seawater temperature (4 °C), and their [Mg^{2+}].

Figure 7 presents the E_h-pH diagrams for As-H_2O (a) and Se-H_2O (b) at 25 °C (black line) and 60 °C (red line) calculated by Geochemical Workbench (GWB Version 6; Bethke, 2006). The redox boundaries of the As(V)/As(III) and Se(IV)/Se(VI) ratio slightly changed, but the speciation estimated from the E_h-pH diagrams were almost conserved at both temperatures. Figure 8 presents the XANES spectra of Se and As incorporated into barite at 60 °C, which show the spectra similar to those obtained at room temperature (25 °C). Thus, the effect of temperature on the distributions of As and Se oxyanions into barite is not important at least for the barite samples collected in the hydrothermal water (60 °C) in this study.

3.2.2. Tamagawa hot spring sample

EPMA analysis showed that barite was present in the hot spring sediment, which could host several elements, such as Pb, Fe, and Ca. An example of elemental maps

for Ba, As, Se, and Fe in the grain obtained by μ-XRF analysis (Fig. 9) showed that the spatial distributions of As and Se were correlated with that of Ba in the samples, suggesting that both As and Se were incorporated into barite (As 6.4 mg/kg; Se 0.20 mg/kg in bulk sample by ICP-MS analysis). Micro-XANES analysis was performed at a spot with a relatively high concentration of As observed in this grain (spot A in Fig. 9b). The XANES spectra obtained from this spot showed that As was mainly incorporated into barite as As(III) in the sample (Fig. 10). Based on the laboratory results, the dominance of As(III) in the sample implied that barite was precipitated under anoxic condition, where As should be dissolved as As(III). This result was consistent with the fact that As was dissolved predominantly as As(III) in this hot spring water under the low pH and E_h conditions (pH 3.4; E_h = 0.59 V) [Ogawa et al., 2012]. The consistency between the laboratory experiments and natural barite sample analysis suggested that the barite–arsenic oxyanion system could work as a proxy to estimate the As(V)/As(III) ratios in water.

3.2.3. Jade Hydrothermal site sample

Figs. 9(e)–(h) present an example of the elemental map by μ-XRF analysis for Ba, As, Se, and Fe in the barite grain collected from Jade hydrothermal site.

Enrichment of Se was not observed in this grain, but both Se and As were enriched in barite as revealed by the analysis after the dissolution of barite (As = 24.3 mg/kg; Se = 2.9 mg/kg in bulk sample by ICP-MS analysis). In addition, a correlation between Se and Ba was observed for other grains, as reported in our previous study [Tokunaga et al., 2013a]. Micro-XANES analysis was performed at a spot with relatively high As concentration in this grain. The XANES spectra obtained from this spot showed that As was mainly incorporated into barite as As(V) in this sample (Fig. 10). The absence of As(III) in the spot suggested that barite was precipitated under oxic or suboxic condition above the redox boundary of As(V)/As(III). In addition, our previous study showed that a part of Se was present as Se(IV) in the sample, which implied that barite was precipitated under suboxic or anoxic conditions. The present and previous results on the speciation of Se and As in barite showed that both Se and As were enriched and incorporated into barite as Se(IV) and As(V), respectively. Based on the information of the two elements, it is suggested that barite precipitated under suboxic condition (Fig. 11), in which both Se(IV) and As(V) were dissolved (Fig. 1).

4. Conclusion

This work showed that the inorganic As(V)/As(III) ratio in water could be estimated by the As(V)/As(III) ratio in barite. Under equilibrium, in terms of the redox condition, the As(V)/As(III) ratio in barite could indicate the redox condition of the depositional environment, and determine whether the redox condition is below or above the redox boundary of As(V)/As(III), or suboxic-anoxic boundary. The estimation of the redox condition based on As speciation in barite has several advantages. This method allows us to estimate (i) the redox condition in the past when barite was precipitated and (ii) the redox condition in an environment where any direct method (e.g., *Pt* electrode) cannot be used to measure E_h, such as in hydrothermal water. Previous studies showed that barite can serve as a geochemical tool to reconstruct paleo-environmental conditions, such as marine productivity [Gonneea and Paytan 2006; Paytan et al., 2007], depositional sea water compositions [Beek et al., 2003; Torres et al., 2003; Snyder et al., 2007], and global perturbations to the sulfur cycle [Huston and Graham, 2004]. Our present studies demonstrated that barite can also be employed as a geochemical probe of the depositional redox condition in the paleo-environmental study. Moreover, coupling of the As(V)/As(III) ratio with the Se(VI)/Se(IV) ratio in barite estimated by XANES could more precisely constrain the

redox environment at the time of deposition of barite in natural systems, as demonstrated in this study for the sediment in the hydrothermal vent site.

References

Andreae, M. O., 1979. Arsenic speciation in seawater and interstitial waters: The influence of biological-chemical interactions on the chemistry of a trace element1. Limnology and Oceanography 24.3, 440-452.

Andrade, R. P., Mello, J. W. V., Windmöller, C. C., Silva, J. B. B., Figueiredo, B. R., 2012. Evaluation of arsenic availability in sulfidic materials from gold mining areas in Brazil. Water, Air, & Soil Pollution 223.8, 4679-4686.

Bethke, C. M., 2005. The Geochemist's Workbench Release 6.0 GWB Reaction Modeling Guide.

Boyle, R. W., Jonasson, I. R., 1973. The geochemistry of arsenic and its use as an indicator element in geochemical prospecting. Journal of Geochemical Exploration 2.3, 251-296.

Breit, George N., Simmons, E. C., Goldhaber, M. B., 1985. Dissolution of barite for the analysis of strontium isotopes and other chemical and isotopic variations using aqueous sodium carbonate. Chemical Geology: Isotope Geoscience section 52.3, 333-336.

Carbonell, B. A., Jugsujinda, A., DeLaune, R. D., Patrick, W. H., Burló, F., Sirisukhodom, S., Anurakpongsatorn, P., 1999. The influence of redox chemistry and pH on chemically active forms of arsenic in sewage sludge-amended soil.

Environment international 25.5, 613-618.

Chao, J. H., Chuang, C. Y., Yeh, S. A., Wu, J. M., 2009. Relationship between radioactivity of radium and concentrations of barium and lead in hokutolite. Applied Radiation and Isotopes 67.4, 650-653.

Chen, C. J., Yu, S. C., 1984. A substructural study on hokutolite. Mem. Geol. Soc. China 6, 229-237.

Cherry, J. A., Shaikh, A. U., Tallman, D. E., Nicholson, R. V., 1979. Arsenic species as an indicator of redox conditions in groundwater, Journal of Hydrology 43.1, 373-392.

Dixit, S., Hering, J. G., 2003. Comparison of arsenic (V) and arsenic (III) sorption onto iron oxide minerals: Implications for arsenic mobility, Environmental Science & Technology 37.18, 4182-4189.

Goh, K. H., Lim, T. T., 2004. Geochemistry of inorganic arsenic and selenium in a tropical soil: effect of reaction time, pH, and competitive anions on arsenic and selenium adsorption. Chemosphere 55.6, 849-859.

Gonneea, M. E., Paytan, A., 2006. Phase associations of barium in marine sediments. Mar. Chem. 100.1, 124-135.

Griffith, E. M., Paytan, A., 2012. Barite in the ocean–occurrence, geochemistry and

palaeoceanographic applications. Sedimentology 59.6, 1817-1835.

Guichard, F., Church, T. M., Treuil, M., Jaffreic, H., 1979. Rare earths in barites: distribution and effects on aqueous partitioning. Geochim. Cosmochim. Acta 43, 983-997.

Hein, J. R., Stamataki, M. G., Dowling, J., 2000. Trace metal-rich Quaternary hydrothermal manganese-oxide and barite deposit, Milos Island, Greece. Trans. Inst. Min. Metall. Sect. B 109, B67–B76.

Huston, D. L., Logan, G. A., 2004. Barite, BIFs and bugs: evidence for the evolution of the Earth's early hydrosphere, Earth Planet. Sci. Lett. 220.1, 41-55.

Ishibashi, J. I., Noguchi, T., Toki, T., Miyabe, S., Yamagami, S., Onishi Y., Yamanaka T., Yokoyama Y., Omori E., Takahashi Y., Hatada K., Nakaguchi Y., Yoshizaki M., Konno U., Shibuya T., Takai K., Inagaki F., Kawagucci S., 2014. Diversity of fluid geochemistry affected by processes during fluid upwelling in active hydrothermal fields in the Izena Hole, the middle Okinawa Trough back-arc basin, Geochemical Journal, 48.4, 357-369.

Jain, C. K., Ali, I., 2000. Arsenic: occurrence, toxicity and speciation techniques, Water Research 34.17, 4304-4312.

Kawagucci, S., Shirai, K., Lan, T. F., Takahata, N., Tsunogai, U., Sano, Y., Gamo, T.,

2010. Gas geochemical characteristics of hydrothermal plumes at the HAKUREI and JADE vent sites, the Izena Cauldron, Okinawa Trough. Geochemical Journal 44.6, 507-518.

Lee, J. S., Wang, H. R., Iizuka, Y., and Yu, S. C., 2005. Crystal structure and Raman spectral studies of $BaSO_4$-$PbSO_4$ solid solution. Zeitschrift für Kristallographie-Crystalline Materials, 220.1, 1-9.

Lowers, H. A., Breit, G. N., Foster, A. L., Whitney, J., Yount, J., Uddin, M. N., Muneem, A. A., 2007. Arsenic incorporation into authigenic pyrite, Bengal Basin sediment, Bangladesh. Geochim. Cosmochim. Acta 71.11, 2699-2717.

Masscheleyn, P. H., Delaune, R. D., Patrick Jr, W. H., 1991. Effect of redox potential and pH on arsenic speciation and solubility in a contaminated soil. Environmental Science & Technology 25.8, 1414-1419.

Ogawa, Y., Ishiyama, D., Shikazono, N., Iwane, K., Kajiwara, M., Tsuchiya, N., 2012. The role of hydrous ferric oxide precipitation in the fractionation of arsenic, gallium, and indium during the neutralization of acidic hot spring water by river water in the Tama River watershed, Japan. Geochim. Cosmochim. Acta 86, 367-383.

Paytan, A., Griffith, E. M., 2007. Marine barite: Recorder of variations in ocean export productivity. Deep Sea Research Part II: Topical Studies in Oceanography 54.5,

687-705.

Prieto, M., Fernandez-Gonzalez, A., and Martin-Diaz, R., 2002. Sorption of chromate ions diffusing through barite-hydrogel composites: Implications for the fate and transport of chromium in the environment. Geochim. Cosmochim. Acta 66, 783–795.

Renard, F., Putnis, C. V., Montes-Hernandez, G., Ruiz-Agudo, E., Hovelmann, J., Sarret, G., 2015. Interactions of arsenic with calcite surfaces revealed by in situ nanoscale imaging. Geochim. Cosmochim. Acta 159, 61-79.

Robins, R. G., 1985. The solubility of barium arsenate: Sherritt's barium arsenate process. Metallurgical and Materials Transactions B 16.2, 404-406.

Sasaki, N., Watanuki, K., 1988. Effects of compositional changes of hot spring water upon mineral precipitate. I. Changes in chemical composition and crystal growth rate of Pb-bearing barite (hokutolite) from Tamagawa hot spring waters. Bulletin of the Chemical Society of Japan 61, 1135-1139.

Sanada, T., Takamatsu, N., Yoshiike, Y., 2006. Geochemical interpretation of long-term variations in rare earth element concentrations in acidic hot spring waters from the Tamagawa geothermal area, Japan. Geothermics 35.2, 141-155.

Savage, K. S., Tingle, T. N., O'Day, P. A., Waychunas, G. A., Bird, D. K., 2000.

Arsenic speciation in pyrite and secondary weathering phases, Mother Lode gold district, Tuolumne County, California. Applied Geochemistry, 15.8, 1219-1244.

Seyler, P., Martin, J. M., 1989. Biogeochemical processes affecting arsenic species distribution in a permanently stratified lake. Environmental Science & Technology 23.10, 1258-1263.

Smedley, P. L., Kinniburgh, D. G., 2002. A review of the source, behaviour and distribution of arsenic in natural waters. Applied geochemistry 17.5, 517-568.

Snyder, G. T., Dickens, G. R., Castellini, D. G., 2007. Labile barite contents and dissolved barium concentrations on Blake Ridge: new perspectives on barium cycling above gas hydrate systems. Journal of Geochemical Exploration, 95.1, 48-65.

Sø, H. U., Postma, D., Jakobsen, R., Larsen, F., 2008. Sorption and desorption of arsenate and arsenite on calcite. Geochim. Cosmochim. Acta 72.24, 5871-5884.

Su, H.Y., Lee, J. S., Yu, S.C., 2002. Dopant effect on hokutolite crystals synthesized with hydrothermal process. Western Pacific Earth Sciences, 2.3, 301-318.

Takano, B., 1969. Effect of chlorocomplex of lead on the deposition of lead-bearing barite from hot spring water. Geochem. J. 3, 117-126.

Terada, Y., Goto, S., Takimoto, N., Takeshita, K., Yamazaki, H., Shimizu, Y.,

Takahashi, S., Ohashi, H., Furukawa, Y., Matsushita, T., Ohata, T., Ishizawa, Y., Uruga, T., Kitamura, H., Ishikawa, T., Hayakawa, S., 2004. Construction and Commissioning of BL37XU at SPring‐8. In SYNCHROTRON RADIATION INSTRUMENTATION: Eighth International Conference on Synchrotron Radiation Instrumentation, AIP Conf. Proc. 705, 376–379.

Tokunaga, K., Yokoyama, Y., Kawagucci, S., Sakaguchi, A., Terada, Y., Takahashi, Y., 2013a. Selenium coprecipitated with barite in marine sediments as a possible redox indicator. Chem. Lett. 42, 1068-1069.

Tokunaga, K., Yokoyama, Y., Takahashi, Y., 2013b. Estimation of Se(VI)/Se(IV) ratio in water by the ratio recorded in barite. Geochemistry, Geophysics, Geosystems 14, 4826-4834.

Torres, M. E., Bohrmann, G., Dubé, T. E., Poole, F. G., 2003. Formation of modern and Paleozoic stratiform barite at cold methane seeps on continental margins. Geology 31, 897-900.

Tsuno, H., Kagi, H., Takahashi,Y., Akagi, T., Nomura, M., 2003. Spontaneously induced reduction of trivalent ytterbium in synthesized crystal of calcite. Chem. Lett., 32, 500-501.

Van Beek, P, Reyss, J. L., Bonte, P., Schmidt, S., 2003. Sr/Ba in barite: a proxy of

barite preservation in marine sediments? Mar. Geol. 199, 205-220.

Yan, X. P., Kerrich, R., Hendry, M. J., 2000. Distribution of arsenic (III), arsenic (V) and total inorganic arsenic in porewaters from a thick till and clay-rich aquitard sequence, Saskatchewan, Canada. Geochim. Cosmochim. Acta 64, 2637-2648.

Yokoyama, Y., Tanaka, K., Takahashi, Y., 2012. Differences in the immobilization of arsenite and arsenate by calcite. Cosmochim. Acta, 91, 202–219.

Yokoyama, Y., Takahashi, Y., Miyoshi, Y., Ishibashi, J. I., Kawagucci, S., 2015. Sediment–Pore Water System Associated with Native Sulfur Formation at Jade Hydrothermal Field in Okinawa Trough. In *Subseafloor Biosphere Linked to Hydrothermal Systems* (pp. 405-419). Springer Japan.

Yoshiike, Y., 2003. Variation in the chemical composition of Obuki Spring, Tamagawa Hot Springs(1951-2000), Geochemical journal 37(6), 649-662.

Zhu, C., 2004. Coprecipitation in the barite isostructural family: 1. Binary mixing properties. Geochim. Cosmochim. Acta 68, 3327-3337.

Zhu, Y., Zhang, X., Xie, Q., Chen, Y., Wang, D., Liang, Y., Lu, J., 2005. Solubility and stability of barium arsenate and barium hydrogen arsenate at 25 ^{o}C. Journal of hazardous materials 120.1, 37-44.

Figure legends

Figure 1. E_h- pH diagrams for Ba-S-H_2O (a), As-H_2O (b), and Se-H_2O(c) at 25 °C and 1.0 bar calculated based on the Visual MINTEQ. The total dissolved concentrations of Ba, As, Se, and S used for the calculations were 270, 80, 140, and 2600 μg/L, respectively, which corresponded approximately to their concentrations in our experimental systems.

Figure 2. (a) As(III) and (b) As(V) speciation as a function of pH.

Figure 3. Normalized As K-edge XANES spectra of the reference materials ($KAsO_2$ and KH_2AsO_4) and As in barite at various pH.

Figure 4. Normalized As K-edge XANES spectra of the reference materials ($KAsO_2$ and KH_2AsO_4) and As in barite at pH 2.0 (a) and pH 11.0 (b) as a function of R_w^{III} (= [As(III)]/[total As]).

Figure 5. Relationship between R_w^{III} and R_w^{III}.

Figure 6. Apparent distribution coefficient of As(III) and As(V), and its partition ratio ($=K_{As(III)}/K_{As(V)}$) at various pH.

Figure 7. E_h-pH diagrams for As-H_2O (a) and Se-H_2O (b) at 25 °C (black line) and 60 °C (red line).

Figure 8. Normalized As K-edge (a) and Se K-edge (b) XANES spectra of the

reference materials ((a) $KAsO_2$ and KH_2AsO_4; (b) $BaSeO_3$ and $BaSeO_4$) and As and Se in barite at 25 °C and 60 °C.

Figure 9. Micro-XRF images of barite samples in Tamagawa Hot Spring (a–d) and Okinawa Hydrothermal samples (e–h). (a and e), (b and f), (c and g), and (d and h) are the μ-XRF images of Ba, As, Se, and Fe, respectively. Small circles on (a), (b), (e), and (f) show the measured points by μ-XANES as spots 1 and 2, respectively. X-ray beam size: 0.5×0.5 μm^2; Step size: 2.0 μm; Measurement time: 0.1 s/point. Incident X-ray: 12.8 keV.

Figure 10. Normalized As K-edge XANES of As reference materials ($KAsO_2$ and KH_2AsVO_4), As in barite at pH 2.0 added as As(III) or As(V) at ba-1 or ba-5 and As in natural barite at spots 1 and 2. The vertical dashed lines indicate the absorption peaks of $KAsO_2$ and KH_2AsVO_4.

Figure 11. E_h-pH range estimated in this study for the sediment sample collected in the Okinawa hydrothermal vent. The boundaries showed the redox boundaries of Se(VI)/Se(IV), As(V)/As(III), and S(0)/S(-II) (Fig. 1). The circle shows the E_h and pH conditions estimated for the pore water in the sediment (E_h = 150 mV; pH 7.1). The yellow range represents the E_h-pH area, which was estimated by the Se(VI)/Se(IV) and As(V)/As(III) ratios in this barite sample by μ-XANES

analysis.

Table 1. Analysis of apparent K_d values and oxidation states of As(III) and As(V)

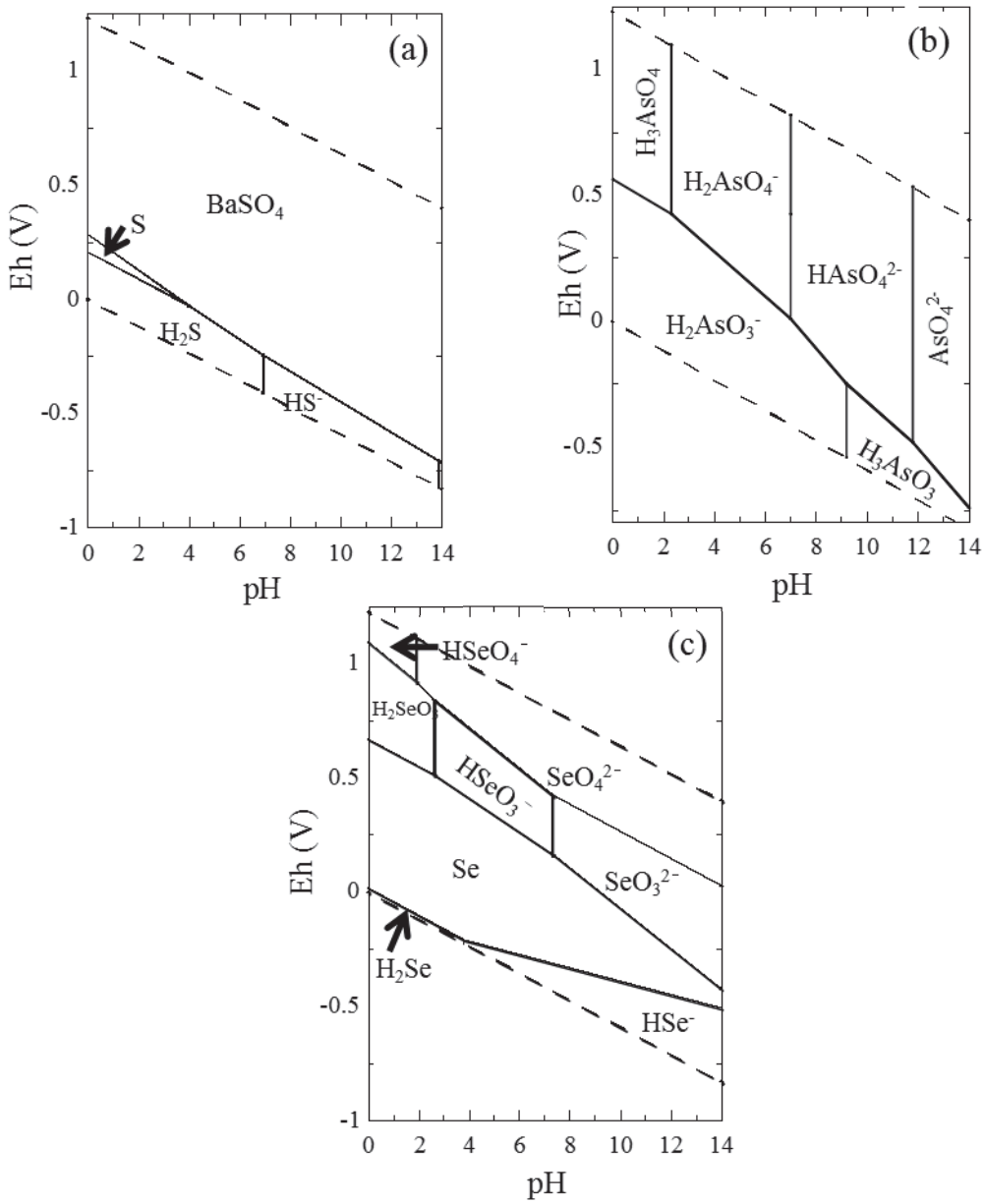

Figure 1. E_h- pH diagrams for Ba-S-H_2O (a), As-H_2O (b), and Se-H_2O(c) at 25 °C and 1.0 bar calculated based on the Visual MINTEQ. The total dissolved concentrations of Ba, As, Se, and S used for the calculations were 270, 80, 140, and 2600 μg/L, respectively, which corresponded approximately to their concentrations in our experimental systems.

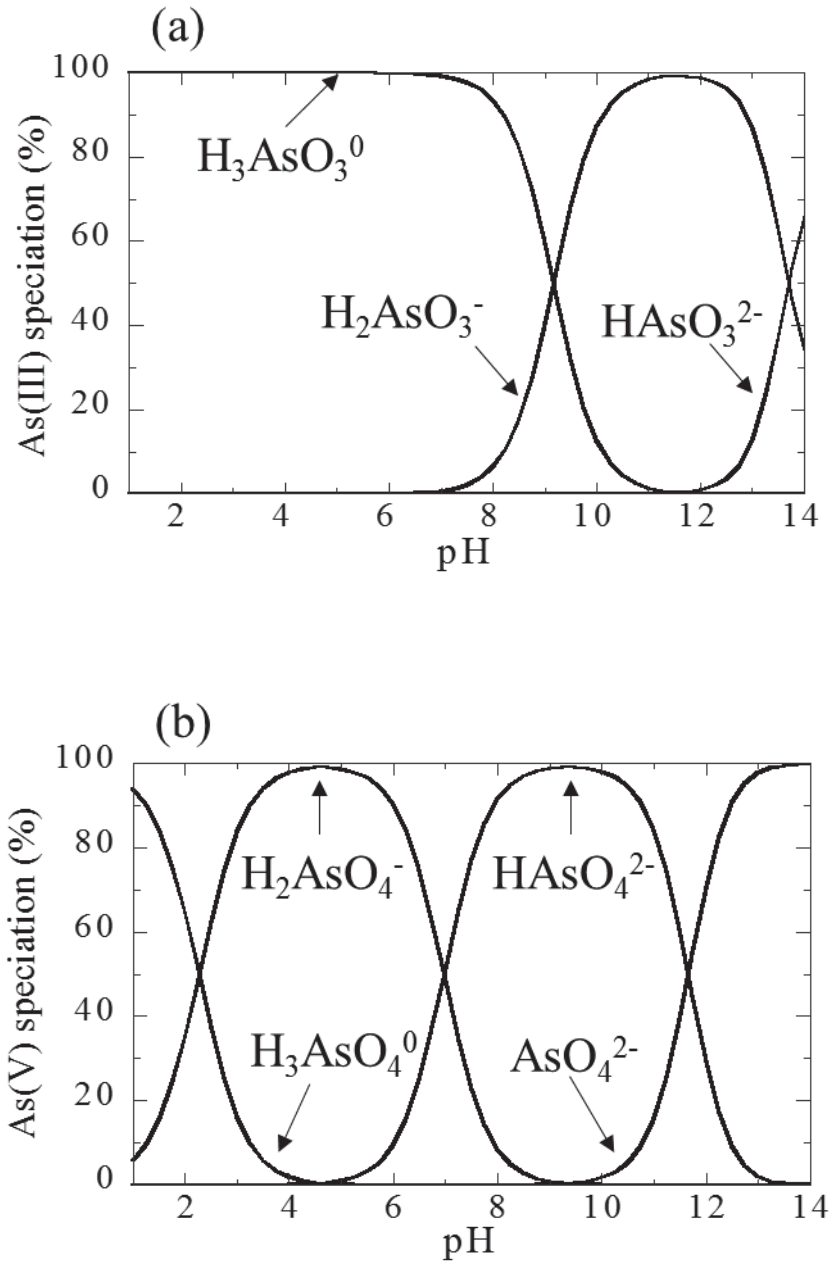

Figure 2. (a) As(III) and (b) As(V) speciation as a function of pH.

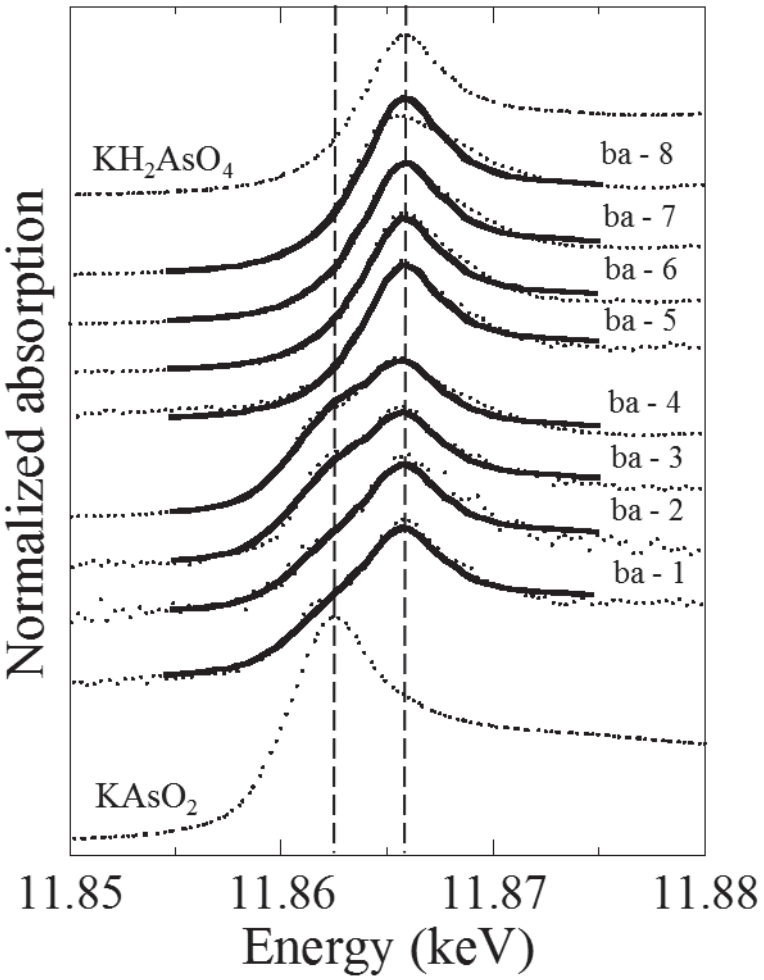

Figure 3. Normalized As K-edge XANES spectra of the reference materials ($KAsO_2$ and KH_2AsO_4) and As in barite at various pH.

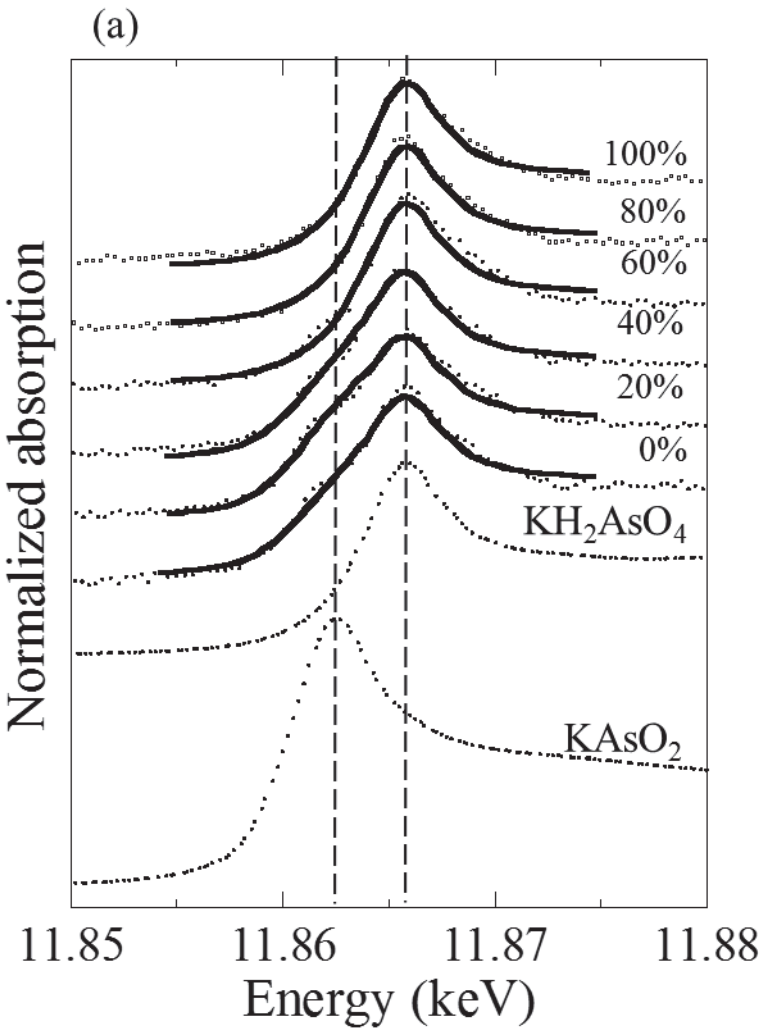

Figure 4. Normalized As K-edge XANES spectra of the reference materials ($KAsO_2$ and KH_2AsO_4) and As in barite at pH 2.0 (a) and pH 11.0 (b) as a function of R_w^{III} (= [As(III)]/[total As]).

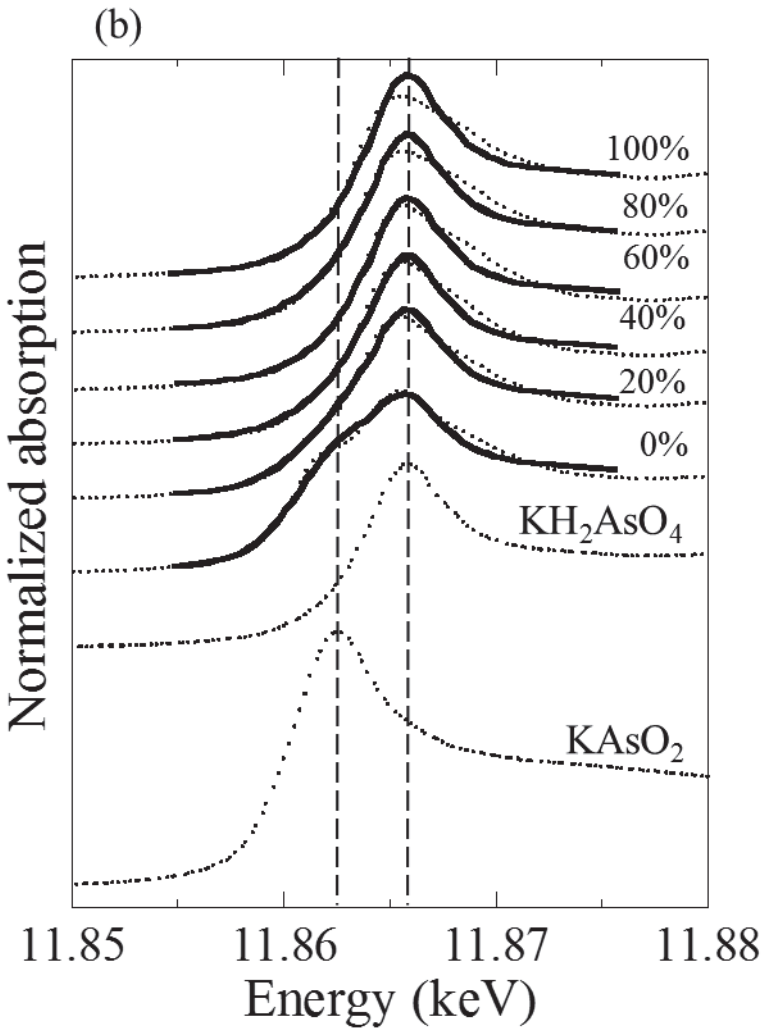

Figure 4. Normalized As K-edge XANES spectra of the reference materials ($KAsO_2$ and KH_2AsO_4) and As in barite at pH 2.0 (a) and pH 11.0 (b) as a function of R_w^{III} (= [As(III)]/[total As]).

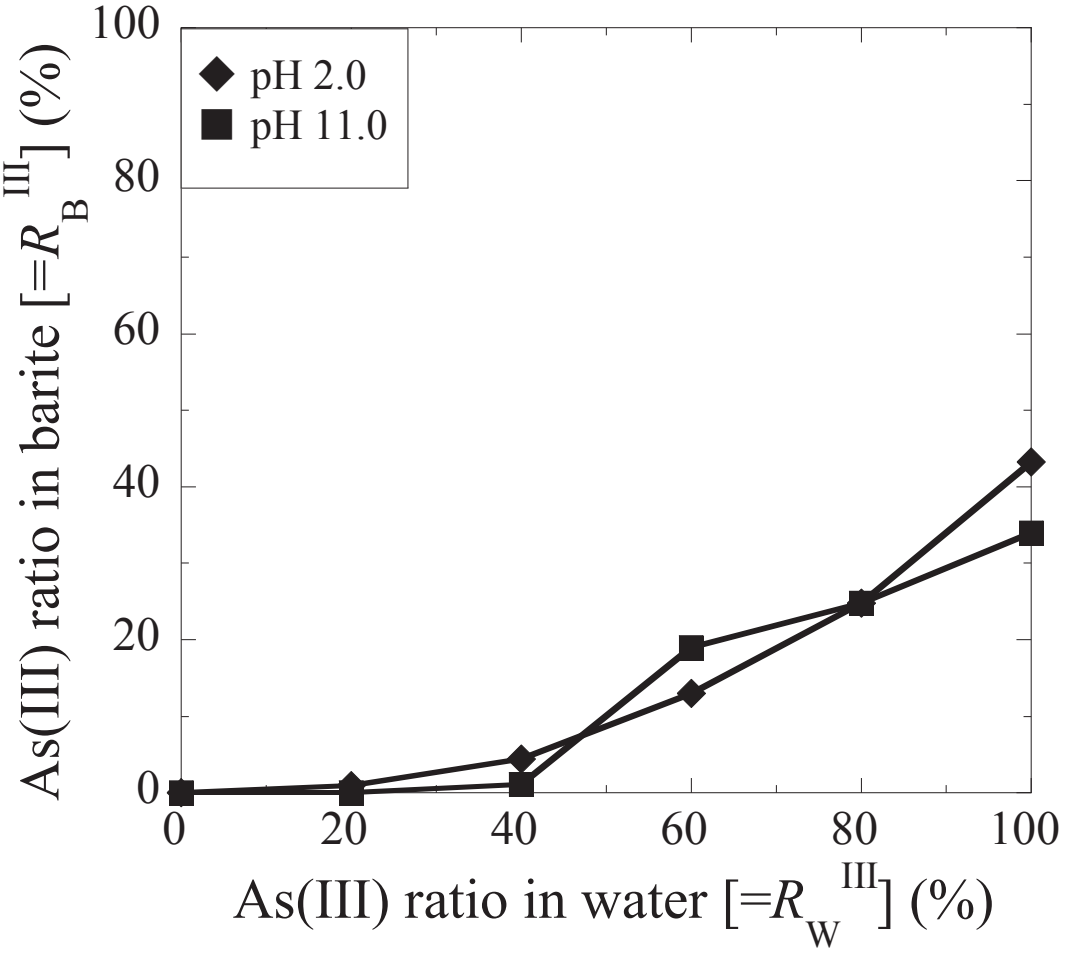

Figure 5. Relationship between R_w^{III} and R_w^{III}.

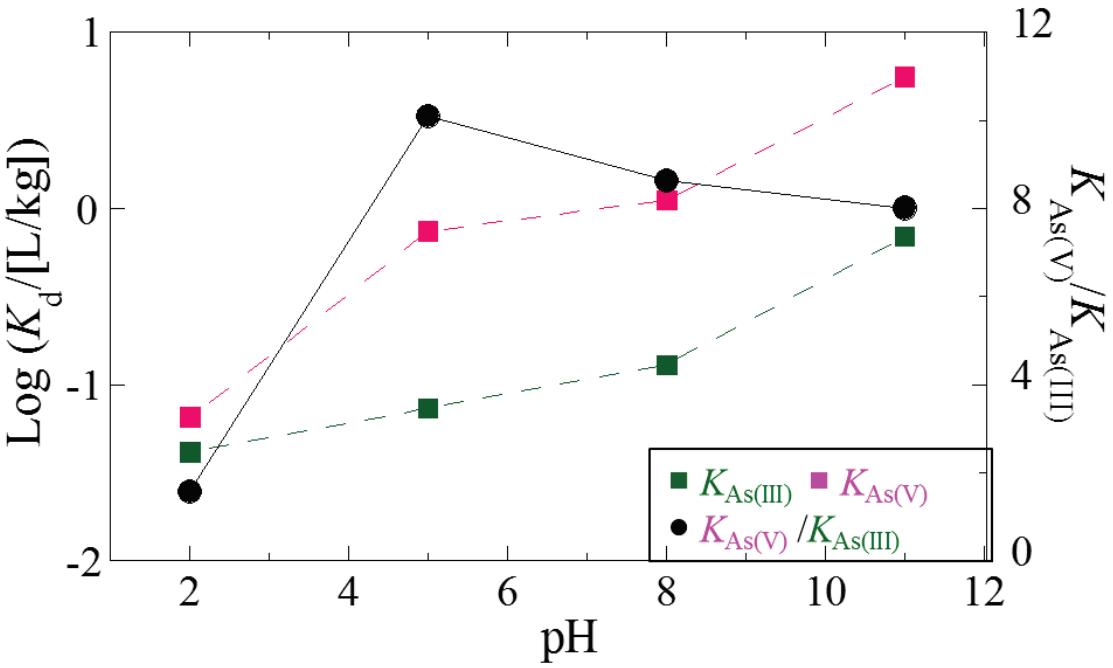

Figure 6. Apparent distribution coefficient of As(III) and As(V), and its partition ratio (=$K_{As(III)}/K_{As(V)}$) at various pH.

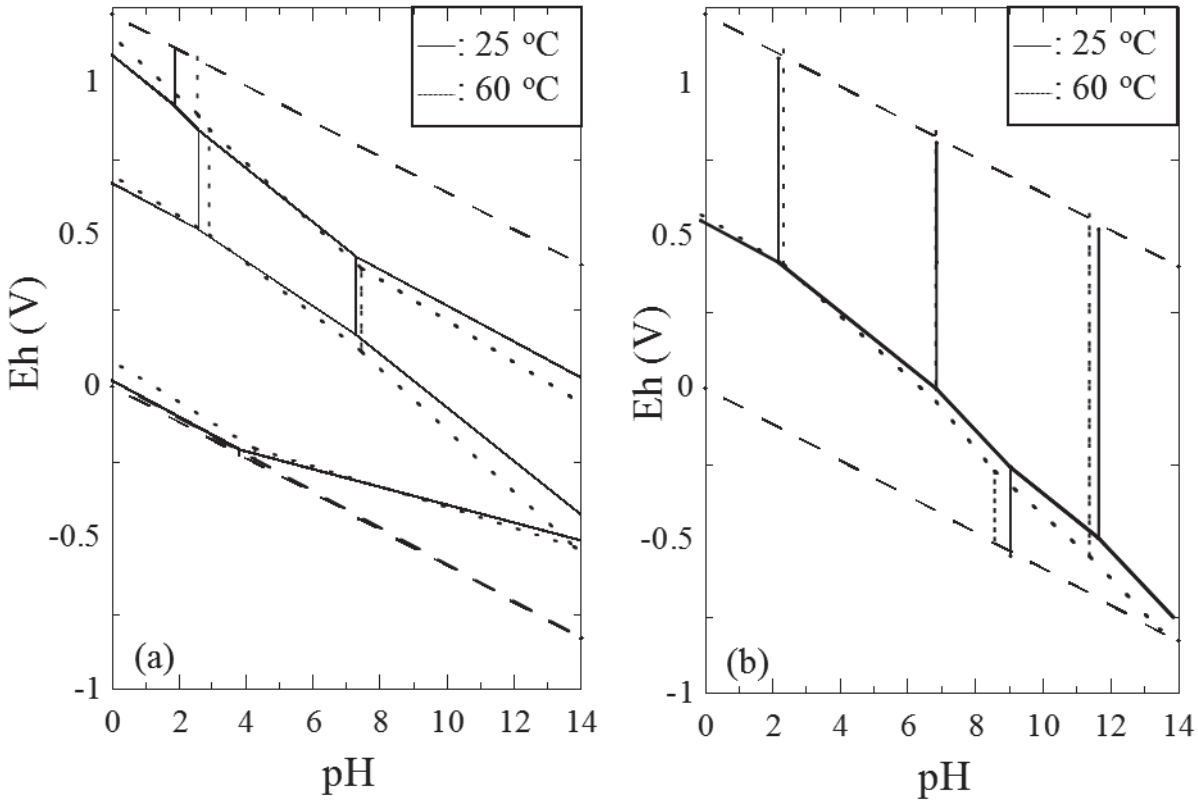

Figure 7. E_h-pH diagrams for As-H_2O (a) and Se-H_2O (b) at 25 °C (black line) and 60 °C (dotted line).

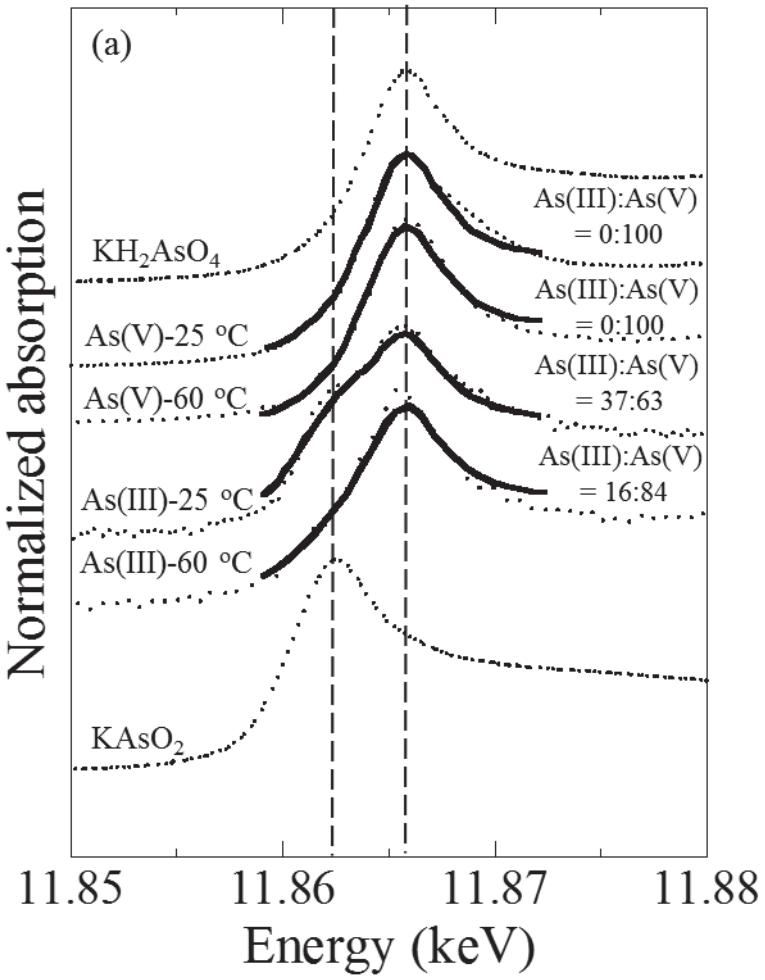

Figure 8. Normalized As K-edge (a) and Se K-edge (b) XANES spectra of the reference materials ((a) $KAsO_2$ and KH_2AsO_4; (b) $BaSeO_3$ and $BaSeO_4$) and As and Se in barite at 25 °C and 60 °C.

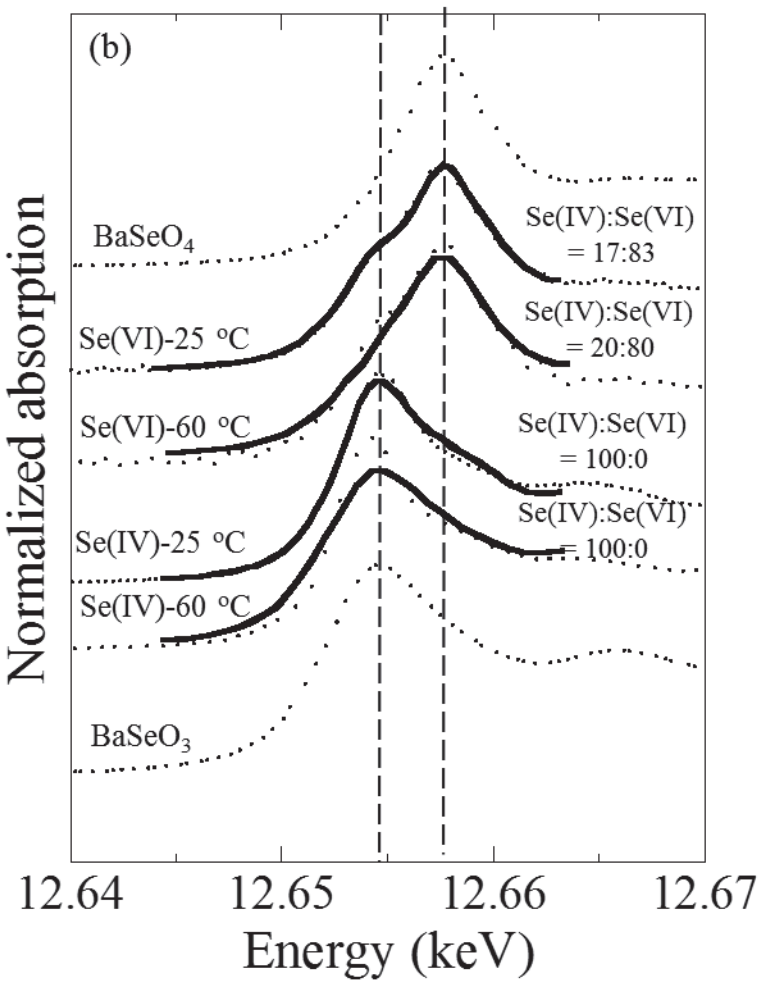

Figure 8. Normalized As K-edge (a) and Se K-edge (b) XANES spectra of the reference materials ((a) $KAsO_2$ and KH_2AsO_4; (b) $BaSeO_3$ and $BaSeO_4$) and As and Se in barite at 25 °C and 60 °C.

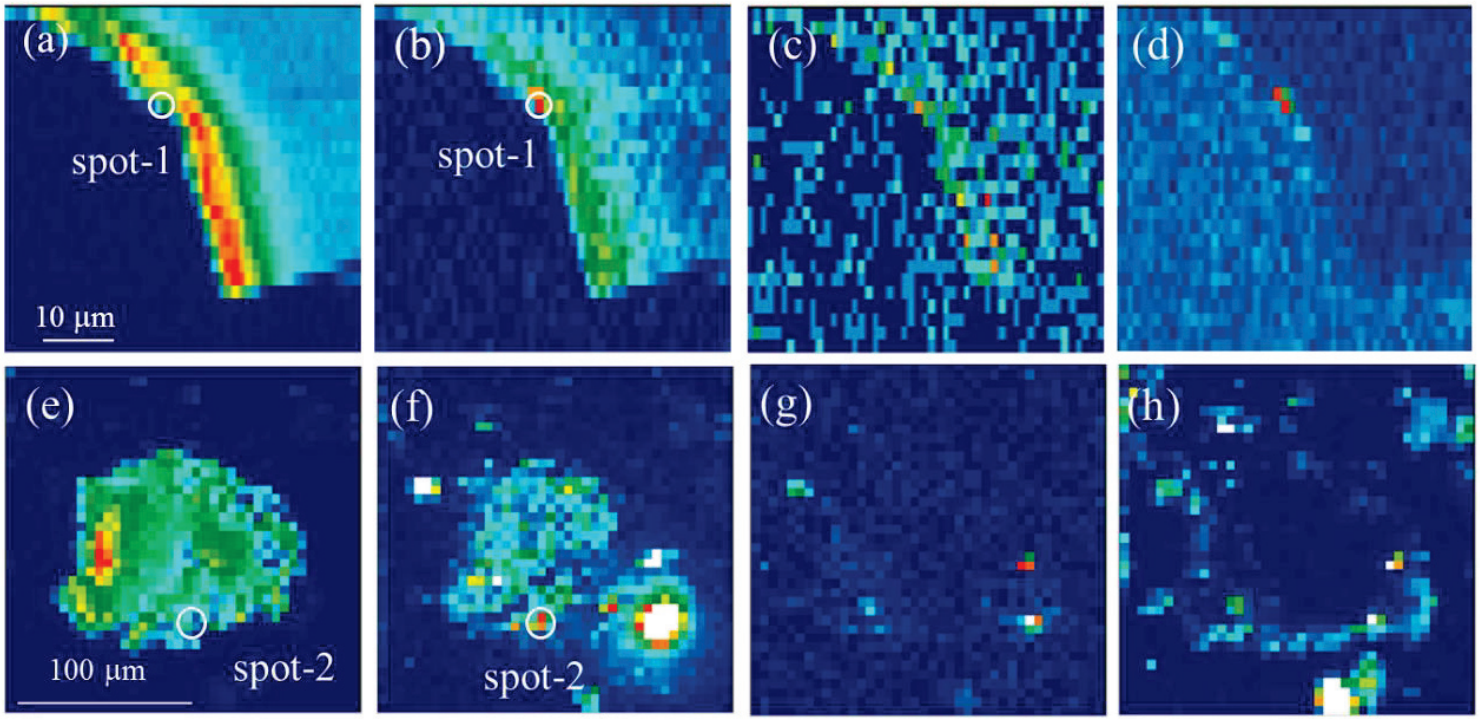

Figure 9. Micro-XRF images of barite samples in Tamagawa Hot Spring (a–d) and Okinawa Hydrothermal samples (e–h). (a and e), (b and f), (c and g), and (d and h) are the μ-XRF images of Ba, As, Se, and Fe, respectively. Small circles on (a), (b), (e), and (f) show the measured points by μ-XANES as spots 1 and 2, respectively. X-ray beam size: 0.5×0.5 μm^2; Step size: 2.0 μm; Measurement time: 0.1 s/point. Incident X-ray: 12.8 keV.

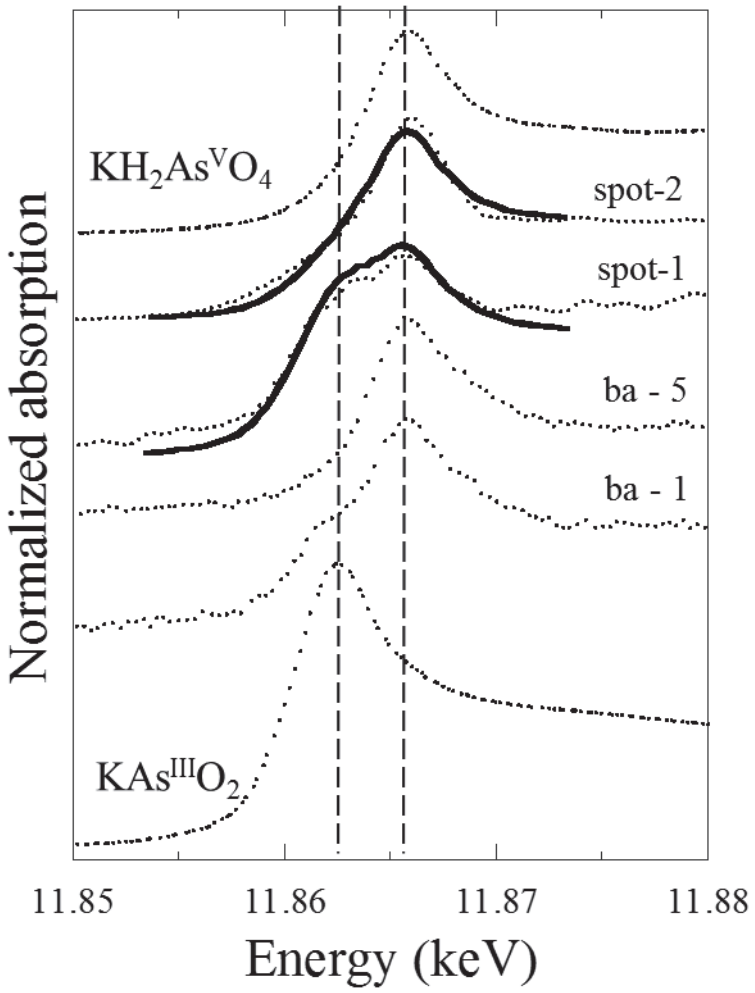

Figure 10. Normalized As K-edge XANES of As reference materials ($KAsO_2$ and KH_2AsVO_4), As in barite at pH 2.0 added as As(III) or As(V) at ba-1 or ba-5 and As in natural barite at spots 1 and 2. The vertical dashed lines indicate the absorption peaks of $KAsO_2$ and KH_2AsVO_4.

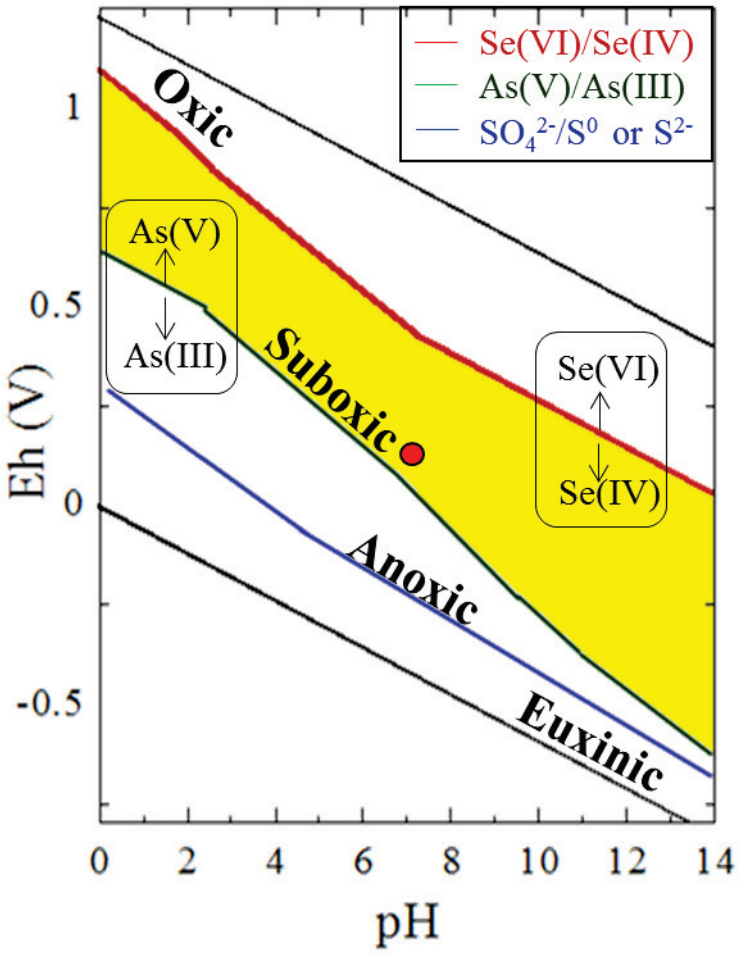

Figure 11. E_h-pH range estimated in this study for the sediment sample collected in the Okinawa hydrothermal vent. The boundaries showed the redox boundaries of Se(VI)/Se(IV), As(V)/As(III), and S(0)/S(-II) (Fig. 1). The circle shows the E_h and pH conditions estimated for the pore water in the sediment (E_h = 150 mV; pH 7.1). The yellow range represents the E_h-pH area, which was estimated by the Se(VI)/Se(IV) and As(V)/As(III) ratios in this barite sample by μ-XANES analysis.

Table 1. Analysis of apparent K_d values and oxidation states of As(III) and As(V)

Run. No	As in input solution				As in barite					
	pH	R_W^V [%]	Conc. [mg/L]	SI of barite	Conc. [mg/L]	R_B^{III} [%]	R_B^V [%]	K_d [L/kg]	$K_{As(III)}$ [L/kg]	$K_{As(V)}$ [L/kg]
ba-1	2	0	63.21	4.21	4.93	34.0	66.0	0.078	0.027	
ba-2	5	0	65.15	4.21	8.53	37.1	63.0	0.131	0.049	
ba-3	8	0	66.67	4.21	14.63	40.1	59.9	0.219	0.088	
ba-4	11	0	67.42	4.21	75.82	43.2	56.8	1.125	0.486	
ba-5	2	100	75.18	4.21	4.89	0	100	0.065		0.065
ba-6	5	100	79.44	4.21	58.78	0	100	0.740		0.740
ba-7	8	100	77.51	4.21	86.62	0	100	1.118		1.118
ba-8	11	100		4.21	437.84	0	100	5.582		5.582

4. Effective removal of selenite and selenate from solution by barite

1. Chapter Introduction

Selenium (Se) is generally a trace element in nature, which occurs in the environment by anthropogenic activities such as mining and combustion of fossil fuels. It is known as an essential but also a potential toxic element for organisms depending on its concentration and chemical form in solution (e.g., 0.05 ppm in the United States and 0.01 ppm in Japan for drinking water limits) and it has a long half-life (about 10^5 years) with high mobility within the eco-environmental system. In the nature, Se exists as four different oxidation state in aqueous (+4, +6) and dissolved as oxyanion (Selenite: $Se^{IV}O_3^{2-}$, Selenate: $Se^{VI}O_4^{2-}$) with high solubility and mobility in aquatic environment under oxic conditions. The fate and transport of Se in contaminated sites are very influenced by its chemical form and speciation, which showed that Se(IV) is strongly adsorbed by soils while Se(VI) is only weakly adsorbed and leached easily [Goh, 2004].

Several techniques can be used to reduce the level of Se from aqueous media such as ion exchange, coprecipitation, bioremediation, chelation, and adsorption to effectively remove Se from wastewater [Kozai et al., 2002; Gezer et al., 2011]. Although ion exchange resins are available for selective separation of Se(IV) or Se(VI), an increase in concentration of sulfate ion in solution significantly reduces an adsorption ability for the

ion exchange separation [Nishimura et al., 2007; Bleiman and Mishael, 2010]. In this study, we designed and characterized methods using barite ($BaSO_4$) and analyzed their efficiencies in adsorbing and incorporating Se(IV) and Se(VI). Barite is a common phase in many geological environments, and can be used to remove toxic and/or radioactive elements from polluted waters. Previous studies also showed the effectiveness of barite as a sequestering phase for some divalent cations (Sr^{2+}, Pb^{2+}, Ra^{2+}) and oxyanions (CrO_4^{2-}, SeO_4^{2-}) [Prieto et al., 2002; Bosbach et al., 2010; Rosenberg et al., 2011a; Rosenberg et al., 2011b; Prieto et al., 2013; Nishimura et al., 2007; Widanagamage et al., 2014; Zhang et al., 2014]. The characteristics of barite is shown Fig. 1, which exhibits (i) extremely low the solubility (ca 10^{-10} at 25 °C, 1 atm; Church and Wolgemuth, 1972), (ii) incorporation of many elements because of the large ionic radii as replaced ions (Ba^{2+} 1.68 Å; SO_4^{2-} 1.48 Å), (iii) high density compared with other mineral (barite 4.5 g/cm^3; calcite 2.7 g/cm^3), and (iv) high crystal stability under wide range of pH, E_h, temperature, and presser conditions. Thus, due to its high crystal stability, barite might also work as a barriers for the retention of radioactive elements. The formation of barite is caused by the mixing of Ba^{2+} and SO_4^{2-} ion, which suggests that the uptake of Se by barite may not be affected by sulfate ion in solution as a competition anion compared to other minerals.

The aim of this chapter is to examine and compare the adsorption and coprecipitation capacities with barite for effective removal of Se(IV) and Se(VI) from contaminated solution. Although the rate of immobilization relies on numerous factors, the critical factor is (i) the charge of the ions relative to the charge of the site and (ii) the size of the ions relative to the substitution site [Blundy and Wood, 2003]. In this chapter, two factors were mainly investigated: one is (i) the stability of the surface complex between surface barium and aqueous speciation (= chemical affinity), and the other is (ii) the stability of the substituting ion in lattice site (= structural affinity). The uptake of Se(IV) and Se(VI) by barite was investigated through a series of batch experiments in barite-equilibrated solutions. The solutions covered a broad range of factors (i) such as pH, ionic strength, and competitive ion, and factors (ii) such as saturation states and sulfate concentration. This study is to understand the factors controlling the distribution of Se(IV) and Se(VI) between barite and water, and we can effectively remove Se(IV) and Se(VI) from solution based on the mechanisms.

2. Methods

2.1. Experiment procedure

In the present studies, Se(IV) and Se(VI) stock solutions were prepared from $NaHSeO_3$ and Na_2SeO_4 (Wako, Japan), respectively. Barite was precipitated from a mixture of (i) Na_2SO_4 solution and (ii) $BaCl_2 \cdot 2H_2O$ solution [Blount, 1974]. Right before the addition of the $BaCl_2 \cdot 2H_2O$ solution, Se(IV) or Se(VI) were added to the sulfate solution. The experimental conditions of pH, saturation states (defined as $SI = \log(IAP/K_{sp})$), barium and sulfate concentration are fixed at pH 8.0, SI 4.2, Ba^{2+} 0.65 mM, and SO_4^{2-} 27 mM, as a standard condition, and one of the parameters was changed depending on the experiment type.

The precipitates of barite and the aqueous phase were separated by filtration with a 0.20 μm membrane filter (mixed cellulose ester, Advantec, Tokyo, Japan) and then rinsed three times with Milli-Q water. The X-ray diffraction (XRD) patterns of the precipitates were measured using a powder X-ray diffractometer (MultiFlex, Rigaku Co., Tokyo, Japan), in which the mineral phase was identified by comparing the XRD patterns to the International Center for Diffraction Data file. Total Se concentrations in the solution and solids were analyzed by ICP-MS (7700cs, Agilent, Tokyo, Japan) after dilution by 2 wt.% HNO_3 solution. A part of the solid sample was dried in an oven at 60 °C and

dissolved into water by adding sodium carbonate [Breit et al., 1985] to determine the Se concentration in the precipitates. The distribution coefficient of Se between barite and water was calculated based on the Se concentration in the water and solid phase. The local structure of Se in the precipitates after filtration without drying were determined by Se K-edge X-ray absorption fine structure (XAFS). A portion of the precipitate was immediately packed into an airtight polyethylene bag and stored at 4 °C until XAFS measurement. The drying process was not conducted to avoid altering the Se(VI)/Se(IV) ratio in barite.

2.2. Experiment producer of each conditions

2.2.1. Effect of pH

The effect of pH on the adsorption/coprecipitation of Se(IV) and Se(VI) was evaluated using 80 ppm Se solutions. The starting solution pH was initially adjusted with HCl and NaOH solutions. Batch experiments were conducted under different pH conditions (pH=2.0, 4.0, 6.0, 8.0, 10.0) and fixed saturation states and sulfate concentration (SI 4.2, SO_4^{2-} 27 mM). The pH values were determined to consider the effect of variation of Se species with pH: (i) Se(IV) is mainly dissolved as H_2SeO_3 (pH 2.0), $HSeO_3^-$ from pH 2.0 to pH 8.0, and SeO_3^{2-} over pH 8.0, whereas (ii) Se(VI) is mainly dissolved as $HSeO_4^-$ (pH 2.0), SeO_4^{2-} from pH 4.0 to pH 10.0 (Fig. 2). The solution compositions are MilliQ water (ionic strength (I) = 0.076; 54 mM Na^+, 27mM SO_4^{2-}, 2.2 mM CO_3^{2-}) and artificial seawater (ASW) (I = 0.534; 440 mM Na^+, 50 mM Mg^{2+}, 9.6 mM Ca^{2+}, 440 mM Cl^-, 27 mM SO_4^{2-}, 2.2 mM CO_3^{2-}).

2.2.2. Effect of ionic strength

The effect of the starting solution ionic strength (I) on the adsorption/coprecipitation of Se(IV) and Se(VI) was evaluated using 80 ppm Se solutions. The starting solution I was initially adjusted with NaCl concentration. Batch experiments were conducted at

different ionic strengths at I = 0.08, 0.15, 0.32, 0.52 M and at fixed pH, saturation states, sulfate concentration, and solution compositions (pH 8.0, SI 4.2, 27 mM SO_4^{2-}, MilliQ water).

2.2.3. Effect of competitive ion

The effect of the competitive ions on the coprecipitation of Se(IV) and Se(VI) was evaluated using 80 ppm Se solutions. Batch experiments were conducted at different concentrations of competitive ions (Mg^{2+}, Ca^{2+} 0.01~10 mM) and at fixed pH, saturation states, sulfate concentration, and solution compositions (pH 8.0, SI 4.2, 27 mM SO_4^{2-}, MilliQ water).

2.2.4. Effect of saturation states of barite

The effect of the saturation states on the adsorption/coprecipitation of Se(IV) and Se(VI) was evaluated using 8 and 80 ppm Se solutions. The saturation states of barite in the initial solution were adjusted with initial barium solution. Batch experiments were conducted under different saturation states (SI=2.9, 3.2, 3.5, 3.8, 4.2, 4.8) and at fixed pH, saturation states, sulfate concentration (pH 8.0, SI 4.2, 27 mM SO_4^{2-}, MilliQ water and ASW).

2.2.5. Effect of host- and substituted-ion ratios

The effect of the host- and substituted-ion ratios (sulfate/Se-oxyanion) on the coprecipitation of Se(IV) and Se(VI) was evaluated using 80 ppm Se solutions. The saturation states of barite in the initial solution were fixed at 4.2, thus barium concentration are also changed as a function of sulfate concentrations. Batch experiments were conducted under different barium and sulfate concentration (Ba^{2+} 0.67~6.40 mM;SO_4^{2-} 1~27 mM) and at fixed pH, saturation states, and solution compositions (pH 8.0, SI 4.2, 27 mM SO_4^{2-}, MilliQ water).

3. Results and discussion

3.1. Effect of chemical affinity

In this chapter, the effects of chemical affinity on the adsorption/coprecipitation of Se(IV) and Se(VI) with barite were investigated in term of solution composition changes. The solutions covered a broad range of pH, ionic strength, and concentrations of cations and at fixed saturation states and sulfate/Se-oxyanion ratios.

3.1.1. Effect of electrostatics by pH

Batch experiments were conducted under different pH conditions (pH=2.0, 4.0, 6.0, 8.0, 10.0) to understand what pH values affect the partition coefficients of Se(IV) and Se(VI) between barite and water. The adsorption and coprecipitation of Se(IV) and Se(VI) with barite as a function of pH is shown in Fig. 3 (Table 1). The adsorption of Se(IV) continued to increase up to 106 mg/kg when the pH values increased from 2.0 to 11.0. However, the adsorption of Se(VI) were constant regardless of pH values. It was found that barite had greater adsorption of Se(IV) than that of Se(VI) from pH 2.0 to 11.0. The uptake of Se(IV) and Se(VI) during coprecipitation with barite also showed similar trend with adsorption although the uptakes in structure during coprecipitation were relatively higher compared with their adsorption on surface.

The distribution difference between Se(IV) and Se(VI) in the adsorption/coprecipitation showed evidence of chemical affinity related to their speciation change. Previous studies showed that the distribution of Se(IV) on minerals was larger than that of Se(VI) because of the larger complexation stability of Se(IV) than that of Se(VI) when a same charge species [Goh and Lim, 2004]. Thus, in the pH range from 4.0 to 11.0, Se(IV) was strongly adsorbed and incorporated with barite compared with Se(VI) because both species are dissolved with same charge as divalent anion (Se(IV) $HSeO_3^-$ and SeO_3^{2-}; Se(VI) SeO_4^{2-}) (Fig. 2). In addition, because the ratio of SeO_3^{2-} to $HSeO_3^-$ continued to increase from pH 5.0 to pH 10.0 (Fig. 2), the degree of Se(IV) adsorption and coprecipitation was also increased. At pH 2.0, the uptake of Se(IV) and Se(VI) by barite were almost identical because Se(IV) is mainly dissolved as a weakly negatively-charged monovalent ($HSeO_3^-$) species than Se(VI) as divalent species. The uptakes of Se(IV) and Se(VI) during coprecipitation with barite were also dependent on the speciation by pH and showed no significant difference with adsorption experiments, which indicates that the uptake of Se(IV) and Se(VI) by barite are mainly controlled by adsorption site on surface rather than substitution site in crystal lattice. Thus, the uptakes of Se(IV) and Se(VI) in barite are mainly controlled by chemical affinity related to the electrostatic repulsion between dissolved ion and the

charged surfaces site, and we can efficiently remove Se(IV) from solutions by coprecipitation with barite under higher pH conditions.

3.1.2. Effect of ionic strength

The degree of uptake Se(IV) and Se(VI) during coprecipitation with barite showed significant difference depending on solution compositions (MilliQ water and ASW) (Fig. 4 and Table 2). It was found that coprecipitations of Se(IV) and Se(VI) with barite under ASW were relatively higher compared to MilliQ water, and the uptake under ASW was about 16 time as high as MilliQ water ,especially for Se(IV) at pH 8.0. The cause of greater coprecipitation under ASW was believed to be due to the different solution compositions by ionic strength (MilliQ water I = 0.076 M; ASW I=0.534 M) and competition (MilliQ water 54 mM Na^{+}, 0 mM Mg^{2+}, 0 mM Ca^{2+}; ASW 440 mM Na^{+}, 50 mM Mg^{2+}, 9.6 mM Ca^{2+}).

In this session, the effect of ionic strength on adsorption and coprecipitation with barite is investigated. Batch experiments were conducted at different ionic strengths at I = 0.08, 0.15, 0.32, 0.52 M to understand the magnitude of effect of ionic strength on the partition coefficients of Se(IV) and Se(VI) between barite and water. The results showed that the amounts of adsorbed Se(IV) and Se(VI) were relatively unaffected by

changes in ionic strength (Fig. 5). Change of ionic strength by one order of magnitude (0.05 to 0.6 M) had little effect on the adsorption of Se(IV) and Se(VI) on barite, and it could be due to the strong specific binding mechanism as an inner-sphere complex between Se(IV) or Se(IV) and barite. The effect of ionic strength on the anion partitioning can be explained to distinguish between inner-sphere and outer-sphere anion surface complexes (Hayes and Leckie, 1988; Sø et al., 2008). Hayes and Leckie (1988) showed that the adsorption of Se(IV) on hydrous ferric oxide (HFO) was little influenced by ionic strength because Se(IV) forms an inner-sphere complex, while that of Se(VI) is markedly decreased by increasing ionic strength because Se(VI) forms an outer-sphere complex. These results are consistent with the Se(IV) and Se(VI) adsorption structure on barite by EXAFS analysis: the Se-Ba shell observed at 3.02 Å shows an evidence of strong bond with barite as an inner-sphere complex (Fig. 6 and Table 3). The uptakes of Se(IV) and Se(VI) during coprecipitation with barite showed no significant difference with adsorption experiments, which indicates the independence of ionic strength on its partitions to barite. Thus, the greater distribution of Se(IV) and Se(VI) under ASW was not due to the ionic strength difference between MilliQ water and ASW.

The adsorption and coprecipitation of As(III) and As(V) with barite as a function of ionic strength is also shown in Fig. 7. The adsorption of As(V) on barite was not

affected by the ionic strength for strong specific binding mechanism as an inner-sphere complex between As(V) and barite, while that of As(III) decreased with increasing ionic strength because As(III) might form weak bond as an outer-sphere complex with barite. Thus, the degree of adsorbed oxyanions by barite as a function of ionic strength was dependent on the chemical affinity related to the complexation speciation with barite.

3.1.3. Effect of competitive ions

Artificial seawater has larger amount of Na^{+}, Mg^{2+}, and Ca^{2+} cations compared with MilliQ water. In this session, the effect of competitive ion on the coprecipitation of Se(IV) and Se(VI) with barite is investigated. Batch experiments were conducted at different cation concentrations to understand the effect of competitive ion on the partition coefficients of Se(IV) and Se(VI) between barite and water. In chapter 2, it is shown that the amount of anions in barite increases in the presence of cation in solution due to the larger distortion of crystal lattice in barite structure by cation substitution.

The distribution coefficient values of Se(IV) and Se(VI) in barite as a function of cation concentrations are shown in Fig. 8 (Table 4). The results showed that the uptakes of Se(IV) and Se(VI) by barite were strongly increased in the presence of Ca^{2+} in solution. The presence of Na^{+} and Mg^{2+} in solution, on the other hand, had little effect on its

partitions of Se(IV) and Se(IV) to barite. Thus, the greater coprecipitation of Se(IV) and Se(VI) with barite under ASW was dependent on the Ca^{2+} in solution, and we can efficiently remove Se(IV) and Se(VI) from solutions by coprecipitation with barite in addition to the high Ca^{2+} concentration in the solutions. These results, however, could not be explained only by chemical affinity related to the aqueous metal speciation, because Se(IV) and Se(VI) were not formed the surface complexes with Ca^{2+} ion. The cause of greater coprecipitation with Ca^{2+} might be attributed to the unit-cell dimensions change in terms of structural affinity discussed in session 3.2.

3.2. Effect of substitution site in barite

In this session, the effects of structural affinity on the adsorption/coprecipitation of Se(IV) and Se(VI) with barite were investigated in terms of substitution site of crystal lattice in barite structure. The solutions covered a broad range of saturation states and sulfate/Se-oxyanion ratio, at fixed pH and ionic strength.

3.2.1. Effect of saturation states of barite

Batch experiments were conducted under various precipitation rates to understand the effect of precipitation rate on the partition coefficients of Se(IV) and Se(VI) between barite and aqueous solution. Previous studies been experimentally studied the effect of precipitation rate on partition coefficients of divalent metals to calcite [Lorens, 1981; Tesoriero and Pankow, 1996; Lakshtanov and Stipp, 2004]. Generally, it was found that the tracer's partition coefficient falls to its equilibrium value when the lower the precipitation rate of the host mineral. Thus, increasing precipitation rate enriches the host mineral with the tracer if its equilibrium partition coefficient, $K_d < 1$, and depletes the host when $K_d > 1$. Previous studies showed that the precipitation rate was proportional to the degree of saturation states in solution [Lorens, 1981; Tesoriero and Pankow, 1996]. Thus, the saturation states of barite in the initial solution were changed

(SI = 2.9, 3.2, 3.5, 3.8, 4.2, 4.8), and the apparent distribution coefficient values of Se(IV) and Se(VI) were calculated to understand incorporation mechanism controlled by the different structural geometry between substituent and host phase ions. Moreover, the changes of the unit-cell parameter as a function of saturation states were also determined to understand the distortion of host lattice itself by saturation states.

The adsorption and coprecipitation of Se(IV) and Se(VI) on/in barite as a function of saturation states are shown in Fig. 9. The adsorption of Se(IV) and Se(VI) on barite surface remained constant as a function of saturation states. The uptake of Se during coprecipitation with barite, on the other hand, showed the different trend between Se(IV) and Se(VI): (i) the coprecipitation of Se(VI) with barite continued to increase significantly from 821 mg/kg to 18287 mg/kg with decreasing saturation states, while (ii) that of Se(IV) were constant regardless of the saturation states. The unit-cell parameters of non-substituted condition as a function of saturation states are listed in Table 5. The unit-cell parameter of barite showed little change in the b- and c-parameters but slightly differences in the a-parameter as shown in Chapter 2 (Fig. 10). The a-parameter of non-substituted barite changed linearly with an increase in saturation states, which showed evidence of structure affinity related to the lattice distortion of the host mineral. The change of a-parameter of non-substituted condition also show similar trend between

solution compositions although ASW caused a large distortion than the MilliQ water.

The distribution coefficient values of Se(IV) and Se(VI) and unit-cell dimensions of a-axis (=k_a value) as a function of saturation states are shown in Fig. 11. The results showed that (i) barite structure became distorted along the crystallographic a-axis by degrees of saturation states, (ii) the adsorption of Se(IV) and Se(VI) on barite surface was constant regardless of saturation states values, and (iii) the uptake of Se(VI) during coprecipitation with barite was dependent on saturation states while that of Se(IV) with barite was independent. The distribution difference between adsorption and coprecipitation showed an evidence of structural affinity related to the substitution difference of incorporation ions between surface- and lattice-site. The transfer of ions from the solution to the surface layer during adsorption results in the electrostatic repulsion between dissolved ion and the charged surfaces site as shown in section 3.1. The uptake of ions from the surface layer to lattice in crystal during coprecipitation, on the other hand, results in the effect of lattice strain created by the radius difference between substituent and host phase ions [Yifeng and Huifang, 2001; Blundy and Wood, 2003]. The change of saturation states leads to a larger distortion of the lattice in barite crystal rather than surface layer, which has little effect on the adsorption of Se(IV) and Se(VI) on barite. These results showed the dependence of saturation states on

substituent site in the barite structure, which is not affected by adsorption site on barite surface.

3.2.2. Effect of saturation states on substitution site

Some of the questions were arising from the experiments. Are the uptake of Se(IV) and Se(VI) during coprecipitation with barite as a function of saturation states shown an inverse correlation ? The radius difference between substituent and host ion can have a significant contribution to metal partitioning. Previous studies showed the distribution coefficient for the divalent and trivalent ions of different ionic radius in calcite as a function of precipitation rate [Robert, 1980; Yifeng and Huifang, 2001]. The K_d values for Co^{2+}, Mn^{2+}, and Cd^{2+}, Fe^{2+}, which have ionic radii smaller than Ca^{2+} ion, decrease with increasing precipitation rate. On the other hand, the K_d values for Sr^{2+} and Ba^{2+}, which have ionic radii larger than Ca^{2+} ion, increase with increasing precipitation rate. The K_d values for rare earth elements (REEs), which have high ionic charge as trivalent ion, are not affected by precipitation rate because their adsorption amount are large and close to the value of the partition coefficient [Shaojun, 1995; Lakshtanov and Stipp, 2004]. These results show the dependence of the charge and size of the trace ion relative to the charge and size of the lattice site on trace component partition as a function

of saturation states. Thus, it is suggested that the distribution difference between Se(IV) and Se(VI) during coprecipitation with barite was related to the geometry of incorporated metals (SeO_3^{2-}, SeO_4^{2-}) in host site (SO_4^{2-}) in barite. In this section, the effect of substituent structure on its partitions by barite is investigated in terms of geometry difference between SeO_3^{2-} and SeO_4^{2-} by XRD and EXAFS analysis.

Previous studies showed that the changes of the unit-cell dimensions with increasing substitution can be related to the ionic structure of incorporated ions in substituted site [Gerth, 1990; Gasser et al., 1996; Kaur et al., 2009]. The aim of this study is to determine what extent of the changes in the unit-cell dimensions can be related to the geometry difference between SeO_3^{2-} and SeO_4^{2-} to substituted ion (SO_4^{2-}) in barite structure. The unit-cell dimensions of pure, Se(IV)-, and Se(VI)-substituted barite at same saturation states are calculated by XRD analysis. The unit-cell parameters of the substituted barite are listed in Table 6. The pure barite and the Se(IV)- and Se(VI)-substituted barite showed little variation in the b- and c-parameter, but considerable differences in the a-parameter. X-ray diffraction patterns of pure- and substituted-barite are also plotted in Fig. 12, which showed the peak shift to larger 2θ by Se(IV)-substituted > Se(VI) -substituted > pure barite. The a-parameter of Se(IV)- and Se(VI)-substituted barite changed linearly with an increase of ion incorporation (Fig. 13). The results

showed a larger distortion in the Se(IV) system than that of Se(VI) system, which indicates the relatively incompatible substitution of SeO_3^{2-} in sulfate site in barite structure. The changes in the a-dimension of substituted barite show the relative instability of the crystal structure. Thus, the cause of greater distortion of Se(IV) is believed to be due to the instability of substitution of crystal lattice in sulfate site. It is considered that SeO_4^{2-}, which has a similar geometry and same charge as the replaced ion of SO_4^{2-}, is incorporated more compatibly in a crystal lattice of sulfate site than SeO_3^{2-}. These results showed that the dependence of substitution geometry as the substituted ion controlls differential incorporation of SeO_3^{2-} and SeO_4^{2-}anions.

X-ray absorption spectroscopy was also used to characterize the local coordination structure of incorporation metals in a host mineral. The Se K-edge EXAFS and the Fourier transforms (FTs) of the barite samples are shown in Fig. 14. In the FTs, the positions and intensities of peaks roughly correspond to the interatomic distances and coordination numbers (CNs), respectively, while phase shift and Debye-Waller factor are not considered in the FTs. The EXAFS spectra of Se for four barite samples were measured: Se(IV)- and Se(VI)-coprecipitated with barite at low and high saturation states (SI = 2.9 and 4.2).

Fitting results show that both Se(IV) and Se(VI) in barite can be explained by the

three shells of one Se-O and two Se-Ba shells named as Se-Ba_1 and Se-Ba_2 shells (Table 7). The CNs and distance of Se-O shows that Se(IV) or Se(VI) are incorporated into barite as SeO_3^{2-} in a trihedral coordination with oxygen or SeO_4^{2-} in a tetrahedral coordination with oxygen, respectively. The CNs and distance of Se-Ba_1 and Se-Ba_2 are similar to that of S-Ba in barite [Gupta et al., 2010], suggesting that Se is incorporated into the barite structure by substitution in sulfate site in barite structure (Fig. 15).

When the local structures of Se(VI) in SI=2.9 and 4.2 samples are compared based on EXAFS, both k- and R-space spectra significantly changed. In particular, the intensity of the Se-Ba_2 around $R + \Delta R = 3.58 – 3.61$ Å (phase shift uncorrected) in the FT clearly increases and similar to the values found for the pure barite at SI=2.9. An increase in the CN values of the Se-Ba_2 is also observed at both SI=2.9 and 4.2, suggesting that Se(VI) is more compatibly incorporated into barite at lower saturation states. When the local structures of Se (IV) in SI=2.9 and 4.2 samples, on the other hand, both k- and R-space spectra rarely changed and the position and intensity of the Se-Ba_2 around $R + \Delta R = 3.69 – 3.70$ Å are similar between SI = 2.9 and 4.2, but very different from pure barite sample. A change of CN values of the Se-Ba_2 shell was not observed at both SI=2.9 and 4.2, which suggested the independence of saturation states on the partitions of Se(IV), because of the incompatibility of Se(IV) in the barite structure.

These findings show that the degree of distortion in barite structure as a function of saturation state is affected by the distribution difference between Se(IV) and Se(VI) during coprecipitation with barite (Fig. 11). XRD results show the distortion difference between Se(IV) and Se(VI) in barite at same saturation states, which indicates that the uptake of Se(IV) became more distorted than that of Se(VI). EXAFS results provide the local information of Se(IV) and Se(VI) in barite structure, which suggests that (i) both Se(IV) and Se(VI) oxyanion are substituted in sulfate site in the barite structure as a trihedral or tetrahedral coordination with oxygen, respectively, and (ii) the change of the CNs and distance of the Se-Ba_2 difference between Se(IV) and Se(VI) are observed as a function of saturation state.

The uptake of Se(VI) during coprecipitation with barite was dependent on saturation states because Se(VI) is compatibly incorporated with little distortion in barite structure. Thus, a change of distortion in barite structure created by the degrees of saturation states is significantly affected on the partition coefficients of Se(VI) to barite (Table 7). At low saturation states (SI=2.9), the CNs and distance of the Se-Ba_2 are similar to the values found for the pure barite and compatible with crystal lattice in barite structure, which results in an increase of Se(VI) in barite. At high initial saturation states (SI=4.2), on the other hand, the CNs and distance of the Se-Ba_2 are very different from the values for

pure barite and observed a distortion of Se(VI) in sulfate site. The cause of the distortion is most likely due to the distortion of host lattice itself by high saturation states, not substitution of Se(VI), which results in a decrease of Se(VI) in barite with increasing saturation states.

On the other hand, the uptake of Se(IV) during coprecipitation with barite was independent on the saturation states because Se(IV) incorporation in barite is incompatible and creates larger distortion in barite structure at any degrees of the saturation states. Thus, the coprecipitation of Se(IV) with barite remained constant regardless of saturation states due to a larger distortion of Se(IV) substitution than that of host lattice itself by saturation states (Table 7).

Previous studies also showed that the extent of incorporation of trace elements into calcite during growth from aqueous solutions was controlled by structural aspects of distortion at sites in the bulk structure [Reede et al., 1999; Alexandratos et al., 2007]. The degree of structural distortion associated with (i) geometry between substituted- and substitution-ion and (ii) host lattice itself in crystal is an important factor for controlling the incorporation of trace elements. Ions having a similar geometry as the substituted ion should be incorporated more efficiently in a crystal lattice than those with different geometry. Thus, the uptakes of Se(IV) and Se(VI) in barite are controlled by structural

affinity related to the distortion of crystal lattice in barite structure, and we can efficiently remove Se(VI) from solutions by coprecipitation with barite at lower saturation states.

3.2.3. *Effect of crystal lattice distortion by competition*

Present results show that, in the presence of Ca^{2+}, we can efficiently remove Se(IV) and Se(VI) from solutions by barite discussed in section 3.2. In this section, the cause of greater incorporation of Se(IV) and Se(VI) with Ca^{2+} ion in barite is investigated to determine the effect of unit-cell parameter of substituted samples on partition coefficients as a function of the concentrations of competitive ions .

The unit-cell parameters of non-substituted and substituted samples in the presence of Na^{+}, Mg^{2+}, and Ca^{2+} are listed in Table 8. In the presence of Ca^{2+} in solution, the unit-cell dimensions of a-axis (k_a values) of these samples were changed as a function of Ca^{2+} concentration, and the order of distortion is the non-substituted < Se(VI) substituted < Se(IV) substituted sample (Fig. 16a). On the other hand, in the presence of Na^{+} or Mg^{2+} in solution, the k_a values were constant regardless of the concentration of the competitive ions (Fig. 16b, 16c). These findings show the dependence of unit-cell dimensions of a-axis in barite structure on the distribution coefficients as a function of the concentration of the competitive ions. Thus, due to a large distortion with Ca^{2+} ion compared with

Na^+ and Mg^{2+}, the K_d values of Se(IV) and Se(VI) were increased with increasing Ca^{2+} in solution, and the uptake of Se(IV) were relatively higher and strongly changed than that of Se(VI) due to a larger distortion of Se(IV) than that of Se(VI) with Ca^{2+}. Thus, the uptakes of Se(IV) and Se(VI) in barite are controlled by structural affinity related to the lattice strain with competitive ions, and we can efficiently remove Se(IV) and Se(VI) from solutions by coprecipitation with barite in the presence of high Ca^{2+} as a competitive ion.

3.2.4. Effect of substituted and substitution component ratios

In this section, the effect of substituted and substitution component ratios (sulfate/Se-oxyanion) on the trace component partitioning is investigated. Present studies shows that both Se(IV) and Se(VI) oxyanions are substituted in sulfate site in the barite as a trihedral or tetrahedral coordination with oxygen, respectively. In other words, sulfate works as a substituted ion for Se(IV) and Se(VI) oxyanions in barite structure, which might control the trace component partitioning to barite. Batch experiments at fixed saturation states (SI=4.2) were conducted under different barium and sulfate concentration (Ba^{2+} 0.67~6.40 mM; SO_4^{2-} 1~27 mM) to understand the effect of substituted component in solution on the partition coefficients of Se(IV) and Se(VI)

between barite and water.

The distribution coefficient values of Se(IV) and Se(VI) in barite as a function of sulfate concentration is shown in Fig. 17 (Table 9). The results showed that both Se(IV) and Se(VI) were incorporated efficiently into barite when the sulfate level was low. The removal of Se(IV) and Se(VI) by barite is also shown in Fig. 17, which suggested that we could efficiently remove Se from solution at lower sulfate level. X-ray diffraction analysis of these samples are also conducted to determine the changes of the unit-cell parameter depending on the degree of sulfate concentration, but independence of the surface accumulation and precipitation of Se. The unit-cell parameter of substituted barite little changed under a wide sulfate concentration range (Se(IV) 1~27mM; Se(VI) 5~27 mM) although a larger distortion of Se(VI) in barite structure was only observed at sulfate = 1 mM (Fig. 18). This might be due to the formation of barium selenate at lowest sulfate condition. X-ray diffraction patterns of substituted barite are also plotted in Fig. 19, which showed the difference between Se(IV) and Se(VI) as a function of sulfate concentration (Table 9). A large distortion of Se(VI) in barite at 1 mM sulfate was due to the larger peak shift in XRD patterns to lower 2θ, which suggested the transformation into barium selenate from barite. On the other hand, the peak shift in XRD patterns of Se(IV) samples exhibits little change at various degrees of sulfate

concentration. Thus, the uptakes of Se(IV) and Se(VI) in barite are controlled by structural affinity related to the substituted and substitution component ratios in initial solution, and we can efficiently remove Se(IV) and Se(VI) from solutions by coprecipitation with barite at lower sulfate concentration in initial solution.

3.3. Effective removal of selenite and selenate from solution by barite

A new remediation method for Se(IV) and Se(VI) by coprecipitation with barite are developed from these results reported here. The uptake of Se(IV) by barite was dependent on pH, Ca^{2+} concentration, and sulfate and selenite ratios, which is strongly affected by the chemical affinity than the structural affinity. The uptake of Se(VI) by barite, on the other hand, was dependent on the Ca^{2+} concentration, saturation states of barite, and sulfate and selenite ratios, which strongly affected by the structural affinity than the chemical affinity. These conditions for selective removal of Se(IV) and Se(VI) are listed in Table 10, and we can effectively remove of Se(IV) or Se(VI), respectively, under ideal conditions. The distribution coefficients of Se(IV) as a function of conditions are shown in Fig. 20 and Table 11. The K_d values of Se(IV) continued to increase significantly from 22 L/kg under a standard condition (pH 8.0, Ca^{2+} 0 mM, SI 4.2, SO_4^{2-} 27 mM) to 662 kg/L under an ideal condition (pH 11.0, Ca^{2+} 10 mM, SI 4.2, SO_4^{2-} 5 mM). Thus, we can effectively remove Se(IV) or Se(VI) from solutions under the ideal conditions, respectively and barite works as a sequestering phase for the removal of Se(IV) and Se(VI) from solutions.

4. Conclusion

These results showed that the uptake of Se in solution by barite were mainly controlled by the chemical affinity related to adsorption on surface and the structural affinity related to geometry of incorporated ions in the substituted site. The transfer of ions from the solution to the surface layer during adsorption results in the electrostatic repulsion between dissolved ion and the charged surfaces site, which can be controlled by pH, ionic strength, and complexation with competitive ions. The uptake of ions from the surface layer to lattice in crystal during coprecipitation results in the lattice strain created by the geometry difference of substitution and substituted ion in the crystal lattice, which can be controlled by saturation states, distortion by competitive ions, and substituted- and substitution-component ratios.

The distribution difference between Se(IV) and Se(VI) are dependent on the properties of substitution ion related to the complexation speciation and substitution geometry. The uptake of Se(IV) by barite is dependent on the speciation by pH, crystal lattice distortion by Ca^{2+}, and sulfate and selenite ratios due to tis high chemical and low structural affinity to barite. The uptake of Se(VI) by barite, on the other hand, is dependent on the crystal lattice distortion by Ca^{2+}, crystal lattice distortion by saturation states, and sulfate and selenate ratios due to its low chemical and high structural affinity

to barite. Thus, we can effectively remove Se(IV) and Se(VI) from solution by barite to understand factors controlling mechanisms of coprecipitation process between barite and water.

References

Alexandratos, V. G., Elzinga, E. J., & Reeder, R. J. (2007). Arsenate uptake by calcite: macroscopic and spectroscopic characterization of adsorption and incorporation mechanisms. *Geochimica et Cosmochimica Acta*, *71*(17), 4172-4187.

Bleiman, N., & Mishael, Y. G. (2010). Selenium removal from drinking water by adsorption to chitosan–clay composites and oxides: batch and columns tests. Journal of Hazardous Materials, 183(1), 590-595.

Blount, C. W. (1974), Synthesis of barite, celestite, anglesite, witherite. and strontianite from aqueous solutions, *Amer. Mineral*., *59*. 1209-1219.

Blundy, J., & Wood, B. (2003). Partitioning of trace elements between crystals and melts. Earth and Planetary Science Letters, 210(3), 383-397.

Bosbach, D., Böttle, M., & Metz, V. (2010). Experimental study on Ra2+ uptake by barite (BaSO4). *Kinetics of solid solution formation via BaSO*, *4*.

Gasser, U. G., Jeanroy, E., Mustin, C., Barres, O., Nüesch, R., Berthelin, J., & Herbillon, A. J. (1996). Properties of synthetic goethites with Co for Fe substitution. Clay Minerals, 31(4), 465-476.

Gerth, J. (1990). Unit-cell dimensions of pure and trace metal-associated goethites. Geochimica et Cosmochimica Acta, 54(2), 363-371.

Gezer, N., Gülfen, M., & Aydın, A. O. (2011). Adsorption of selenite and selenate ions

onto thiourea‐formaldehyde resin. Journal of Applied Polymer Science, 122(2), 1134-1141.

Goh, K. H., & Lim, T. T. (2004). Geochemistry of inorganic arsenic and selenium in a tropical soil: effect of reaction time, pH, and competitive anions on arsenic and selenium adsorption. Chemosphere, 55(6), 849-859.

Goh, K. H., Lim, T. T., & Dong, Z. (2008). Application of layered double hydroxides for removal of oxyanions: a review. Water research, 42(6), 1343-1368.

Gupta, A., P. Singh, and C. Shivakumara (2010), Synthesis of nanoparticles by precipitation method using sodium hexa metaphosphate as a stabilizer, *Solid State Communications*, *150*, 386-388.

Hayes, K. F., & Leckie, J. O. (1987). Modeling ionic strength effects on cation adsorption at hydrous oxide/solution interfaces. Journal of Colloid and Interface Science, 115(2), 564-572.

Kaur, N., Singh, B., & Kennedy, B. J. (2009). Copper substitution alone and in the presence of chromium, zinc, cadmium and lead in goethite (α-FeOOH). Clay Minerals, 44(3), 293-310.

Kozai, N., Ohnuki, T., & Komarneni, S. (2002). Selenium oxyanions: Highly selective uptake by a novel anion exchanger. Journal of materials research, 17(12), 2993-2996.

Lakshtanov, L. Z., & Stipp, S. L. S. (2004). Experimental study of europium (III) coprecipitation with calcite. Geochimica et cosmochimica acta, 68(4), 819-827.

Lorens, R. B. (1981), Sr, Cd, Mn and Co distribution coefficients in calcite as a function of calcite precipitation rate, *Geochim. Cosmochim. Acta, 45*, 553-561.

Nishimura, T., Hashimoto, H., & Nakayama, M. (2007). Removal of Selenium (VI) from Aqueous Solution with Polyamine ‐ type Weakly Basic Ion Exchange Resin. Separation Science and Technology, 42(14), 3155-3167.

Reeder, R. J., Lamble, G. M., & Northrup, P. A. (1999). XAFS study of the coordination and local relaxation around Co2+, Zn2+, Pb2+, and Ba2+ trace elements in calcite. *American Mineralogist*, *84*(7-8), 1049-1060.

Rosenberg, Y. O., Metz, V., & Ganor, J. (2011). Co-precipitation of radium in high ionic strength systems: 1. Thermodynamic properties of the Na–Ra–Cl–SO 4–H 2 O system–estimating Pitzer parameters for RaCl 2. *Geochimica et Cosmochimica Acta*, *75*(19), 5389-5402.

Rosenberg, Y. O., Metz, V., Oren, Y., Volkman, Y., & Ganor, J. (2011). Co-precipitation of radium in high ionic strength systems: 2. Kinetic and ionic strength effects. *Geochimica et Cosmochimica Acta*, *75*(19), 5403-5422.

Prieto, M., Fernández-González, Á., & Martín-Díaz, R. (2002). Sorption of chromate ions

diffusing through barite-hydrogel composites: Implications for the fate and transport of chromium in the environment. *Geochimica et Cosmochimica Acta*, *66*(5), 783-795.

Prieto, M., Astilleros, J. M., & Fernández-Díaz, L. (2013). Environmental remediation by crystallization of solid solutions. Elements, 9(3), 195-201.

Sø, H. U., Postma, D., Jakobsen, R., & Larsen, F. (2008). Sorption and desorption of arsenate and arsenite on calcite. Geochimica et Cosmochimica Acta, 72(24), 5871-5884.

Tesoriero, A. J., & Pankow, J. F. (1996). Solid solution partitioning of Sr 2+, Ba 2+, and Cd 2+ to calcite. Geochimica et Cosmochimica Acta, 60(6), 1053-1063.

Wang, Y., & Xu, H. (2001). Prediction of trace metal partitioning between minerals and aqueous solutions: a linear free energy correlation approach.*Geochimica et Cosmochimica Acta*, *65*(10), 1529-1543.

Widanagamage, I. H., Schauble, E. A., Scher, H. D., & Griffith, E. M. (2014). Stable strontium isotope fractionation in synthetic barite. Geochimica Et Cosmochimica Acta, 147, 58-75.

Zhang, T., Gregory, K., Hammack, R. W., & Vidic, R. D. (2014). Co-precipitation of radium with barium and strontium sulfate and its impact on the fate of radium during treatment of produced water from unconventional gas extraction. *Environmental*

science & technology, *48*(8), 4596-4603.

Zhong, S., & Mucci, A. (1995). Partitioning of rare earth elements (REEs) between calcite and seawater solutions at 25 C and 1 atm, and high dissolved REE concentrations. Geochimica et Cosmochimica Acta, 59(3), 443-453.

Figure legends

Figure 1. The characteristics of barite in natural environments.

Figure 2. Aqueous (a) Se(VI) and (b) Se(V) species in water as a function of pH calculated by *Visual Minteq*.

Figure 3. The (a) uptake amounts and (b) apparent K_d values of Se(IV) and Se(VI) during adsorption and coprecipitation with barite as a function of pH.

Figure 4. The apparent K_d values of Se(IV) and Se(VI) during coprecipitation with barite as a function of pH between MilliQ water and ASW.

Figure 5. The (a) uptake amounts and (b) apparent K_d values of Se(IV) and Se(VI) during adsorption and coprecipitation with barite as a function of ionic strength.

Figure 6. The Se K-edge EXAFS and the Fourier transforms (FTs) of the Se(VI) on/in barite

Figure 7. The (a) uptake amounts and (b) apparent K_d values of As(III) and As(V) during adsorption and coprecipitation with barite as a function of ionic strength.

Figure 8. The apparent K_d values of Se(IV) and Se(VI) during coprecipitation as a function of (a) Ca^{2+} , (b) Mg^{2+}, (c) Na^{+} concentrations.

Figure 9. The (a) uptake amounts and (b) apparent K_d values of Se(IV) and Se(VI) during adsorption and coprecipitation as a function of saturation states

Figure 10. The unit-cell dimensions of (a) a-, b-, and c-axis and (b) a-axis in non-substituted barite as a function of saturation states between MilliQ water and ASW.

Figure 11. The apparent K_d values of Se(IV) and Se(VI) and unit-cell dimensions of a-axis (=k_a value) during coprecipitation as a function of saturation states

Figure 12. X-ray diffraction patterns of pure- and Se(IV) or Se(VI) substituted-barite at pH 8.0 and SI 4.2.

Figure 13. The (a) uptake amount of Se(IV) and Se(VI) and (a) unit-cell dimensions of a-, b-, and c-axis in Se(IV)- and Se(VI)-substituted barite as a function of Se concentration in solution.

Figure 14. The (a) Se K-edge EXAFS and (b) Fourier transforms (FTs) of the Se(IV) and Se(VI) in barite at high and low saturation states

Figure 15. The structure of (a) oxyanions such as SO_4^{2-}, SeO_3^{2-}, and SeO_4^{2-} barite and (b) Se(IV) subatituted- and (c) Se(VI) substituted-barite.

Figure 16. The unit-cell dimensions of Se(IV) and Se(VI) in substituted- and non-substituted-barite as a function of (a) Ca^{2+} , (b) Mg^{2+}, (c) Na^{+} concentrations.

Figure 17. The apparent K_d values and removal ratios of Se(IV) and Se(VI) during coprecipitation with barite as a function of sulfate concentration in solution.

Figure 18. The unit-cell dimensions of a-, b-, and c-axis in Se(IV)- and Se(VI)-substituted

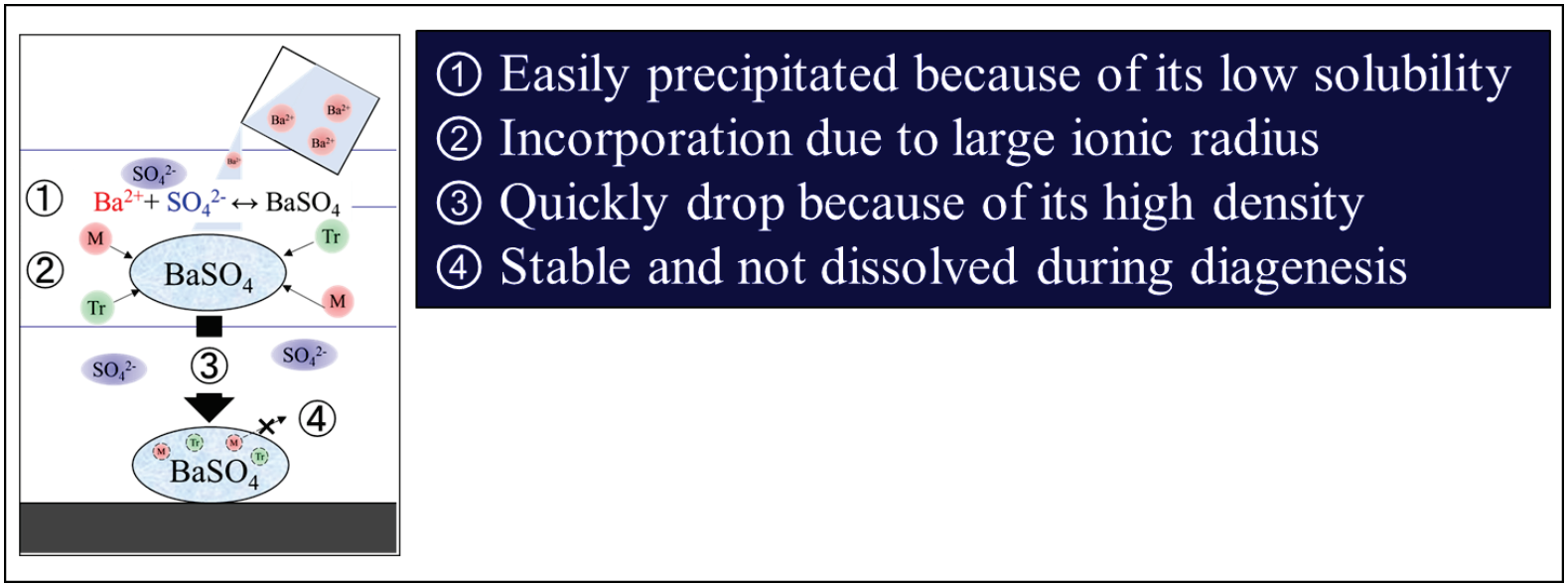

Figure 1. The characteristics of barite in natural environments.

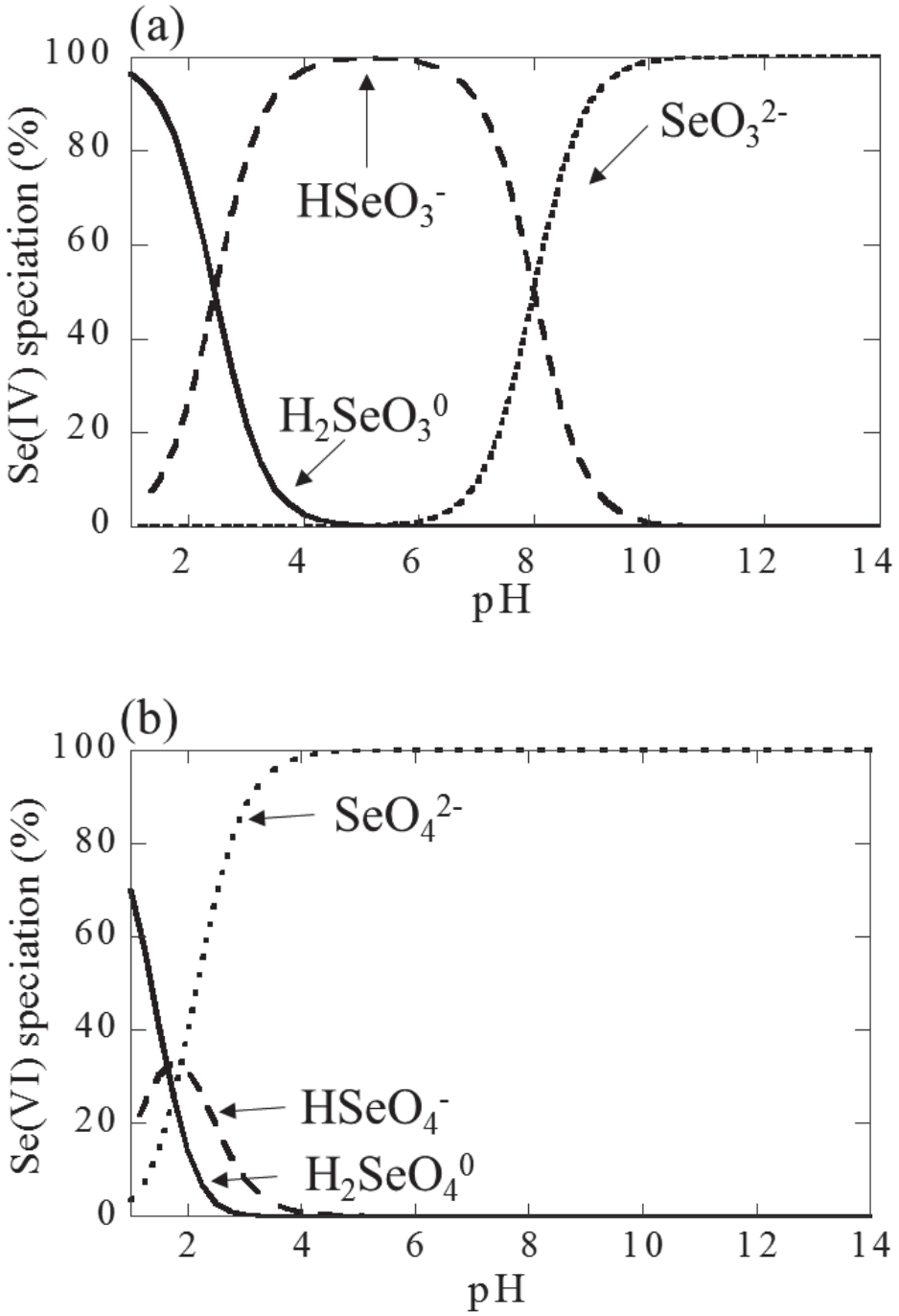

Figure 2. Aqueous (a) Se(VI) and (b) Se(V) species in water as a function of pH calculated by *Visual Minteq*.

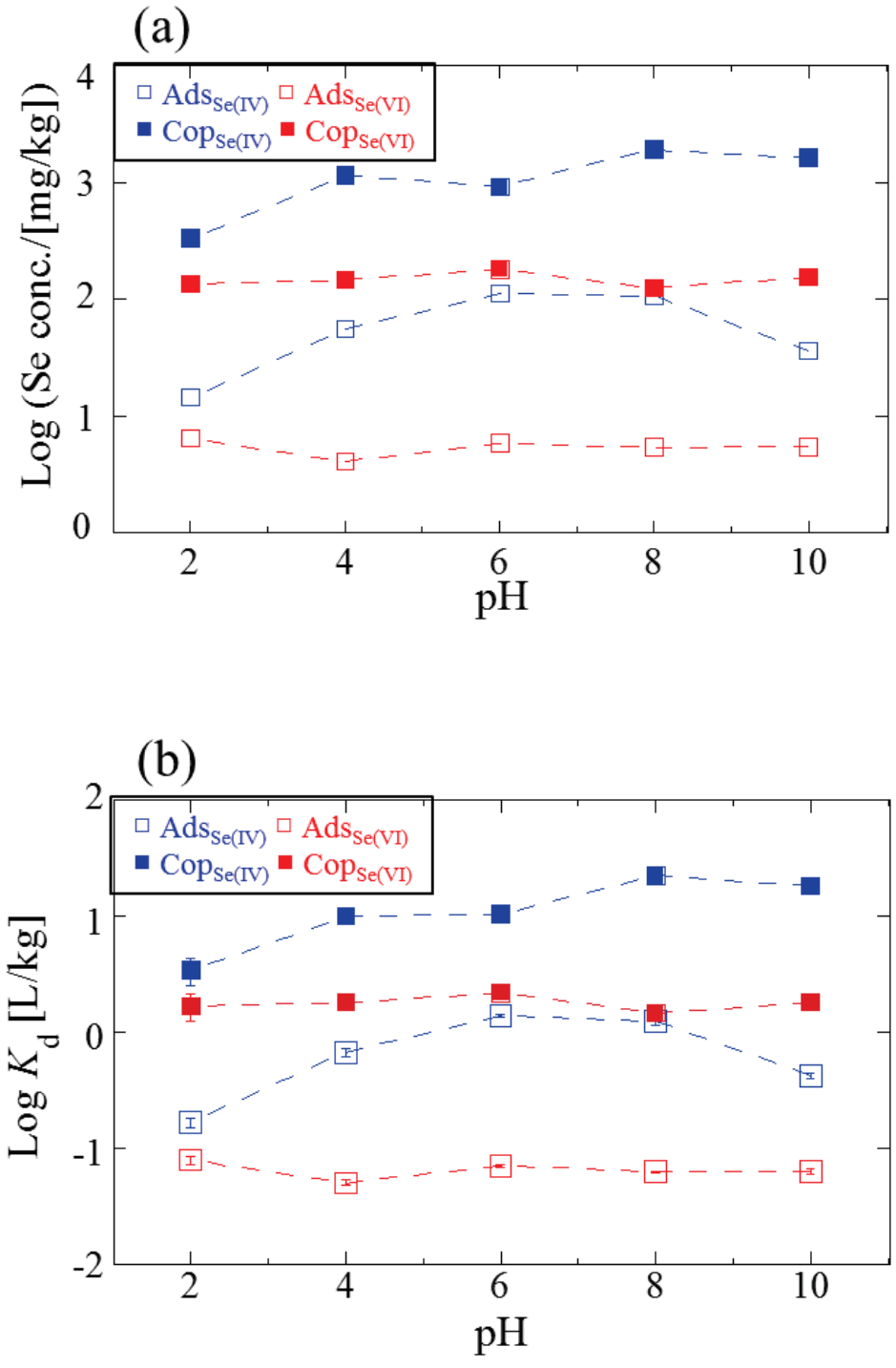

Figure 3. The (a) uptake amounts and (b) apparent K_d values of Se(IV) and Se(VI) during adsorption and coprecipitation with barite as a function of pH.

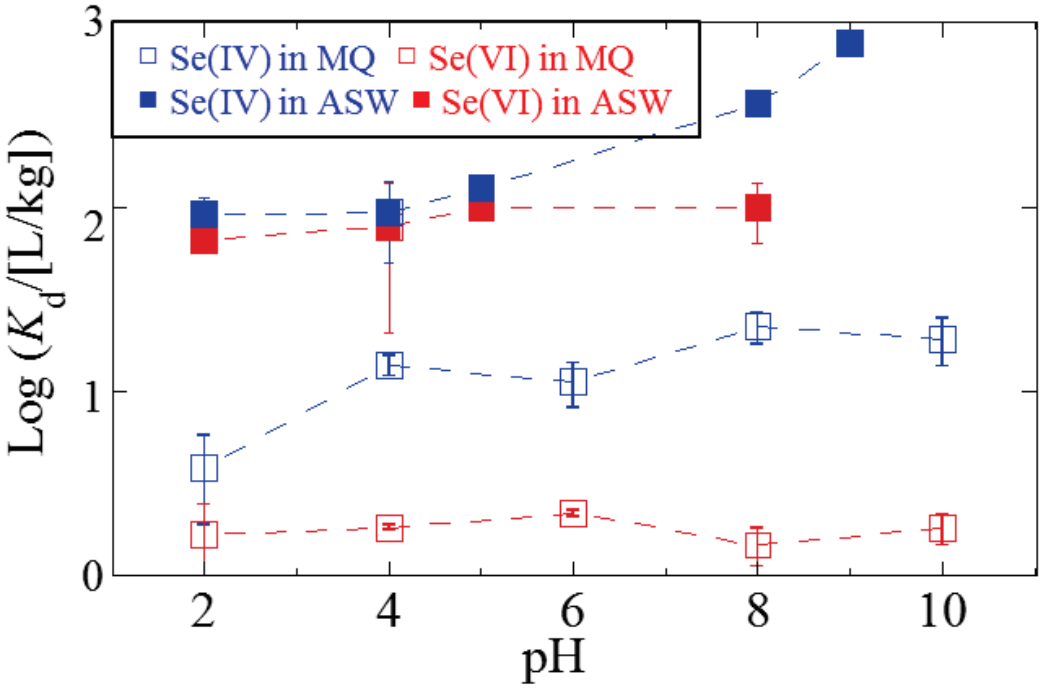

Figure 4. The apparent K_d values of Se(IV) and Se(VI) during coprecipitation with barite as a function of pH between MilliQ water and ASW.

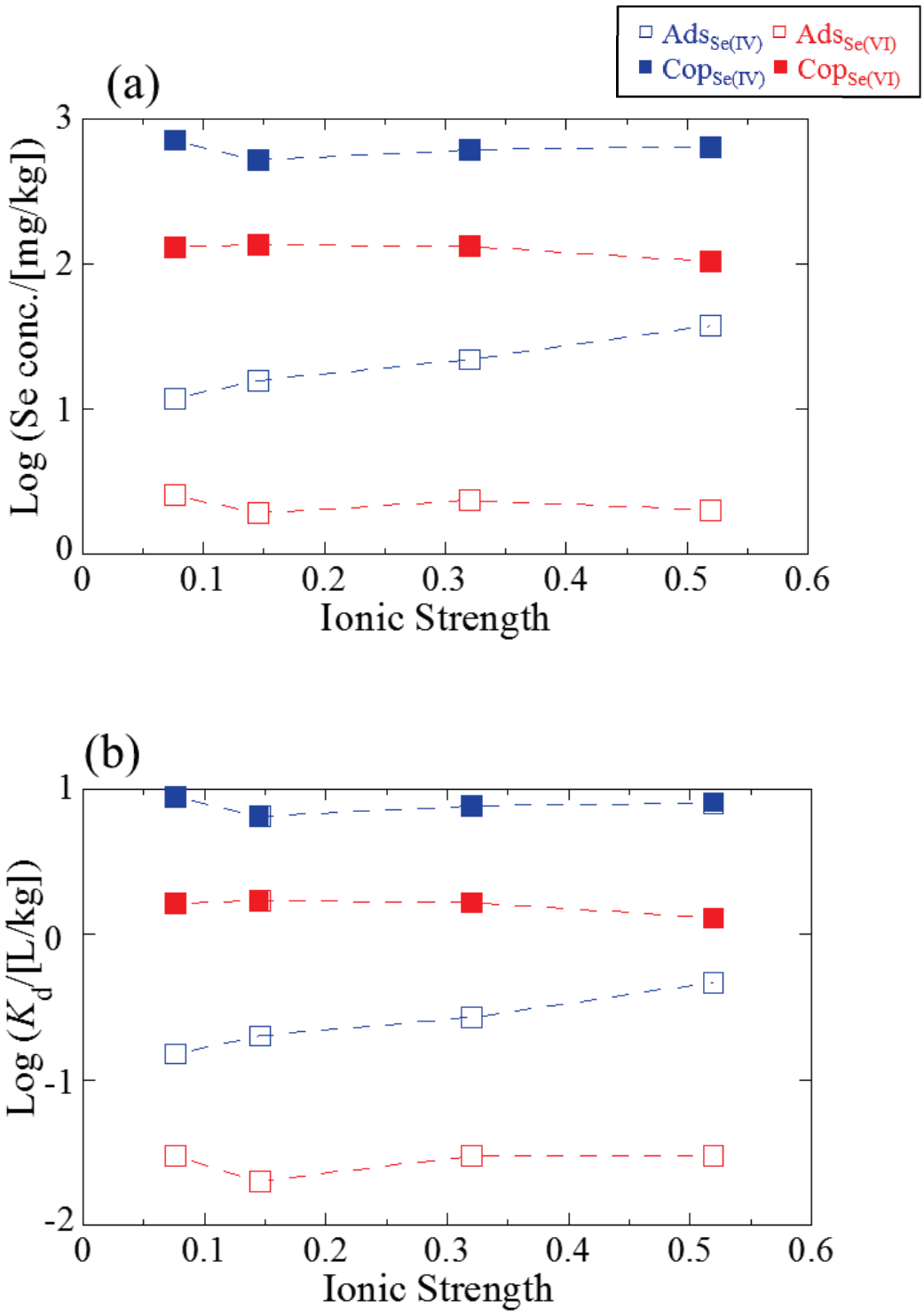

Figure 5. The (a) uptake amounts and (b) apparent K_d values of Se(IV) and Se(VI) during adsorption and coprecipitation with barite as a function of ionic strength.

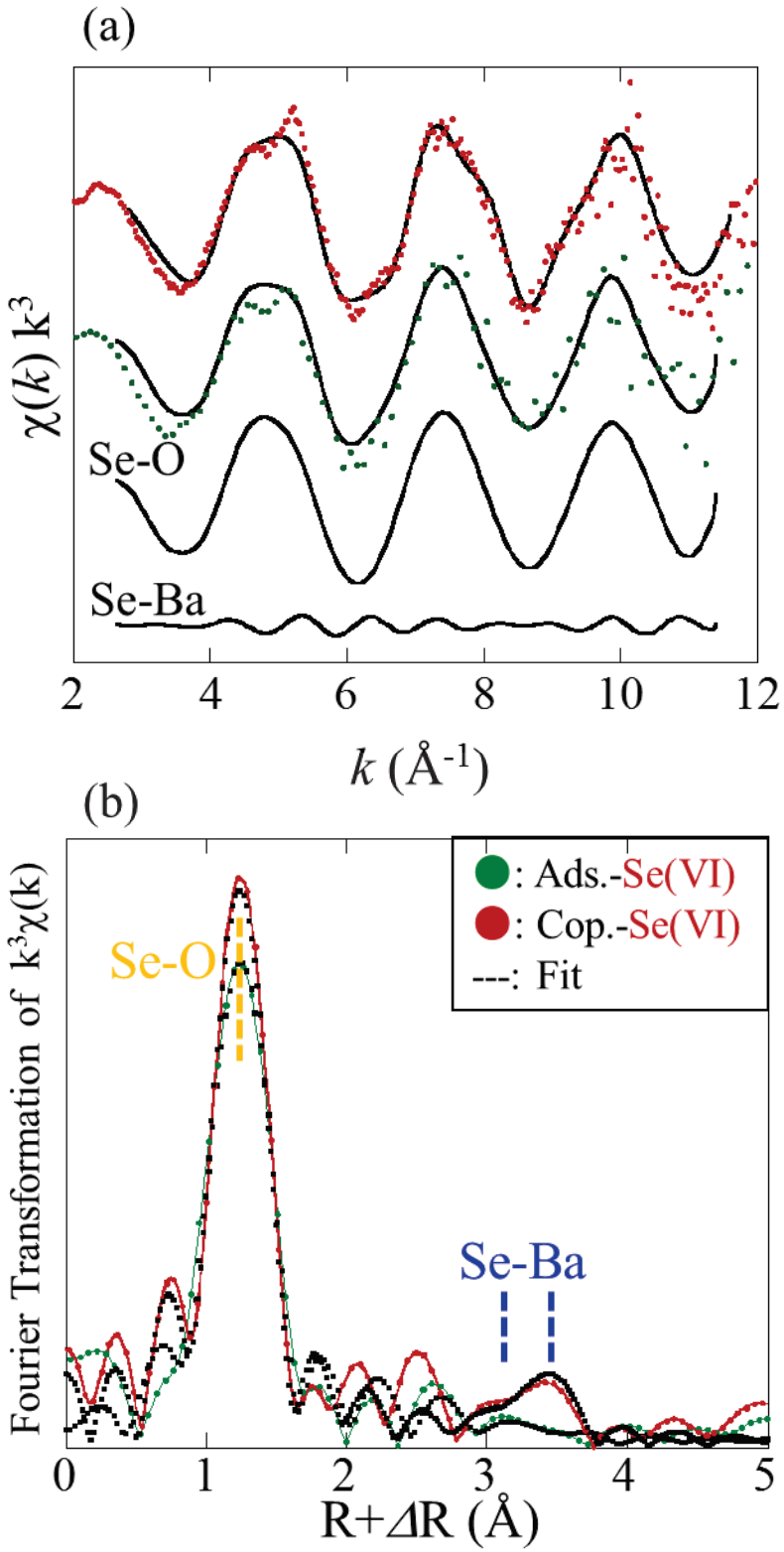

Figure 6. The Se K-edge EXAFS and the Fourier transforms (FTs) of the Se(VI) on/in barite

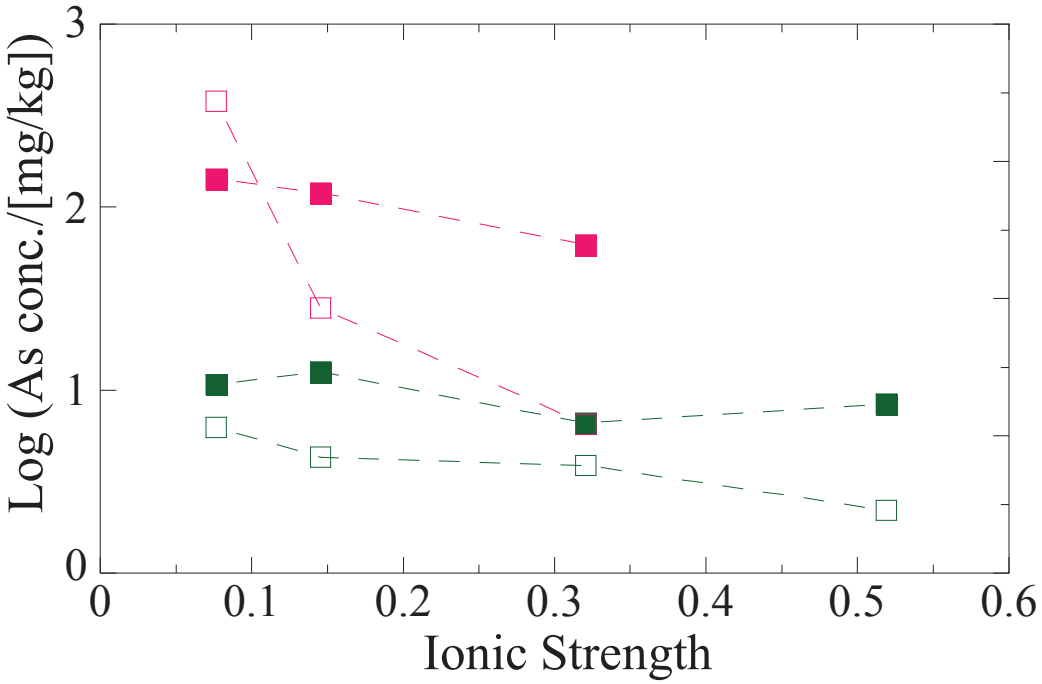

Figure 7. The (a) uptake amounts and (b) apparent K_d values of As(III) and As(V) during adsorption and coprecipitation with barite as a function of ionic strength.

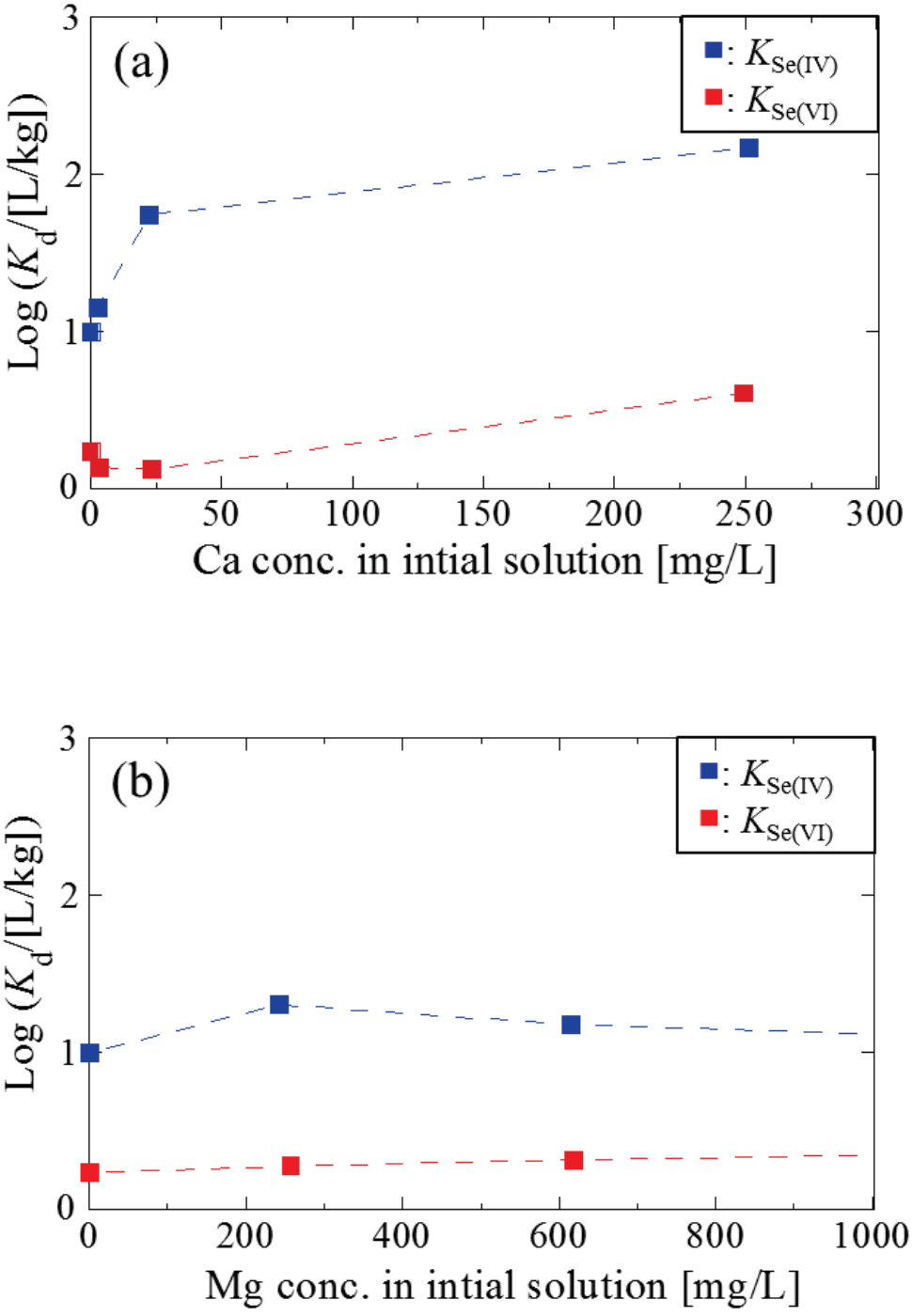

Figure 8. The apparent K_d values of Se(IV) and Se(VI) during coprecipitation as a function of (a) Ca^{2+}, (b) Mg^{2+}, and (c) Na^{+} concentrations.

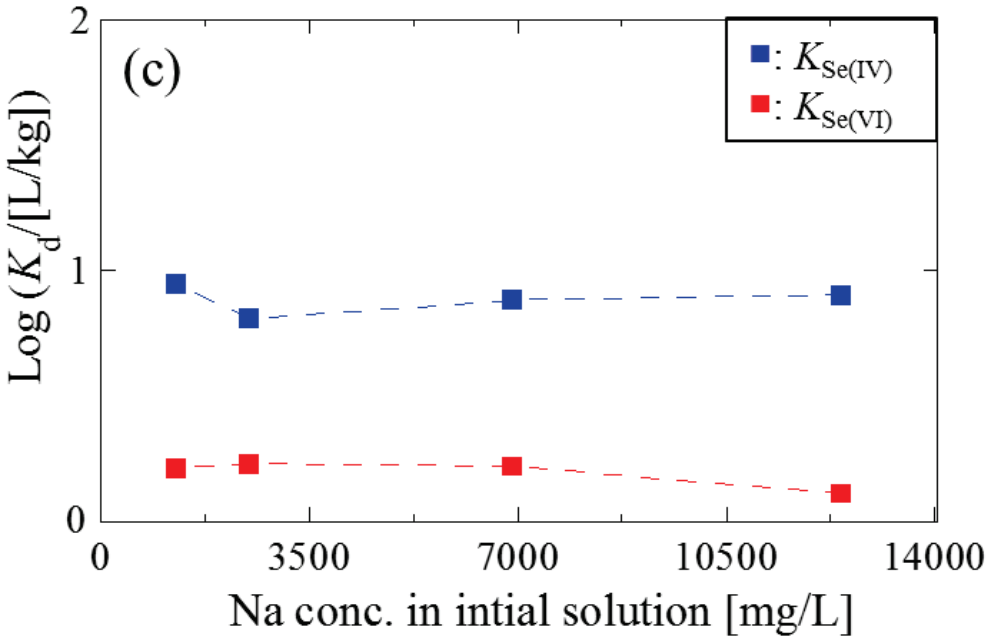

Figure 8. The apparent K_d values of Se(IV) and Se(VI) during coprecipitation as a function of (a) Ca^{2+}, (b) Mg^{2+}, and (c) Na^{+} concentrations.

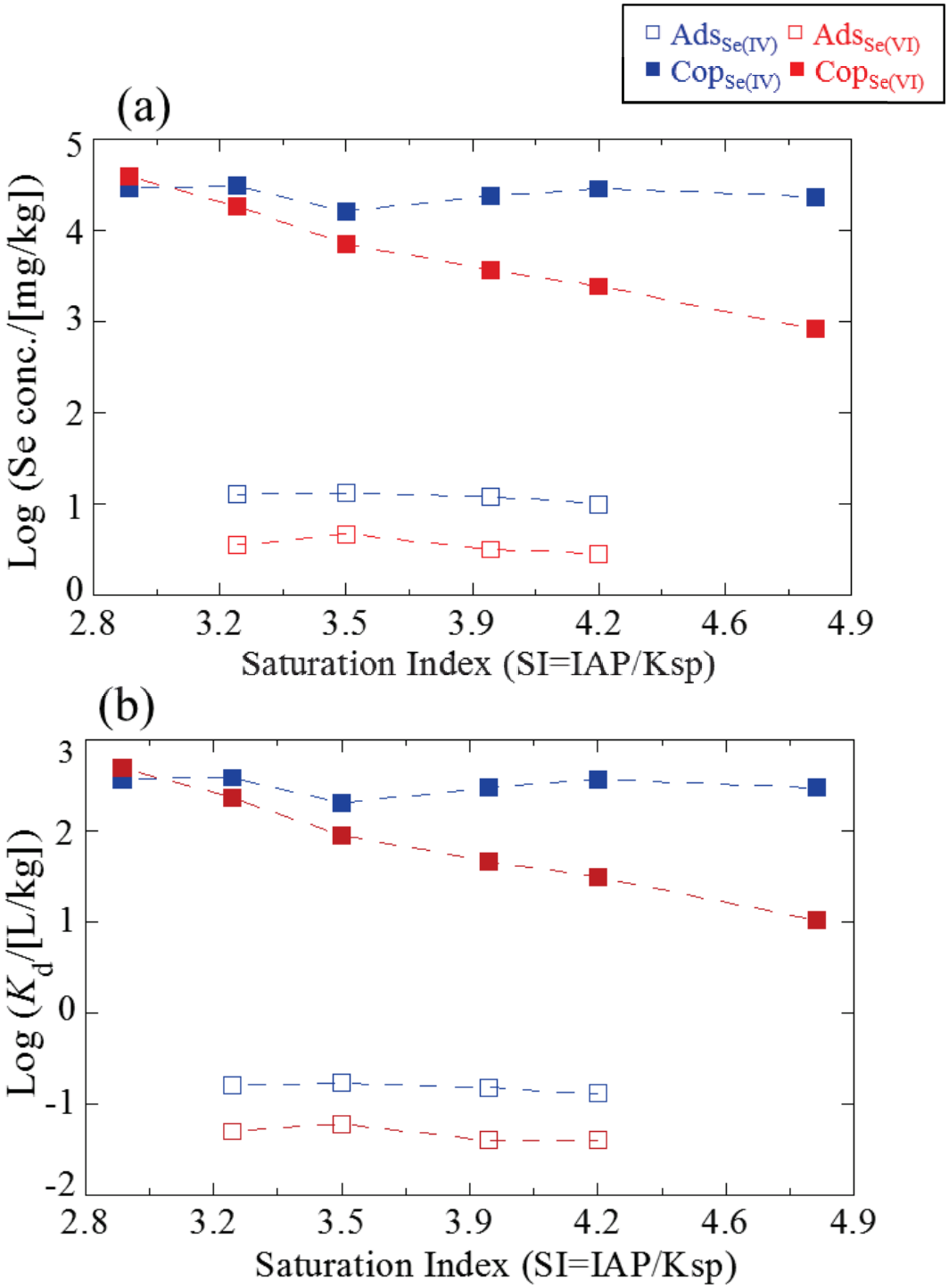

Figure 9. The (a) uptake amounts and (b) apparent K_d values of Se(IV) and Se(VI) during adsorption and coprecipitation as a function of saturation states

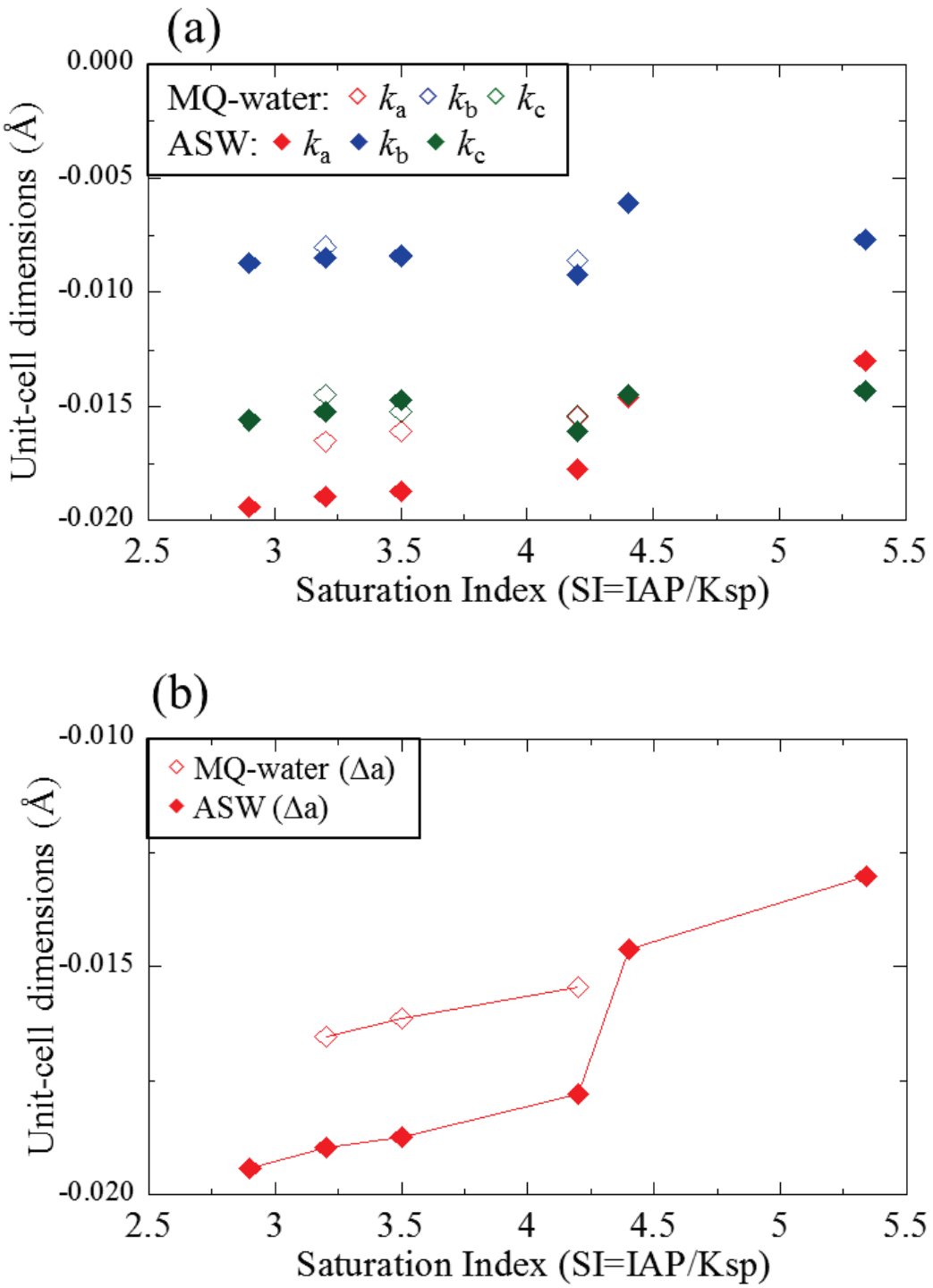

Figure 10. The unit-cell dimensions of (a) a-, b-, and c-axis and (b) a-axis in non-substituted barite as a function of saturation states between MilliQ water and ASW.

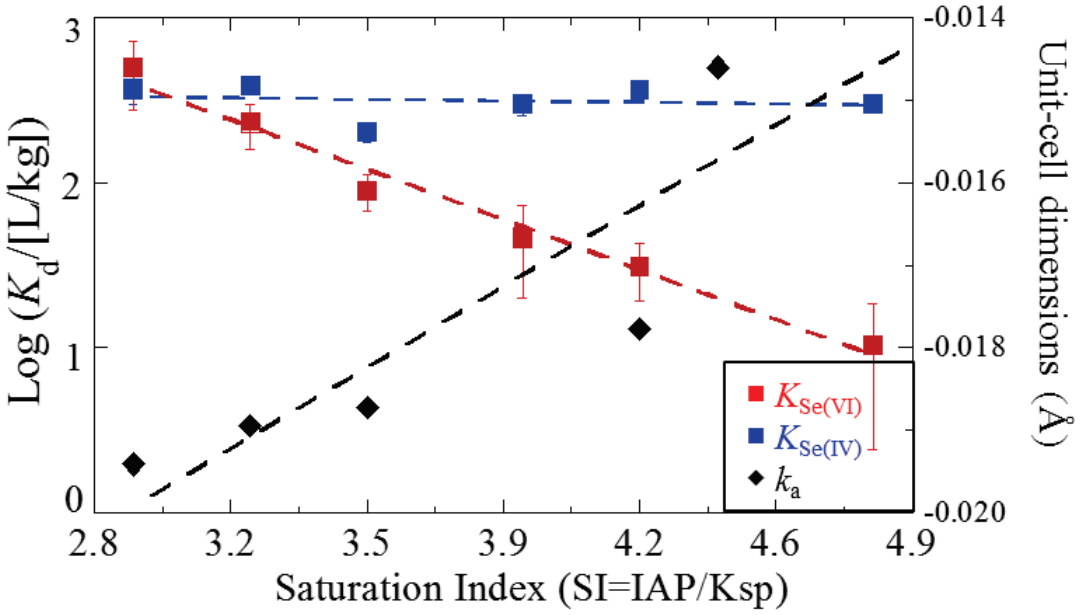

Figure 11. The apparent K_d values of Se(IV) and Se(VI) and unit-cell dimensions of a-axis (=k_a value) during coprecipitation as a function of saturation states

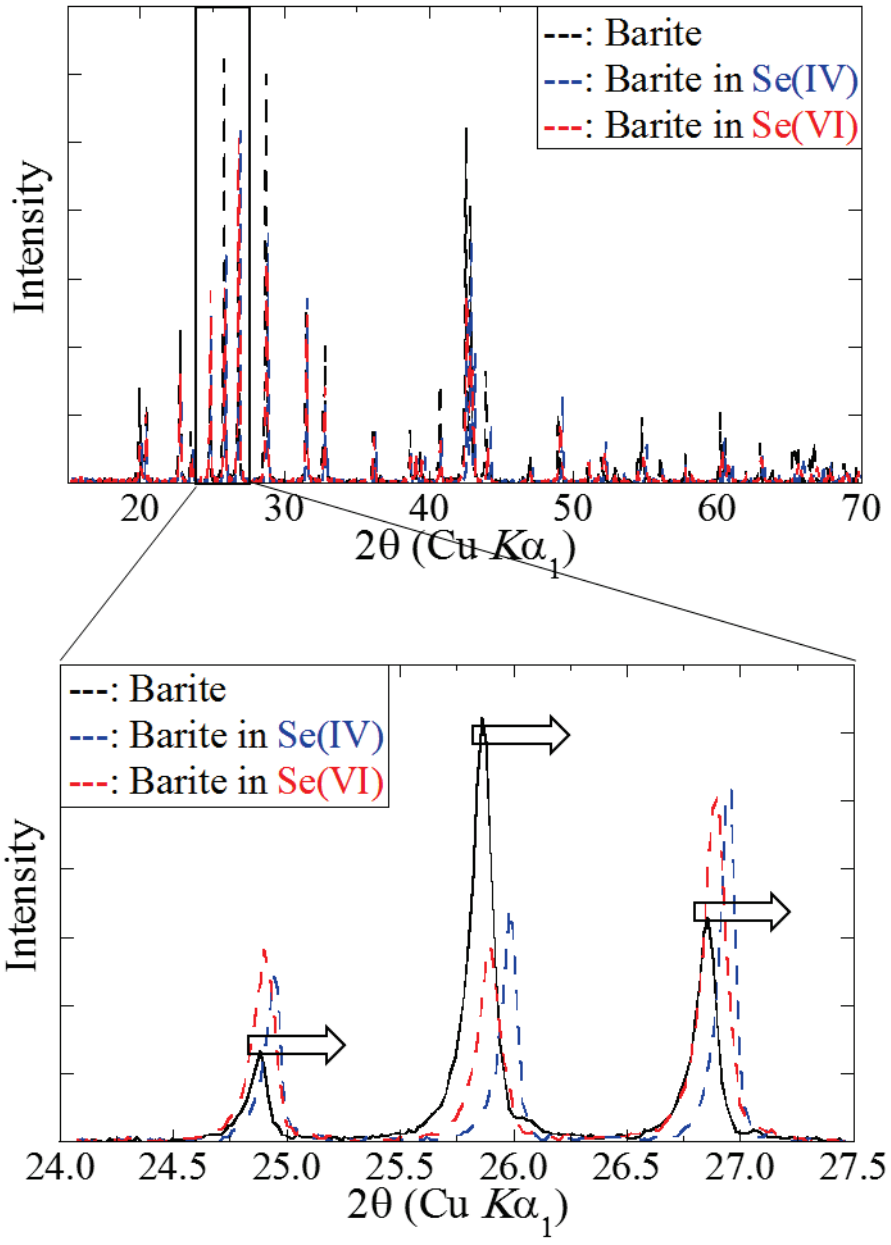

Figure 12. X-ray diffraction patterns of pure- and Se(IV) or Se(VI) substituted-barite at pH 8.0 and SI 4.2.

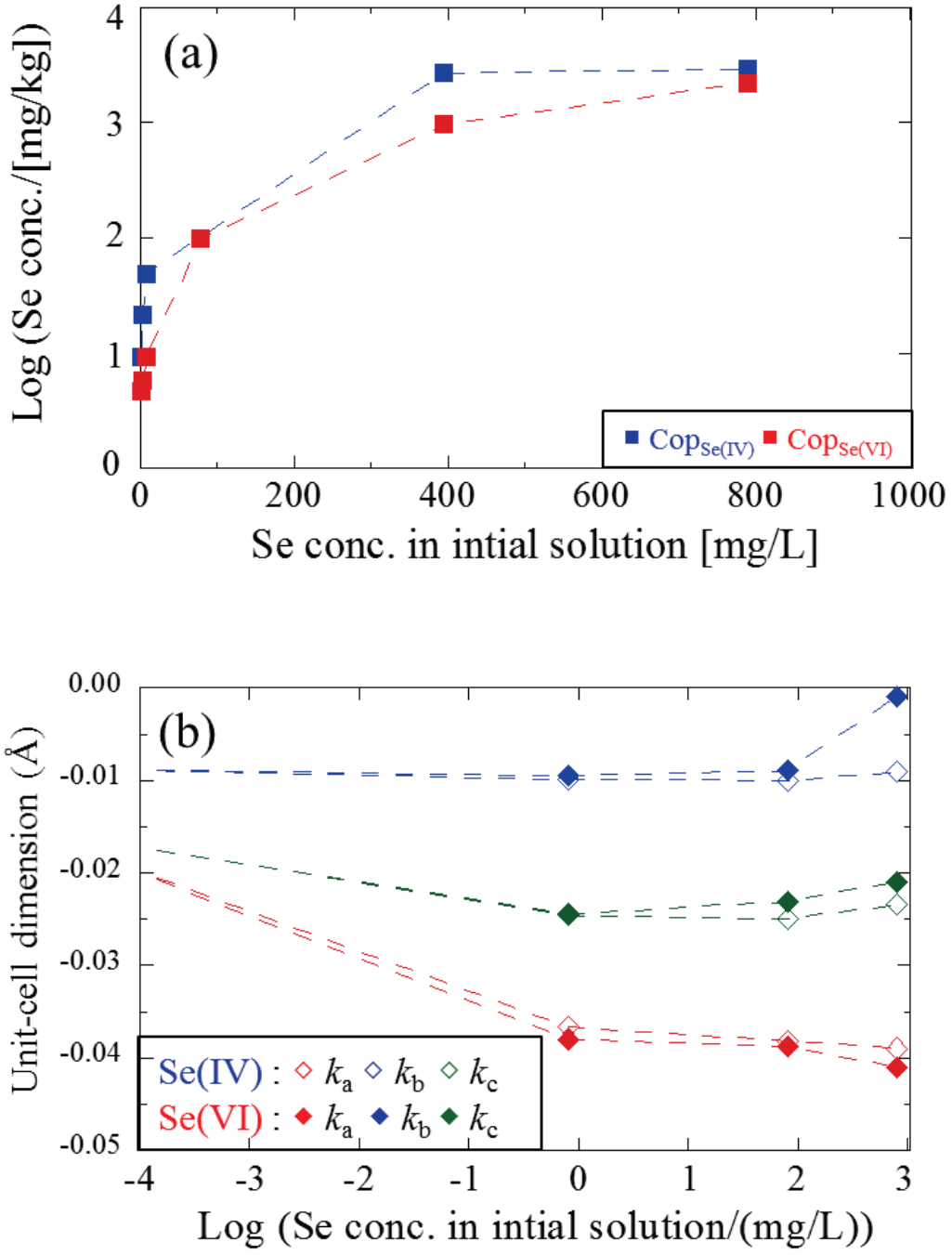

Figure 13. The (a) uptake amount of Se(IV) and Se(VI) and (a) unit-cell dimensions of a-, b-, and c-axis in Se(IV)- and Se(VI)-substituted barite as a function of Se concentration in solution.

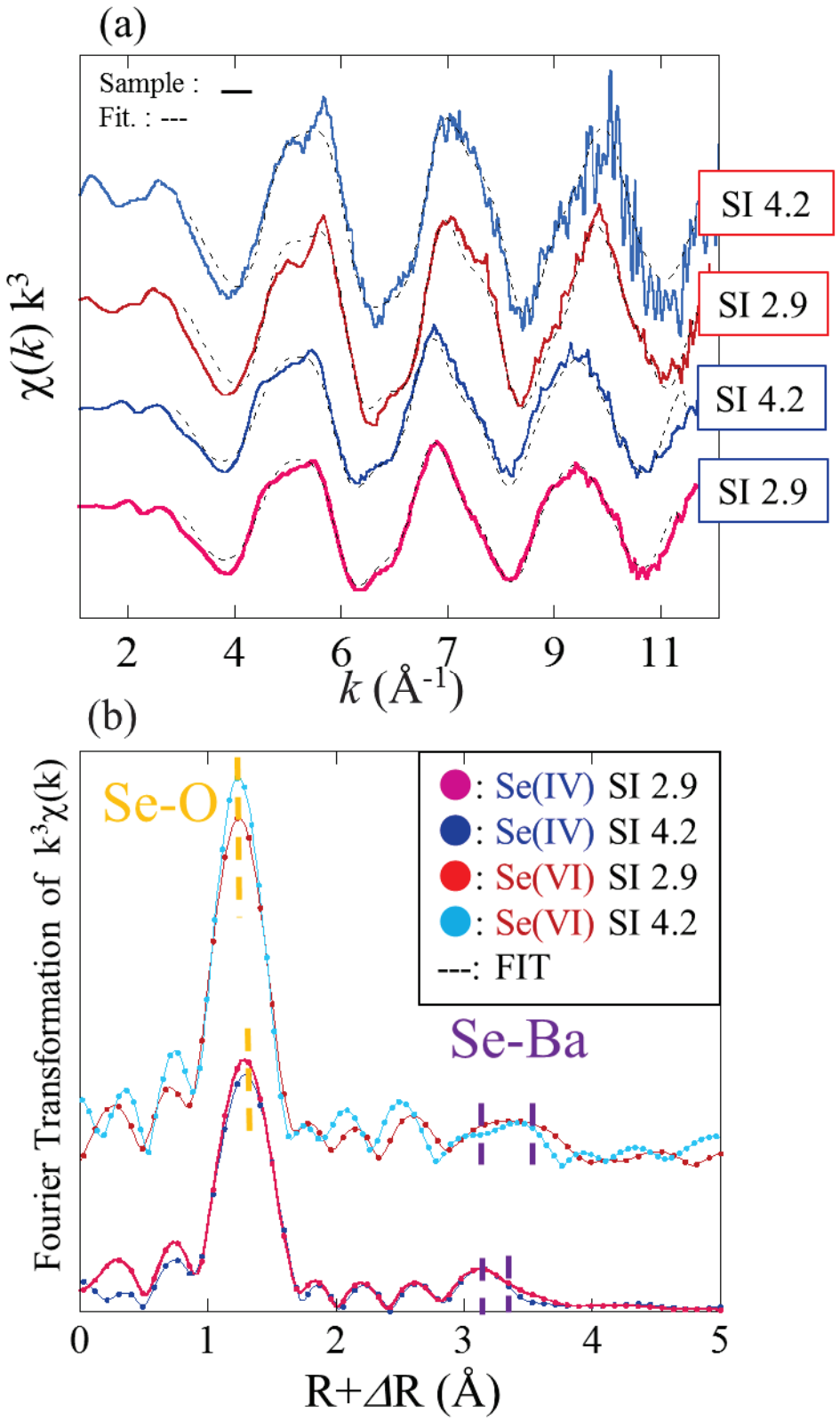

Figure 14. The (a) Se K-edge EXAFS and (b) Fourier transforms (FTs) of the Se(IV) and Se(VI) in barite at high and low saturation states

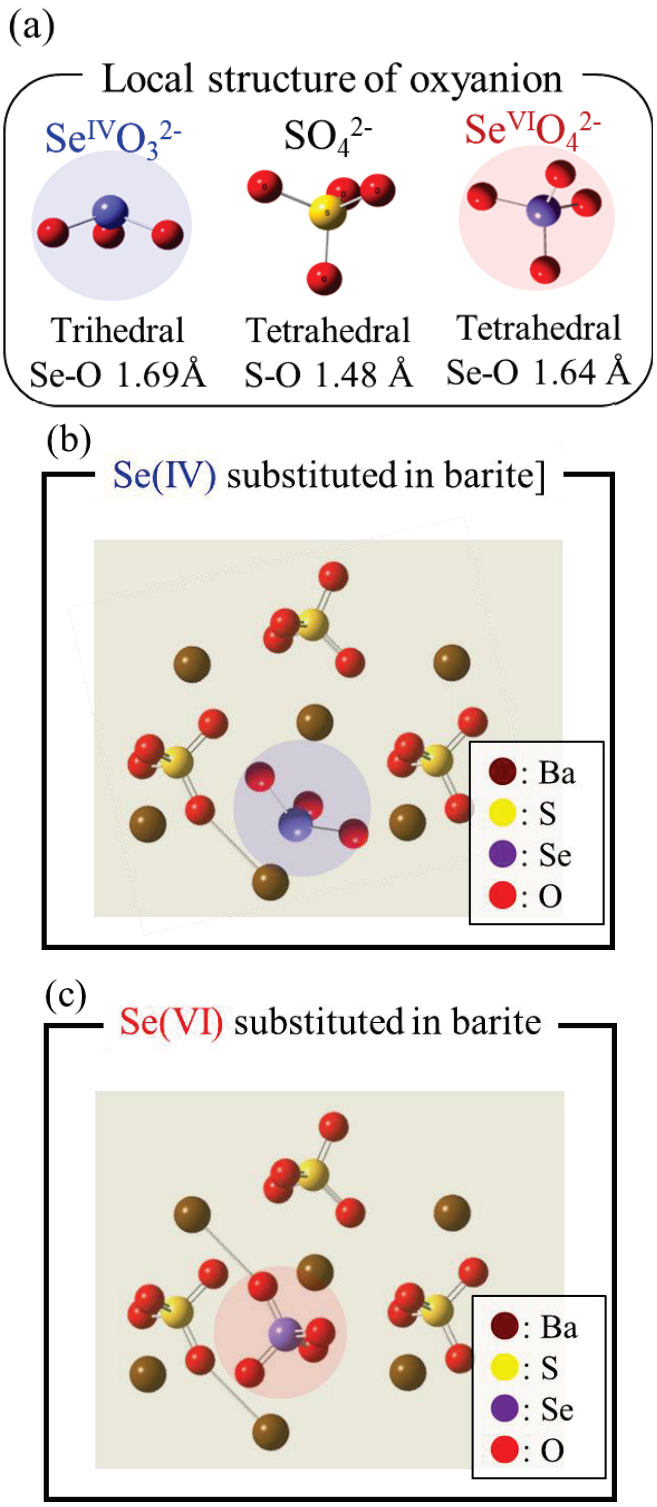

Figure 15. The structure of (a) oxyanions such as SO_4^{2-}, SeO_3^{2-}, and SeO_4^{2-} barite and (b) Se(IV) subatituted- and (c) Se(VI) substituted-barite.

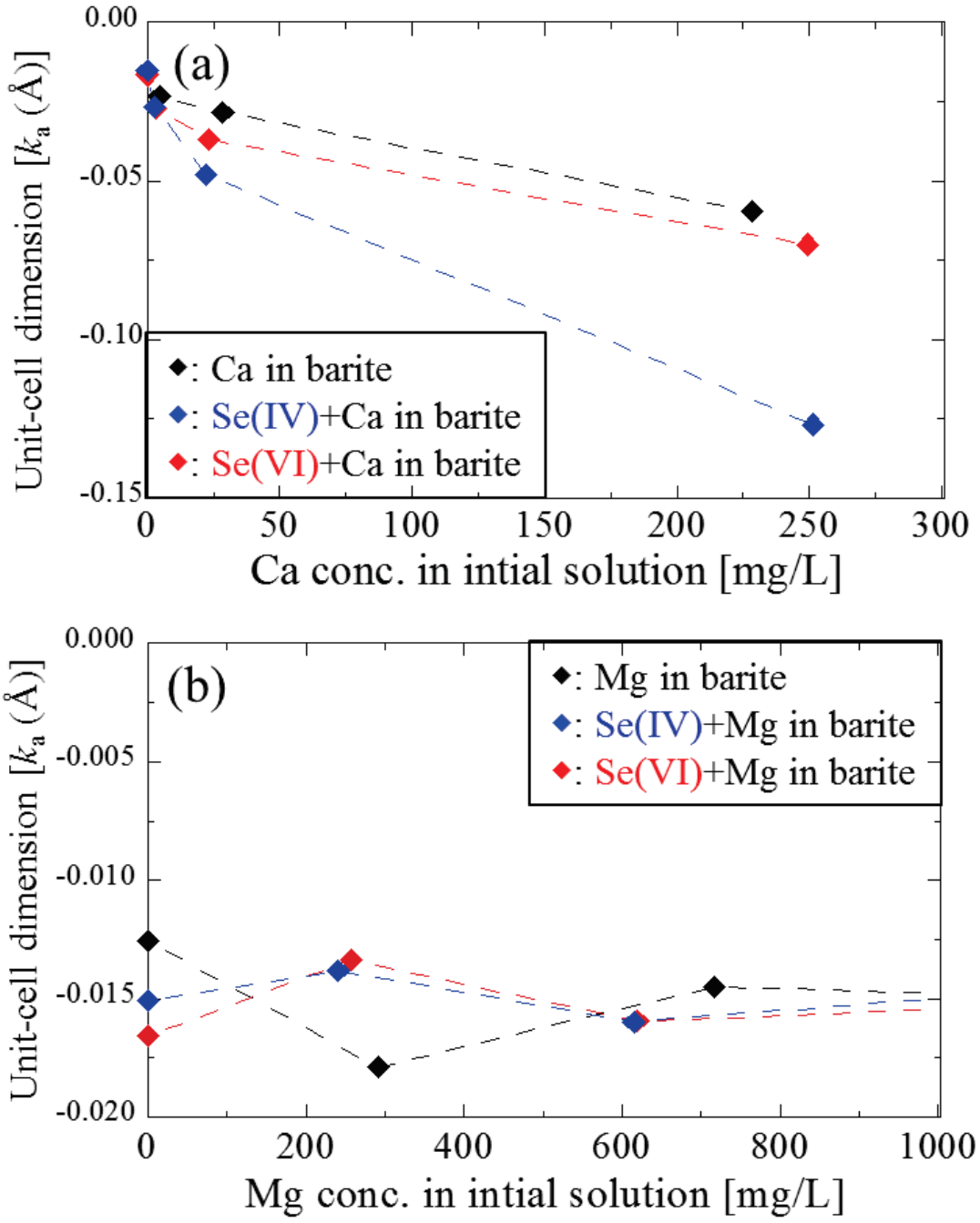

Figure 16. The unit-cell dimensions of Se(IV) and Se(VI) in substituted- and non-substituted-barite as a function of (a) Ca^{2+}, (b) Mg^{2+}, and (c) Na^{+} concentrations.

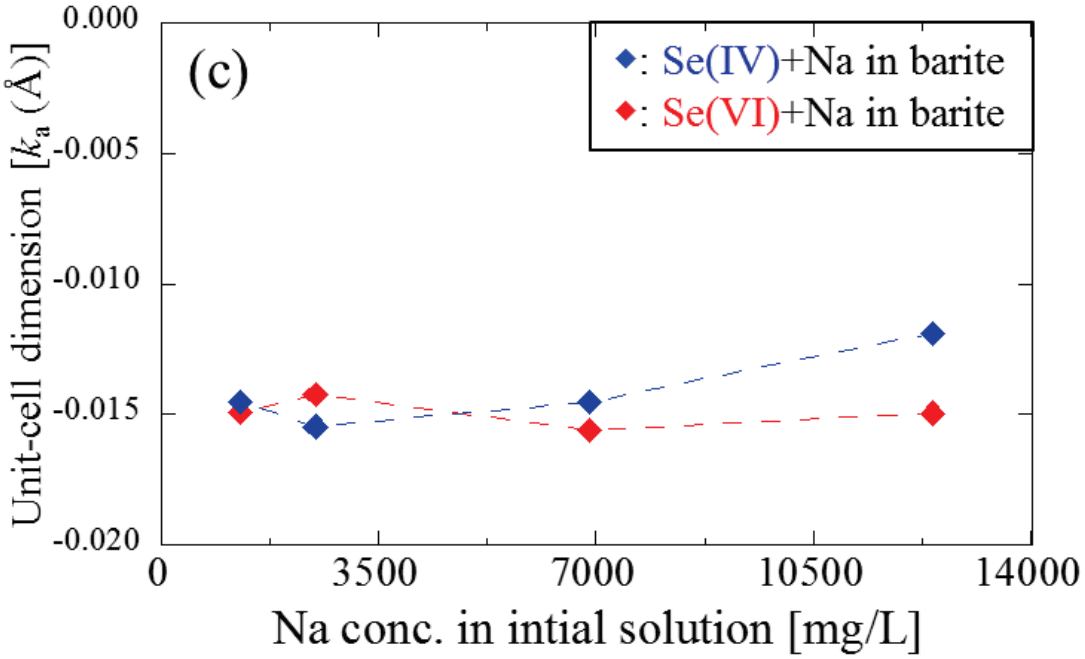

Figure 16. The unit-cell dimensions of Se(IV) and Se(VI) in substituted- and non-substituted-barite as a function of (a) Ca^{2+}, (b) Mg^{2+}, and (c) Na^{+} concentrations.

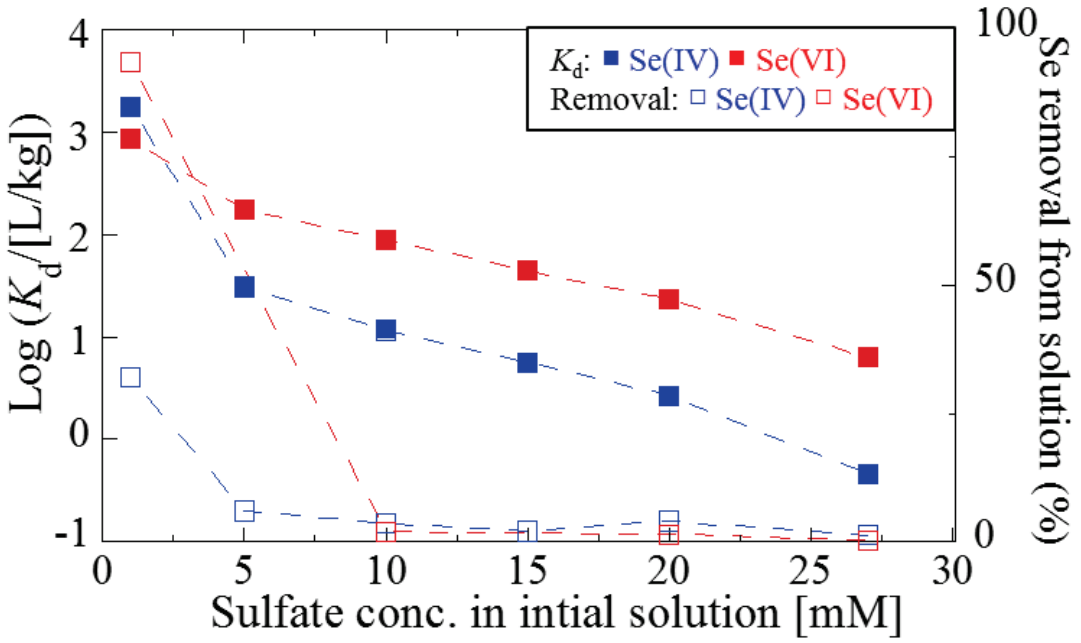

Figure 17. The apparent K_d values and removal ratios of Se(IV) and Se(VI) during coprecipitation with barite as a function of sulfate concentration in solution.

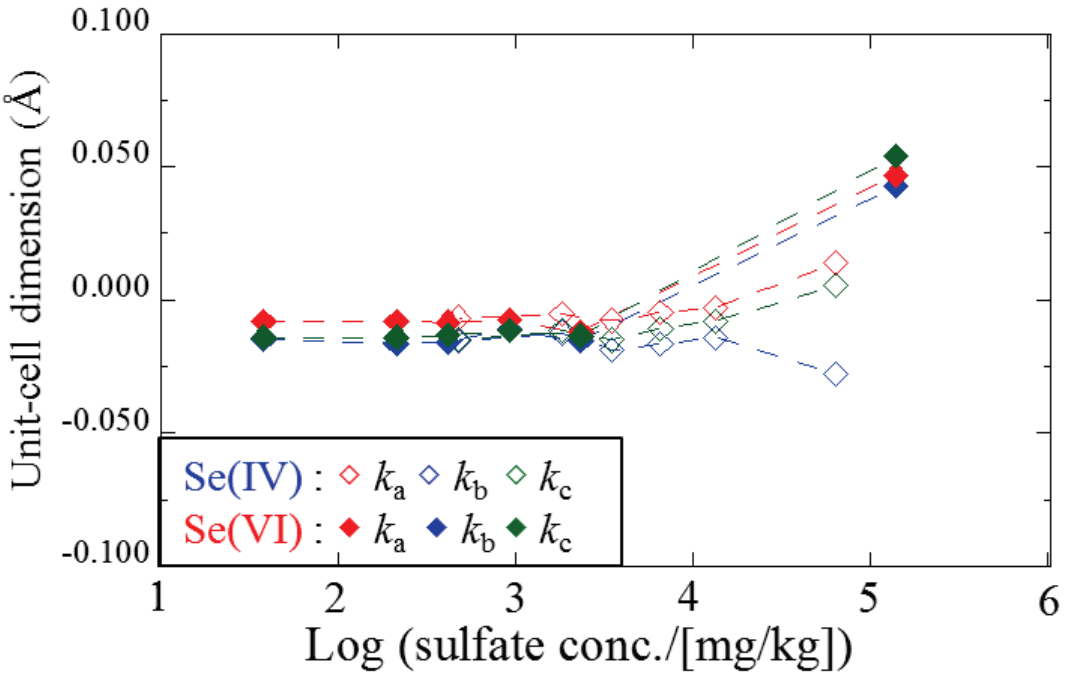

Figure 18. The unit-cell dimensions of a-, b-, and c-axis in Se(IV)- and Se(VI)-substituted barite as a function of sulfate concentration in solution.

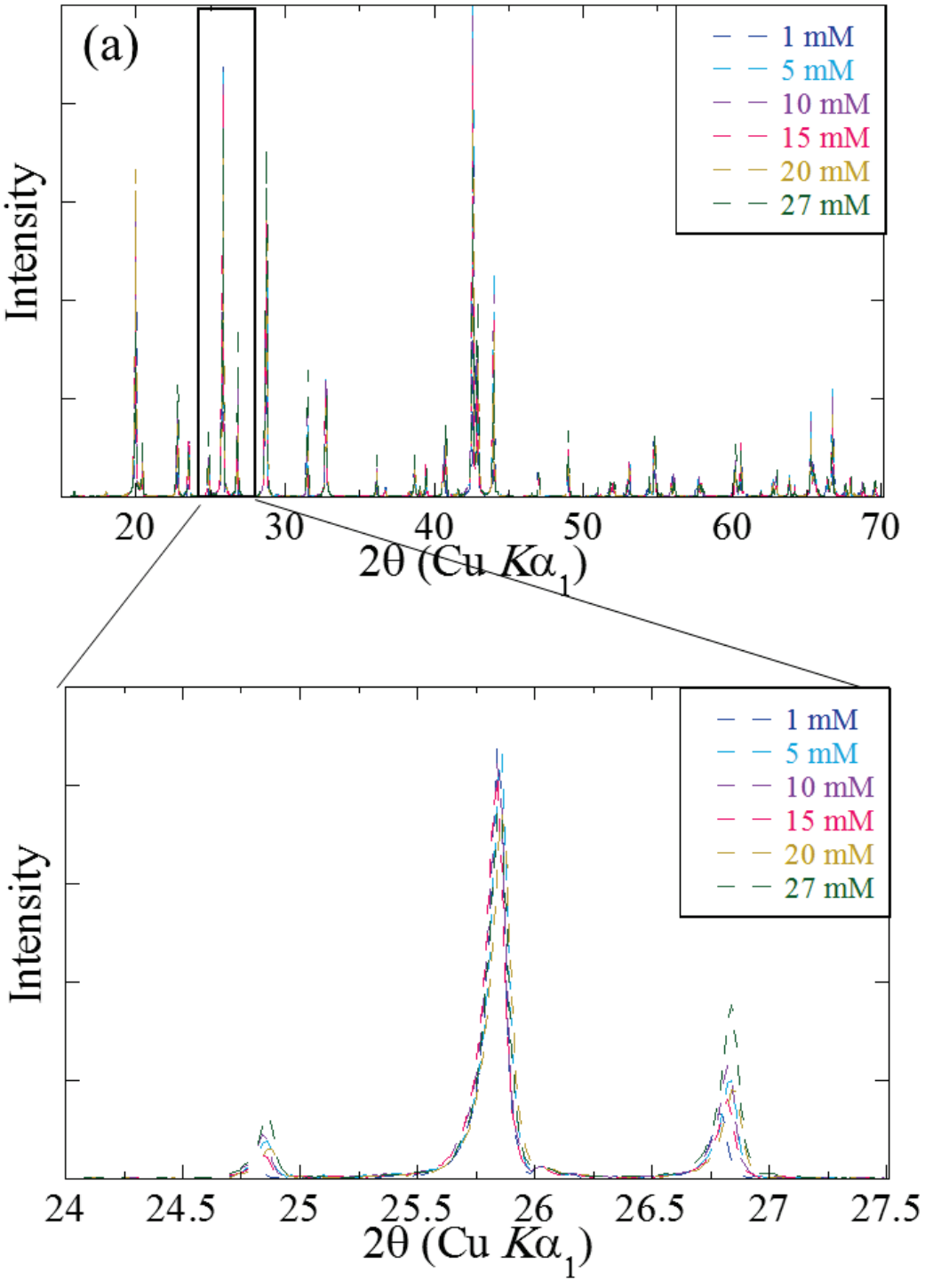

Figure 19. X-ray diffraction patterns of (a) Se(IV)- and (b) Se(VI)-substituted barite as a function of sulfate concentration in solution.

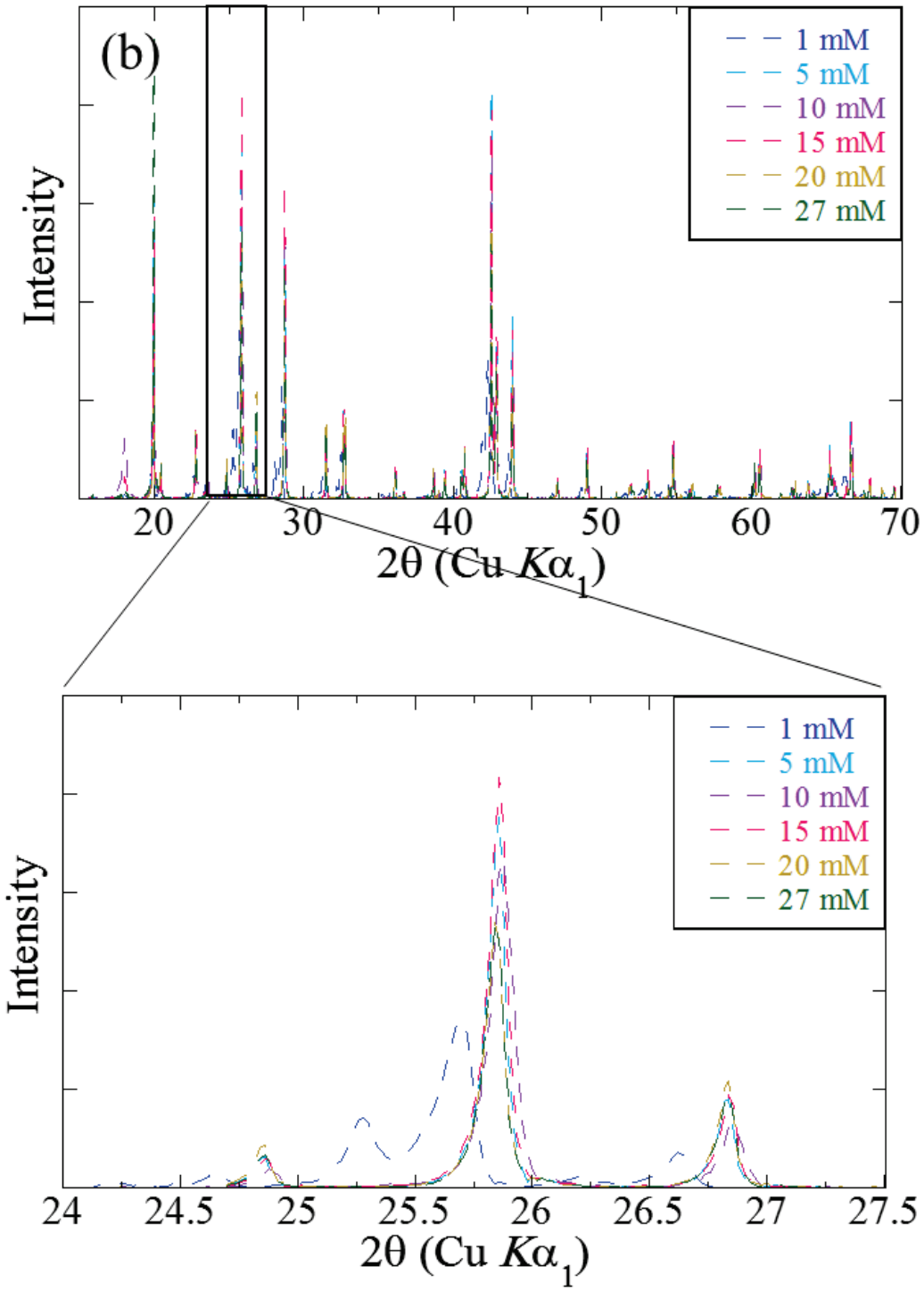

Figure 19. X-ray diffraction patterns of (a) Se(IV)- and (b) Se(VI)-substituted barite as a function of sulfate concentration in solution.

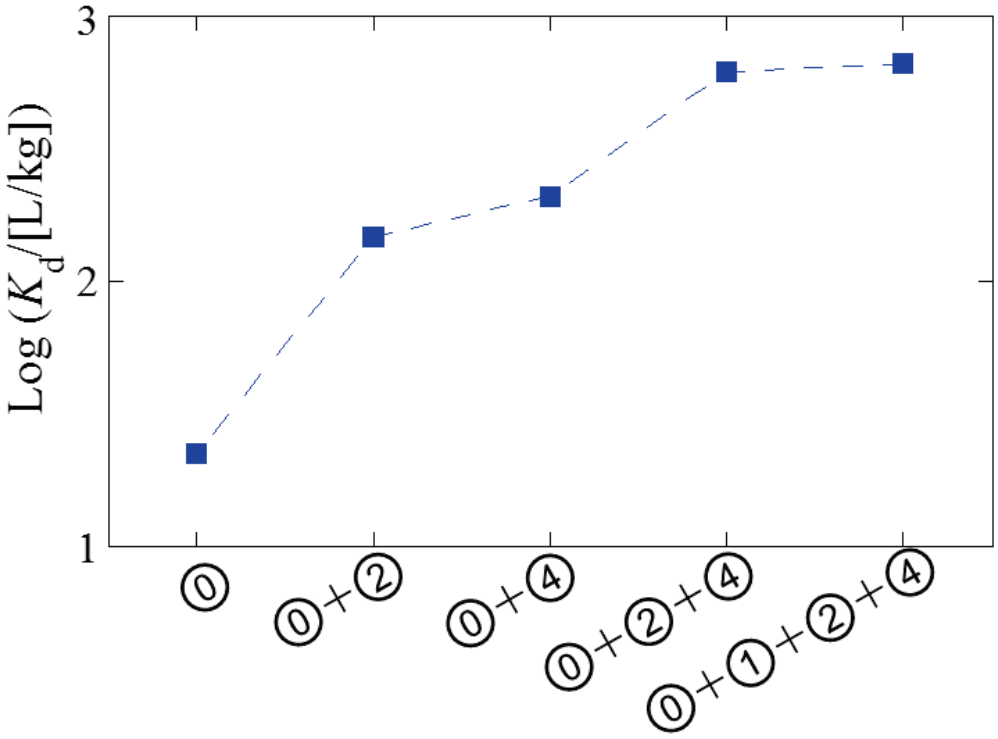

Figure 20. The apparent K_d values of Se(IV) during coprecipitation as a function of ideal conditions.

Table 1. Analysis of apparent K_d values of Se(IV) and Se(VI) during adsorption and coprecipitation with barite as a function of pH

system	Se in input solution				Se in barite						
	pH	R_W^{VI} [%]	$Tr_{initial}$ [mg/L]	SI of barite	$Tr_{on\ barite}$ [mg/kg]	$Tr_{in\ barite}$ [mg/kg]	K_d [L/kg]	R_B^{IV} [%]	R_B^{V} [%]	$K_{Se(IV)}$ [L/kg]	$K_{Se(VI)}$ [L/kg]
MQ water	2.0	0	85.8	4.21	14.5	330.3	3.8	90.0		3.5	
(= IS 0.076 mol; 54	4.0	0	82.6	4.21	55.7	1151.0	13.9	72.3		10.1	
mM Na^+ ; 2.2 mM	6.0	0	81.1	4.21	113.0	916.2	11.3	93.0		10.5	
CO_3^{2-})	8.0	0	85.2	4.21	106.6	1910.7	22.4	100.0		22.4	
	10.0	0	85.1	4.21	36.2	1639.1	19.3	96.0		18.5	
	2.0	100	81.1	4.21	6.5	136.8	1.7		99.6		1.7
	4.0	100	80.7	4.21	4.1	147.2	1.8		86.9		1.6
	6.0	100	82.4	4.21	5.9	181.1	2.2		100.0		2.2
	8.0	100	85.0	4.21	5.4	125.4	1.5		83.2		1.2
	10.0	100	86.0	4.21	5.5	155.8	1.8		100.0		1.8

Table 2. Analysis of apparent K_d values of (a) Se(IV) and Se(VI) and (b) As(III) and As(V) during adsorption and coprecipitation with barite as a function of ionic strength

(a)

Ionic strength (M)	$Tr_{on\ barite}$ [mg/kg]		$Tr_{in\ barite}$ [mg/kg]		K_d [L/kg]		k_a(Å)		k_b(Å)		k_c(Å)	
	Se(IV)	Se(VI)	Se(IV)	Se(VI)	Se(IV)	Se(VI)	Se(IV)	Se(VI)	Se(IV)	Se(VI)	Se(IV)	Se(VI)
0.08	11.8	2.6	707.5	130.8	8.8	1.6	-0.0149	-0.0145	-0.0072	-0.0075	-0.0144	-0.0154
0.15	15.8	1.9	514.9	136.0	6.4	1.7	-0.0142	-0.0155	-0.0068	-0.0079	-0.0138	-0.0150
0.32	21.9	2.3	608.9	132.9	7.6	1.7	-0.0156	-0.0145	-0.0072	-0.0074	-0.0145	-0.0141
0.52	37.6	2.0	640.1	103.7	8.0	1.3	-0.0150	-0.0119	-0.0068	-0.0053	-0.0141	-0.0113

(b)

Ionic strength (M)	$Tr_{on\ barite}$ [mg/kg]		$Tr_{in\ barite}$ [mg/kg]		K_d [L/kg]		k_a(Å)		k_b(Å)		k_c(Å)	
	As(III)	As(V)	As(III)	As(V)	As(III)	As(V)	As(III)	As(V)	As(III)	As(V)	As(III)	As(V)
0.08	6.2	34.4	10.7	142	0.1	1.9	-0.0116	-0.0142	-0.0067	-0.0079	-0.0129	-0.0148
0.15	4.3	19.3	12.5	120	0.2	1.6	-0.0139	-0.0139	-0.0079	-0.0073	-0.0146	-0.0142
0.32	3.9	10.8	6.6	62.1	0.1	0.8	-0.0160	-0.0148	-0.0090	-0.0082	-0.0159	-0.0154
0.52	2.2	41.1	8.4		0.1		-0.0158	-0.0152	-0.0067	-0.0083	-0.0146	-0.0155

Table 3. Analysis of the CNs and distance of Se-O, Se-Ba_1, Se-Ba_2 on/in barite between (a) Se(IV) and (b) Se(VI)

(a)

Shell	Adsorption-Se(VI)		Coprecipitation-Se(VI)		Barite (Gupta et al., 2010)	
	CN	R (Å)	CN	R (Å)	CN	R (Å)
M-O	4.1 (0.3)	1.65 (0.01)	4.3 (0.2)	1.64 (0.00)	4	1.48
M-Ba	1.0 (1.3)	3.02 (0.08)	1.4 (1.0)	3.15 (0.05)	1	3.38
M-Ba	1.1 (1.8)	3.58 (0.11)	3.1 (1.2)	3.58 (0.03)	4	3.62

(b)

Shell	Adsorption-Se(IV)		Coprecipitation-Se(IV)		Barite (Gupta et al., 2010)	
	CN	R (Å)	CN	R (Å)	CN	R (Å)
M-O	2.9 (0.3)	1.69 (0.01)	3.2 (0.2)	1.69 (0.01)	4	1.48
M-Ba	1.7 (1.1)	3.14 (0.06)	1.9 (1.1)	3.20 (0.04)	1	3.38
M-Ba	1.1 (1.6)	3.68 (0.12)	2.2 (1.4)	3.70 (0.04)	4	3.62

Table 4. Analysis of apparent K_d values of Se(IV) and Se(VI) during adsorption and coprecipitation with barite as a function of saturation states

system	solution compositions		Se(IV) in barite			Se(VI) in barite		
	SI of barite	pH	$Tr_{on\ barite}$ [mg/kg]	$Tr_{in\ barite}$ [mg/kg]	K_d [L/kg]	$Tr_{on\ barite}$ [mg/kg]	$Tr_{in\ barite}$ [mg/kg]	K_d [L/kg]
Artificial seawater	2.9	8.0			371.0			498.5
(= IS 0.534 mol;	3.2	8.0	12.7	30610.8	387.7	3.6	18286.8	231.6
442 mM Na^+; 50	3.5	8.0	13.3	16022.4	202.9	4.7	7087.8	89.8
mM Mg^{2+}; 9.6 mM	3.9	8.0	12.0	23660.7	299.7	3.2	3656.5	46.3
Ca^{2+}; 509 mM Cl^-;	4.2	8.0	10.0	28758.4	364.2	2.9	2454.9	31.1
2.2 mM; CO_3^{2-})	4.4	8.0						
+ 0.1 mM Se	4.8	8.0		23528.2	298.0		821.5	10.4
	5.3	8.0						

Table 5. Analysis of unit-cell dimensions of a-, b-, and c-axis in non-subatituted barite as a function of saturation states

Sat. Index	k_a(Å)		k_b(Å)		k_c(Å)	
	MQ-water	ASW	MQ-water	ASW	MQ-water	ASW
2.9		-0.0194		-0.0087		-0.0156
3.2	-0.0165	-0.0190	-0.0080	-0.0085	-0.0145	-0.0152
3.5	-0.0161	-0.0187	-0.0084	-0.0084	-0.0152	-0.0147
4.2	-0.0154	-0.0178	-0.0086	-0.0092	-0.0154	-0.0161
4.4		-0.0146		-0.0061		-0.0145
4.9						
5.3		-0.0130		-0.0077		-0.0143

Table 6. Analysis of unit-cell dimensions of a-, b-, and c-axis in non-subatituted barite as a function of Se concentration in solution

Se conc. (mg/L)	k_a(Å)		k_b(Å)		k_c(Å)	
	Se(IV)	Se(VI)	Se(IV)	Se(VI)	Se(IV)	Se(VI)
0	-0.01543	-0.01543	-0.00860	-0.00860	-0.01540	-0.01540
0.8	-0.03800	-0.03670	-0.00950	-0.00990	-0.02450	-0.02460
80	-0.03880	-0.03820	-0.00890	-0.01000	-0.02310	-0.02500
800	-0.04100	-0.03900	-0.00100	-0.00910	-0.02100	-0.02340

Table 7. Analysis of the CNs and distance of Se-O, Se-Ba_1, Se-Ba_2 at low and high saturation states between (a) Se(IV) and (b) Se(VI).

(a)

Shell	Se(IV) in barite at SI 2.9		Se(IV) in barite at SI 4.2		Barite (Gupta et al., 2010)	
	CN	R (Å)	CN	R (Å)	CN	R (Å)
M-O	3.1 (0.2)	1.70 (0.01)	3.2 (0.2)	1.69 (0.01)	4	1.48
M-Ba	1.8 (1.0)	3.19 (0.04)	1.9 (1.1)	3.20 (0.04)	1	3.38
M-Ba	1.8 (1.4)	3.69 (0.05)	2.2 (1.4)	3.70 (0.04)	4	3.62

(b)

Shell	Se(VI) in barite at SI 2.9		Se(VI) in barite at SI 4.2		Barite (Gupta et al., 2010)	
	CN	R (Å)	CN	R (Å)	CN	R (Å)
M-O	4.2 (0.3)	1.65 (0.01)	4.3 (0.2)	1.64 (0.00)	4	1.48
M-Ba	1.4 (1.4)	3.11 (0.07)	1.4 (0.8)	3.13 (0.04)	1	3.38
M-Ba	4.2 (1.9)	3.61 (0.03)	2.9 (1.1)	3.58 (0.02)	4	3.62

Table 8. Analysis of unit-cell dimensions of a-, b-, and c-axis and apparent K_d values of Se(IV) and Se(VI) during coprecipitation with barite as a function of the as a function of (a) Ca^{2+} , (b) Mg^{2+}, (c) Na^{+} concentrations.

(a)

	k_a(Å)	k_b(Å)	k_c(Å)	K_d (L/kg)
Ca (250 mg/L)	-0.060	-0.0118	-0.0363	
Se(IV)+Ca	-0.127	-0.019	-0.058	147
Se(VI)+Ca	-0.015	-0.007	-0.014	9.88

(b)

	k_a(Å)	k_b(Å)	k_c(Å)	K_d (L/kg)
Mg (600 mg/L)	-0.014	-0.008	-0.014	
Se(IV)+Mg	-0.016	-0.008	-0.014	14.96
Se(VI)+Mg	-0.016	-0.007	-0.014	4.11

(c)

	k_a(Å)	k_b(Å)	k_c(Å)	K_d (L/kg)
Na (12400 mg/L)				
Se(IV)+Na	-0.015	-0.007	-0.01	8.0
Se(VI)+Na	-0.012	-0.005	-0.01	1.3

Table 9. Analysis of the apparent K_d values, removal ratios, and unit-cell dimensions of a-, b-, and c-axis in Se(IV)- and (b) Se(VI)-substituted barite as a function of sulfate concentration in solution

Seulfate (mM)	K_d (L/kg)		Removal of Se (%)		k_a(Å)		k_b(Å)		k_c(Å)	
	Se(IV)	Se(VI)	Se(IV)	Se(VI)	Se(IV)	Se(VI)	Se(IV)	Se(VI)	Se(IV)	Se(VI)
1.00	869.11	1767.62	32.1	93.6	-0.0277	0.0430	0.0141	0.0470	0.0055	0.0540
5.00	176.16	30.90	6.0		-0.0141	-0.0153	-0.0031	-0.0120	-0.0079	-0.0134
10.00	89.52	11.76	3.7	2.0	-0.0164	-0.0110	-0.0047	-0.0077	-0.0106	-0.0113
15.00	44.13	5.70	2.1		-0.0187	-0.0156	-0.0075	-0.0084	-0.0151	-0.0132
20.00	23.32	2.65	4.1	1.5	-0.0123	-0.0163	-0.0052	-0.0081	-0.0116	-0.0138
27.00	6.31	0.46	1.2	0.4	-0.0152	-0.0146	-0.0067	-0.0079	-0.0148	-0.0139

Table 10. Analysis of the selective removal of Se(IV) and Se(VI) conditions through present experiments.

	① speciation by pH	② compentitive ions	③ saturation states	④ Sulfate/Se oxyanion
Se(IV)	◎	◎		○
Se(VI)		○	◎	◎

Table 11. Analysis of the apparent K_d values of Se(IV) during coprecipitation with barite as a function of conditions.

	$K_{Se(IV)}$ (L/kg)	Conditions
⓪	22	pH8, SI 4.2, Sulfate 27 mM
⓪+②	147	⓪ + Ca 10mM
⓪+④	210	⓪ - Sulfate 22 mM (SI 4.56)
⓪+②+④	617	⓪ + Ca 10mM - Sulfate 22mM
⓪+①+②+④	662	⓪ + pH11 + Ca 10mM -Sulfate 22mM

Chapter 6. Conclusions

In this study, the systematics of major and trace elements behaviors to barite was investigated to use barite as (i) a geochemical tracer to estimate redox condition in the past and (ii) a sequester phase for the removal of toxic and/or radioactive elements from solutions.

Chapter 2 shows the systematic of incorporation ions between barite and water in terms of the partition coefficients and unit-cell dimensions of these ions in barite as a function of ionic radius. Analysis of the partition coefficients values of incorporation ions for barite showed that ions having a smaller or slightly larger radii as a substituted ion could be incorporated more efficiently in a crystal lattice than those with much larger radii. Analysis of unit-cell dimensions of incorporation ions for barite also showed that larger ions formed a larger distortion of crystal lattice in barite structure. Thus, the systematics of element behaviors provides a good estimates of partition coefficients to mineral for larger incorporation of trace elements (of geochemical rules for larger incorporation of trace elements by minerals).

Chapter 3 and 4 shows that barite can be employed as a geochemical probe of the depositional redox condition in the paleo-environmental study. The inorganic As(V)/As(III) or Se(VI)/Se(IV) ratio in water could be estimated as the As(V)/As(III)

or Se(VI)/Se(IV) ratio in barite, respectively. Especially under equilibrium, in terms of the redox condition, both species ratios in barite could indicate the redox condition of the depositional environment, and determine whether the redox condition is below or above the redox boundary of Se(VI)/Se(IV) or As(V)/As(III). Given that the redox boundary of Se(VI)/Se(IV) is at a higher redox potential rather than the As(V)/As(III) boundary, the coupling of the As(V)/As(III) ratio with the Se(VI)/Se(IV) ratio in barite estimated by XANES could more precisely constrain the redox environment at the time of deposition of barite in natural systems, which can suggest whether barite is precipitated under oxic, suboxic, or anoxic redox environments.

Chapter 5 shows the factors controlling the distribution of Se(IV) and Se(VI) between barite and water to effectively remove Se(IV) and Se(VI) from solutions by barite. The results showed that the uptake of Se in solution by barite were mainly controlled by the chemical affinity related to adsorption on surface and the structural affinity related to geometry of incorporated metals in substituted site. The transfer of ions from the solution to the surface layer during adsorption results in the electrostatic repulsion between dissolved ion and the charged surfaces site, and controlled by pH, ionic strength, and complexation with competitive ion. The uptake of ions from the surface layer to lattice in crystal during coprecipitation results in the

lattice strain created by the geometry difference of substitution and substituted ion in the crystal lattice, which can be controlled by saturation states, distortion by competitive ions, and substituted- and substitution-component ratios. The uptake of Se(IV) by barite is dependent on the speciation by pH, crystal lattice distortion by competitive ion of Ca^{2+}, and sulfate and selenite ratios due to tis high chemical and low structural affinity to barite. The uptake of Se(VI) by barite, on the other hand, is dependent on the crystal lattice distortion by competitive ion of Ca^{2+}, crystal lattice distortion by saturation states, and sulfate and selenate ratios due to its low chemical and high structural affinity to barite. Thus, we can effectively remove Se(IV) and Se(VI) from solution by barite to understand mechanisms of coprecipitation with barite.

These results allow us to conclude that barite can be used as (i) a new proxy to estimate redox conditions in the past because of the incorporation and preservation of As(V)/As(III) and Se(VI)/Se(IV) ratio in barite and (ii) a sequestering phase for effective removal of toxic and/or radioactive elements from polluted waters by understanding factors controlling the distribution of the incorporation ions between barite and water.

Acknowledgements

I am grateful to Prof. Yoshio Takahashi for his encouragements and suggestion through entire period of my study. I have learned various things from his behaviors for 6 years, not only scientific skills and knowledge, but also the positive and creative attitudes toward science and educations.

I would like to express my thanks to the following financial supports.

The study described in Chapter 3 was supported by a Grant-in-Aid for Scientific Research. This work was performed with the approval of KEK-PF (Nos. 2012G111, 2013B052, 2013G052) and SPring-8 (Nos. 2011B1742, 2012A1240, 2012B1684, 2012B1428, 2013A1177, and 2013B1212). The present work was supported by TAIGA project.

The study described in Chapter 4 was supported by a Grant-in-Aid for Scientific Research. This work was performed with the approval of KEK-PF (Nos. 2015G664) and SPring-8 (Nos. 2015A1768, 2015B1839).

The study described in Chapter 5 was supported by a Grant-in-Aid for Scientific Research. This work was performed with the approval of KEK-PF (Nos. 2013G052, 2015G664) and SPring-8 (Nos. 2013B1212, 2015A1768, and 2015B1839).

This work was supported by JSPS (DC1) for 3 years.

Some traveling fees for a national and international conference were supported by by the Sasagawa Scientific Grants.

This study is greatly improved by supports from following peoples.

I would like to express my thanks to my seniors; Dr. Kazuya Tanaka, Dr. Masato Tanaka. Scientific discussions with them were valuable to improve my study.

I would like to express my sincere thanks to the laboratory member. Daily discussions with following people were really exciting and greatly matured my scientific skills.